Electronic and Vibrational Spectroscopy of Cold Protonated Amino Acids in the Gas Phase

THÈSE N^{O} 4155 (2008)

PRÉSENTÉE LE 28 AOÛT 2008

À LA FACULTE SCIENCES DE BASE

Laboratoire de chimie physique moléculaire

SECTION DE CHIMIE ET GÉNIE CHIMIQUE

ÉCOLE POLYTECHNIQUE FÉDÉRALE DE LAUSANNE

POUR L'OBTENTION DU GRADE DE DOCTEUR ÈS SCIENCES

PAR

Sébastien MERCIER

ingénieur chimiste diplômé EPF
de nationalité suisse et originaire de Lausanne (VD)

acceptée sur proposition du jury:

Prof. H. Girault, président du jury
Prof. T. Rizzo , directeur de thèse
Prof. C. Jouvet, rapporteur
Prof. J. Maier, rapporteur
Prof. Y. Tsybin, rapporteur

ÉCOLE POLYTECHNIQUE
FÉDÉRALE DE LAUSANNE
Lausanne, EPFL
2008

Abstract

In this thesis report, we describe a novel home-built instrument designed to study the spectroscopy of biomolecular ions in the gas phase and at low temperature, and we present the first experimental results obtained on protonated aromatic amino acids. The apparatus consists in a tandem mass spectrometer equipped with a nanospray ion source and a cryocooled 22-pole ion trap. The charged species produced by the source traverse a first quadrupole mass filter and mass-selected ions are then accumulated and thermalized in the ion trap, where their vibrational temperature can be lowered to ~ 10 K. Two setups allow us to generate ultraviolet and infrared laser light to spectroscopically probe the trapped ions by photodissociation. The resulting fragment ions are finally released from the trap and mass analyzed by a second quadrupole spectrometer.

Photodissociation electronic spectra have been measured for the protonated amino acids tryptophan ($TrpH^+$) and tyrosine ($TyrH^+$), as well as for hydrated complexes of the former. The spectrum of $TyrH^+$ exhibits sharp, fully resolved vibronic transitions, which attests to the low temperature of the ions. In contrast, that of tryptophan shows a broad absorption band that covers several hundreds of wavenumbers. This has been attributed to lifetime broadening related to an ultrafast (< ~ 100 fs) deactivation mechanism of the $TrpH^+$ $S_1(\pi\pi^*)$ excited state. This phenomenon is caused by a strong coupling between this $\pi\pi^*$ state and a nearby dissociative state of $\pi\sigma^*$ character mainly localized on the charged ammonium group. Solvation of $TrpH^+$ by only two water molecules is sufficient to significantly destabilize the σ^* orbitals and reduce that coupling, which results in a longer excited-state lifetime and a fully resolved electronic spectrum. These interpretations are supported by *ab initio* and density functional theory (DFT) calculations.

Infrared-ultraviolet double resonance spectroscopic techniques have been successfully implemented to identify the different conformers of $TyrH^+$ and doubly hydrated protonated tryptophan ($TrpH^+\cdot W_2$) by measuring conformer-specific vibrational and electronic spectra for each of them. By comparison with the results of DFT geometry and harmonic frequency calculations, we could confidently determine the structures of the $TyrH^+$ conformers and suggest possible assignments for those of $TrpH^+ \cdot W_2$. Two important stabilizing interactions could be inferred from these results: (i) the attraction between the charged ammonium group and the π-electron cloud of the aromatic ring; (ii) the hydrogen-bonding interaction of a donor water molecule to the acceptor indole ring of $TrpH^+ \cdot W_2$.

Keywords: electronic spectroscopy, vibrational spectroscopy, double resonance spectroscopy, photodissociation, electrospray, nanospray, tandem mass spectrometry, quadrupole, 22-pole ion trap, protonated amino acids, tryptophan, tyrosine, peptides, cold ions, microsolvation.

Résumé

Ce travail de thèse décrit la construction d'un nouvel instrument conçu pour l'étude spectroscopique d'ions biomoléculaires en phase gazeuse et à basse température, et nous en présentons les premiers résultats expérimentaux obtenus sur des acides aminés aromatiques protonnés. Cet appareil consiste en un spectromètre de masse en tandem équipé d'une source d'ions nanospray et d'une trappe ionique à 22 pôles cryoréfrigérée. Les espèces chargées produites par la source passent au travers d'un premier filtre de masse quadrupolaire et les ions ainsi sélectionnés sont accumulés et thermalisés dans la trappe, où leur température vibrationnelle peut être abaissée jusqu'à ~ 10 K. Deux installations laser nous permettent de générer de la lumière ultraviolette et infrarouge afin d'étudier par photodissociation la spectroscopie des ions piégés. Les fragments ainsi formés sont finalement libérés de la trappe, puis analysés par un second spectromètre quadrupolaire.

Des spectres électroniques de photodissociation ont pu être mesurés pour les formes protonnées des acides aminés tyrosine (TyrH^+) et tryptophane (TrpH^+), ainsi que pour des complexes hydratés de ce dernier. Le spectre de TyrH^+ est constitué de transitions vibroniques étroites et parfaitement résolues, ce qui démontre la basse température des ions. En revanche, celui de TrpH^+ montre une large bande d'absorption qui couvre plusieurs centaines de cm^{-1}. Cela est attribué à un élargissement lié à la très courte durée de vie de l'état excité $S_1(\pi\pi^*)$ de TrpH^+ causée par un mécanisme de désactivation ultrarapide (< ~ 100 fs). Ce phénomène est provoqué par un important couplage entre cet état $\pi\pi^*$ et un état dissociatif voisin de type $\pi\sigma^*$ qui est principalement localisé sur le groupe ammonium chargé. La solvatation de TrpH^+ par seulement deux molécules d'eau suffit à considérablement déstabiliser les orbitales σ^* et à diminuer ce couplage, avec pour conséquence un allongement de la durée de vie de l'état excité et l'obtention d'un spectre électronique parfaitement résolu. Ces interprétations sont corroborées par des calculs *ab initio* et de théorie de la fonctionnelle de densité (DFT).

Des techniques spectroscopiques de double résonance infrarouge-ultraviolet ont été appliquées avec succès pour identifier les différents conformères de $TyrH^+$ et du complexe doublement hydraté du tryptophane protonné ($TrpH^+ \cdot W_2$) en mesurant des spectres vibrationnels et électroniques spécifiques pour chaque conformation. Par comparaison avec des résultats de calculs DFT de géométries et de fréquences harmoniques, nous avons pu déterminer avec certitude les structures des conformères de $TyrH^+$, ainsi que proposer de possibles attributions pour ceux de $TrpH^+ \cdot W_2$. Ces résultats ont permis de mettre en évidence deux interactions particulièrement stabilisatrices: (i) l'attraction entre le groupe ammonium chargé et le nuage d'électrons π du noyau aromatique; (ii) la liaison hydrogène entre une molécule d'eau «donneuse» et le noyau indole «accepteur» de $TrpH^+ \cdot W_2$.

Mots-clés: spectroscopie électronique, spectroscopie vibrationnelle, spectroscopie de double résonance, photodissociation, electrospray, nanospray, spectrométrie de masse en tandem, quadrupôle, trappe ionique à 22 pôles, acides aminés protonnés, tryptophane, tyrosine, peptides, ions froids, microsolvatation.

Contents

1 Introduction 1

1.1 Why in the gas phase? 3
1.2 Why use spectroscopy? 6
1.3 Why study ions? 8
1.4 Why at low temperature? 10
1.5 Interplay with theory 12
1.6 Goals and outline 13
References 15

2 Description and characterization of the tandem mass spectrometer .. 23

2.1 The home-built apparatus and techniques it relies on 23
  2.1.1 Machine overview 23
  2.1.2 Electrospray ionization 29
  2.1.3 Quadrupole mass filtering 33
  2.1.4 The 22-pole ion trap 36
2.2 Characterization of the ion trap 41
  2.2.1 Helium pumping time 41
  2.2.2 Ion trapping time 45
  2.2.3 Ion cooling efficiency 46
2.3 Description of the laser setups 51
  2.3.1 Generation of UV laser light 51
  2.3.2 Generation of IR laser light 52
References 54

3 Spectroscopic techniques 57

3.1 Timing of events 57

3.2 Measurement of a photofragment mass spectrum ... 59
3.3 Measurement of a photodissociation UV or IR spectrum ... 60
3.3.1 Spectroscopic schemes ... 61
3.3.2 Corrections to the measured ion signal ... 62
3.3.3 Molecular size and lifetime considerations ... 64
3.4 Conformer-specific spectra by IR-UV double resonance spectroscopy ... 69
3.4.1 Existing strategies for distinguishing different conformers ... 70
3.4.2 Adaptation to the spectroscopy of cold trapped ions ... 71
References ... 74

4 UV spectroscopy of protonated amino acids: $TrpH^+$ and $TyrH^+$ ... 79

4.1 Electronic spectrum of protonated tryptophan ... 81
4.1.1 Photofragment mass spectra at room temperature and 6 K ... 81
4.1.2 Electronic spectra at room temperature and 6 K ... 84
4.2 Electronic spectrum of protonated tyrosine ... 86
4.2.1 Photofragment mass spectra at room temperature and 6 K ... 86
4.2.2 Electronic spectra at room temperature and 6 K ... 89
4.3 Discussion ... 91
4.3.1 Sharpness and broadness of the spectra ... 92
4.3.2 Excited-state lifetime and what determines it ... 93
References ... 98

5 UV spectroscopy of hydrated $TrpH^+$ ... 101

5.1 Electronic spectra of hydrated $TrpH^+$ complexes ... 103
5.1.1 Photofragment mass spectra at room temperature and 6 K ... 103
5.1.2 Electronic spectra at low temperature ... 108
5.2 Discussion ... 111
5.2.1 Lifetime lengthening upon hydration ... 111
5.2.2 Computation of the lowest-energy structures ... 112
5.2.3 Excited-state energy and dynamics calculations ... 115
5.2.4 Generality of the observed phenomenon ... 119
References ... 122

6 Identification of conformers by IR-UV double resonance spectroscopy 125

6.1 Detailed analysis of the $TyrH^+$ electronic spectrum 126

6.1.1 Conformer-specific vibrational spectra of $TyrH^+$ 126

6.1.2 IR-UV hole-burning and vibronic assignment of $TyrH^+$ 129

6.1.3 Alternative method for conformer assignment of peaks 133

6.2 Detailed analysis of the $TrpH^+{\cdot}W_2$ electronic spectrum........ 134

6.2.1 Conformer-specific vibrational spectra of $TrpH^+{\cdot}W_2$ 134

6.2.2 IR-UV hole-burning and vibronic assignment of $TrpH^+{\cdot}W_2$ 138

6.3 Discussion 142

6.3.1 Geometrical assignment of $TyrH^+$ conformers 142

6.3.2 Geometrical assignment of $TrpH^+{\cdot}W_2$ conformers 143

References 146

7 Conclusions 149

7.1 Summary 149

7.2 Future perspectives 152

References 154

List of figures 157

List of tables 159

List of abbreviations and acronyms 161

Acknowledgements 163

Curriculum vitae 165

Chapter 1 Introduction

It has been long established that molecular recognition, i.e., the high specificity of intra- and intermolecular interactions, plays a determinant role in all biological processes taking place in living organisms (see for instance references [1, 2], as well as this whole issue of *Chemical Reviews* dedicated to that subject). It is equally well known that the shape of biological molecules is closely related to their particular function, as exemplified by various phenomena such as enzymatic activity, signal transduction, molecular switches and motors, antibody-antigen complexation, etc. For these reasons, numerous different techniques have been developed over the past decades to determine the structures of various biomolecular entities, and this research field has known an exponential growth of activity since the middle of the 20th century. A simple search on an online database of scientific literature suffices to illustrate this trend, as depicted in Figure 1.1 for a search performed on the ISI Web of Knowledge^{SM} (http://isiwebofknowledge.com) with «protein structure» as a criterion. The first method that allowed the elucidation of large biomolecular geometries on an atomic scale was X-ray crystallography, with the famous discovery of DNA structure in 1953 [3-6] and the first high-resolution three-dimensional maps of globular proteins near 1960 [7, 8]. Despite its remarkable resolving power, an important limitation of this technique is the necessity of obtaining large enough crystals of the substance of interest, which remains a challenging task for many biological macromolecules, as for instance membrane proteins. However, recent advances in the domain suggest the possibility of extending the method to noncrystalline samples by using femtosecond X-ray pulses [9]. Alternative approaches to conventional X-ray crystallography have already been developed, which are able to provide images of nearly the same resolution. One of them is electron crystallography (or electron cryomicroscopy), which only requires two-dimensional crystals, but whose application can be restricted due to the damage of molecules caused by electron radiation [10, 11]. Another powerful technique, now widely used for biomolecular structure determination, is multidimensional nuclear magnetic resonance (NMR) spectroscopy, which has the considerable advantage of probing molecules in the solution phase [12-14]. Traditionally, its implementation has been limited to relatively small biomolecules, owing to the overlap of a large number of peaks. However, continuous improvement and innovation in the applied methodologies are pushing back this mass limit and, currently, molecules of more than 100 kDa can be investigated [15].

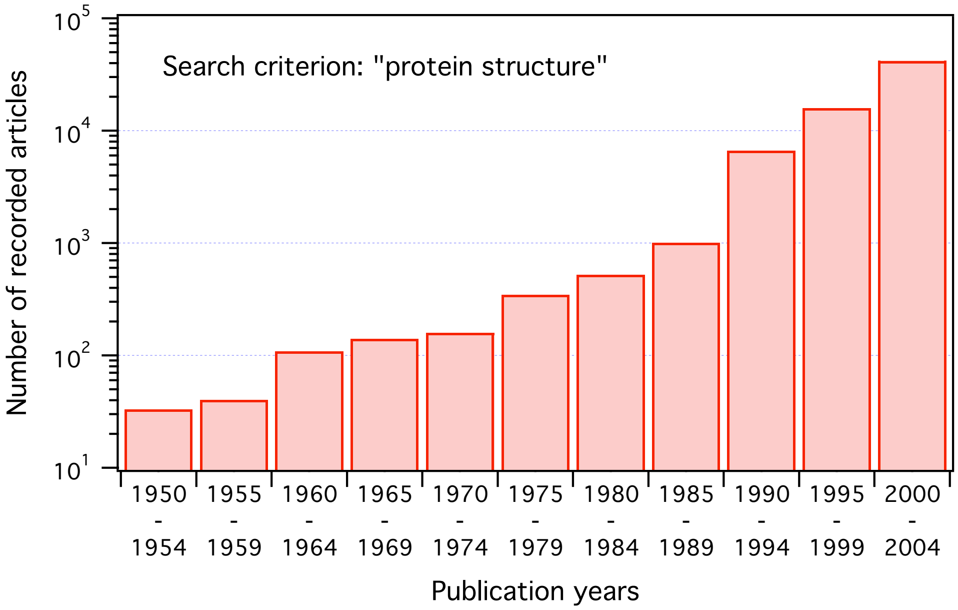

Figure 1.1: Illustration of the exponential growth of activity in the field of biomolecular structure determination since the 1950s. The histogram shows the number of results returned by the ISI Web of Knowledge^{SM} literature database for the term «protein structure». Note the logarithmic vertical scale.

Besides the aforementioned high-resolution techniques, there exists a variety of other experimental strategies providing lower-resolution structural information on biomolecules, such as the relative amounts of different secondary structures in proteins, the distance between specific sites on a molecule or even measurements of the dynamics of conformational changes (e.g., protein folding). Among these, one can cite in particular several spectroscopic approaches like Fourier transform infrared spectroscopy (FTIR; [16]), circular dichroism (CD; [17-20]), various fluorescence-based techniques (e.g., FRET: Förster resonance energy transfer; [21, 22]), or chemical modifications such as hydrogen/deuterium (H/D) exchange [23, 24].

All the methods presented thus far are mainly concerned with the exploration of biomolecules *in a condensed medium*, be it solid, liquid or membranous. In contrast, as conveyed by the title of this doctoral dissertation, we propose to study biologically related molecules by measuring the spectroscopic properties of their protonated form *in the gas phase* and at low temperature. In the remainder of this introduction, we will detail our motivations for adopting such an approach.

1.1 Why in the gas phase?

At first glance, it may appear somewhat irrelevant to investigate the properties of biomolecules in the gas phase, while their *in vivo* activity essentially takes place in solution or in cell membranes. However, it has become evident, over the past decades, that the specific geometries of biomolecular entities result, for the most part, from a subtle balance between intramolecular and intermolecular noncovalent interactions, in particular with the surrounding solvent. Therefore, condensed-phase studies face the problem of understanding the equilibrium produced by a tremendous number of such interactions. As a consequence, in spite of the enormous efforts devoted to these questions for many years, the exact mechanisms governing the folding and stability of even medium-sized biomolecules remain very unclear. Hence, one of the major motivations for probing these species in the gas phase is to apply a bottom-up strategy and start to understand the relative importance of different interactions at the most fundamental level. By removing a molecule from its aqueous environment, one can study its intrinsic properties free from any external perturbation and thus focus on the identification of the intramolecular forces that control its conformation. The influence of solvation can then be investigated by sequentially adding solvent molecules to the bare species and observing how it affects the structural preferences of the complex.

In order to measure the properties of biomolecules in the gas phase, one obviously needs a means to volatilize them in sufficient quantity. Basic thermal methods suffer from a severe limitation in that regard, since even relatively small biomolecules have very low vapor pressures and are highly labile, so that they mostly decompose upon heating rather than evaporate. Therefore, a multitude of different techniques have been invented to facilitate the volatilization of large nonvolatile molecules, only some of which will be mentioned hereafter. One of the first that achieved such a goal, near the end of the 1960s, was field desorption (FD) [25-27]. A thin wire covered with graphitic microneedles is dipped in a sample solution and submitted *in vacuo* to a high voltage. A very strong electric field results at the needles' tips and, upon gentle heating, sample molecules get ionized and desorb from the wire's surface, already at temperatures well below their boiling (or sublimation) point. Nonetheless, as the size of the studied molecule increases, the required heating reaches levels where thermal decomposition starts to occur. This and other technical problems related to FD made necessary the development of alternative methods. Around 1980, several approaches emerged which were based on the ejection of material from a sample-covered surface by using, for instance, a beam of neutral atoms (FAB: fast atom bombardment [28-30]) or intense laser light (LD: laser desorption [31, 32]). Others, such as thermospray [33-36] and electrospray ionization (ESI; [37-39]), used the nebulization of a sample solution through a capillary to produce a mist of charged droplets from which intact pseudomolecular ions can desorb (ESI, which we use to produce our ions, will be described in more detail in *Chapter 2*). All these techniques made possible the volatilization of macromolecules of several kilodaltons and heavier. Two of them have become widely popular in both the academic research and the industry: ESI and matrix-assisted laser desorption/ionization (MALDI; [32, 40-42]), an improved version of LD where the sample molecules are embedded in a matrix. Both methods can bring into the gas phase and without degradation large proteins having masses > 100 kDa.

These volatilizing techniques were all designed with a view to producing large gas-phase molecules in an ionized state and subsequently study them with mass spectrometry. Originally, the structural information that could be obtained with this approach on polypeptides or proteins was mainly related to the primary structure of such molecules (peptide sequencing), using mass analysis to identify the peptide fragments produced either in solution (by chemical or enzymatic degradation) or directly in the gas phase (e.g., by photo-induced or collision-induced dissociation) [43-53]. This powerful methodology is universally used nowadays in the field of proteomics. However, the amino acid sequence of a polypeptide chain gives few hints on its three-dimensional geometry, and in order to gain insight into the spatial architecture of proteins (secondary and tertiary structures), several different innovative techniques have been developed. One of them, briefly mentioned earlier, is H/D exchange. The basic principle is to expose a molecule to a deuterated solvent (e.g., D_2O or CH_3OD) for a certain time, and then to detect how many of its potentially labile hydrogen atoms have been replaced by deuterium [54]. Such measurements can provide some information on the conformation of proteins, because the exchange rate of labile hydrogens depends, among other things, on their accessibility to solvent and on their «availability», so that hydrogen atoms buried in the core of a protein or involved in hydrogen bonds will exchange slower than free hydrogens on the protein surface. H/D exchange experiments have been first performed in solution, where conformational changes of proteins could be observed, along with their dynamics, by monitoring the number of exchanged hydrogens, using for instance two-dimensional NMR [23] or ESI mass spectrometry [55]. A second approach has been to first volatilize the proteins and then to bring them into contact with a gaseous deutared solvent, which allowed the investigation of the gas-phase conformational preferences of several multiply charged proteins, as well as their folding and unfolding [56-58]. Using the same method, Freitas and Marshall studied bradykinin, a nonapeptide containing two arginine residues, and arrived at the conclusion that its protonated form exists in the gas phase as a zwitterionic (and possibly salt-bridged) structure, having both arginine side chains protonated and the terminal acidic group deprotonated [59].

Another strategy to assess the three-dimensional structure of large gas-phase ions is to carry out ion mobility studies. Briefly, generated ions are dragged, under the influence of a weak uniform electric field, through a drift tube containing several millibars of a buffer gas. Ions differing in their number of charges and/or conformations will have distinct mobilities and will thus exit the tube at different arrival times [60]. From these measurements, the collision cross sections of individual conformations can be calculated and compared with model structures. For instance, Jarrold and coworkers have probed the conformations and folding properties of proteins such as cytochrome c (104 residues) [61, 62] and bovine pancreatic trypsin inhibitor (BPTI; 58 residues) [62], and observed the formation of helical structures in small model peptides [63]. A fairly recent variation of this ion mobility technique has been developed by Guevremont and coworkers: high-field asymmetric waveform ion mobility spectrometry (FAIMS) [64]. Instead of traveling in a constant electric field, ions in FAIMS are carried by a gas flow and subjected to alternating high and low transverse electric fields. Although its fundamental principles are not fully understood yet, FAIMS is based on the varying mobilities of the ions at high field, so that even distinct conformations of similar collision cross sections can be separated [65, 66]. Some groups have combined ion mobility and H/D exchange experiments to compare the results of both approaches, using either conventional ion mobility measurements [67, 68] or FAIMS [69].

In the mid 1990s, the group of Williams started to use a new technique to measure the dissociation energetics of trapped gas-phase ions. Termed blackbody infrared radiative dissociation (BIRD), the method consists in measuring, typically in a Fourier transform ion cyclotron resonance mass spectrometer (FT-ICR), the kinetics of ion dissociation induced by the slow absorption of blackbody radiation from the vacuum chamber walls [70]. Temperature-dependent experiments allow the extraction of activation energies and frequency factors for the lowest-energy dissociation pathways of mass-selected ions. Acquiring these parameters for a given molecule and a set of judiciously chosen analogues makes possible the inference of structural properties. Some examples are the evidence reported by this group for the formation of Watson-Crick base pairing of short strands of oligonucleotides [71] and for the salt-bridged structure of protonated bradykinin [72], as well as the suggestion that small hydrated complexes of cationized valine might be zwitterionic [73, 74] (although the latter fact has been questioned by experiments conducted in our laboratory [75, 76]).

In addition to the few methods just presented, biologically related molecules in the gas phase have also been investigated by a variety of spectroscopic techniques. Some of them will be described in the following sections.

1.2 Why use spectroscopy?

Techniques such as H/D exchange, ion mobility or BIRD, despite their undeniable potential to help decipher many gas-phase ion properties, provide only limited structural information. The extent of isotopic exchange and the collision cross section of an ion give an overall but undetailed picture of its geometry. Its dissociation energetics revealed by BIRD are obviously important characteristics, yet they constitute a rather indirect means to probe conformational preferences. On the other hand, the spectroscopic properties of a molecule are extremely sensitive to the three-dimensional arrangement of its atoms and even minute changes in its conformation can give rise to detectable spectroscopic shifts. For example, accurate values of a molecule's rotational constants, and hence of its moments of inertia, can be obtained from various spectroscopic approaches. In particular, the geometries of different conformers of neutral jet-cooled analogues of the three aromatic amino acids (tryptophan, tyrosine and phenylalanine), and some of their hydrated complexes, have been successfully assigned by microwave spectroscopy [77, 78], rotational coherence spectroscopy [79, 80], and fully [81-84] or partially [85-89] rotationally resolved electronic spectroscopy. Of course, vibrational spectroscopy is a very powerful probe of chemical structure as well, since the vibrational frequency of a given bond is highly dependent on its local environment. Several examples of such measurements carried out on gas-phase biomolecules will be presented further below. Finally, electronic spectroscopy can also reveal subtle geometrical features through the influence on a chromophore's photophysics of a nearby charge, a hydrogen bond or even the orientation of a neighboring dipole. As a typical illustration of this latter fact, one can simply cite the case of 2-naphthol (2-hydroxynaphthalene), which possesses two stable isomers, *syn* and *anti*, differing only in the orientation of the O-H bond and whose electronic origin transitions are separated by 317 cm^{-1} [90].

The first electronic spectrum of a gas-phase amino acid was reported in the mid 1980s by the group of Levy, who measured vibrationally resolved resonantly enhanced two-photon ionization spectra (R2PI) and laser-induced fluorescence spectra (LIF) of jet-cooled neutral tryptophan [91-93] and some of its derivatives [94]. Through power dependence and dispersed fluorescence studies, they demonstrated the presence of several conformers in the molecular beam. They later carried out similar experiments on tyrosine and phenylalanine [95]. Following this pioneering work, a number of groups applied the same methods to larger peptides and many other biomolecules, and developed innovative double resonance spectroscopic techniques (e.g., UV-UV hole-burning or IR-UV depletion spectroscopy), which made possible the acquisition of conformer-specific electronic and vibrational spectra [96-106]. Over the past twenty years, the size of peptides probed by this approach gradually increased from single amino acids up to capped tripeptides (i.e., tetrapeptide analogues), mapping at each step the conformational preferences of these molecules. In the larger ones, some secondary structure of the peptide backbone, such as β- and γ-turns or 3_{10}-helices, is observed to emerge [107-109]. An excellent review of this whole subject has recently been written by Chin et al. [110]. In the past few years, some groups have started to explore even longer oligopeptides (e.g., gramicidin, a 15-mer) [111-113]. Other analogous investigations aimed at understanding the influence of solvation on the conformations of peptides by examining their hydrated clusters [86, 87, 114-118], or probed the formation of β-sheet structures in short peptide dimers [119-121]. These techniques have also been used to study the nucleotide bases [122-126], as well as their pairing [127-130]. A recent review by de Vries and Hobza covers this particular research field [131]. Finally, one can mention the elaboration of two inventive spectroscopic schemes by Zwier and coworkers, which further complete this arsenal of methods. One consists in using the absorption of an IR photon by a specific conformer to transfer part of its population into the potential wells of others [132-135]. This technique enables the detailed exploration of the potential energy surface (PES) and the estimation of energy barriers between conformers, and holds great promise for the study of isomerization dynamics in flexible biomolecules. The second, brand new technique proposed by this group is a *triple* resonance spectroscopic scheme, IR-IR-UV hole-burning, that makes possible the measurement of conformer-specific vibrational spectra even in cases where two conformers have indistinguishable electronic spectra [136].

1.3 Why study ions?

All the spectroscopic studies referred to in the previous section were concerned with gas-phase biomolecules in their neutral form. However, these same molecules *in vivo* are often globally or locally charged. It is well known, for instance, that most amino acids in solution at physiological pH (~ 7) are zwitterions, having a deprotonated carboxylate group (COO^-) and a protonated ammonium group (NH_3^+). Moreover, peptides and proteins can contain multiple residues with acidic (aspartic and glutamic acids) or basic (lysine, arginine and histidine) side chains, so that the entire molecule generally possesses an overall net charge [137]. Besides, very important biological processes involve metal ions, e.g., in the case of transmembrane ion channels or pumps. Therefore, the study of charged biomolecules is at least equally important as that of their neutral counterparts. Since the development, near 1990, of the new volatilizing methods presented above (ESI, MALDI), a profusion of mass spectrometric investigations on large gas-phase biomolecular ions have been undertaken. On the other hand, it took significantly more time before *optical* spectroscopy began to tackle these species, and the first publications on such studies appeared only at the dawn of the new millennium. A nonexhaustive overview of this research field is given in the following.

McLafferty and coworkers were among the first to report optical spectra of biomolecular ions in the gas phase. Using resonant infrared multiphoton dissociation (R-IRMPD) in an FT-ICR spectrometer, they obtained vibrational spectra of noncovalently bound fragments of ubiquitin [138] and of various proton-bound complexes of amino acids [139]. This method is being increasingly employed, notably by using free-electron lasers, because their high power and wide tunability allow the acquisition of infrared spectra over the whole «fingerprint» region (< 2500 cm^{-1}), even for covalently bonded species. Such measurements have been used to elucidate the structures of many amino acids, small peptides and other biomolecules that are either protonated [140-149] or cationized [150-152]. The most stable tautomers of several protonated nucleobases could also be identified [153], and the technique was even applied to cytochrome c in different charge states, although the structural information obtained for this large protein was obviously more qualitative [154]. Other photodissociation experiments were carried out with less cumbersome infrared lasers, like optical parametric oscillators (OPO), to record vibrational spectra in the hydride stretch region (~ 2800 to 3800 cm^{-1}). Since these lasers are also less powerful, their use is in principle restricted to the dissociation of more weakly bound species, as for example the hydrated complexes of protonated or cationized amino acids [75, 76, 155]. However, Williams and coworkers recently managed to measure the spectra of *unsolvated* cationized arginine by radiatively heating the ions before laser irradiation (see the description of BIRD above) [156]. Some of these results provided evidence for the existence of gas-phase zwitterionic amino acids.

In contrast to the flourishing number of articles about infrared spectral data of isolated biomolecular ions, corresponding reports on their electronic properties are still much scarcer in the scientific literature. One of the earliest example was the publication of the electronic excitation spectra of the green fluorescent protein chromophore in its protonated and deprotonated forms [157, 158]. It was not until 2004 that Nolting et al. announced the measurement of the first photodissociation electronic spectrum of a protonated amino acid in the gas phase, tryptophan [159], followed the next year by that of the protonated nucleobase adenine [160]. Dugourd and coworkers reported an analogous spectrum of protonated tryptophan, although on a wider wavelength range and at lower resolution, and conducted a detailed analysis of its various photofragmentation channels [161]. The group of Parks adopted a different approach, also based on electronic photoexcitation, by monitoring the temperature-dependent fluorescence of trapped dye-tagged biomolecular ions, in order to probe their conformational dynamics. With this method, they could observe an intermediate state in the dissociation («unzipping») of oligonucleotide duplexes [162], and studied structural changes in several small polypeptides and proteins [163, 164].

Another essential feature of electronic spectroscopy, besides the information that it provides on a molecule's electronic structure, is that it also allows one to investigate its excited-state dynamics, which is imperative to understand the remarkable photostability of biological chromophores like the DNA bases or the aromatic amino acids, not to mention the processes of vision or photosynthesis. A few groups have recently begun to address these questions by examining the gas-phase ions of such species. Nielsen and coworkers recorded the decay of cationic and anionic mono- and dinucleotides in an ion storage ring following photoexcitation. Although their apparatus only allows the direct observation of relatively slow decays ($\tau \gtrsim 1\ \mu s$), hence related to statistical dissociation processes, the measured amount of total ion depletion led them to the conclusion that photofragmentation occurs predominantly through nonstatistical channels, in particular for the protonated species [165, 166]. Other groups have explored the electronic excited-state dynamics of biochromophore ions on a much shorter timescale by implementing femtosecond pump-probe laser schemes. With this approach, they determined the excited-state lifetimes of protonated aromatic amino acids [167-170] and of di- or tripeptides containing them [171-173], as well as that of protonated adenine [174]. Some of these experiments are closely related to the work presented here and will thus be further discussed in later chapters.

1.4 Why at low temperature?

As already mentioned earlier, a primary motivation for studying biomolecules *in vacuo* rather than in their native aqueous environment is to disentangle the stabilizing (or destabilizing) contributions resulting from intermolecular and intramolecular interactions. A direct consequence of this strategy in the case of spectroscopic measurements is a substantial simplification of the acquired spectra. Indeed, molecules in solution interact with a more or less extended shell of solvent molecules in constant motion, so that, at any instant, each solute molecule experiences a different local environment than the others and thus possesses slightly different spectroscopic properties. Therefore, a solution-phase spectrum represents the average of a multitude of distinct individual spectra, each of which might be simple and sharp in itself, which results in considerably broadened transitions from which detailed information has been smudged. In contrast, molecules that are isolated in a vacuum all experience the same environment and the inhomogeneous broadening of their spectrum is thus significantly reduced.

Notwithstanding, the spectrum of a given substance measured in the gas phase at ambient temperature may still present important inhomogeneous broadening, particularly in the case of large flexible species such as most biomolecules. There are mainly two reasons for that. First, a flexible molecule can usually adopt several different conformations and a number of them may be sufficiently stable to have a nonnegligible relative population at room temperature. Since each conformation can have a distinct spectrum, the result will be a superposition of transitions originating from these different conformers. Secondly, even molecules that have identical geometries will not necessarily be in the same quantum state at the moment of irradiation, which again gives rise to different absorption characteristics. This effect is especially important for large flexible molecules, because they possess many vibrational excited states of low energy that can be appreciably populated at room temperature. It immediately appears from these considerations that both sources of inhomogeneous broadening can be minimized by decreasing the temperature of the gaseous sample, so that only the most stable conformers and the lowest vibrational (and rotational) energy levels will be populated. For neutrals, these objectives are successfully achieved through the technique of jet cooling, where the sample molecules are entrained in the supersonic expansion of a carrier gas and internally cooled by collisions with the latter. The typical temperatures attainable with this method for the different degrees of freedom are < 1 K for translations, a few kelvins for rotations and a few tens of kelvins for vibrations. An early review of the principles of supersonic expansion cooling and its utilization for laser spectroscopy is given in reference [175], and examples of applications to the study of biomolecules include all the ones presented above in section *1.2 Why use spectroscopy?*.

In the case of ions, cooling is usually performed by confining them in a trap maintained at low temperature and allowing them to collide with a buffer gas for thermalization. Various implementations have been reported on different types of ion traps. For instance, Weinkauf and coworkers, for their measurement of the electronic spectrum of protonated tryptophan, have connected a quadrupole ion trap to reservoirs of liquid nitrogen and could reach a temperature of ~ 140 K [159]. The group of Williams have carried out some of their BIRD experiments at subambient temperatures by wrapping an FT-ICR cell in a thermal jacket cooled by liquid nitrogen, thus bringing the temperature in the center of the cell down to about 180 K [176]. Another design consists in mounting a linear multipole ion trap on a liquid-helium cryocooler, which makes it possible to attain temperatures as low as 10 K [177]. However, a requirement for achieving effective ion cooling at such low temperatures is the use of a trap with a sufficiently large number of poles. The reasons for this will be detailed in *Chapter 2*, where we describe the 22-pole ion trap that we use in our instrument.

A potentially promising technique for the production of jet-cooled ions has been recently put forward by Simons and coworkers [143-146]. They have developed a new photochemical scheme to protonate biomolecules in the gas phase, where the molecule of interest forms a complex with a proton donor (e.g., phenol) in a supersonic expansion. Proton transfer from the donor to the molecule is initiated by R2PI of the former, and detachment of the resulting neutral radical leaves behind the protonated species. As yet, the method generates warm ions, but their jet-cooling could possibly be obtained by triggering the R2PI step early enough in the expansion.

1.5 Interplay with theory

Even though it has not been mentioned explicitly, all the studies cited in this introduction and being concerned with the determination of gas-phase molecular structure – whether by purely mass spectrometric methods or by optical spectroscopy, on small neutrals or on large ions, leading to a detailed geometrical assignment or to an overall picture of the molecular shape – all depended intimately on the results of theoretical predictions in order to optimally interpret the experimental ones. The applied methods range from simple force-field molecular mechanics to high-level *ab initio* or density functional theory (DFT) calculations using large basis sets. Which method is eventually chosen depends mainly on the size and complexity of the system under investigation, on the desired accuracy of the theoretical prediction, and on the computational power and time that one is willing (or able) to invest in this task.

The strategy typically adopted consists in first performing low-level geometry and energy calculations on the molecule to explore as thoroughly as possible its conformational space and determine which structures are potentially the most stable. The conformers selected in this way are then further optimized at an increasingly higher level of theory and some of their properties, such as, for instance, their vibrational spectra or collision cross sections, are computed in order to be compared with experimental findings. Ideally, this methodology can lead up to unambiguous geometrical assignments of the species probed experimentally.

In some cases, however, no satisfactory agreement is found between the experimental results and the theoretical predictions. If the former are established with enough confidence, this can reveal insufficiencies in the employed computational methods, which must then be corrected, e.g., by adjusting parameters in a particular force field or DFT functional, or by developing new algorithms. Hence, the relationship between theory and experiment is made of continuous mutual contributions, where the predictions obtained through calculations are used to analyze data acquired in the laboratory, which in turn can serve as test cases to improve the computational procedures.

1.6 Goals and outline

This introduction has given an overview of some of the advances and experimental techniques implemented in the past decades for the study of gas-phase biomolecules and the determination of their structures and properties. Our objective has been to combine several of these approaches and to develop new methodologies, in order to address some of the yet unanswered questions in this research field and to extend the range of tractable problems. The first step was to build an instrument that would bring together the advantages of mass selectivity inherent to tandem mass spectrometry, of sensitive structural probing offered by laser spectroscopy, and of spectral simplification achieved in low-temperature experiments. The apparatus is a tandem mass spectrometer using an ESI source for ion generation and made of two quadrupole mass filters to select parent ions and analyze fragments. In between these two mass filters is a cryocooled 22-pole ion trap, in which mass-selected ions can be accumulated and thermalized to ~ 10 K. The vacuum chamber features two windows aligned on the trap axis, thus providing a clear path for the laser beams that are used to induce photodissociation of the ions.

The characteristics of this ion trap mass spectrometer make it a unique tool for investigating the spectroscopy of biomolecular ions. Its key component is the low-temperature 22-pole trap, which provides efficient cooling of the ions, so that their measured spectra attain an unprecedented resolution, comparable to that achieved in supersonic molecular beams. This opens new perspectives for the structural determination of small and large closed-shell ions produced by electrospray, such as peptides and nucleotides, as well as their hydrated complexes. Moreover, the increased spectral resolution gives the possibility to implement double resonance spectroscopic schemes analogous to those routinely used nowadays for jet-cooled molecules, thus enabling the measurement of specific spectra for each individual conformer. This will be demonstrated in the work presented here.

The primary goals of this thesis have been to build this novel apparatus and to establish the feasibility of such spectroscopic measurements on cold electrosprayed ions. In that purpose, the first two systems that we chose to study are the aromatic amino acids tryptophan and tyrosine. Experiments have also been conducted on the hydrated clusters of protonated tryptophan, which revealed considerable changes in photophysical behavior in comparison with the bare ion. Finally, double resonance techniques have been put into practice to distinguish and characterize the different conformers of these molecules.

The outline of this dissertation is the following. *Chapter 2* gives a detailed description of the experimental instrument and presents some of the most important principles of its major components: the electrospray ion source, the quadrupole mass filters and the 22-pole ion trap. Some experimental results are then presented, which characterize the functioning properties of the ion trap, in particular its cooling efficiency. The last section of *Chapter 2* describes the two laser setups that we used to generate ultraviolet and infrared laser light. In

Chapter 3, we depict the timing of events in a typical pulsed experiment and explain in detail the different types of measurements that are carried out: the recording of a photofragment mass spectrum, a standard ultraviolet photodissociation spectrum, and double resonance infrared and ultraviolet spectra. We also discuss the expected range of applicability of these techniques, notably as regards the size of the studied molecules. The first electronic spectra measured in our apparatus for protonated tryptophan and tyrosine are presented in *Chapter 4*. The contrast between room-temperature and low-temperature spectra illustrates the efficiency of ion cooling, and the fundamental differences between the cold spectra of protonated tryptophan (broad) and tyrosine (sharp) are discussed in terms of excited-state lifetimes. *Chapter 5* deals with the ultraviolet spectra recorded for small hydrated complexes of protonated tryptophan. It is shown that solvation by only two water molecules dramatically increases the excited-state lifetime of that species, which results in a fully vibrationally resolved electronic spectrum. A mechanism based on the interaction of different excited states is proposed to explain this phenomenon, and support is provided by the results of quantum chemical calculations. In *Chapter 6*, we report the conformer-specific vibrational spectra of protonated tyrosine and of the doubly hydrated complex of protonated tryptophan, obtained by IR-UV double resonance spectroscopy. These results are used to analyze in detail the sharp electronic spectra of these two species, and geometrical assignments of their different conformers are proposed with the aid of theoretical structures and spectra calculated at the DFT level. Finally, *Chapter 7* gives a summary of the main results presented in this thesis and presents suggestions for future research directions and possible improvements of the instrumentation.

References

[1] S. H. Gellman, *Chemical Reviews* **1997**, *97*, 1231-1232.
[2] A. D. Robertson and K. P. Murphy, *Chemical Reviews* **1997**, *97*, 1251-1267.
[3] J. D. Watson and F. H. C. Crick, *Nature* **1953**, *171*, 737-738.
[4] M. H. F. Wilkins, A. R. Stokes and H. R. Wilson, *Nature* **1953**, *171*, 738-740.
[5] R. E. Franklin and R. G. Gosling, *Nature* **1953**, *171*, 740-741.
[6] F. H. C. Crick and J. D. Watson, *Proceedings of the Royal Society of London, Series A: Mathematical and Physical Sciences* **1954**, *223*, 80-96.
[7] J. C. Kendrew, R. E. Dickerson, B. E. Strandberg, R. G. Hart, D. R. Davies, D. C. Phillips and V. C. Shore, *Nature* **1960**, *185*, 422-427.

[8] M. F. Perutz, M. G. Rossmann, A. F. Cullis, H. Muirhead, G. Will and A. C. T. North, *Nature* **1960**, *185*, 416-422.

[9] J. W. Miao, H. N. Chapman, J. Kirz, D. Sayre and K. O. Hodgson, *Annual Review of Biophysics and Biomolecular Structure* **2004**, *33*, 157-176.

[10] R. M. Glaeser, *Annual Review of Physical Chemistry* **1985**, *36*, 243-275.

[11] R. Henderson, J. M. Baldwin, T. A. Ceska, F. Zemlin, E. Beckmann and K. H. Downing, *Journal of Molecular Biology* **1990**, *213*, 899-929.

[12] M. P. Williamson, T. F. Havel and K. Wüthrich, *Journal of Molecular Biology* **1985**, *182*, 295-315.

[13] K. Wüthrich, *Science* **1989**, *243*, 45-50.

[14] K. Wüthrich, *Accounts of Chemical Research* **1989**, *22*, 36-44.

[15] A. G. Tzakos, C. R. R. Grace, P. J. Lukavsky and R. Riek, *Annual Review of Biophysics and Biomolecular Structure* **2006**, *35*, 319-342.

[16] M. S. Braiman and K. J. Rothschild, *Annual Review of Biophysics and Biophysical Chemistry* **1988**, *17*, 541-570.

[17] L. Velluz and M. Legrand, *Angewandte Chemie, International Edition* **1965**, *4*, 838-845.

[18] W. B. Gratzer, *Proceedings of the Royal Society of London, Series A: Mathematical and Physical Sciences* **1967**, *297*, 163-170.

[19] S. Beychok, *Annual Review of Biochemistry* **1968**, *37*, 437-462.

[20] N. J. Greenfield, *Analytical Biochemistry* **1996**, *235*, 1-10.

[21] L. Stryer, *Annual Review of Biochemistry* **1978**, *47*, 819-846.

[22] X. Michalet, A. N. Kapanidis, T. Laurence, F. Pinaud, S. Doose, M. Pflughoefft and S. Weiss, *Annual Review of Biophysics and Biomolecular Structure* **2003**, *32*, 161-182.

[23] H. Roder, G. A. Elove and S. W. Englander, *Nature* **1988**, *335*, 700-704.

[24] S. W. Englander, *Annual Review of Biophysics and Biomolecular Structure* **2000**, *29*, 213-238.

[25] H. D. Beckey, *International Journal of Mass Spectrometry and Ion Physics* **1969**, *2*, 500-503.

[26] H. D. Beckey and H. R. Schulten, *Angewandte Chemie, International Edition* **1975**, *14*, 403-415.

[27] H. R. Schulten, U. Bahr and P. B. Monkhouse, *Journal of Biochemical and Biophysical Methods* **1983**, *8*, 239-269.

[28] M. Barber, R. S. Bordoli, R. D. Sedgwick and A. N. Tyler, *Journal of the Chemical Society, Chemical Communications* **1981**, 325-327.

[29] D. J. Surman and J. C. Vickerman, *Journal of the Chemical Society, Chemical Communications* **1981**, 324-325.

[30] M. Barber, R. S. Bordoli, G. J. Elliott, R. D. Sedgwick and A. N. Tyler, *Analytical Chemistry* **1982**, *54*, 645A-657A.

[31] M. A. Posthumus, P. G. Kistemaker, H. L. C. Meuzelaar and M. C. Ten Noever de Brauw, *Analytical Chemistry* **1978**, *50*, 985-991.

[32] R. J. Levis, *Annual Review of Physical Chemistry* **1994**, *45*, 483-518.

[33] C. R. Blakley, J. J. Carmody and M. L. Vestal, *Journal of the American Chemical Society* **1980**, *102*, 5931-5933.

[34] C. R. Blakley, J. J. Carmody and M. L. Vestal, *Analytical Chemistry* **1980**, *52*, 1636-1641.

[35] C. R. Blakley and M. L. Vestal, *Analytical Chemistry* **1983**, *55*, 750-754.

[36] D. Pilosof, H. Y. Kim, D. F. Dyckes and M. L. Vestal, *Analytical Chemistry* **1984**, *56*, 1236-1240.

[37] M. Yamashita and J. B. Fenn, *Journal of Physical Chemistry* **1984**, *88*, 4451-4459.

[38] M. Yamashita and J. B. Fenn, *Journal of Physical Chemistry* **1984**, *88*, 4671-4675.

[39] J. B. Fenn, M. Mann, C. K. Meng, S. F. Wong and C. M. Whitehouse, *Science* **1989**, *246*, 64-71.

[40] M. Karas, D. Bachmann, U. Bahr and F. Hillenkamp, *International Journal of Mass Spectrometry and Ion Processes* **1987**, *78*, 53-68.

[41] M. Karas and F. Hillenkamp, *Analytical Chemistry* **1988**, *60*, 2299-2301.

[42] F. Hillenkamp, M. Karas, R. C. Beavis and B. T. Chait, *Analytical Chemistry* **1991**, *63*, 1193A-1202A.

[43] Y. Wada, A. Hayashi, T. Fujita, T. Matsuo, I. Katakuse and H. Matsuda, *Biochimica et Biophysica Acta* **1981**, *667*, 233-241.

[44] T. Matsuo, H. Matsuda, I. Katakuse, Y. Shimonishi, Y. Maruyama, T. Higuchi and E. Kubota, *Analytical Chemistry* **1981**, *53*, 416-421.

[45] D. H. Williams, C. V. Bradley, S. Santikarn and G. Bojesen, *Biochemical Journal* **1982**, *201*, 105-117.

[46] H. Y. Kim, D. Pilosof, D. F. Dyckes and M. L. Vestal, *Journal of the American Chemical Society* **1984**, *106*, 7304-7309.

[47] D. P. Little, J. P. Speir, M. W. Senko, P. B. O'Connor and F. W. McLafferty, *Analytical Chemistry* **1994**, *66*, 2809-2815.

[48] V. S. K. Kolli and R. Orlando, *Journal of the American Society for Mass Spectrometry* **1995**, *6*, 234-241.

[49] R. Kaufmann, D. Kirsch and B. Spengler, *International Journal of Mass Spectrometry and Ion Processes* **1994**, *131*, 355-385.

[50] P. Jungblut and B. Thiede, *Mass Spectrometry Reviews* **1997**, *16*, 145-162.

[51] C. Fenselau, *Annual Review of Biophysics and Biophysical Chemistry* **1991**, *20*, 205-220.

[52] K. Biemann, *Annual Review of Biochemistry* **1992**, *61*, 977-1010.

[53] J. R. Yates, *Journal of Mass Spectrometry* **1998**, *33*, 1-19.

[54] S. W. Englander, *Journal of the American Society for Mass Spectrometry* **2006**, *17*, 1481-1489.

[55] V. Katta and B. T. Chait, *Journal of the American Chemical Society* **1993**, *115*, 6317-6321.

[56] B. E. Winger, K. J. Lightwahl, A. L. Rockwood and R. D. Smith, *Journal of the American Chemical Society* **1992**, *114*, 5897-5898.

[57] D. Suckau, Y. Shi, S. C. Beu, M. W. Senko, J. P. Quinn, F. M. Wampler and F. W. McLafferty, *Proceedings of the National Academy of Sciences of the United States of America* **1993**, *90*, 790-793.

[58] T. D. Wood, R. A. Chorush, F. M. Wampler, D. P. Little, P. B. O'Connor and F. W. McLafferty, *Proceedings of the National Academy of Sciences of the United States of America* **1995**, *92*, 2451-2454.

[59] M. A. Freitas and A. G. Marshall, *International Journal of Mass Spectrometry* **1999**, *183*, 221-231.

[60] G. von Helden, M. T. Hsu, N. Gotts and M. T. Bowers, *Journal of Physical Chemistry* **1993**, *97*, 8182-8192.

[61] D. E. Clemmer, R. R. Hudgins and M. F. Jarrold, *Journal of the American Chemical Society* **1995**, *117*, 10141-10142.

[62] K. B. Shelimov, D. E. Clemmer, R. R. Hudgins and M. F. Jarrold, *Journal of the American Chemical Society* **1997**, *119*, 2240-2248.

[63] M. F. Jarrold, *Physical Chemistry Chemical Physics* **2007**, *9*, 1659-1671.

[64] R. W. Purves, R. Guevremont, S. Day, C. W. Pipich and M. S. Matyjaszczyk, *Review of Scientific Instruments* **1998**, *69*, 4094-4105.

[65] R. W. Purves, D. A. Barnett and R. Guevremont, *International Journal of Mass Spectrometry* **2000**, *197*, 163-177.

[66] R. Guevremont, *Journal of Chromatography A* **2004**, *1058*, 3-19.

[67] S. J. Valentine and D. E. Clemmer, *Journal of the American Chemical Society* **1997**, *119*, 3558-3566.

[68] S. J. Valentine and D. E. Clemmer, *Journal of the American Society for Mass Spectrometry* **2002**, *13*, 506-517.

[69] E. W. Robinson and E. R. Williams, *Journal of the American Society for Mass Spectrometry* **2005**, *16*, 1427-1437.

[70] W. D. Price, P. D. Schnier and E. R. Williams, *Analytical Chemistry* **1996**, *68*, 859-866.

[71] P. D. Schnier, J. S. Klassen, E. E. Strittmatter and E. R. Williams, *Journal of the American Chemical Society* **1998**, *120*, 9605-9613.

[72] P. D. Schnier, W. D. Price, R. A. Jockusch and E. R. Williams, *Journal of the American Chemical Society* **1996**, *118*, 7178-7189.

[73] R. A. Jockusch, A. S. Lemoff and E. R. Williams, *Journal of Physical Chemistry A* **2001**, *105*, 10929-10942.

[74] A. S. Lemoff and E. R. Williams, *Journal of the American Society for Mass Spectrometry* **2004**, *15*, 1014-1024.

[75] A. Kamariotis, O. V. Boyarkin, S. R. Mercier, R. D. Beck, M. F. Bush, E. R. Williams and T. R. Rizzo, *Journal of the American Chemical Society* **2006**, *128*, 905-916.

[76] A. Kamariotou, *Infrared photofragment spectroscopy of charged amino acid water clusters in the gas phase*, Ph.D. Thesis, EPFL, Lausanne, 2006.

[77] W. Caminati, *Physical Chemistry Chemical Physics* **2004**, *6*, 2806-2809.

[78] R. Sanchez, W. Caminati, J. C. López and J. L. Alonso, *Chemical Physics Letters* **2005**, *414*, 226-229.

[79] L. L. Connell, T. C. Corcoran, P. W. Joireman and P. M. Felker, *Chemical Physics Letters* **1990**, *166*, 510-516.

[80] P. M. Felker, *Journal of Physical Chemistry* **1992**, *96*, 7844-7857.

[81] D. W. Pratt, *Annual Review of Physical Chemistry* **1998**, *49*, 481-530.

[82] T. V. Nguyen, T. M. Korter and D. W. Pratt, *Molecular Physics* **2005**, *103*, 1603-1613.

[83] J. T. Yi and D. W. Pratt, *Physical Chemistry Chemical Physics* **2005**, *7*, 3680-3684.

[84] T. V. Nguyen and D. W. Pratt, *Journal of Chemical Physics* **2006**, *124*, 054317/1-6.

[85] L. A. Philips and D. H. Levy, *Journal of Chemical Physics* **1988**, *89*, 85-90.

[86] J. A. Dickinson, P. W. Joireman, R. W. Randall, E. G. Robertson and J. P. Simons, *Journal of Physical Chemistry A* **1997**, *101*, 513-521.

[87] M. R. Hockridge, S. M. Knight, E. G. Robertson, J. P. Simons, J. McCombie and M. Walker, *Physical Chemistry Chemical Physics* **1999**, *1*, 407-413.

[88] M. Mons, E. G. Robertson, L. C. Snoek and J. P. Simons, *Chemical Physics Letters* **1999**, *310*, 423-432.

[89] Y. H. Lee, J. W. Jung, B. Kim, P. Butz, L. C. Snoek, R. T. Kroemer and J. P. Simons, *Journal of Physical Chemistry A* **2004**, *108*, 69-73.

[90] J. R. Johnson, K. D. Jordan, D. F. Plusquellic and D. W. Pratt, *Journal of Chemical Physics* **1990**, *93*, 2258-2273.

[91] T. R. Rizzo, Y. D. Park, L. Peteanu and D. H. Levy, *Journal of Chemical Physics* **1985**, *83*, 4819-4820.

[92] T. R. Rizzo, Y. D. Park, L. A. Peteanu and D. H. Levy, *Journal of Chemical Physics* **1986**, *84*, 2534-2541.

[93] T. R. Rizzo, Y. D. Park and D. H. Levy, *Journal of Chemical Physics* **1986**, *85*, 6945-6951.

[94] Y. D. Park, T. R. Rizzo, L. A. Peteanu and D. H. Levy, *Journal of Chemical Physics* **1986**, *84*, 6539-6549.

[95] S. J. Martinez, J. C. Alfano and D. H. Levy, *Journal of Molecular Spectroscopy* **1992**, *156*, 421-430.

[96] J. R. Cable, M. J. Tubergen and D. H. Levy, *Journal of the American Chemical Society* **1987**, *109*, 6198-6199.

[97] J. R. Cable, M. J. Tubergen and D. H. Levy, *Journal of the American Chemical Society* **1988**, *110*, 7349-7355.

[98] J. R. Carney and T. S. Zwier, *Journal of Physical Chemistry A* **2000**, *104*, 8677-8688.

[99] R. Cohen, B. Brauer, E. Nir, L. Grace and M. S. de Vries, *Journal of Physical Chemistry A* **2000**, *104*, 6351-6355.

[100] L. C. Snoek, E. G. Robertson, R. T. Kroemer and J. P. Simons, *Chemical Physics Letters* **2000**, *321*, 49-56.

[101] L. C. Snoek, R. T. Kroemer, M. R. Hockridge and J. P. Simons, *Physical Chemistry Chemical Physics* **2001**, *3*, 1819-1826.

[102] B. C. Dian, A. Longarte, S. Mercier, D. A. Evans, D. J. Wales and T. S. Zwier, *Journal of Chemical Physics* **2002**, *117*, 10688-10702.

[103] L. I. Grace, R. Cohen, T. M. Dunn, D. M. Lubman and M. S. de Vries, *Journal of Molecular Spectroscopy* **2002**, *215*, 204-219.

[104] I. Hünig and K. Kleinermanns, *Physical Chemistry Chemical Physics* **2004**, *6*, 2650-2658.

[105] D. Reha, H. Valdes, J. Vondrasek, P. Hobza, A. Abu-Riziq, B. Crews and M. S. de Vries, *Chemistry-a European Journal* **2005**, *11*, 6803-6817.

[106] Y. Inokuchi, Y. Kobayashi, T. Ito and T. Ebata, *Journal of Physical Chemistry A* **2007**, *111*, 3209-3215.

[107] W. Chin, M. Mons, J. P. Dognon, F. Piuzzi, B. Tardivel and I. Dimicoli, *Physical Chemistry Chemical Physics* **2004**, *6*, 2700-2709.

[108] W. Chin, J. P. Dognon, F. Piuzzi, B. Tardivel, I. Dimicoli and M. Mons, *Journal of the American Chemical Society* **2005**, *127*, 707-712.

[109] W. Chin, F. Piuzzi, J. P. Dognon, L. Dimicoli, B. Tardivel and M. Mons, *Journal of the American Chemical Society* **2005**, *127*, 11900-11901.

[110] W. Chin, F. Piuzzi, I. Dimicoli and M. Mons, *Physical Chemistry Chemical Physics* **2006**, *8*, 1033-1048.

[111] J. M. Bakker, C. Plützer, I. Hünig, T. Häber, I. Compagnon, G. von Helden, G. Meijer and K. Kleinermanns, *Chemphyschem* **2005**, *6*, 120-128.

[112] A. Abo-Riziq, J. E. Bushnell, B. Crews, M. Callahan, L. Grace and M. S. de Vries, *Chemical Physics Letters* **2006**, *431*, 227-230.

[113] A. Abo-Riziq, B. O. Crews, M. P. Callahan, L. Grace and M. S. de Vries, *Angewandte Chemie, International Edition* **2006**, *45*, 5166-5169.

[114] E. G. Robertson and J. P. Simons, *Physical Chemistry Chemical Physics* **2001**, *3*, 1-18.

[115] T. S. Zwier, *Journal of Physical Chemistry A* **2001**, *105*, 8827-8839.

[116] P. Çarçabal, R. T. Kroemer, L. C. Snoek, J. P. Simons, J. M. Bakker, I. Compagnon, G. Meijer and G. von Helden, *Physical Chemistry Chemical Physics* **2004**, *6*, 4546-4552.

[117] H. Fricke, A. Gerlach, C. Unterberg, P. Rzepecki, T. Schrader and M. Gerhards, *Physical Chemistry Chemical Physics* **2004**, *6*, 4636-4641.

[118] T. Ebata, T. Hashimoto, T. Ito, Y. Inokuchi, F. Altunsu, B. Brutschy and P. Tarakeshwar, *Physical Chemistry Chemical Physics* **2006**, *8*, 4783-4791.

[119] M. Gerhards and C. Unterberg, *Physical Chemistry Chemical Physics* **2002**, *4*, 1760-1765.

[120] M. Gerhards, C. Unterberg, A. Gerlach and A. Jansen, *Physical Chemistry Chemical Physics* **2004**, *6*, 2682-2690.

[121] H. Fricke, A. Funk, T. Schrader and M. Gerhards, *Journal of the American Chemical Society* **2008**, *130*, 4692-4698.

[122] E. Nir, L. Grace, B. Brauer and M. S. de Vries, *Journal of the American Chemical Society* **1999**, *121*, 4896-4897.

[123] E. Nir, C. Janzen, P. Imhof, K. Kleinermanns and M. S. de Vries, *Journal of Chemical Physics* **2001**, *115*, 4604-4611.

[124] M. Mons, I. Dimicoli, F. Piuzzi, B. Tardivel and M. Elhanine, *Journal of Physical Chemistry A* **2002**, *106*, 5088-5094.

[125] Y. Lee, M. Schmitt, K. Kleinermanns and B. Kim, *Journal of Physical Chemistry A* **2006**, *110*, 11819-11823.

[126] K. Seefeld, R. Brause, T. Häber and K. Kleinermanns, *Journal of Physical Chemistry A* **2007**, *111*, 6217-6221.

[127] E. Nir, K. Kleinermanns and M. S. de Vries, *Nature* **2000**, *408*, 949-951.

[128] E. Nir, C. Plützer, K. Kleinermanns and M. de Vries, *European Physical Journal D* **2002**, *20*, 317-329.

[129] C. Plützer, I. Hünig, K. Kleinermanns, E. Nir and M. S. de Vries, *Chemphyschem* **2003**, *4*, 838-842.

[130] J. M. Bakker, I. Compagnon, G. Meijer, G. von Helden, M. Kabelac, P. Hobza and M. S. de Vries, *Physical Chemistry Chemical Physics* **2004**, *6*, 2810-2815.

[131] M. S. de Vries and P. Hobza, *Annual Review of Physical Chemistry* **2007**, *58*, 585-612.

[132] B. C. Dian, A. Longarte and T. S. Zwier, *Science* **2002**, *296*, 2369-2373.

[133] B. C. Dian, J. R. Clarkson and T. S. Zwier, *Science* **2004**, *303*, 1169-1173.

[134] B. C. Dian, A. Longarte, P. R. Winter and T. S. Zwier, *Journal of Chemical Physics* **2004**, *120*, 133-147.

[135] T. S. Zwier, *Journal of Physical Chemistry A* **2006**, *110*, 4133-4150.

[136] V. A. Shubert and T. S. Zwier, *Journal of Physical Chemistry A* **2007**, *111*, 13283-13286.

[137] L. Stryer *Biochemistry*, 4th ed.; W.H. Freeman: New York, 1995.

[138] H. Oh, K. Breuker, S. K. Sze, Y. Ge, B. K. Carpenter and F. W. McLafferty, *Proceedings of the National Academy of Sciences of the United States of America* **2002**, *99*, 15863-15868.

[139] H. B. Oh, C. Lin, H. Y. Hwang, H. L. Zhai, K. Breuker, V. Zabrouskov, B. K. Carpenter and F. W. McLafferty, *Journal of the American Chemical Society* **2005**, *127*, 4076-4083.

[140] B. Lucas, G. Grégoire, J. Lemaire, P. Maître, J. M. Ortega, A. Rupenyan, B. Reimann, J. P. Schermann and C. Desfrançois, *Physical Chemistry Chemical Physics* **2004**, *6*, 2659-2663.

[141] B. Lucas, G. Grégoire, J. Lemaire, P. Maître, F. Glotin, J. P. Schermann and C. Desfrançois, *International Journal of Mass Spectrometry* **2005**, *243*, 105-113.

[142] L. Mac Aleese, A. Simon, T. B. McMahon, J. M. Ortega, D. Scuderi, J. Lemaire and P. Maître, *International Journal of Mass Spectrometry* **2006**, *249*, 14-20.

[143] N. A. MacLeod and J. P. Simons, *Physical Chemistry Chemical Physics* **2004**, *6*, 2821-2826.

[144] N. A. MacLeod and J. P. Simons, *Molecular Physics* **2007**, *105*, 689-700.

[145] T. D. Vaden, T. S. J. A. de Boer, N. A. MacLeod, E. M. Marzluff, J. P. Simons and L. C. Snoek, *Physical Chemistry Chemical Physics* **2007**, *9*, 2549-2555.

[146] T. D. Vaden, T. S. J. A. de Boer, J. P. Simons and L. C. Snoek, *Physical Chemistry Chemical Physics* **2008**, *10*, 1443-1447.

[147] G. Grégoire, M. P. Gaigeot, D. C. Marinica, J. Lemaire, J. P. Schermann and C. Desfrançois, *Physical Chemistry Chemical Physics* **2007**, *9*, 3082-3097.

[148] R. H. Wu and T. B. McMahon, *Journal of the American Chemical Society* **2007**, *129*, 11312-11313.

[149] R. H. Wu and T. B. McMahon, *Journal of the American Chemical Society* **2007**, *129*, 4864-4865.

[150] C. Kapota, J. Lemaire, P. Maître and G. Ohanessian, *Journal of the American Chemical Society* **2004**, *126*, 1836-1842.

[151] N. C. Polfer, B. Paizs, L. C. Snoek, I. Compagnon, S. Suhai, G. Meijer, G. von Helden and J. Oomens, *Journal of the American Chemical Society* **2005**, *127*, 8571-8579.

[152] N. C. Polfer, J. Oomens and R. C. Dunbar, *Physical Chemistry Chemical Physics* **2006**, *8*, 2744-2751.

[153] J. Y. Salpin, S. Guillaumont, J. Tortajada, L. MacAleese, J. Lemaire and P. Maître, *Chemphyschem* **2007**, *8*, 2235-2244.

[154] J. Oomens, N. Polfer, D. T. Moore, L. van der Meer, A. G. Marshall, J. R. Eyler, G. Meijer and G. von Helden, *Physical Chemistry Chemical Physics* **2005**, *7*, 1345-1348.

[155] M. F. Bush, J. S. Prell, R. J. Saykally and E. R. Williams, *Journal of the American Chemical Society* **2007**, *129*, 13544-13553.

[156] M. F. Bush, J. T. O'Brien, J. S. Prell, R. J. Saykally and E. R. Williams, *Journal of the American Chemical Society* **2007**, *129*, 1612-1622.

[157] S. B. Nielsen, A. Lapierre, J. U. Andersen, U. V. Pedersen, S. Tomita and L. H. Andersen, *Physical Review Letters* **2001**, *87*, 228102/1-4.

[158] L. H. Andersen, A. Lapierre, S. B. Nielsen, I. B. Nielsen, S. U. Pedersen, U. V. Pedersen and S. Tomita, *European Physical Journal D* **2002**, *20*, 597-600.

[159] D. Nolting, C. Marian and R. Weinkauf, *Physical Chemistry Chemical Physics* **2004**, *6*, 2633-2640.

[160] C. Marian, D. Nolting and R. Weinkauf, *Physical Chemistry Chemical Physics* **2005**, *7*, 3306-3316.

[161] F. O. Talbot, T. Tabarin, R. Antoine, M. Broyer and P. Dugourd, *Journal of Chemical Physics* **2005**, *122*, 074310/1-5.

[162] A. S. Danell and J. H. Parks, *International Journal of Mass Spectrometry* **2003**, *229*, 35-45.

[163] A. T. Iavarone, D. Duft and J. H. Parks, *Journal of Physical Chemistry A* **2006**, *110*, 12714-12727.

[164] A. T. Iavarone, A. Patriksson, D. van der Spoel and J. H. Parks, *Journal of the American Chemical Society* **2007**, *129*, 6726-6735.

[165] S. B. Nielsen, J. U. Andersen, J. S. Forster, P. Hvelplund, B. Liu, U. V. Pedersen and S. Tomita, *Physical Review Letters* **2003**, *91*, 048302/1-4.

[166] E. S. Worm, I. H. Andersen, J. U. Andersen, A. I. S. Holm, P. Hvelplund, U. Kadhane, S. B. Nielsen, J. C. Poully and K. Stochkel, *Physical Review A* **2007**, *75*, 042709/1-7.

[167] H. Kang, C. Dedonder-Lardeux, C. Jouvet, S. Martrenchard, G. Grégoire, C. Desfrançois, J. P. Schermann, M. Barat and J. A. Fayeton, *Physical Chemistry Chemical Physics* **2004**, *6*, 2628-2632.

[168] H. Kang, C. Dedonder-Lardeux, C. Jouvet, G. Grégoire, C. Desfrançois, J. P. Schermann, M. Barat and J. A. Fayeton, *Journal of Physical Chemistry A* **2005**, *109*, 2417-2420.

[169] H. Kang, C. Jouvet, C. Dedonder-Lardeux, S. Martrenchard, C. Charrière, G. Grégoire, C. Desfrançois, J. P. Schermann, M. Barat and J. A. Fayeton, *Journal of Chemical Physics* **2005**, *122*, 084307/1-7.

[170] H. Kang, C. Jouvet, C. Dedonder-Lardeux, S. Martrenchard, G. Grégoire, C. Desfrançois, J. P. Schermann, M. Barat and J. A. Fayeton, *Physical Chemistry Chemical Physics* **2005**, *7*, 394-398.

[171] G. Grégoire, H. Kang, C. Dedonder-Lardeux, C. Jouvet, C. Desfrançois, D. Onidas, V. Lepere and J. A. Fayeton, *Physical Chemistry Chemical Physics* **2006**, *8*, 122-128.

[172] D. Nolting, T. Schultz, I. V. Hertel and R. Weinkauf, *Physical Chemistry Chemical Physics* **2006**, *8*, 5247-5254.

[173] G. Grégoire, C. Dedonder-Lardeux, C. Jouvet, C. Desfrançois and J. A. Fayeton, *Physical Chemistry Chemical Physics* **2007**, *9*, 78-82.

[174] D. Nolting, R. Weinkauf, I. V. Hertel and T. Schultz, *Chemphyschem* **2007**, *8*, 751-755.

[175] D. H. Levy, *Annual Review of Physical Chemistry* **1980**, *31*, 197-225.

[176] R. L. Wong, K. Paech and E. R. Williams, *International Journal of Mass Spectrometry* **2004**, *232*, 59-66.

[177] D. Gerlich, *Journal of the Chemical Society, Faraday Transactions* **1993**, *89*, 2199-2208.

Chapter 2 Description and characterization of the tandem mass spectrometer

This chapter describes the apparatus that we built to carry out the experiments presented in this thesis. A detailed presentation of the machine is followed by explanations of the different techniques used to produce, select and trap the ions. We then present some results showing the trapping and cooling performances of the cold ion trap. Finally, the last section of the chapter gives a description of the UV and IR laser setups used to perform photodissociation spectroscopy measurements on the trapped ions.

2.1 The home-built apparatus and techniques it relies on

2.1.1 Machine overview

A schematic of the tandem mass spectrometer is shown in Figure 2.1. It consists of a vacuum chamber with six differentially pumped vacuum stages, which contain all the ion optical system needed to guide the ions from the first stage, where they enter the chamber from the atmospheric region where they are produced, until the last stage, where they are detected. This system includes quadrupole mass filters, multipole ion guides, quadrupole deflectors, a 22-pole ion trap mounted on a cold head and many cylindrical electrodes in between these components.

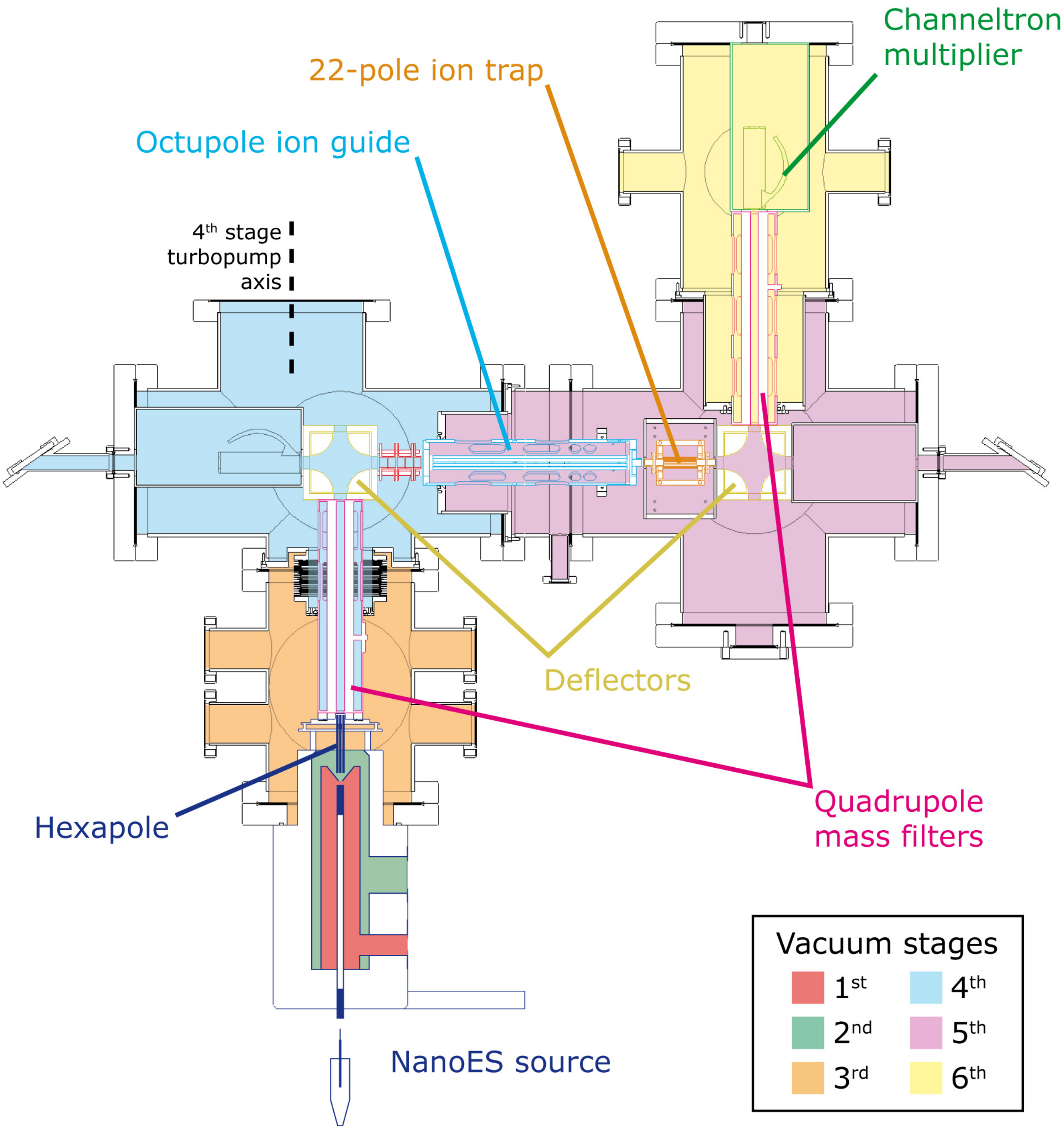
Channeltron multiplier
22-pole ion trap
Octupole ion guide
4th stage turbopump axis
Deflectors
Hexapole
Quadrupole mass filters
NanoES source
Vacuum stages
1st
2nd
3rd
4th
5th
6th

Figure 2.1: Section view (from the top) of the tandem mass spectrometer.

The diagram in Figure 2.2 summarizes the successive steps that the ions go through, along their path in the machine, during a typical experiment.

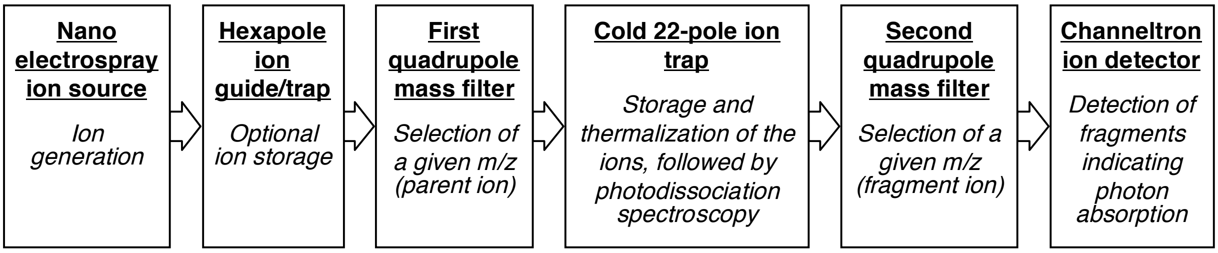
Nano electrospray ion source
Ion generation
Hexapole ion guide/trap
Optional ion storage
First quadrupole mass filter
Selection of a given m/z (parent ion)
Cold 22-pole ion trap
Storage and thermalization of the ions, followed by photodissociation spectroscopy
Second quadrupole mass filter
Selection of a given m/z (fragment ion)
Channeltron ion detector
Detection of fragments indicating photon absorption

Figure 2.2: Sequence of events experienced by the ions during a typical photodissociation experiment.

As can be seen in Figure 2.1, the machine is not linear, but rather Z-shaped, with two quadrupole deflectors giving two 90° turns to the ion beam. There are two reasons to justify this design. The main one is that it creates a clear path for the laser beams on the axis of the 22-pole ion trap, allowing them to enter and exit the vacuum chamber through windows placed at Brewster's angle. This should ideally prevent any clipping of the lasers, which could produce photoelectrons or heat up the cold ion trap. The alignment of the lasers on the axis of the trap is simply to maximize the overlap between the radiation field and the trapped ion cloud. The second reason for bending the ion path is related to the nature of the ion source. Because electrospray produces ions at atmospheric pressure before transmitting them to the first vacuum stage (through a long glass capillary; see *2.1.2 Electrospray ionization* below for details), the vacuum chamber is continuously submitted to a constant gas load. However, the ions of interest constitute only a minor fraction of this gas, the rest being neutral molecules. Therefore, the first quadrupole deflector separates the ions to be studied, while the beam of neutrals, not affected by the electric field, continues on its way to the 4th stage turbomolecular pump. It should be noted that the latter has been intentionally mounted with its shaft being shifted by a few centimeters with respect to the neutral beam (see Figure 2.1: the pump axis and the first quadrupole mass filter are not aligned). In this way, the neutral molecules hit directly the blades of the turbine instead of its shaft, thus improving the pumping speed. The purpose of this design is to efficiently reduce the background pressure in the subsequent vacuum stages.

The ion source consists in a commercial electrospray source (Analytica of Brandford, Inc., CT, USA) whose atmospheric section, which was of a regular electrospray design, has been replaced by a nano-electrospray source kit (model ES025A from Proxeon Biosystems, DK). The sample to be studied is put in solution and sprayed at atmospheric pressure from a metal-coated glass needle towards the entrance of a nickel-coated glass capillary. The ions formed by this process are dragged by the airflow through this 24 cm long capillary until its other end in the first vacuum stage. This stage, which is contained in the block of the electrospray source, is evacuated by a 60 $m^3 \cdot h^{-1}$ mechanical pump (model 2063 from Alcatel, FR) to reach a pressure of ~ 2 mbar. After passing through a skimmer, the ions enter a 6 cm long linear hexapole, which spans the 2nd and 3rd vacuum stages. The 2nd stage is also part of the electrospray source and is pumped to ~ $3 \cdot 10^{-2}$ mbar by a 60 $L \cdot s^{-1}$ turbomolecular drag pump (model TMU 071 P from Pfeiffer Vacuum, DE), itself backed by a 20 $m^3 \cdot h^{-1}$ mechanical pump (model DUO 20 from Pfeiffer Vacuum, DE). The 3rd stage, corresponding to the second half of the hexapole, is part of the custom-built vacuum chamber and is evacuated by a 520 $L \cdot s^{-1}$ turbodrag pump (model TMU 521 from Pfeiffer Vacuum, DE) down to a pressure of ~ $4 \cdot 10^{-5}$ mbar. An exit electrode at this end of the hexapole can be submitted to a pulsed voltage, in order to trap and accumulate ions continuously produced by the source and later release them as a denser ion packet. More details about the ion source are given in the following subsection, *2.1.2 Electrospray ionization*.

The ions produced by electrospray and exiting the hexapole can be of different kinds, even if a single substance was put in the sample solution. First of all, not all ions are necessarily completely desolvated and some solvent molecules can still be attached to the molecular ion, depending on the conditions applied to the source. This is indeed an advantage and gives the possibility to investigate the solvation of the ions. Second, if the molecule in solution is large enough, it could potentially carry several electric charges and present a variety of charge states in the vacuum. For these reasons, the hexapole is followed by a quadrupole mass filter to select only the species of ions (so-called parent ions) to be subsequently trapped and studied, according to their mass-to-charge ratio (*m/z*). The principles of mass selection with linear quadrupoles are explained in a later subsection (see *2.1.3 Quadrupole mass filtering*).

As explained above, the mass-selected ion beam is then turned 90° by the first quadrupole deflector to be separated from the beam of neutral molecules and oriented along the laser axis. While for standard experiments the turn is usually to the right in the direction of the 22-pole ion trap, it is possible to swap the voltages between the two pairs of opposite poles of the deflector, so as to bend the ions to the left, towards an intermediate ion detector. This detector can be used to optimize the voltages and maximize the transmission of ions for this first portion of the ion path. When turned to the right, the ions then travel through a stack of five consecutive cylindrical electrodes intended to decelerate them before trapping. The first quadrupole mass filter, the first deflector and this stack of electrodes are part of the 4th vacuum stage of the chamber. As already mentioned, this stage is evacuated by a turbomolecular drag pump, which is of the same model as that of the 3rd stage (TMU 521 from Pfeiffer Vacuum, DE). The pressure attained is ~ $3 \cdot 10^{-7}$ mbar.

The 5th vacuum stage begins where the ions leave the 5-lens stack and enter the octupole ion guide. It also contains the 22-pole ion trap and the second quadrupole deflector. The function of the 20 cm long linear octupole, which is operated in an rf-only (radio frequency) mode, is to transmit the ions into the ion trap. About 1 ms prior to the arrival of the ion packet, the trap is filled by a pulse of helium gas, provided by a pulse valve (General Valve Series 99 with copper gasket from Parker, US). The purpose of this gas is twofold. First, the initial collisions of the incoming ions with the He atoms make them lose their kinetic energy, so that they can be trapped axially in an electric potential well, created by setting the pole bias voltage of the trap lower than those of its entrance and exit electrodes. Secondly, the gas serves as a heat exchanger between the ions and the surrounding walls of the trap. As mentioned earlier, the trap is installed on the cold head of a cryocooler which can reach 6 K (model SRDK-408R from Sumitomo Heavy Industries, Ltd., JP). Ideally, thermalization of the ions to this temperature would remove most of their internal energy and leave them essentially in their ground electronic and vibrational states, which results in spectral simplification. The design and properties of the ion trap are further discussed below (see *2.1.4 The 22-pole ion trap*).

Once trapped and thermalized, the mass-selected parent ions are irradiated with the appropriate UV and/or IR laser radiations. If photons are absorbed by the ions such that their internal energy is high enough to lead to photodissociation on a reasonable timescale, fragment ions will be produced and trapped as well, at least for a fraction of them. The content of the trap is then released by lowering the voltage of the exit electrode and the outcoming ion beam is turned 90° by the second quadrupole deflector towards the next vacuum stage. Just as the two previous vacuum stages, this 5th stage is pumped by a 520 $L \cdot s^{-1}$ turbodrag pump (TMU 521 from Pfeiffer Vacuum, DE). Its base pressure, i.e., when no helium is pulsed, is on the order of $(0.5 \text{ to } 1) \cdot 10^{-8}$ mbar.

The ion beam entering the 6th vacuum stage is composed of remaining parent ions and, if dissociation occurred in the trap, of one or more types of fragment ions. Thus, a second quadrupole mass filter is used to select only the ions of a given *m/z* and guide them to the ion detector. The latter consists of two parts: (i) a conversion dynode, which is set at a high negative voltage (for positive ions), typically -5 kV, and emits electrons upon the impact of the accelerated ions; (ii) a channeltron multiplier, which collects these electrons and amplifies the electron current. The resulting signal is sent to a fast preamplifier (model VT120 from Ortec, TN, US) and then to a gated pulse counter (model SR400 from Stanford Research Systems, Inc., CA, US). Setting the second quadrupole mass filter to the mass of a given fragment enables one to detect the amount of photodissociation at the used laser wavelength (subtracting, if needed, the background fragmentation signal obtained without the laser). On the other hand, transmitting the mass of the parent ion gives the possibility to measure the fluctuations of the ion source and can be used to normalize the fragmentation signal.

This 6th and last vacuum stage is evacuated by a turbomolecular drag pump similar but smaller (230 $L \cdot s^{-1}$, model TMU 261 from Pfeiffer Vacuum, DE) than those of the previous stages. Its pressure when helium is not pulsed in the ion trap is usually lower than the measurable range of the installed pressure gauge, i.e., $< 2 \cdot 10^{-9}$ mbar. The turbodrag pumps of vacuum stages 3, 4 and 6 are backed by diaphragm pumps (3.3 $m^3 \cdot h^{-1}$, model MVP 055-3 from Pfeiffer Vacuum, DE), while the 5th stage turbopump is backed by a piston pump (7.5 $m^3 \cdot h^{-1}$, model XtraDry 150-2 from Pfeiffer Vacuum, DE). This combination of turbodrag pumps and dry backing pumps ensures an essentially oil-free vacuum environment. It is crucial to the planned experiments to minimize the vapor pressure of hydrocarbons that could cover the electrodes and multipole rods with an insulating dielectric coating, especially for the 22-pole ion trap whose very low temperature will favor the condensation of material. The pressure at different points in the vacuum system is measured by two types of vacuum gauges. For the 1st and 2nd vacuum stages and between each turbopump and the corresponding backing pump, Pirani gauges are used (model TPR 261 from Pfeiffer Vacuum, DE). For the higher vacuum of stages 3 to 6, the pressure is measured by cold cathode gauges (model IKR 261 from the same company).

With the exception of the 22-pole ion trap, which was home-built, all the ion optics following the hexapole (mass filters, deflectors, octupole, electrodes and ion detectors), as well as their controlling electronics, were bought from Extrel CMS, PA, US. All these devices are driven by the supplied PC-based software: Merlin Automation Data System, version 1.0.15.

2.1.2 Electrospray ionization

This subsection summarizes the principles of electrospray ionization and describes in more detail the ion source used in this work, from the nano-electrospray (or nanospray) needle until the hexapole ion guide/trap.

The electrospray phenomenon, i.e., the production of a spray of fine droplets by submitting a liquid surface to an intense electric field, was already known and studied at the beginning of the 20th century [1, 2]. However, it is only at the end of the 1960s that it started to be used in the development of an ion source for mass spectrometry by Dole and coworkers [3]. Major improvements by John Fenn's research group in the mid 1980s [4-6] prepared the ground for the spread of ESI as a method of choice to bring large thermally labile molecules into the gas phase. Since then, several source designs have been developed to comply with different applications in a variety of both fundamental and applied research fields.

Figure 2.3 illustrates the mechanisms taking place in the atmospheric part of an electrospray ion source. An analyte is dissolved in a polar solvent and the solution flows through a conductive needle. A high voltage difference is applied between the latter and a counter-electrode, usually the entrance of the vacuum system. Under the influence of the strong electric field present at the needle tip, positive charges (in the positive ion mode example of the figure) accumulate at the liquid surface and cause the formation of a so-called «Taylor cone» [7]. When the charge density at the apex of this cone is high enough so that charge repulsion overcomes the surface tension of the liquid, charged droplets are created and carried away by the electric field in a spray towards the counter-electrode. As they travel through atmosphere, these droplets undergo solvent evaporation and shrink, which increases their charge density until they reach the «Rayleigh limit» [8]. At this point, similarly to what happens at the Taylor cone, surface tension is weaker than charge repulsion and the droplet emits a stream of smaller droplets carrying the excess charge. Several occurrences of this evaporation/fission sequence eventually lead to the formation of solvated ions. There is no definite consensus yet concerning the exact mechanism by which these solvated ions are produced, but two theories are currently considered. According to the «charge residue» model, the smallest final droplets emitted by fission simply undergo complete solvent evaporation to yield solvated ions [3, 9]. On the other hand, the «ion evaporation» theory states that the solvated ions are in fact evaporated from the surface of charged nanodroplets [10, 11]. Recent contributions to this debate include references [12-18]. Whatever mechanism better describes their formation, the solvated ions finally leave the high electric field region and enter the vacuum interface of the source.

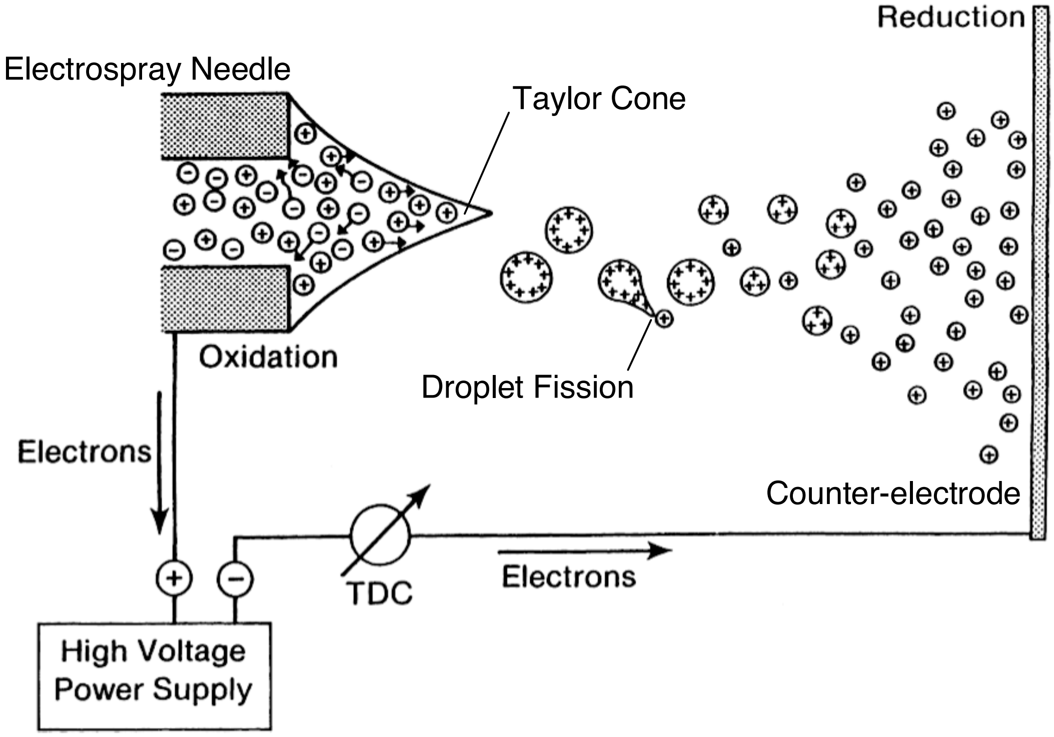

Figure 2.3: Spray formation and droplet fission in the atmospheric part of an ESI source. (Adapted from Kebarle and Tang [19].)

As mentioned previously, the ESI source used in this work is of an early design, but the atmospheric part was replaced with a recent nanospray setup. Nano-electrospray, whose development started in the mid 1990s [20, 21], gets its name from the much lower liquid flow rates applied (~ 1 nL·min^{-1} to 1 µL·min^{-1}) compared to conventional electrospray (~ 1 µL·min^{-1} to 1 mL·min^{-1}). The principles of spray formation are identical for the two techniques, the difference being the smaller inner diameter of the nanospray needle (a few micrometers versus ~ 100 µm for electrospray). There are several benefits of using narrower needles and lower flow rates. First, the onset voltage V_{on} [kV] needed to initiate a stable spray is reduced, as can be derived from the following equation [22], where r [µm] is the needle inner radius, γ [N·m^{-1}] the surface tension of the liquid and d [mm] the distance of the needle tip to the counter-electrode:

$$V_{\mathrm{on}} \approx 0.2\sqrt{r\gamma}\ln\left(\frac{4000d}{r}\right) \qquad \text{(Eq. 2.1)}$$

Using typical values for γ and d, a decrease of the needle diameter from 60 µm to 10 µm causes approximately a twofold reduction of the onset potential. The equation also shows that smaller needle tips make it possible to use solvents of higher surface tension, such as pure water as opposed to water/methanol mixtures, while keeping the needle voltage low enough to prevent electric discharges to the counter-electrode. Moreover, working with lower flow rates extends the running time of a given sample volume, with no concomitant decrease of the ion count rate at the detector [21, 23]. This better ionization efficiency of nanospray is attributed to the smaller size of the initial droplets, whose desolvation is then faster. Consequently, the amount of «wasted» material that enters the vacuum and covers the ion optics is also diminished, which slows down the contamination of the vacuum interface.

The ion source that we used is schematically depicted in Figure 2.4. The sample assembly consists in a metallic source head holding a 1.5 mL Eppendorf vial and a Au/Pd-coated borosilicate capillary serving as the nanospray needle (~ 1 µm i.d. at the opening). The vial and the capillary are filled with the sample solution, which typically has an analyte concentration of $2\cdot10^{-4}$ M in a 1:1 water/methanol mixture with 0.2% acetic acid added. The source head is mounted on an electrically insulated xyz-manipulator and connected to a high-voltage power supply. The assembly is also airtight, so that a very slight pressure can be applied to the solution and facilitate the formation of a spray. In the positive ion mode, the needle is floated ~ 500 V to 1 kV above ground potential, depending on the conditions. The charged spray droplets travel towards the Ni-coated entrance end of a 24 cm long glass capillary, which is grounded and serves as the counter-electrode. A gentle counter-current flow of (optionally heated) nitrogen gas can be used to assist desolvation of the droplets. The gas-phase solvated ions formed at atmospheric pressure are entrained by viscous forces through the whole glass capillary (i.d. of 500 μm), whose other end is in the first vacuum stage.

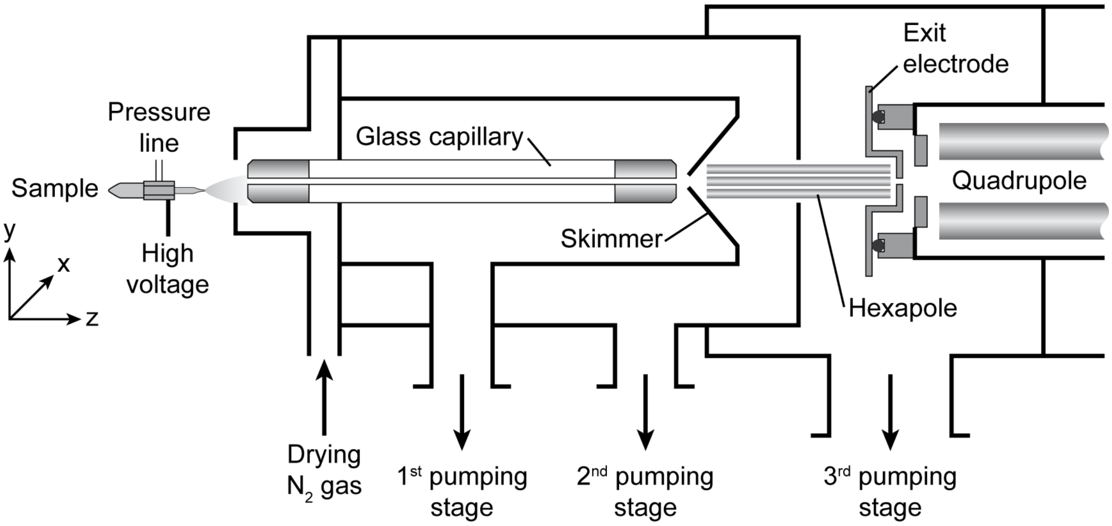

Figure 2.4: The nano-electrospray ion source used in this work, combined with an older vacuum interface from Analytica of Brandford.

When exiting the transfer capillary, the gas creates a free-jet expansion that could potentially cool the ions and contribute to their condensation with solvent molecules. However, both the capillary exit, also Ni-coated, and the skimmer behind it can be maintained at different potentials, so that a more or less strong electric field exists between them. Upon acceleration in this low vacuum region, the solvated ions can undergo collision-induced dissociation (CID) with background gas molecules to complete their desolvation. High-energy collisions can induce fragmentation of covalent bonds, whereas a moderate acceleration allows the possibility of transmitting solvated ions to the mass spectrometer for microsolvation studies.

Following the skimmer, that is, in the 2nd vacuum stage, the ions enter a 6 cm long linear hexapole (1 mm diameter rods on a 3.5 mm inscribed diameter). The second half of the hexapole is situated in the 3rd vacuum stage, where pressure is almost 1000 times lower. So, when travelling from the high-pressure side to the low-pressure side of the hexapole, the ions pass from a region of viscous flow, where they still undergo collisions with background gas molecules, to a region of molecular flow, where the mean free path is much larger than the instrument dimensions. Therefore, the floating voltage of the rods (the pole bias) defines the potential of zero kinetic energy for the ions, and the voltages of the ion optics downstream have to be set according to this reference, so as to maximize ion transmission.

The hexapole is run in an rf-only mode (5.3 MHz; 500 V peak-to-peak) and thus functions as a guide to transfer the ions to the first quadrupole mass filter. However, as previously mentioned, we have the possibility of applying a pulsed voltage to the exit electrode and trap the ions axially for a certain amount of time. There are mainly two advantages of doing so. One is that it turns the continuous nanospray source into a pulsed ion source. It then better matches the duty cycle of our experiments, which are intrinsically discontinuous because of the pulsed lasers and the ion trapping in the 22-pole trap. The other benefit of pretrapping in the hexapole is that it thermalizes the ion packet and hence reduces the spread of ion kinetic energies. This should improve the transmission efficiency of ions through the tandem mass spectrometer. Conversely, the major drawback of pretrapping is that the accumulation of too many ions in a confined volume can produce space charge effects leading to the fragmentation of ions [24-26]. This is especially critical when the studied species are weakly bound complexes such as solvated ions. For this reason, the duration of pretrapping must be carefully adjusted to maximize the parent ion signal, and for some of the presented experiments, pretrapping was not even used.

Comprehensive information about the mechanisms, instrumentation and applications of electrospray can be found in the aforementioned references, as well as in several textbooks (e.g., references [27, 28]).

2.1.3 Quadrupole mass filtering

The origin of the quadrupole mass spectrometer dates back to the 1950s, when Paul et al. had the idea of using an electrodynamic quadrupole field instead of a magnetic field to separate charged particles of different mass-to-charge ratios [29]. The first developments of the apparatus followed, mostly by the same group [30, 31]. A simplified explanation of the underlying principles of this technique is presented here.

Figure 2.5 represents the electric potential generated by four electrodes of hyperbolic cross section, aligned along the *z* axis and equally spaced on an inscribed circle, with a pair of opposite electrodes (on the *x* axis) set at a given potential, while the other pair (on the *y* axis) is set at a lower potential. This saddle-shaped potential is expressed by the following equation:

$$\Phi = \Phi_0 \frac{x^2 - y^2}{r_0^2} \qquad \text{(Eq. 2.2)}$$

Φ_0 is half the difference of potential between the two pairs of poles and r_0 is the radius of the inscribed circle. If one considers a positive ion travelling in this potential in the *z* direction (but off-axis), it clearly appears that the trajectory in the *xz* plane will consist of periodic oscillations and thus be stable, while the trajectory in the *yz* plane will diverge from the *z* axis and the ion will eventually crash on one of the *y* electrodes. Note that in practice, the field is approximated by cylindrical electrodes, which are easier to manufacture.

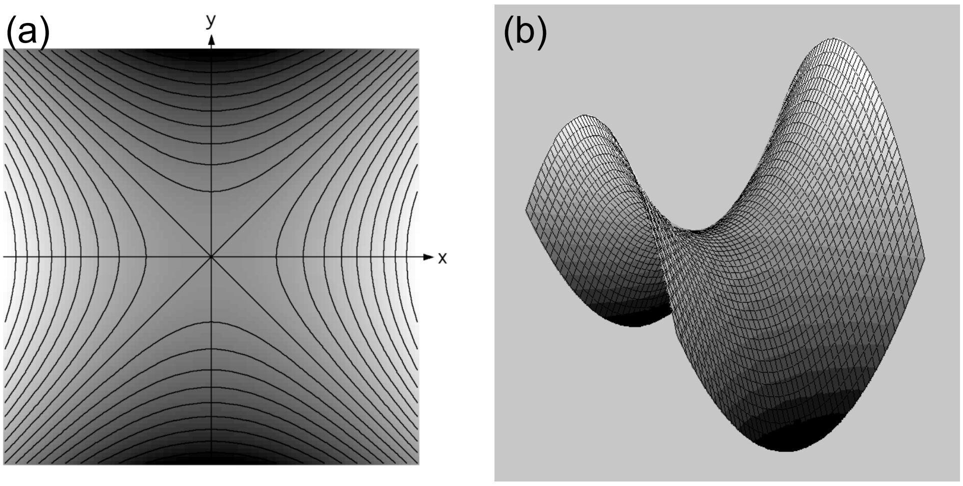

Figure 2.5: The static quadrupole potential in the *xy* plane, represented as (a) a contour plot and (b) a three-dimensional surface.

On the other hand, if instead of having a static Φ_0 potential one makes it a periodic function of time, the ion trajectory would be alternately stable in one of the *xz* and *yz* planes, while diverging in the other. Using a high enough frequency for Φ_0, such that the ion does not have the time to escape in the *xy* plane, it is possible to confine the ion radially between the poles. This is the principle of operation of an rf-only multipole ion guide [32].

Mass discrimination arises when a small DC component is added to the oscillating potential Φ_0, which can then be written $\Phi_0 = U + V\cos(\omega t)$. U is the DC component, V the amplitude of the oscillation and ω its angular frequency. In this case, the behavior of the ion trajectory in the x and y directions differs depending on the mass of the ion (singly charged ions are considered for simplicity). Light ions have a tendency to follow the oscillatory field, while heavier ions are less influenced by it and hence show a relative higher sensitivity to the DC voltage. Therefore, in the x direction, where the poles have a positive value of U, trajectories are more stable for heavy ions, whereas light ions trajectories are amplified and destabilized by the oscillatory field. Conversely, the negative DC value in the y direction defocusses heavier ions, while light ions can be stabilized by an appropriate AC component. As a consequence, the values of U, V and ω can be chosen so as to stabilize the trajectories of ions within a given mass range, while lighter or heavier ions will be unstable in the x or y direction, respectively.

The conditions of stability can be determined by solving the equations of motion for a singly charged ion in the quadrupole mass filter. The results are usually represented in a stability diagram (Figure 2.6), displaying stability regions as a function of two dimensionless parameters, a and q, defined as follows, e being the elementary charge:

$$a = \frac{8eU}{mr_0^2\omega^2} \qquad \text{and} \qquad q = \frac{4eV}{mr_0^2\omega^2} \qquad \text{(Eq. 2.3)}$$

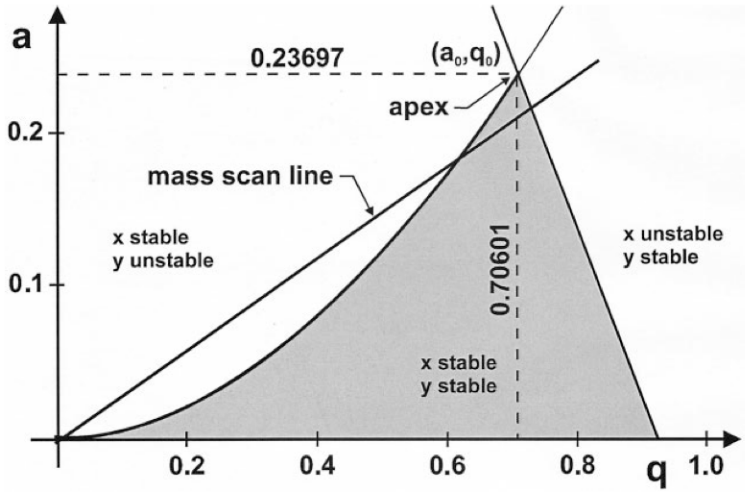

Figure 2.6: Stability diagram showing the lower stability region in the (*a*,*q*) plane. (Taken from Blaum et al. [33].)

Considering a fixed geometry (r_0) and frequency (ω), a point in the stability diagram determines the values of U/m and V/m. Using a U/V ratio corresponding to the so-called mass scan line, which intersects the stability region near its apex, only a narrow mass range will have stable ion trajectories through the length of the mass filter. A mass spectrum is obtained by scanning the values of U and V, while maintaining their ratio constant. Increasing this ratio to bring the mass scan line closer to the apex gives a higher mass resolution.

Detailed information about quadrupole mass spectrometry (mathematical principles, instrumentation, applications) can be found in many textbooks and reviews (see for instance references [32, 34, 35]).

2.1.4 The 22-pole ion trap

2.1.4.1 Principles and advantages

The development and application of the 22-pole rf ion trap around 1990 is due to Gerlich and coworkers in their research about ion–molecule reactions relevant to the chemistry of interstellar clouds [36]. The motivation was to reproduce the conditions of low temperature and low density of such environments. An important benefit of ion trapping is the possibility to store the ions for relatively long periods, thus giving them enough time to react before releasing the products for detection. The particular advantage of the 22-pole trap is that it creates an electric potential which is suitable for an efficient cooling of the ions, as explained below.

The trajectory of an ion in an inhomogeneous rf field of high enough frequency can be described as the superposition of a smooth trajectory and a fast oscillatory motion [37]. The smooth motion can be associated with a time-independent effective potential V^*. In the case of $2n$-multipoles, this effective potential is expressed as a function of the radial position r by the following formula [38]:

$$V^*(r) = \frac{1}{8} \cdot \frac{(qV_0)^2}{\varepsilon} \left(\frac{r}{r_0}\right)^{2n-2} \qquad \text{where} \qquad \varepsilon = \left(\frac{1}{2n^2}\right) m\omega^2 r_0^2 \qquad \text{(Eq. 2.4)}$$

The ion is characterized by its charge q and mass m, and the $2n$-multipole by its inscribed radius r_0, as well as the amplitude V_0 and the frequency ω of the rf voltage applied to the electrodes. ε is named the characteristic energy. The form of the potential is represented in Figure 2.7 for three different geometries (quadrupole, octupole and 22-pole).

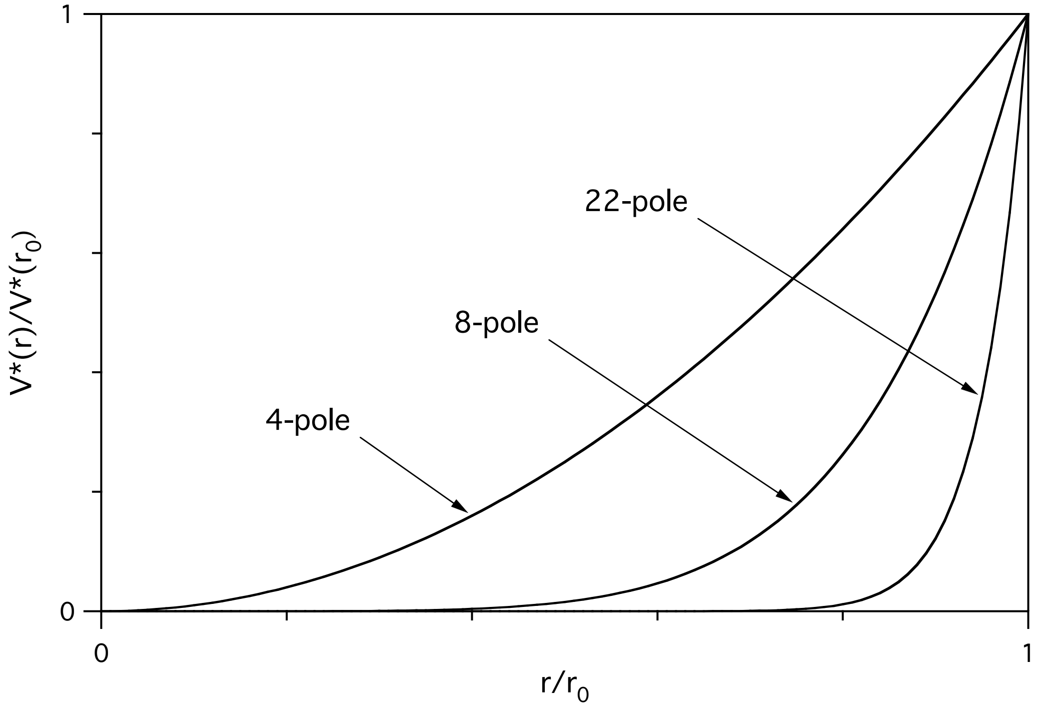

Figure 2.7: Relative effective potentials as a function of the distance from the axis for a quadrupole, an octupole and a 22-pole. The repulsive wall for the three cases rises as r^2, r^6 and r^{20}, respectively.

When buffer gas is introduced between the poles to trap and thermalize the ions, collisions with the neutrals in regions of high electric field cause some heating of the ions due to their fast oscillatory motion. This makes the average temperature of the ions higher than that of the gas. The influence of an effective potential with steep walls on the ion motion is depicted by the calculation of ion trajectories in an octupole and a 32-pole ion trap (Figure 2.8). It shows that, for higher-order multipoles, the wiggling motion occurs only in the close vicinity of the poles, leaving a large volume for non-accelerated trajectories.

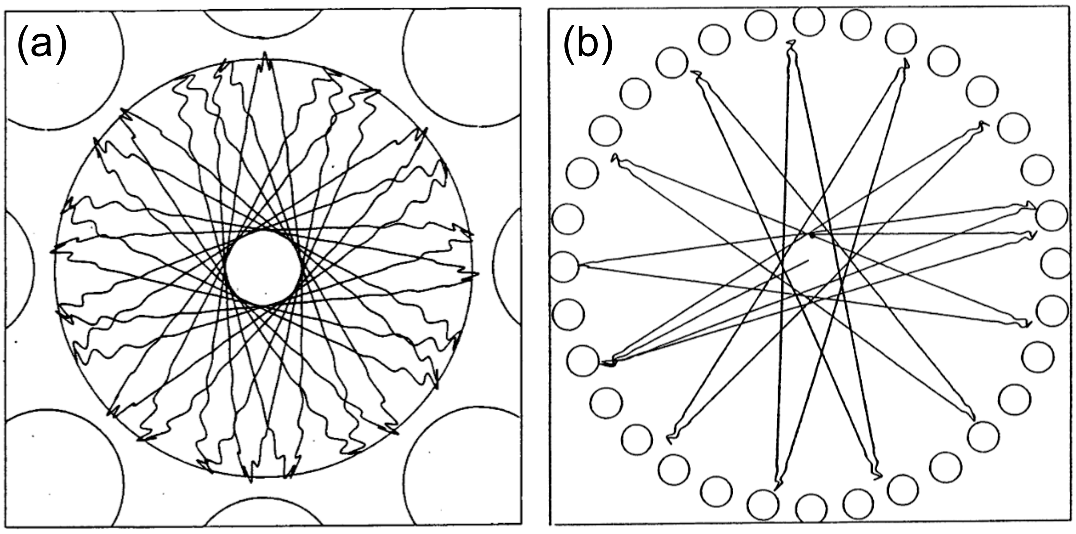

Figure 2.8: Calculated trajectories of an ion in the potential of (a) an octupole and (b) a 32-pole rf trap. (Taken from Gerlich [39].)

Thus, the wider field-free region of high-order multipoles reduces the proportion of energetic collisions and brings the ion energy distribution closer to the Maxwell-Boltzmann distribution of the buffer gas. Figure 2.9 illustrates this for the case of C^+ ions stored in a ring-electrode trap, having an effective potential comparable to that of the 22-pole, with H_2 as the buffer gas [36]. The curve obtained for a quadrupole is also shown. Although the logarithmic scales make it hard to visualize, the majority of the ions in the quadrupole are near room temperature, whereas only a small fraction is significantly warmer than the buffer gas in the ring-electrode trap. Thermalization is even better in a 22-pole potential, which has steeper repulsive walls, and when the mass of the ion is higher relative to that of the buffer gas molecules. Hence, it will be very efficient for the amino acids and peptides in a He buffer gas studied in our experiments. In conclusion, these properties of long trapping times and excellent thermalization capabilities make the 22-pole ion trap an ideal device to explore the photodissociation spectroscopy of cold biomolecular ions, as proposed in this doctoral thesis.

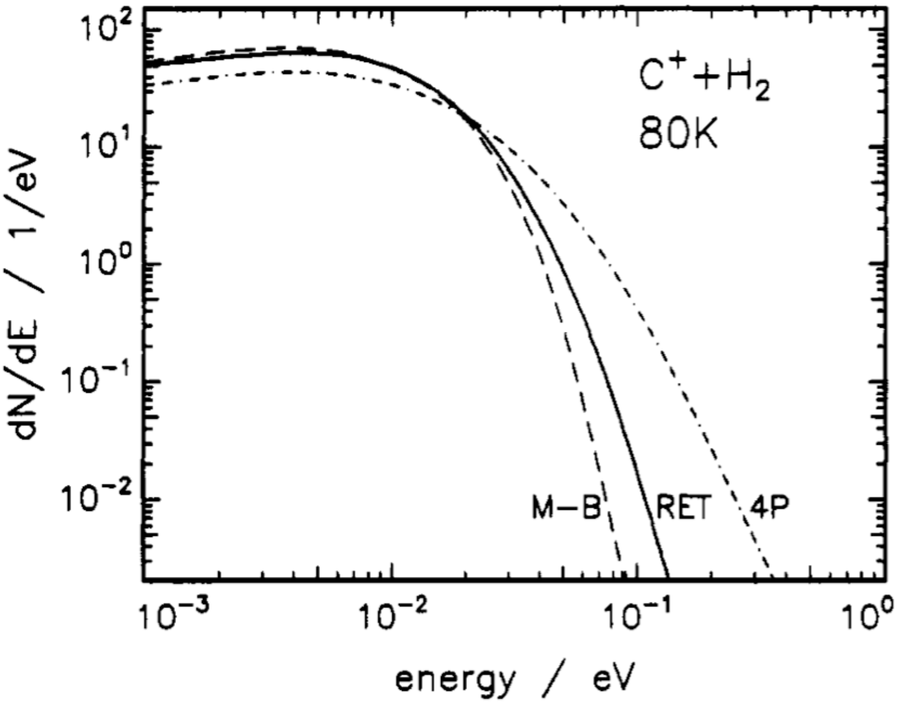

Figure 2.9: Numerically determined energy distribution of C^+ ions in a ring-electrode trap (RET) with H_2 buffer gas at 80 K. The case of the linear quadrupole trap (4P) and the Maxwell-Boltzmann distribution (M-B) are also represented. (Taken from Gerlich and Horning [36].)

2.1.4.2 Design of the home-built ion trap

The 22-pole ion trap has been designed and built in our laboratory by Dr. Oleg Boyarkin, based on the publications from the group of Dieter Gerlich [36, 39-41]. Figure 2.10 shows a schematic diagram of the trap mounted onto the cold head and a picture of it uncovered. It consists in 22 stainless steel rods, 50 mm long and 1 mm in diameter, equally spaced on a 5 mm inscribed radius. The rods are supported by two copper holders, each of them being electrically connected to a set of 11 alternate rods, while insulated from the other 11 by ceramic sleeves (see picture in Figure 2.10). Equal rf voltages of opposite phase are applied to these two holders, which are separated from the rest of the trap housing (copper baseplate and cover) by 0.5 mm thick sapphire sheets, thus providing electrical insulation but good thermal conductivity. A silicon diode temperature sensor (model DT-670, Lake Shore Cryotronics, Inc., OH, USA) is connected to the housing and measures the nominal temperature of the trap. A resistance heater (25 W) is also attached to the housing and switched on during the warm-up procedure to minimize condensation of gaseous material onto the trap components. Two pairs of cylindrical electrodes (numbered L1 to L4 along the ion path) are installed at the entrance and exit of the trap and are used to allow the ions in, confine them and finally release them after photodissociation. An individual voltage is applied to each electrode and the two inner ones, L2 and L3, which slightly protrude in between the 22 rods, can be added a pulsed voltage of adjustable duration and amplitude for trapping purposes.

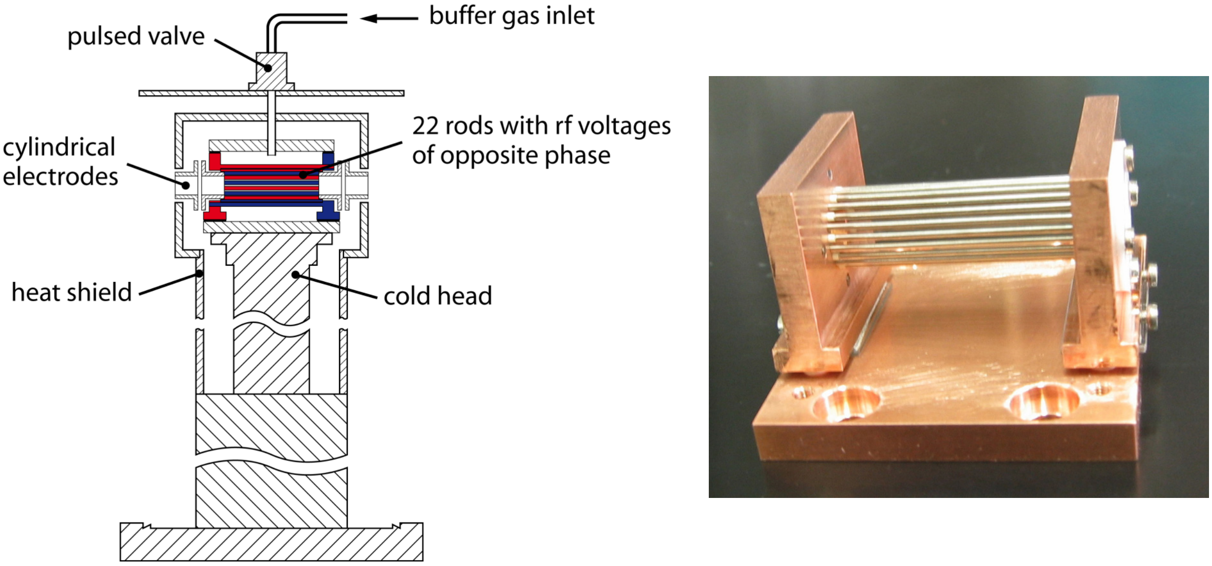

Figure 2.10: Schematic section view of the 22-pole ion trap and cold head assembly, and picture of the 22 rods mounted onto their holders.

The whole trap assembly is fixed directly onto the cold head, which constitutes the second stage of a closed-cycle liquid-helium cryocooler reaching a nominal temperature of 6 K, as measured by the temperature sensor. A heat shield is connected to the first stage of the cryocooler and surrounds the cold head, the trap and all its electrical leads. It maintains a precooling temperature of about 50 K (according to the constructor), thus reducing the radiative and conductive heat flow to the trap and allowing for lower final temperatures. A pulsed valve is fastened onto an independent plate near this heat shield and injects the He thermalization gas into the 22-pole trap, *via* a short teflon tube (see Figure 2.10).

The electronics used to supply the rf voltages to the ion trap were built in-house by our electrical workshop. The rf power supply delivers a sinusoidal tension of 4 MHz whose amplitude can be varied from zero to a few hundred volts peak-to-peak by means of an external DC power supply (model MCL 140-650, F.u.G. Elektronik GmbH, DE).

2.2 Characterization of the ion trap

The operating conditions and procedures to maximize the production and transmission of ions through our tandem mass spectrometer have been established by Dr. Anthi Kamariotou on the previous version of this machine [26]. Therefore, the present section will focus on the characterization of the newly added device, namely the cold 22-pole ion trap.

Collisional cooling of ions in linear multipole ion traps is a fairly complicated process that depends on many parameters (molecular weight of the ionic and neutral species involved, pressure of the buffer gas, characteristics of the rf field, etc.). This subject has been studied in detail by many authors for over three decades (see for instance references [42-44], as well as references therein). The aim of the experiments presented below is not to contribute significantly to this domain, but merely to get some quantitative idea of the performances of the 22-pole trap, so as to optimize the conditions for our spectroscopic studies of cold biomolecular ions.

The goal of the first experiment is to evaluate the pumping time of the helium buffer gas pulsed in the trap, in order to decide on the timing of the other pulsed events and obtain good trapping of both the parent and fragment ions. The second set of measurements estimates the trapping efficiency as a function of the trapping time, thus giving an approximate span of dissociative lifetimes that can be probed. Finally, the third characteristic to be examined here is the cooling efficiency of the trap, i.e., to quantify the internal temperature of the cooled ions.

2.2.1 Helium pumping time

As pointed out earlier in this chapter, our experiments are pulsed in nature, and spectroscopic measurements consist in firing laser pulses on individual trapped and thermalized ion packets. The repetition rate of a given experiment must be an integral fraction of that of the lasers (20 Hz). The confinement of incoming ions in the electric potential well of the 22-pole trap is achieved by damping their kinetic energy through collisions with a helium buffer gas. The latter is introduced into the trap by applying a ~ 200 μs electric pulse to a solenoid pulsed valve. An upper limit is imposed on this valve opening time by the maximum average pressure acceptable in the vacuum chamber, which we decided to be ~ 10^{-5} mbar. The duration of the electric pulse needed to reach this upper limit obviously depends on the repetition rate and the pressure in the helium line (typical values are 10 Hz or 20 Hz and 2 bar, respectively). Given this restriction, the main question to be addressed is: how fast do the He atoms escape from the 22-pole ion trap? In other words, how long after the pulse is there still enough helium in the trap to effectively decelerate and confine incoming parent or produced fragment ions? Answering this question will determine how the helium pulse must be timed with respect to other events, e.g., the release of a parent ion packet pretrapped in the hexapole or the firing of the laser(s).

Clearly, the fraction of incoming ions collisionally trapped should increase with the density of He atoms, at least over a certain density range. Therefore, the method used here consists in pulsing helium in the 22-pole and, after a given delay, trapping a «slice» of continuous ion signal using the entrance and exit electrodes. As the delay between these two events increases, the helium density will decrease, and so will the trapping efficiency. Hence, by varying this delay while measuring the intensity of the trapped signal, the time evolution of the density of He atoms can be mapped. This is illustrated by the timing diagram in Figure 2.11, showing the sequence of different pulses and the change in the ion signal measured at the detector (note: for simplicity, the delay due to the ion time-of-flight until the detector is neglected). A continuous flow of mass-selected ions is passing through the ion trap, whose entrance (L2) and exit (L3) electrodes are set low, i.e., «open». Prior to the helium pulse, a 10 ms portion of ion signal is acquired on channel B of the counter, in order to compensate for ESI source variations by normalization. When helium is pulsed into the trap, the continuous ion signal slightly increases, probably due to improved transmission efficiency by «collisional focusing» [42]. Some delay after the helium pulse, L3 is closed for a few milliseconds during which incoming ions can be trapped *via* collisions with the remaining He atoms. The ion packet is released by lowering L3 and measured on channel A of the counter. Synchronously with the opening of L3, a positive voltage pulse is applied to L2, serving two purposes: (i) it helps expelling the trapped ion packet; (ii) it blocks the continuous ion flow and thus makes the measurement of trapped ions background-free.

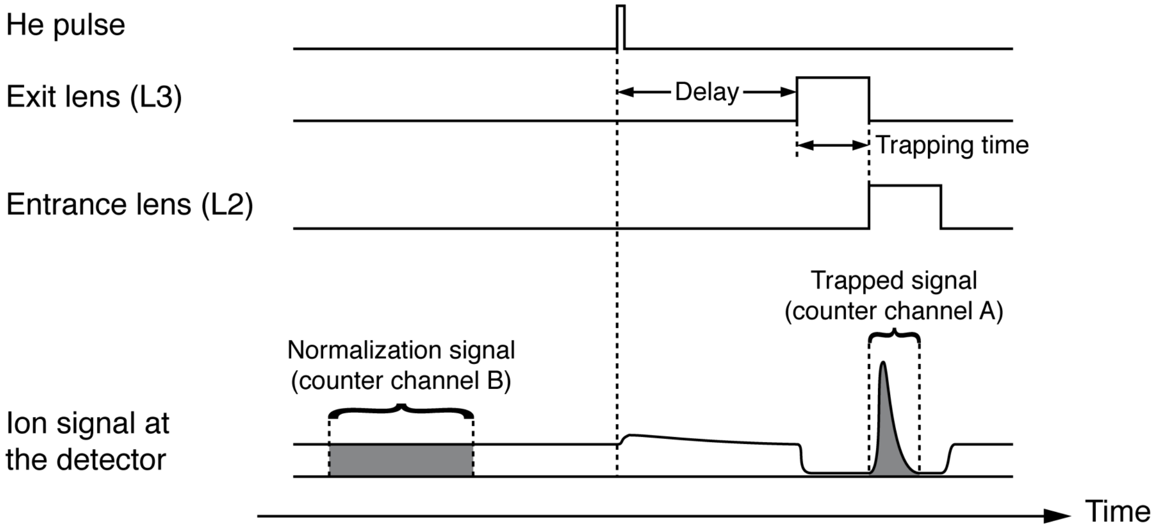

Figure 2.11: Timing diagram of the experiment used to probe the time needed to pump helium out of the 22-pole ion trap. See text for details.

This procedure has been applied both at room temperature and with the cryocooler in operation (~ 6 K), using a beam of protonated tryptophan (TrpH^+, *m/z* 205). In the first case, where helium leaves the trap quite fast, a trapping time of 2 ms was used (L3 pulse width). At low temperature, motions are much slower and ions were trapped for 10 ms. In both cases, a repetition rate of only 2 Hz was applied, to ensure that most of the helium is evacuated between two consecutive pulses, and 100 trapping sequences were measured for each delay and subsequently averaged. The results are shown in Figure 2.12 by plotting the normalized intensity of the trapped signal versus the varying delay between the helium pulse and the trapping gate. The error bars on each point represent the standard deviation of the 100 measurements averaged for that point. At room temperature (Figure 2.12(a)), the blocking voltage pulse on L2 was not used, which explains the non-zero baseline corresponding to a 0.8 ms «slice» of continuous ion signal counted on channel A. Nevertheless, it can be seen that the trapping efficiency is maximal at the beginning of the helium pulse, decreases by 50% after ~ 8 ms and is practically zero after 15 ms. On the other hand, when the trap is cooled to 6 K (Figure 2.12(b)), the He atoms leak out of the trap on a much longer timescale, indicating that the buffer gas rapidly equilibrates to the temperature of the surrounding walls. It takes about 50 ms for the trapping efficiency to decrease by a factor of two and over 100 ms to reach zero.

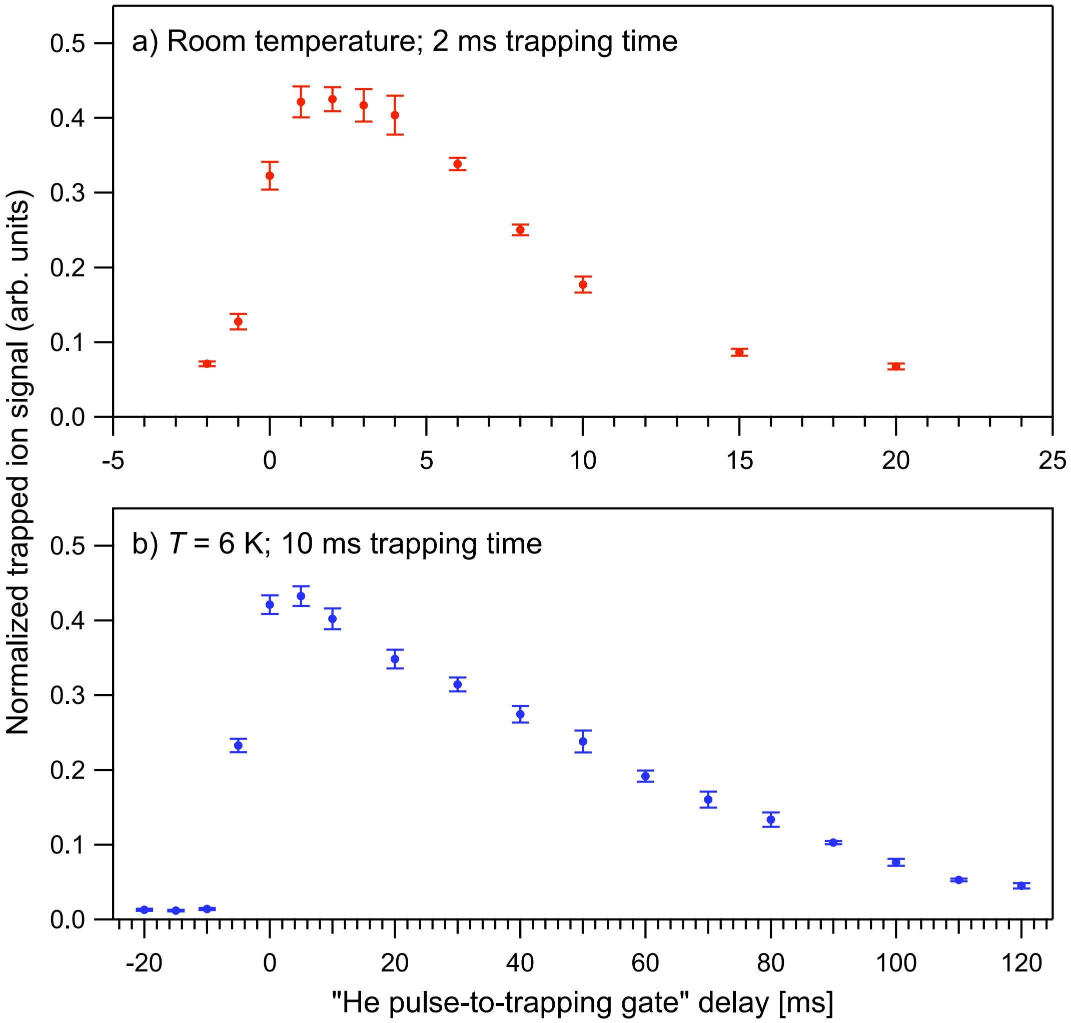

Figure 2.12: Variation of the trapping efficiency in the 22-pole as the helium buffer gas is evacuated. A continuous beam of $TrpH^+$ ions was trapped during (a) 2 ms at room temperature and (b) 10 ms at 6 K. Note the difference in timescales between the two graphs.

This lengthening of the pumping time by a factor of roughly 6 to 7 is consistent with calculations of conductance, which is proportional to $\sqrt{T}$ [45], thus predicting a change between room temperature and 6 K by a factor $\sqrt{\frac{293}{6}} \cong 7$. From a practical point of view, some useful information can be deduced from these results. First, the fact that a hexapole-pretrapped ion packet, whose width is typically shorter than 1 ms, will be most efficiently trapped in the 22-pole if it arrives at the beginning of the helium pulse. In situations where pretrapping is not used (e.g., for some weakly bound complexes) and the 22-pole is filled by a continuous flow of parent ions, trapping at room temperature would only be efficient during the first few milliseconds following the helium pulse. On the other hand, the filling of the trap at low temperature can be done for tens of milliseconds.

Trapping the photofragments can also be a matter of concern, depending on how they are produced. If the absorbed photon energy is significantly higher than the dissociation energy for a given fragment ion, the latter may carry part of the energy difference as kinetic energy, then making it difficult to confine in the effective potential of the trap. Collisional damping of this excess energy by the remaining buffer gas is a way to improve the collection of fragments to be detected. Therefore, the graphs presented above provide some insight about the relative timing to choose between the helium pulse and the photodissociation process (dissociation lifetimes, if long enough, should also be considered). Another possibility, especially at room temperature, would be to use an additional pulse of helium to help trapping the photofragments.

2.2.2 Ion trapping time

A few measurements, although not extensive, have been done to evaluate how long the ions can be efficiently trapped inside the 22-pole. These experiments were carried out with trapping parameters (voltages, He pulse duration, etc.) close to those used for the spectroscopic studies conducted at that moment, i.e., no thorough optimization of the conditions has been achieved to maximize the trapping time.

An example is given in Figure 2.13, showing the parent ion signal intensity of protonated tryptophan ($TrpH^+$) as a function of the trapping time between 25 ms and 20 s. It appears that the number of trapped ions decreases in a more or less exponential way, with a time constant on the order of 1 s. Other results (not shown) revealed that the *m/z* 160 fragments of protonated tryptophylglycine ($TrpGlyH^+$) irradiated by 275 nm laser light could be trapped for durations between 0.1 ms and 20 ms with no significant loss of intensity. Hence, photoexcited ions with dissociation lifetimes of up to several tens of milliseconds could easily be probed in our instrument.

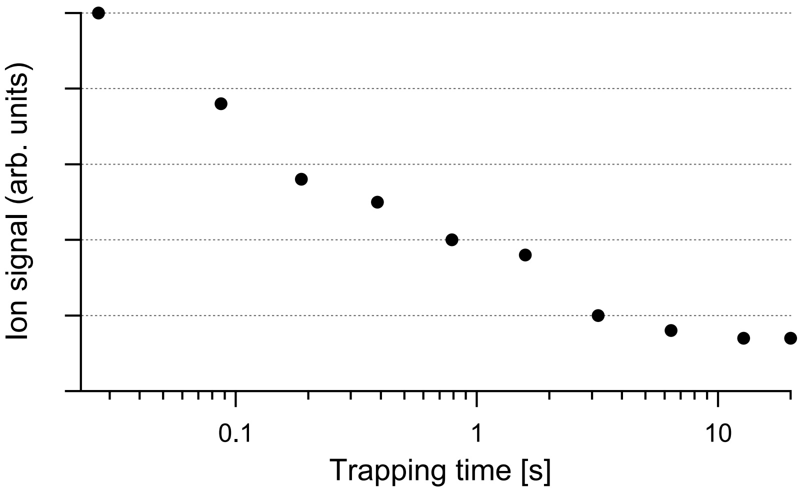

Figure 2.13: Evolution of the intensity of parent TrpH$^+$ ions trapped inside the 22-pole as a function of the trapping time.

It must be noted that these estimations were performed at room temperature and that their low-temperature counterparts have not been carried out. However, Gerlich and coworkers, using a similar 22-pole ion trap, reported storage times of cold ions as long as several minutes with no loss [36, 46]. This suggests that optimizing our instrument to achieve longer trapping times should be possible, if a particular experiment requires it.

2.2.3 Ion cooling efficiency

The purpose of cooling the ions is to trap them in their lowest vibrational state, thus simplifying their optical spectra. However, the nominal temperature measured by the sensor on the walls of the cold ion trap (6 K) does not necessarily reflect the actual internal temperature of the trapped ions. The latter must then be evaluated through indirect means.

2.2.3.1 Formation of He-ion complexes

A first qualitative evidence of the coldness of the trapped ions was the detection of He-ion complexes formed in the trap. Several mass spectra of protonated amino acids measured at low temperature revealed the presence of a small peak 4 u above the mass of the parent ion. An example is given in Figure 2.14 for the case of protonated tyrosine (TyrH$^+$). Therefore, the internal temperature of the trapped ions is low enough for a fraction of them to form these weakly bound complexes.

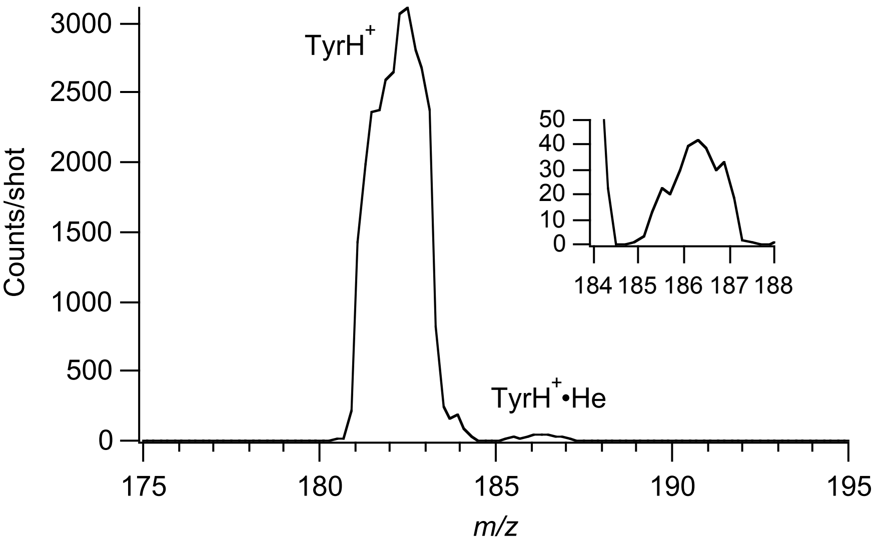

Figure 2.14: Mass spectrum of protonated tyrosine (TyrH$^+$) trapped at low temperature, showing the parent ion peak (*m/z* 182) and a small amount of TyrH$^+$·He complexes formed in the cold trap (*m/z* 186).

With a few assumptions, an estimate of the temperature of the ions can be deduced from the relative intensities of the two peaks shown in Figure 2.14. Let's consider the following reaction of complex formation:

$$\mathrm{TyrH^+ + He \rightleftarrows TyrH^+{\cdot}He} \qquad \text{(Eq. 2.5)}$$

We start by assuming that the three species of this reaction constitute an ideal gas mixture inside the trap. Therefore, we can relate the concentration-based equilibrium constant K_c to the partition functions of the reactants and products, as follows [47]:

$$\frac{\rho_{\mathrm{TyrHe}}}{\rho_{\mathrm{Tyr}}\rho_{\mathrm{He}}} = K_c = \frac{\left(q_{\mathrm{TyrHe}}/V\right)}{\left(q_{\mathrm{Tyr}}/V\right)\left(q_{\mathrm{He}}/V\right)} \qquad \text{(Eq. 2.6)}$$

where ρ_{A} and q_{A} are the number density and molecular partition function of species A, respectively, while V is the volume of the reaction vessel. The left-hand side of this equation will be evaluated from experimental measurements. The right-hand side, as will be shown below, is dependent on the equilibrium temperature. The latter will thus be determined so as to make both sides equal.

The right-hand side of Equation 2.6 can be developed using statistical thermodynamics [47]. First, we can express $q_{\mathrm{A}} = q_{\mathrm{A}}^{\mathrm{trans}} q_{\mathrm{A}}^{\mathrm{rot}} q_{\mathrm{A}}^{\mathrm{vib}} q_{\mathrm{A}}^{\mathrm{elec}}$ for TyrH^+ and $\mathrm{TyrH}^+\cdot\mathrm{He}$, and $q_{\mathrm{He}} = q_{\mathrm{He}}^{\mathrm{trans}} q_{\mathrm{He}}^{\mathrm{elec}}$ for He. We further assume that the complexation with a He atom does not significantly change the rotational and vibrational partition functions of TyrH^+, which implies $q_{\mathrm{TyrHe}}^{\mathrm{rot}} q_{\mathrm{TyrHe}}^{\mathrm{vib}} \approx q_{\mathrm{Tyr}}^{\mathrm{rot}} q_{\mathrm{Tyr}}^{\mathrm{vib}}$ (see reference [48]). The translational part is given by $q_{\mathrm{A}}^{\mathrm{trans}} = \left(\frac{2\pi m_{\mathrm{A}} k_{\mathrm{B}} T}{h^2}\right)^{\frac{3}{2}} V$, where m_{A} is the mass of species A, k_{B} is the Boltzmann constant, T is the equilibrium temperature and h is the Planck constant. Concerning the electronic partition functions, it is reasonable to say that the population of each species A is entirely in its electronic ground state of energy E_{A}, thus leading to $q_{\mathrm{A}}^{\mathrm{elec}} = e^{-\frac{E_{\mathrm{A}}}{k_{\mathrm{B}} T}}$. Rearranging everything brings the following equation:

$$K_c \approx \left(\frac{m_{\mathrm{TyrHe}}}{m_{\mathrm{Tyr}} m_{\mathrm{He}}}\right)^{\frac{3}{2}} \left(\frac{h^2}{2\pi k_{\mathrm{B}} T}\right)^{\frac{3}{2}} e^{\frac{D_e}{k_{\mathrm{B}} T}} \qquad \text{(Eq. 2.7)}$$

where $D_e = E_{\mathrm{Tyr}} + E_{\mathrm{He}} - E_{\mathrm{TyrHe}}$ is the dissociation energy of the complex. To our knowledge, this energy has never been calculated or measured for this specific complex. We can nonetheless deduce an approximate value based on data from the literature. First of all, the He atom is most likely attached to the charged ammonium group of TyrH^+. It is thus reasonable to draw a comparison with the $\mathrm{NH_4}^+\cdot\mathrm{He}$ complex, for which a dissociation energy of 170 cm^{-1} has been calculated by Dopfer and coworkers [49]. Moreover, the dissociation energy of proton-bound dimers has been shown to be inversely proportional to the difference in the proton affinities (PA) of the two bound entities [50, 51]. Knowing the proton affinities of He (178 $\mathrm{kJ\cdot mol^{-1}}$), $\mathrm{NH_3}$ (854 $\mathrm{kJ\cdot mol^{-1}}$) and Tyr (926 $\mathrm{kJ\cdot mol^{-1}}$; all values from reference [52]), a dissociation energy $D_e = 150\ \mathrm{cm}^{-1}$ can be estimated for the $\mathrm{TyrH}^+\cdot\mathrm{He}$ complex. We finally have an expression of K_c as a function of only the temperature T.

Let's now consider the left-hand side of Equation 2.6. To evaluate it, we will make two more assumptions. First, we suppose that both the thermal and chemical equilibria are quickly attained (within a few milliseconds), so that the density of helium ρ_{He} can be considered constant and equal to the density right after the pulse. Second, we assume that the complex ion-to-bare ion ratio at equilibrium, $\rho_{\mathrm{TyrHe}}/\rho_{\mathrm{Tyr}}$, is equal to the ratio measured at the ion detector. In reality, the density of He decreases over time and so does the fraction of He-ion complexes. Hence, our method overestimates ρ_{He} and underestimates $\rho_{\mathrm{TyrHe}}/\rho_{\mathrm{Tyr}}$ compared to a hypothetical equilibrium, then yielding an underestimated value of K_c. As a consequence, the temperature obtained from this procedure will be an upper limit to the real value, since K_c decreases as T increases (see Equation 2.7).

By measuring the background pressure of helium inside the 5th vacuum stage (where the ion trap is) during a pulsed experiment, one can calculate the initial value of ρ_{He}, either based on the pumping speed of the turbopump or from the pumping times presented in a previous section (see *2.2.1 Helium pumping time*). Both methods return a number density on the order of 10^{15} cm^{-3}. As regards the $\rho_{\mathrm{TyrHe}}/\rho_{\mathrm{Tyr}}$ ratio, several mass spectra, such as that depicted in Figure 2.14, consistently give a value of about 0.015. From these numerical values, Equations 2.6 and 2.7 result in an upper limit for the equilibrium temperature of 15 K.

2.2.3.2 Low intensities of vibrational hot bands

A better estimate of the cooling efficiency can be determined by measuring the resolved electronic spectra of cold trapped ions, e.g., protonated amino acids. This spectroscopic approach represents an easy method of obtaining an estimate of the vibrational temperature of the ions. By identifying, on either side of a band origin, a 1←0 vibronic transition of a low-frequency vibration and the corresponding hot band (0←1 transition), the vibrational temperature can be inferred from the comparison of their relative intensities (assuming an ion packet at thermal equilibrium described by a Maxwell-Boltzmann distribution). Indeed, if the Franck-Condon factors for both transitions are similar, their measured intensities should be simply proportional to the populations of the initial states. Hence, the temperature T is obtained from the intensities $I_{1\leftarrow 0}$ and $I_{0\leftarrow 1}$ as follows:

$$\frac{I_{1\leftarrow 0}}{I_{0\leftarrow 1}} = \mathrm{e}^{\frac{\Delta E}{k_{\mathrm{B}}T}} \quad \Rightarrow \quad T = \frac{\Delta E}{k_{\mathrm{B}} \ln\left(\frac{I_{1\leftarrow 0}}{I_{0\leftarrow 1}}\right)} \qquad \text{(Eq. 2.8)}$$

ΔE is the energy difference between the initial states, i.e., the difference between the band origin and the hot band.

This procedure has been used to evaluate the vibrational temperature of doubly hydrated protonated tryptophan ions ($TrpH^+ \cdot W_2$, where W represents water) for two different thermalization times: 5 ms and 25 ms. The goal of this experiment is to determine how fast the trapped ions can be cooled. Briefly, the ion trap exit electrode is closed synchronously with the helium pulse to start the accumulation and thermalization of an ion packet. After the chosen delay, a UV laser pulse is fired to photodissociate the parent ions and the ion packet is immediately released for detection of fragments. The laser wavelength is scanned across the origin region to obtain the aforementioned transition intensities. This region is shown in Figure 2.15 for the electronic spectrum of $TrpH^+ \cdot W_2$. The temperature estimates for thermalization delays of 5 ms and 25 ms are summarized in Table 2.1.

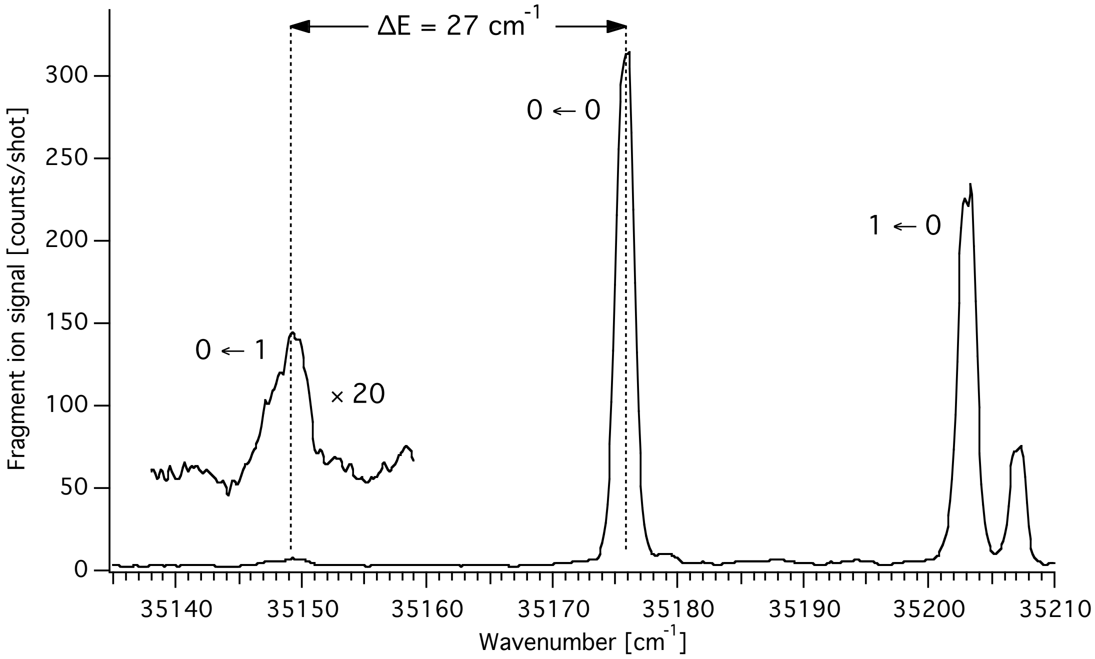

Figure 2.15: Origin region of the electronic spectrum of $TrpH^+ \cdot W_2$ at low temperature, monitoring the $TrpH^+$ fragment.

Table 2.1: Estimates of the vibrational temperature of $TrpH^+ \cdot W_2$ ions in the cold trap (nominal temperature of 6 K) after different thermalization delays.

Thermalization time [ms]	$I_{1\leftarrow 0}$ [normalized]	$I_{0\leftarrow 1}$ [normalized]	Vibrational temperature [K]
5	$(62\pm2)\cdot10^{-3}$	$(2.5\pm0.5)\cdot10^{-3}$	12±1
25	$(47\pm2)\cdot10^{-3}$	$(1.4\pm0.2)\cdot10^{-3}$	11±1

Although not exhaustive, this simple study shows that only a few milliseconds of thermalization are enough to bring the ion internal temperature to equilibrium, at least for an ion of this size. Moreover, this temperature is sufficiently low (~ 10 K) that the lowest vibrational excited state, 27 cm^{-1} above the ground state in the case of TrpH^{+}·W$_2$, is barely populated. The objective of spectral simplification upon ion cooling is then totally fulfilled, as exemplified by the sharp vibronic transitions shown in Figure 2.15.

2.3 Description of the laser setups

2.3.1 Generation of UV laser light

The UV laser light used for electronic excitation of chromophores is produced by frequency doubling the visible output of a dye laser pumped by the second or third harmonic of a Nd:YAG (yttrium aluminum garnet) laser. This is schematically depicted in Figure 2.16.

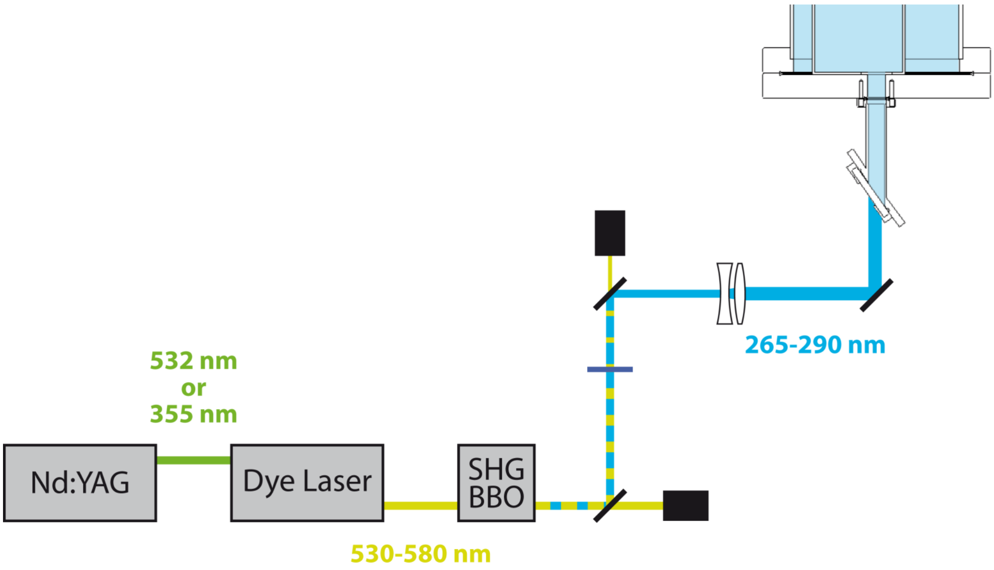

Figure 2.16: Schematic diagram of the UV generation setup. See text for details.

Depending on the UV range to be scanned, different laser dyes are used, which must be pumped at different frequencies. Therefore, the pulsed Nd:YAG laser (Spectra Physics GCR-250) can be set up to output either the second (532 nm) or the third harmonic (355 nm) of the 1064 nm fundamental. On the basis of their individual properties (wavelength range covered, working lifetime, conversion efficiency), we have mainly worked with the following dyes (all from Exciton, OH, US): Coumarin 540A (530-580 nm), Pyrromethene 580 (550-575 nm) and Rhodamine 590 (550-570 nm). Typical Nd:YAG pulse energies used to pump the dyes, at a 10 Hz or 20 Hz repetition rate, are on the order of 200 mJ for the green (532 nm) and 150 mJ for the UV (355 nm). The actual pumping power is adjusted to obtain a maximum pulse energy of 50 mJ out of the dye laser (Lumonics model HD-500). This upper limit is imposed by the damage threshold of the BBO crystal (beta barium borate) used in the next stage to convert the visible into ultraviolet light by second harmonic generation (SHG). This crystal is mounted in an Autotracker III (Inrad, NJ, US), along with a fused silica compensator, and both are automatically rotated to the phase-matching angle as the visible wavelength is scanned.

The resulting UV beam is separated from the remaining visible light *via* reflections on two dichroic mirrors and the use of a color filter. Its diameter is then optionally expanded or reduced by a telescope and sent into the vacuum chamber, on the side of the 4th vacuum stage, through a BaF_2 window placed at Brewster's angle (see Figure 2.1). The UV pulses obtained have a duration of 5 to 10 ns and an energy of 5 to 10 mJ. The typical linewidth in the UV is ~ 0.07 cm^{-1}.

2.3.2 Generation of IR laser light

The optical layout for the generation of infrared laser light for our experiments (3260 to 3800 cm^{-1}) is more complicated than the UV setup. It consists of two stages of nonlinear frequency conversion used to obtain light near 3 μm by mixing two near infrared (1064 nm) and one visible (645-665 nm) laser beams. A schematic representation of the setup is given in Figure 2.17. A pulsed Nd:YAG laser (Spectra Physics GCR-250) is adjusted to produce 10 Hz pulses of 1064 nm and 532 nm light with energies of ~ 600 mJ and 300 mJ, respectively. The 532 nm beam is used to pump a dye laser (Lambda Physik ScanMate) containing a DCM dye (from Exciton, OH, US) and generate tunable visible light around 650 nm of ~ 50 mJ per pulse. Scanning the dye laser changes the wavelength of the infrared light finally obtained. The 1064 nm fundamental is sent through a half-wave plate (λ/2) and a polarizing beam splitter (PBS), the former being rotated so that the latter separates the beam into two fractions of perpendicular polarizations with 150 mJ and 400 mJ per pulse, respectively.

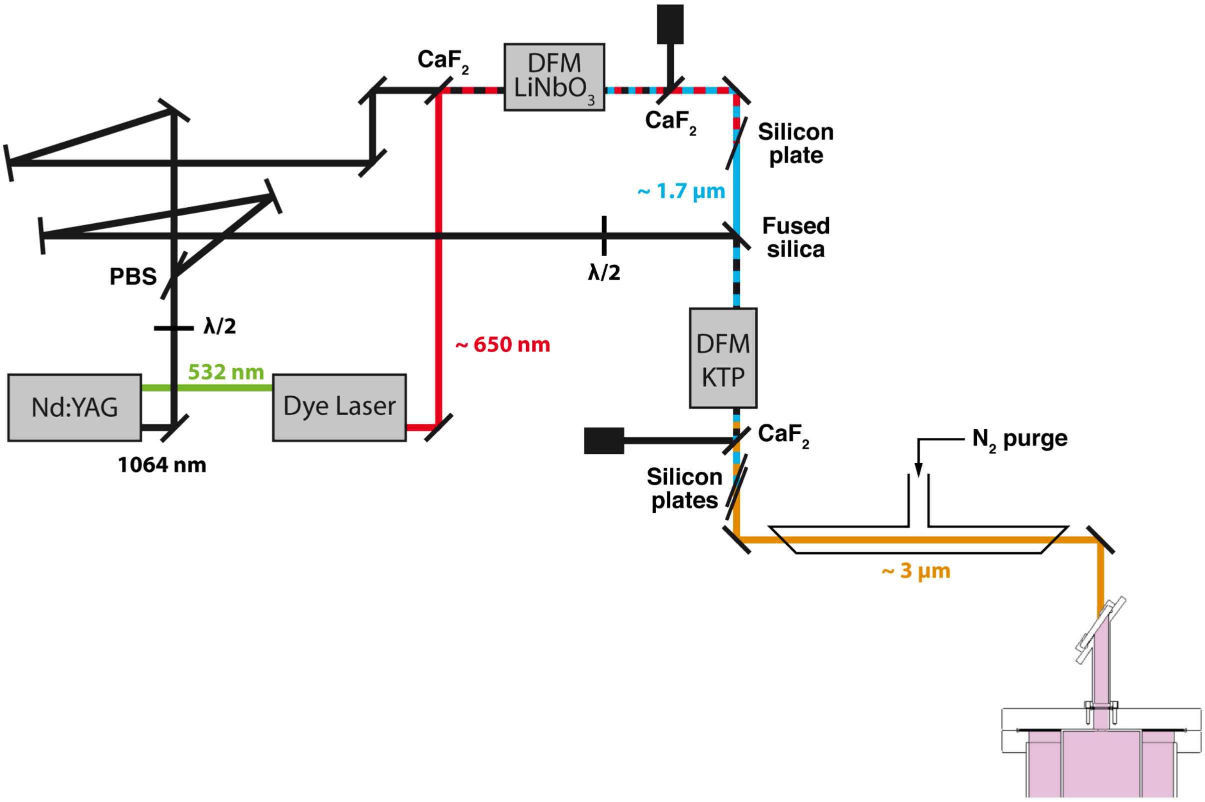

Figure 2.17: Schematic diagram of the IR generation setup. See text for details.

The visible output of the dye laser and the low-energy fraction of 1064 nm are combined using a CaF_2 dichroic mirror and sent to the first stage of difference frequency mixing (DFM). It comprises a lithium niobate crystal ($LiNbO_3$) and a CaF_2 compensator mounted in an Autotracker III (Inrad, NJ, US), which automatically adjusts their positions to the phase-matching angle. This stage produces ~ 5 mJ per pulse of 1.7 µm light, which is separated from the residual 1064 nm by a CaF_2 dichroic mirror and from the visible by a silicon plate.

The polarization of the high-energy fraction of 1064 nm is rotated 90° by a half-wave plate and reflected on a fused silica dichroic mirror for combination with the 1.7 µm beam. Both are then passed through the second stage of DFM. This one contains two 25 mm long KTP crystals ($KTiOPO_4$) mounted on temperature-controlled counter-rotating holders. A stepper motor driven by a LabVIEW computer program adjusts their positions to the phase-matching angle by following a prerecorded calibration curve. Depending on the actual wavelength, between 7 and 15 mJ of the desired 3 µm light is produced and separated from the residual 1064 nm and 1.7 μm beams by another CaF_2 dichroic mirror and a pair of silicon plates, respectively. The outcoming beam, whose linewidth is on the order of 1 cm^{-1}, is finally directed to the BaF_2 window placed at Brewster's angle on the 5th stage of the vacuum chamber (see Figure 2.1). Because atmosperic water molecules have many strong absorption bands in the 3 μm region, an N_2-purged tube is placed between the second DFM stage and the vacuum chamber, so as to minimize the loss in laser power.

References

[1] J. Zeleny, *Physical Review* **1914**, *3*, 69-91.
[2] J. Zeleny, *Physical Review* **1917**, *10*, 1.
[3] M. Dole, L. L. Mack and R. L. Hines, *Journal of Chemical Physics* **1968**, *49*, 2240-2249.
[4] M. Yamashita and J. B. Fenn, *Journal of Physical Chemistry* **1984**, *88*, 4451-4459.
[5] M. Yamashita and J. B. Fenn, *Journal of Physical Chemistry* **1984**, *88*, 4671-4675.
[6] C. M. Whitehouse, R. N. Dreyer, M. Yamashita and J. B. Fenn, *Analytical Chemistry* **1985**, *57*, 675-679.
[7] G. Taylor, *Proceedings of the Royal Society of London, Series A: Mathematical and Physical Sciences* **1964**, *280*, 383-397.
[8] Lord Rayleigh, *Philosophical Magazine* **1882**, *14*, 184-186.
[9] G. Schmelzeisen-Redeker, L. Bütfering and F. W. Röllgen, *International Journal of Mass Spectrometry and Ion Processes* **1989**, *90*, 139-150.
[10] J. V. Iribarne and B. A. Thomson, *Journal of Chemical Physics* **1976**, *64*, 2287-2294.
[11] B. A. Thomson and J. V. Iribarne, *Journal of Chemical Physics* **1979**, *71*, 4451-4463.
[12] P. Kebarle and M. Peschke, *Analytica Chimica Acta* **2000**, *406*, 11-35.
[13] P. Kebarle, *Journal of Mass Spectrometry* **2000**, *35*, 804-817.
[14] A. T. Iavarone and E. R. Williams, *Journal of the American Chemical Society* **2003**, *125*, 2319-2327.
[15] T. C. Rohner, N. Lion and H. H. Girault, *Physical Chemistry Chemical Physics* **2004**, *6*, 3056-3068.
[16] S. Nguyen and J. B. Fenn, *Proceedings of the National Academy of Sciences of the United States of America* **2007**, *104*, 1111-1117.
[17] K. McQuinn, F. Hof and J. S. McIndoe, *Chemical Communications* **2007**, 4099-4101.
[18] D. Touboul, M. C. Jecklin and R. Zenobi, *Rapid Communications in Mass Spectrometry* **2008**, *22*, 1062-1068.
[19] P. Kebarle and L. Tang, *Analytical Chemistry* **1993**, *65*, 972A-986A.
[20] M. S. Wilm and M. Mann, *International Journal of Mass Spectrometry and Ion Processes* **1994**, *136*, 167-180.
[21] M. Wilm and M. Mann, *Analytical Chemistry* **1996**, *68*, 1-8.
[22] D. P. H. Smith, *IEEE Transactions on Industry Applications* **1986**, *22*, 527-535.
[23] S. Geromanos, G. Freckleton and P. Tempst, *Analytical Chemistry* **2000**, *72*, 777-790.
[24] K. Sannes-Lowery, R. H. Griffey, G. H. Kruppa, J. P. Speir and S. A. Hofstadler, *Rapid Communications in Mass Spectrometry* **1998**, *12*, 1957-1961.

[25] K. A. Sannes-Lowery and S. A. Hofstadler, *Journal of the American Society for Mass Spectrometry* **2000**, *11*, 1-9.

[26] A. Kamariotou, *Infrared photofragment spectroscopy of charged amino acid water clusters in the gas phase*, Ph.D. Thesis, EPFL, Lausanne, 2006.

[27] R. B. Cole *Electrospray ionization mass spectrometry : fundamentals, instrumentation, and applications*; Wiley: New York, 1997.

[28] B. N. Pramanik, A. K. Ganguly and M. L. Gross, Eds. *Applied electrospray mass spectrometry*; Marcel Dekker: New York, 2002.

[29] W. Paul and H. Steinwedel, *Zeitschrift Für Naturforschung Section a-a Journal of Physical Sciences* **1953**, *8*, 448-450.

[30] W. Paul and M. Raether, *Zeitschrift Fur Physik* **1955**, *140*, 262-273.

[31] W. Paul, H. P. Reinhard and U. Vonzahn, *Zeitschrift Fur Physik* **1958**, *152*, 143-182.

[32] P. H. Dawson *Quadrupole mass spectrometry and its applications*; Elsevier Scientific Pub. Co.: Amsterdam, 1976.

[33] K. Blaum, C. Geppert, P. Muller, W. Nortershauser, E. W. Otten, A. Schmitt, N. Trautmann, K. Wendt and B. A. Bushaw, *International Journal of Mass Spectrometry* **1998**, *181*, 67-87.

[34] P. H. Dawson, *Mass Spectrometry Reviews* **1986**, *5*, 1-37.

[35] R. E. March and J. F. J. Todd *Quadrupole ion trap mass spectrometry*, 2nd ed.; Wiley-Interscience: Hoboken, N.J., 2005.

[36] D. Gerlich and S. Horning, *Chemical Reviews* **1992**, *92*, 1509-1539.

[37] E. Teloy and D. Gerlich, *Chemical Physics* **1974**, *4*, 417-427.

[38] D. Gerlich In *Electronic and atomic collisions : invited papers of the XIV International Conference on the Physics of Electronic and Atomic Collisions, Palo Alto, California, 24-30 July, 1985*; D. C. Lorents, W. E. Meyerhof, J. R. Peterson, Eds.; Elsevier: Amsterdam, 1986, p. 541.

[39] D. Gerlich, *Advances in Chemical Physics* **1992**, *82*, 1-176.

[40] D. Gerlich, *Journal of the Chemical Society, Faraday Transactions* **1993**, *89*, 2199-2208.

[41] A. Sorgenfrei, *Ion-Molekül-Reaktionen kleiner Kohlenwasserstoffe in einem gekühlten Ionen-Speicher*, Ph.D. Thesis, Albert-Ludwigs-Universität, Freiburg im Breisgau, 1994.

[42] D. J. Douglas and J. B. French, *Journal of the American Society for Mass Spectrometry* **1992**, *3*, 398-408.

[43] T. Covey and D. J. Douglas, *Journal of the American Society for Mass Spectrometry* **1993**, *4*, 616-623.

[44] A. V. Tolmachev, H. R. Udseth and R. D. Smith, *International Journal of Mass Spectrometry* **2003**, *222*, 155-174.

[45] J. M. Lafferty *Foundations of vacuum science and technology*; Wiley: New York, 1998.

[46] A. Luca, S. Schlemmer, I. Cermak and D. Gerlich, *Review of Scientific Instruments* **2001**, *72*, 2900-2908.

[47] D. A. McQuarrie and J. D. Simon *Physical chemistry : a molecular approach*; University Science Books: Sausalito, Calif., 1997.

[48] H. A. Jimenez-Vazquez, J. Tamariz and R. J. Cross, *Journal of Physical Chemistry A* **2001**, *105*, 1315-1319.

[49] N. M. Lakin, R. V. Olkhov and O. Dopfer, *Faraday Discussions* **2001**, *118*, 455-476.

[50] M. Meotner, *Journal of the American Chemical Society* **1984**, *106*, 1257-1264.
[51] D. Roth, O. Dopfer and J. P. Maier, *Physical Chemistry Chemical Physics* **2001**, *3*, 2400-2410.
[52] E. P. L. Hunter and S. G. Lias, *Journal of Physical and Chemical Reference Data* **1998**, *27*, 413-656.

Chapter 3 Spectroscopic techniques

In this chapter, the techniques used to acquire different types of spectra are described in detail. First, the timing of the successive events taking place during a single experiment (i.e., on a single ion packet) is presented. Then comes the description of how a mass spectrum of photofragments is obtained, followed by the measurement of simple UV or IR spectra of molecular ions. Finally, we describe a technique of IR-UV double resonance spectroscopy used for the acquisition of conformer-specific IR or UV spectra.

3.1 Timing of events

The duration of a photodissociation experiment on a single ion packet, from the generation of the latter until the detection of the photofragments, is typically of 50 ms or 100 ms. This experiment is then repeated at a rate of 20 Hz or 10 Hz, and for a number of times varying between 10 and 100, depending on the intensities of the measured signals. All these measurements would later be averaged to obtain a single point for each signal of the spectrum being acquired. A parameter is then changed by a small increment, e.g., the mass of the photofragments to be detected or the laser wavelength, and the next series of measurements is done. This whole process is iterated until a complete spectrum is acquired.

The sequence of events taking place during a single experiment can be illustrated by a timing diagram, such as that presented in the previous chapter for an experiment characterizing the cold ion trap (see Figure 2.11). Most of the photodissociation experiments presented in the next chapters were conducted according to the timing diagram shown in Figure 3.1. The ion packets are produced and trapped at a frequency of 20 Hz, whereas the photodissociating laser is pulsed at 10 Hz. Let's consider the first 50 ms of the diagram. A first packet of ions, which were pretrapped for about 40 ms in the hexapole of the ESI source, is released by lowering the exit lens potential of the latter. The parent ions, mass-selected by the first quadrupole Q1, enter the 22-pole ion trap and are collisionally trapped by the helium buffer gas pulsed ~ 1 ms prior to their arrival. After a storage time of ~ 35 ms, a laser pulse is fired through the 22-pole trap to induce photodissociation of the parent ions. Almost immediately (delay of ~ 100 µs), the trap is opened by lowering its exit electrode potential, the ions travel towards the analyzing quadrupole Q3 and the latter selects the fragments of a given m/z for detection. The count of fragment ions is recorded on channel A of the pulse counter. During the second 50 ms period of the diagram, the packet of parent ions is formed and trapped in exactly the same manner, but no laser pulse is fired and the mass command of Q3 is set to select the parent ion mass. The corresponding signal is measured on channel B of the counter and is later used to normalize the fragment ion signal, so as to compensate for slow variations of the nano-electrospray signal.

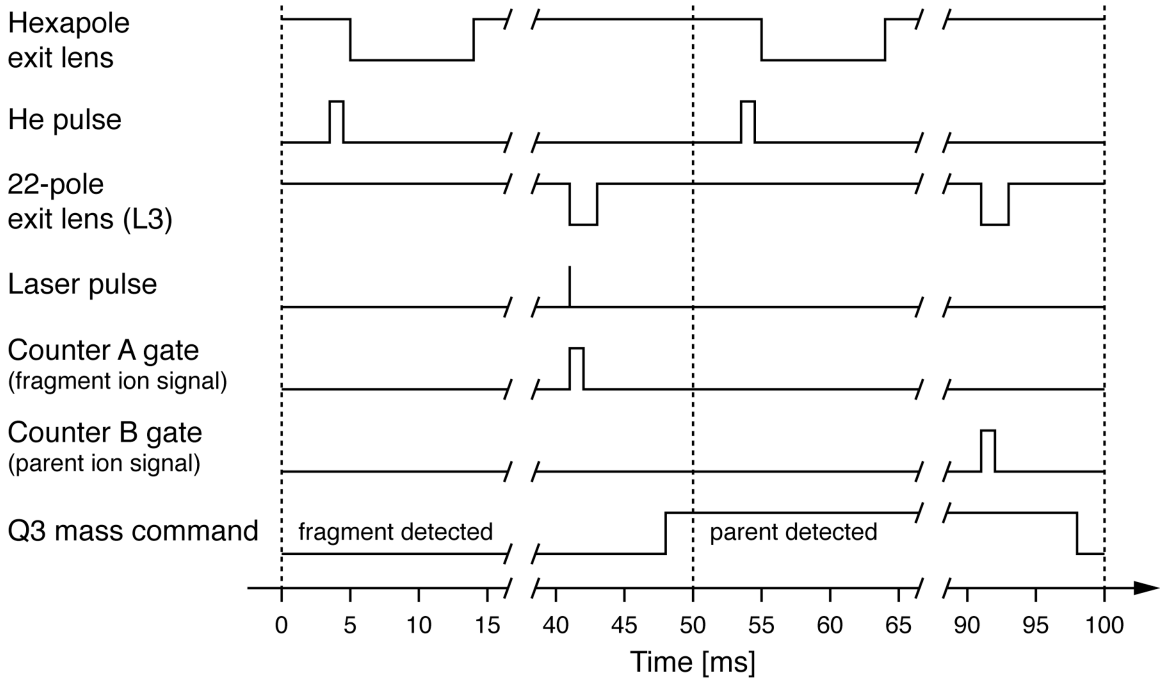
Hexapole exit lens
He pulse
22-pole exit lens (L3)
Laser pulse
Counter A gate (fragment ion signal)
Counter B gate (parent ion signal)
Q3 mass command
fragment detected
parent detected
0
5
10
15
40
45
50
55
60
65
90
95
100
Time [ms]

Figure 3.1: Typical timing diagram for a photodissociation experiment. The first half (0-50 ms) corresponds to the photodissociation of an ion packet with the subsequent detection of fragment ions, while the second half (50-100 ms) is the measurement of the parent ion signal used for normalization purposes.

As already mentioned in the preceding chapter (see *2.1.2 Electrospray ionization*), pretrapping in the hexapole is not always used, because of the space charge effects that it can produce and the subsequent fragmentation of weakly bound complexes. In such cases, the hexapole exit lens is left open to fill the 22-pole trap with a continuous flow of ions. Only a 6 ms long closing pulse is applied to stop the ion flow during the photodissociation process.

3.2 Measurement of a photofragment mass spectrum

Before being able to acquire the optical spectrum of a parent ion by measuring the intensity of a given photofragment as a function of the laser wavenumber, one should know the mass-to-charge ratio of the possible fragments and set the mass command of the analyzing quadrupole Q3 accordingly. Depending on the parent ion, fragmentation mass spectra can already be found in the literature. However, the dissociation process is sometimes fundamentally different from ours (e.g., collision-induced, electron capture or electron impact dissociations), leading to significant differences in the observed fragmentation patterns [1-5]. Even when comparing fragmentation mass spectra obtained by photodissociation, different experimental conditions (wavelength used, ion temperature, etc.) can produce variations in the relative fragment intensities [2, 6]. When going to large parent ions such as polypeptides, it gets even more unlikely to find literature data of fragmentation mass spectra measured in conditions that are similar to ours. For these reasons, we must be able to measure ourselves the mass spectrum of photofragments produced by any parent ion.

Because our analyzing mass spectrometer is a quadrupole, only a particular fragment mass can be measured for any single experiment on an ion packet. Therefore, the acquisition of a fragmentation mass spectrum must be obtained by successively dissociating many ion packets while incrementing the mass of the fragments to be detected, as described at the beginning of this chapter. To do so, a synchronization must be achieved between the computer that acquires the data and the one that controls the mass spectrometers. This is done by establishing a handshake communication between them. Two simple routines are run in parallel, written in LabVIEW for the data acquisition program and in the PAW Macro Language for the Merlin software controlling the mass filters. Once a given point of the mass spectrum is acquired, TTL pulses are exchanged between the two computers to increment the mass command and start the measurement of the next point.

An important parameter to consider before measuring a photofragmentation mass spectrum is of course the wavelength of the laser radiation to use. The exact positions of the electronic or vibrational transitions are *a priori* not known for a new species to be investigated. For that reason, the fragmentation mass spectra are first measured at room temperature, in order to benefit from the wide absorption bands caused by inhomogeneous broadening. The laser wavelength is chosen in a region where it is likely that the studied chromophore will absorb. A first overview of the possible fragment ions is thus obtained, although their relative intensities might greatly differ at low temperature. Depending on the parent ion (e.g., for water complexes), a significant amount of unimolecular «background» dissociation can take place without the laser. Hence, the laser-off signal is generally acquired alternately with the laser-on signal and subtracted from the latter.

Once the masses of the main fragment ions are known, they can be monitored to measure optical spectra at low temperature, where transitions are expected to be much narrower. The laser wavelength can then be fixed on a specific transition and the corresponding fragmentation mass spectrum, in its turn, can be measured at low temperature. As will be demonstrated in a following chapter, different fragmentation patterns can be obtained in this way from transitions belonging to distinct conformers of the same parent ion.

3.3 Measurement of a photodissociation UV or IR spectrum

Because of the relatively low density of ions in the 22-pole trap compared to condensed media, direct absorption spectroscopy cannot be carried out with sufficient sensitivity. Therefore, one has to use an indirect way of revealing photon absorption by detecting a consequence of the latter (action spectroscopy). The strategy applied here, as already mentioned, is to photodissociate the parent ions and measure the appearance of fragment ions. The advantage of this method when working with charged species is the ability to collect, transmit and detect them with high efficiency. Moreover, the possibility to measure separately fragments of different masses can provide more detailed information on the spectroscopy of the parent ions. On the other hand, some drawbacks stem from the fact that an action spectrum is not the same as an absorption spectrum, since the quantum yield of photodissociation can be wavelength-dependent. This subject will be further discussed below.

3.3.1 Spectroscopic schemes

The spectroscopic scheme of photodissociation *via* electronic excitation of a trapped parent ion is illustrated by the energy level diagram in Figure 3.2(a). The parent molecular ion AB taken here as an example has (a+b) positive charges and lies in the lowest vibrational state of its ground electronic state S_0. This would be the case for most trapped ions when the 22-pole is refrigerated to 6 K, as demonstrated in section *2.2.3 Ion cooling efficiency*. At higher temperatures, a significant fraction of the ions may populate excited vibrational levels of low frequency.

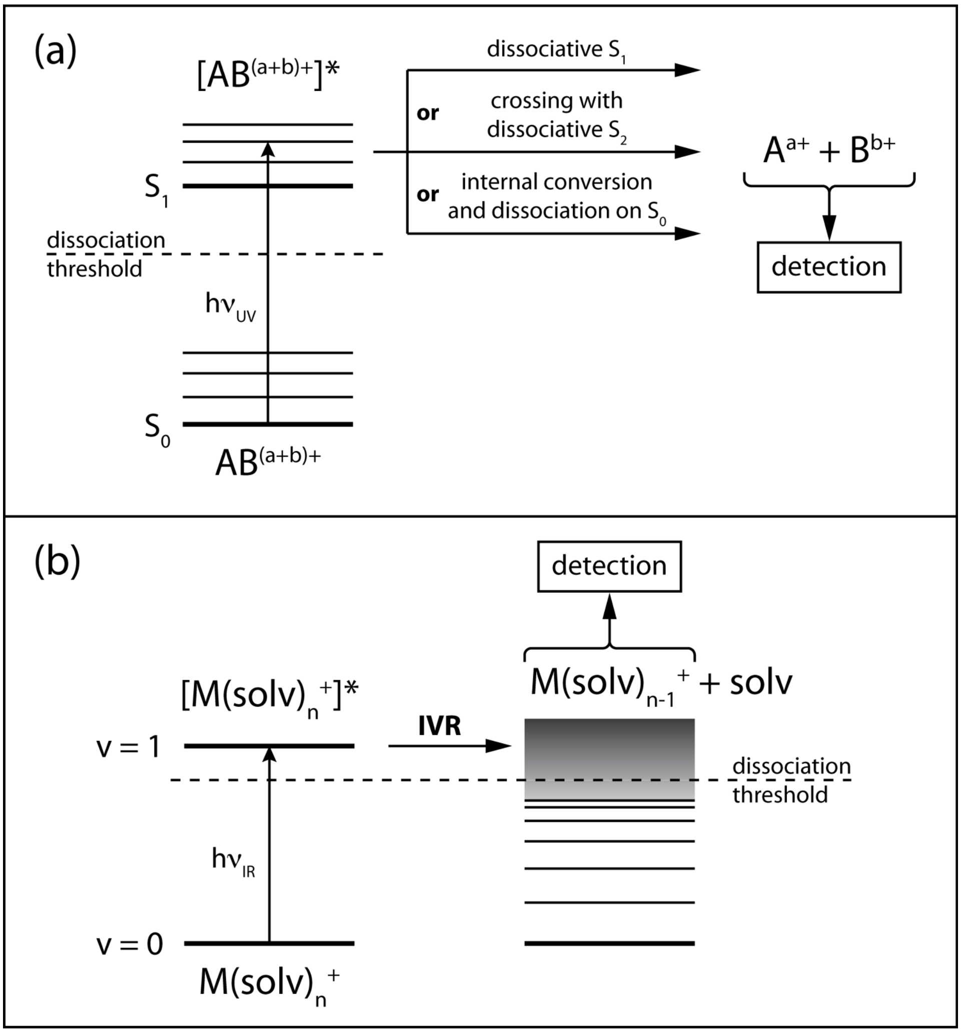
(a)
[AB(a+b)+]*
S1
dissociation threshold
hνUV
S0
AB(a+b)+
dissociative S1
or
crossing with dissociative S2
or
internal conversion and dissociation on S0
Aa+ + Bb+
detection
(b)
detection
[M(solv)n+]*
M(solv)n-1+ + solv
IVR
v = 1
dissociation threshold
hνIR
v = 0
M(solv)n+

Figure 3.2: General spectroscopic schemes of photodissociation after (a) an electronic excitation and (b) a vibrational excitation. The detailed mechanism leading to fragmentation can vary, depending on the photophysics of the parent ion.

When irradiated by UV (or visible) laser light of resonant frequency, some of the ions are excited to the electronic state S_1. Provided that the energy of the photons $h\nu_{\mathrm{UV}}$ is high enough to bring the ion above its dissociation threshold, different mechanisms can lead to fragmentation, some of which are indicated in the figure. There can be direct dissociation if S_1 is purely repulsive in the direction of a given bond. In other cases, a bound S_1 state can cross a repulsive state S_2 through which dissociation occurs. Another possibility is internal conversion from S_1 back to S_0, but above the dissociation threshold, so that fragmentation takes place on the ground potential energy surface. Which mechanism holds for a particular ion is usually not easy to determine and depends on its electronic state structure. The produced fragments, represented as A^{a+} and B^{b+} in this general case, can then be selectively detected.

Photodissociation spectroscopy through the vibrational excitation of a parent ion is shown in Figure 3.2(b). Since the energy of the infrared photons used in vibrational spectroscopy (up to ~ 3700 cm^{-1} for hydride stretches) is much lower than the dissociation energy of a covalent bond (on the order of 20 000 cm^{-1}), vibrational spectroscopy based on this scheme is limited to weakly bound entities that can be dissociated by absorbing the energy of a single (or a few) IR photon(s). The example presented in this diagram corresponds to the type of weakly bound species that have been studied in our instrument to this day [7, 8]: a molecular ion M^+ (e.g., a protonated amino acid) complexed with a defined number n of solvent molecules, usually water or methanol. When the frequency of the IR laser is resonant with a vibrational transition of the complex, absorption of a photon can lead to the fragmentation of the latter if its internal energy overcomes the dissociation threshold. What is most commonly observed is the detachment of a single solvent molecule, possibly occurring after intramolecular vibrational redistribution (IVR), as schematized in the figure. The resulting charged fragment of lower mass is then detected to reveal photon absorption.

3.3.2 Corrections to the measured ion signal

Some corrections must be applied to the raw fragment ion signal measured by the counter to obtain the final optical action spectrum. All have already been mentioned previously, but are recapitulated here for convenience. First, in cases where the monitored fragmentation channel shows significant signal in the absence of laser irradiation, the amount of this background dissociation must be measured and subtracted from the laser-on signal. Practically, this is done by producing the ion packets at twice the frequency of the pulsed laser and acquiring the laser-off signal on every other packet. In principle, background fragmentation is likely to become important only when working with weakly bound species (e.g., van der Waals complexes), which can dissociate collisionally inside the ion trap. This is especially critical for experiments at room temperature. Moreover, it is problematic by the fact that it creates parasitic ions that can absorb light in the same region, produce the same detected fragment and thus «pollute» the parent ion spectrum. For this reason, it is necessary to reduce as much as possible the background fragmentation of parent ions, typically by finding voltage conditions that allow a smooth introduction of the ions into the trap.

The second correction, which applies in all cases, is to compensate for the varying number of parent ions in the trap due to fluctuations in the nano-electrospray signal. These fluctuations are evaluated by measuring, on every other ion packet, either the parent ion signal (as explained in section *3.1 Timing of events*) or the amount of background fragmentation (as detailed in the above paragraph). The fragment signal is then «parent normalized» by dividing it by the parent (or background) signal acquired almost simultanesously(1). Obviously, such a mathematical treatment assumes a linear dependency between the two measured signals. Although it turned out to be inexact, this approach is satisfactory when the fluctuations are small enough.

Finally, the ion signal must be corrected for variations of the laser intensity as the wavelength is scanned («power normalization»). Therefore, one divides the fragment signal by the laser power measured on every shot with a pyroelectric detector(1). Here again, a linear dependency on the laser power is assumed as a first approximation. Nonlinearity could be caused, for instance, by the saturation of some spectroscopic transitions (which would be overcorrected) or if multiphoton processes are involved (for which a linear normalization would be insufficient).

---

(1) The whole spectrum is usually multiplied by the average parent (or background) signal afterwards, so as to keep a sense of the absolute fragment count. Similarly, after power normalization, the spectrum is multiplied by the average laser power.

3.3.3 Molecular size and lifetime considerations

The underlying principle of photodissociation spectroscopy is that the ions (or molecules) under study will fragment upon absorption of one or more photons. This is a fundamental condition for the measured photodissociation spectrum to reflect the actual absorption spectrum of the particles. Ideally, the fragmentation yield (ratio of dissociating ions to excited ions) and detection efficiency would be independent of the photon wavelength and the intensity of the photofragment signal would be proportional to the absorption cross-section at each point of the spectrum. Of course, this is usually not the case, since the dissociation efficiency depends on the internal energy of the ion and hence on that of the absorbed photon. However, if the spectral range measured is relatively small (almost constant energy) and the absorbing chromophore of the molecule is the same throughout the spectrum (localized excitation), one can assume that the photofragment intensities are reasonably faithful to the absorption intensities.

3.3.3.1 Thermodynamic and kinetic barriers to dissociation

For a stable molecule to dissociate, its internal energy must overcome a certain threshold, E_0, below which the breaking of a bond can simply not occur. Several groups have measured dissociation threshold energies for biomolecular ions such as peptides, proteins or oligonucleotides, which are the types of species that we plan to investigate in our apparatus. These experiments are based on the measurement of the dissociation kinetics as a function of temperature, using various dissociating techniques such as CID [9, 10], surface-induced dissociation (SID) [10] or blackbody infrared radiative dissociation (BIRD) [11-14]. For instance, the Williams group, using BIRD, studied the lowest-energy dissociation pathways of different electrosprayed peptides and proteins, and determined threshold energies on the order of 1.0 to 1.5 eV for molecules such as leucine enkephalin (560 Da) [14], bradykinin (1.06 kDa) [12, 13] or ubiquitin (8.6 kDa) [11]. This suggests that the absorption of a photon of at least this energy, about 10 000 cm^{-1}, should be able to induce dissociation of a protein ion.

The three naturally occurring aromatic amino acids tryptophan (Trp), tyrosine (Tyr) and phenylalanine (Phe) are UV chromophores that absorb light around 270 to 280 nm, i.e., with energy above 35 000 cm^{-1} [15-17]. Absorption of a single photon of this wavelength would bring the internal energy of any protein ion far above dissociation threshold, even at very low temperature where the initial thermal energy of the ion is negligible. In the case of vibrational spectroscopy of solvated ions, schematized in Figure 3.2(b), the numbers are not as favorable: the binding energy between water molecules and protonated peptides is on the order of 10 kcal·mol^{-1} (3500 cm^{-1}) [18], which is about the same as the highest-frequency vibrations of such molecules. Additional energy would be necessary to overcome the dissociation threshold with a single photon, for instance in the form of thermal energy, thus preventing IR photodissociation at very low temperature. At 298 K, the average thermal energy contained in a peptide is estimated to be approximately 30 cm^{-1} per vibrational mode, based on data in reference [19]. This corresponds to a contribution of 1000 to 2500 cm^{-1} per amino acid, depending on its size, to the internal energy of the peptide.

The excitation energy and the dissociation threshold are not the only parameters to take into account when considering the possibility for a molecule to dissociate. In most cases, the excitation energy, even if initially localized, gets rapidly dispersed among the other vibrational degrees of freedom through IVR [20]. As a consequence, the average energy in each vibrational mode can drop well below the dissociation threshold and the probability that enough energy concentrates in a single mode to induce the breaking of a bond decreases. This trend becomes more important as molecules get larger, because of the increasing number of degrees of freedom over which the energy is diluted. Therefore, for given excitation energy and dissociation threshold, the lifetime of a molecular ion is expected to get longer with increasing size. Griffin and McAdoo performed RRKM (Rice-Ramsperger-Kassel-Marcus) calculations, based on statistical rate theories, to evaluate the dissociation rates of model peptides as a function of their size and internal energy [19]. They predicted that the dissociation lifetime of a $(\text{AlaGly})_{16}$ ion (2.1 kDa) at room temperature absorbing a 193 nm photon would be on the order of 3 ms, assuming a dissociation threshold energy of 100 kJ·mol^{-1} (8360 cm^{-1}). This lifetime increases to almost 3 hours for $(\text{AlaGly})_{107}$ (13.7 kDa)! These considerations lead us to reflect on the maximum size of ions that we can expect to photodissociate and detect on the timescale of our experiment, and on the ways to improve this limit.

3.3.3.2 Increasing the size limit of dissociable ions

With the advent of new ionization techniques permitting to volatilize ever bigger molecules, such as ESI or MALDI, mass spectrometrists started to study the dissociation of large biomolecular ions and quickly had to deal with that problem of long dissociation lifetimes. They named it the kinetic shift (KS), i.e., the amount of excess internal energy that is required above the dissociation threshold in order to observe fragmentation of the precursor ions on the timescale of a given mass spectrometer [20]. A number of methods have been applied to circumvent this limitation and achieve the dissociation of increasingly heavier ions. A first approach is to lengthen the observation time by replacing sector instruments, linear quadrupoles or time-of-flight (TOF) analyzers by trapping mass spectrometers, such as Fourier transform ion cyclotron resonance (FT-ICR) instruments or quadrupole ion traps. This shifts the range of measurable lifetimes from microseconds or hundreds of microseconds up to several tens of seconds [21]. In the case of our 22-pole ion trap, we could improve on the upper limit of our apparatus by carefully optimizing the different voltages to obtain the highest trapping efficiency. Another parameter to take into account is the residual pressure of background gas, which can limit the observable dissociation lifetimes by collisional deactivation of the excited ions. This is especially critical in trapping experiments, whenever a buffer gas is used to assist in decelerating the incoming ions. That restriction can be easily circumvented, if necessary, by increasing the delay between the gas introduction and the activation of parent ions. However, there is an intrinsic limitation to the maximum dissociation lifetime of an ion: IR radiative cooling. When an excited ion has internal energy in excess compared to the temperature of its environment, relaxation of this energy will occur through the emission of infrared photons [20, 22]. According to Dunbar [22, 23], this should limit the lifetime of a metastable ion to a few tens of milliseconds at most.

Another possible strategy is to accelerate the dissociation rates of large ions by using activation methods that increase considerably their internal energy. Some examples are multiple-collision activation (MCA-CID), infrared multiphoton dissociation (IRMPD) or SID. These techniques have been reviewed in reference [21]. Concerning our own experiments, the objective is not ion dissociation itself, but the spectroscopic information that we can acquire through it. It is therefore important that alternative excitation methods, i.e., other than single-photon absorption, do not alter significantly the measured optical spectrum of the ion. A first option could be to trap the ions in the 22-pole for more than one laser cycle and irradiate the ion cloud with multiple laser shots, so as to pump enough energy into them and induce their fragmentation. Besides the necessity of a very good trapping efficiency, a potential drawback of this approach is the photodissociation of primary fragments by additional laser shots if some of their transitions overlap with those of the precursor ion. This would bias the relative intensities of the recorded spectrum. A second possibility is to use an auxiliary CO_2 laser to overcome the dissociation threshold of preexcited ions *via* IRMPD. Various groups have successfully used CO_2 lasers, both continuous-wave [24-27] and pulsed [6], to photodissociate protein ions as large as ubiquitin (8.6 kDa), cytochrome c (12.4 kDa) or porcine albumin (67 kDa). For us, the challenge would be to find conditions for which preexcited ions show an important dissociation yield, while non-excited ions do not. Implementation of this method will be facilitated by the expertise of our group in a similar technique (called IRLAPS, for infrared laser-assisted photofragment spectroscopy) applied to the measurement of high vibrational overtone spectra of small neutral molecules [28-30].

There is a third parameter that we can work on, besides the observation timescale and the excitation energy, in order to make the dissociation of high molecular weight ions easier: the dissociation threshold energy. Numerous studies have demonstrated that the dissociation lifetime or the amount of excitation energy required to fragment large ions are reduced when the charge of the ions increases. Smith and coworkers carried out calculations on a simplified «charges on a string» model of peptides to evaluate qualitatively the influence of multiple charging on the kinetics and thermodynamics of ion dissociation [31]. They predicted that the coulombic interactions in a highly charged ion not only have a significant effect on its thermodynamic stability, but can also appreciably lower the activation energy for dissociation, thereby resulting in a large increase of the dissociation rate. Experimental evidence of this effect was provided by a number of studies based on different approaches, e.g., thermally induced dissociation (TID) [9, 31, 32], IRMPD [6, 24], BIRD [12, 13], or UV photodissociation [33]. Consequently, the property of electrospray to produce multiply charged ions can be advantageously used to promote the dissociation of large biomolecules.

3.3.3.3 Complete IVR under debate

The discussion above suggests that, for a given mass spectrometer, the maximum size of dissociable peptide ions would be essentially limited by the amount of excitation energy imparted to them. Considering low-temperature spectroscopic experiments in our apparatus, for which the initial internal energy of precursor ions is negligible, one could expect this maximum size to be rather modest, especially if the excitation energy is restricted to a single photon. However, several studies have put into doubt the general assumption that the excitation energy is randomized by IVR among all vibrational degrees of freedom before dissociation has time to take place. To explain the observation of large molecules fragmenting at much higher rates than predicted by the RRKM theory, Schlag and Levine proposed that at low levels of vibrational excitation, i.e., below one quantum per mode, the rate of vibrational relaxation is significantly slower than assumed by statistical theories and the energy may remain localized for a sufficiently long time to induce dissociation [34]. Thus, a fraction of the excited molecules may undergo nonstatistical dissociation and produce fragments on an unexpectedly short timescale compared to RRKM estimations. The remaining fraction would go through complete IVR and possibly dissociate, according to a statistical rate constant [35, 36].

Starting in the mid 1980s, the first photodissociations by UV laser light (193 nm) of oligopeptides trapped in FT-ICR mass spectrometers have been reported [1, 3, 37, 38]. In 1989, Russell and coworkers observed the prompt dissociation of derivatized amino acids and peptides by visible (~ 500 nm) and low-energy UV (~ 350 nm) lasers and estimated dissociation lifetimes in the submicrosecond time range [2]. A few years later, owing to the development of ESI and MALDI, ever larger protein ions have been photodissociated by UV laser radiation [33, 39]. Again, the Russell group demonstrated that a single 193 nm photon is sufficient to induce the dissociation of protein ions as large as bovine insulin and lysozyme (5.7 kDa and 14.3 kDa, respectively) with rate constants above 10^6 s^{-1} [33]. Gabryelski and Li, using a 266 nm laser, obtained photofragments of small Trp- and Tyr-containing oligopeptides in the first microseconds following irradiation [4], although it is not clear whether dissociation resulted from a single or multiphoton absorption. Kim's laboratory also reported 266 nm photodissociation experiments of synthetic peptide and protein ions, and suggested that nonstatistical fragmentation might take place before complete IVR [40, 41].

For their part, Reilly and coworkers have used higher energy vacuum ultraviolet laser light (VUV; 157 nm) to photodissociate oligopeptide ions and noticed unusual fragmentation patterns, from which they deduced that the cleavage mechanism may well be nonstatistical («nonergodic») [5, 42]. Recently, Grégoire et al. demonstrated, with a femtosecond pump-probe experiment, that the UV excitation of protonated tryptophan-leucine ions leads to both a statistical fragmentation following internal conversion from the electronically excited state and a direct dissociation through the rapid nonstatistical loss of a hydrogen atom [43]. Using a different approach, the group of Nielsen also observed both statistical and nonstatistical dissociations when irradiating electrosprayed oligonucleotides with UV light around 260 nm. According to their measurements, the fraction of the total parent ion depletion due to nonstatistical fragmentation is greater than 90% and sometimes 95% [44, 45].

All these experiments suggest that there may in fact be no practical upper limit to the size of molecular ions that we can photodissociate in our instrument. At least, for the protonated amino acids or oligopeptides that will first be investigated, the preclusion of dissociation by relaxation of the excitation energy through IVR should not be a significant problem.

3.4 Conformer-specific spectra by IR-UV double resonance spectroscopy

When the UV or IR spectrum of an electrosprayed sample is acquired according to the procedure described above, the mass selectivity provided by the first quadrupole, Q1, ensures that the spectroscopic measurement is carried out on a single ion species, inasmuch as no fragmentation or complexation of the latter occurs in the meantime. Nevertheless, in the case of flexible molecules such as peptides, there may be several conformers of the same ion present in the 22-pole trap, each of which can have a distinct optical spectrum. The obtained spectrum would thus be a superposition of the spectra of the individual conformers. Being able to disentangle these different spectra would help interpret the spectroscopic information in each of them and, to a certain extent, would give an idea of the relative populations of the conformers, based on the intensities of their respective transitions. This last point, however, can be hindered by differences in the dissociation branching ratios and fragmentation efficiencies between the conformers.

3.4.1 Existing strategies for distinguishing different conformers

Research groups studying flexible neutral molecules or clusters entrained in a molecular beam encountered this problem of separate conformers all contributing to an optical spectrum. Various strategies have been developed to identify the number of conformers contributing to a composite spectrum and assign their individual transitions. In the mid 1980s, Rizzo et al. used R2PI saturation spectroscopy [15, 46, 47] and dispersed fluorescence spectroscopy [46, 48] to demonstrate the presence of several conformers of tryptophan and some of its analogs in supersonic expansions. Analysis of rotationally resolved, or partially resolved, vibronic spectra can also assist in distinguishing different conformers and, in combination with quantum chemical computation, attributing a specific geometry to each of them [49-53]. Towards the end of the 1980s, double resonance hole-burning spectroscopic techniques started to be applied for the investigation of jet-cooled molecules having multiple stable conformations. Colson and coworkers first proved the possibility of differentiating between the conformers of *m*-cresol by using UV-UV hole-burning spectroscopy [54]. The principle of this method is as follows. A pulsed laser, the «probe», is set on a given vibronic transition in the electronic spectrum previously measured for the jet-cooled molecules and serves to monitor the ground state population of the corresponding conformer. A second pulsed laser, the «pump», is fired a little earlier (e.g., 500 ns) and is scanned across the spectrum. Whenever it gets resonant with a transition of that same conformer, part of the ground-state population is preexcited and will show a different behavior than the remaining ground-state molecules upon arrival of the second laser pulse. As a consequence, a dip (or sometimes a gain) occurs in the signal induced by the probe laser, thus producing a conformer-specific vibronic spectrum. A similar scheme was also designed, IR-UV hole-burning, where the first laser pulse is from an IR laser fixed at a frequency in resonance with a vibrational transition specific to a particular conformer, while the wavelength of the UV probe laser is scanned. In this case, the difference between the UV spectra measured with and without the IR «burn» laser reveals the transitions belonging to the probed conformer. Finally, one can use the exact same arrangement, but keep the UV fixed and scan the IR wavelength. With this method, commonly referred to as resonant ion-dip (for R2PI detection) or fluorescence-dip (for LIF) IR spectroscopy, the IR spectrum of the conformer probed by the UV laser can be recorded independently. These IR-UV double resonance techniques were pioneered by Lee and coworkers to explore the IR and UV spectroscopy of jet-cooled benzene molecules and dimers [55, 56]. They have then been rapidly developed and applied by many other groups, in order to sort out the different conformers of flexible molecules or clusters observed in supersonic expansions. Some examples of studies taking advantage of such spectroscopic tools are given by references [57-71] and extensive reviews of the subject can be found in references [72-75].

3.4.2 Adaptation to the spectroscopy of cold trapped ions

In our apparatus, the photofragment ions, which constitute our signal, are trapped along with the parent ions until they are released and mass analyzed by the second quadrupole, Q3. Therefore, a UV-UV hole-burning scheme cannot be implemented, because one would have no way of discriminating between the fragments produced by the first and the second UV laser pulses. On the other hand, IR-UV hole-burning is conceivable and even supported by our observation of notable variations between the fragmentation patterns of room-temperature and low-temperature photofragment mass spectra. Figure 3.3 exemplifies this for the case of protonated tyrosine.

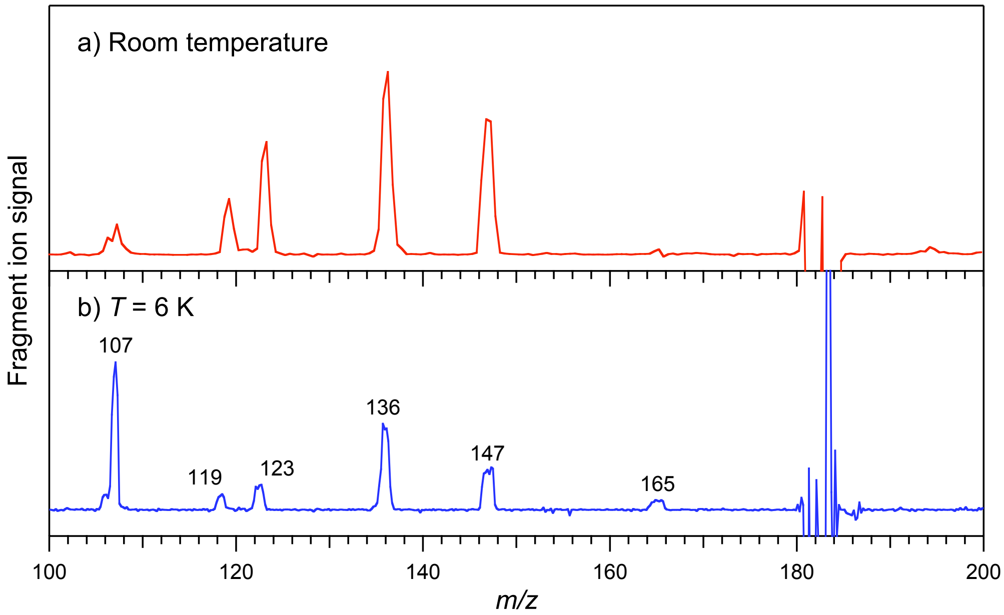

Figure 3.3: Photofragment mass spectra of protonated tyrosine (TyrH$^+$) irradiated by UV laser light at 35 082 cm^{-1}, recorded (a) at room temperature and (b) with the trap at 6 K. The signal at the parent ion mass, *m/z* 182, shows a depletion (laser-on minus laser-off), but appears here very noisy due to variations in the parent ion intensity.

The most striking difference is the change in the intensity of the peak at *m/z* 107, which is the highest one at 6 K and is drastically reduced in the room-temperature spectrum. Based on this result, we hypothesized that the absorption of an IR photon could have an effect on the cold ions similar to a temperature raise and cause a depletion of the *m/z* 107 photofragment. Experimental verification demonstrated the feasibility of this approach, as will be illustrated in a following chapter. Hence, IR-UV double resonance experiments analogous to those described above, i.e., IR dip spectroscopy and IR-UV hole-burning, can be carried out on the ion cloud trapped in the cold 22-pole, in order to identify different conformers and measure their individual vibrational and electronic spectra. The corresponding spectroscopic schemes are shown in Figure 3.4.

Practically, the procedure is the following. After acquiring the electronic spectrum of a cold ion species that may possess several stable conformers, a well-resolved vibronic transition is chosen and photofragment mass spectra, with the UV set at the corresponding frequency ν_{UV}, are measured both at room and low temperature. By comparing them, a fragment is identified, whose intensity is significantly lower at room temperature (e.g., *m/z* 107 in the case of $TyrH^+$ shown previously). An IR dip spectrum can then be measured by setting the UV laser at ν_{UV} and monitoring the intensity of that fragment while scanning the IR frequency (see Figure 3.4(a)). When the IR laser, fired ~ 100 ns prior to the UV, becomes resonant with a vibrational transition of the conformer absorbing at ν_{UV}, these ions are «heated» by the absorption of an IR photon, thus reducing the dissociation yield of the recorded mass channel. As a result, the fragment signal presents dips where the probed conformer absorbed IR radiation. Experimentally, the IR laser is pulsed at half the frequency of the UV laser (10 Hz and 20 Hz, respectively) and the IR-off photofragment signal is acquired on alternate ion packets. The IR-on signal is subsequently subtracted from the IR-off signal to generate the conformer-specific vibrational spectrum.

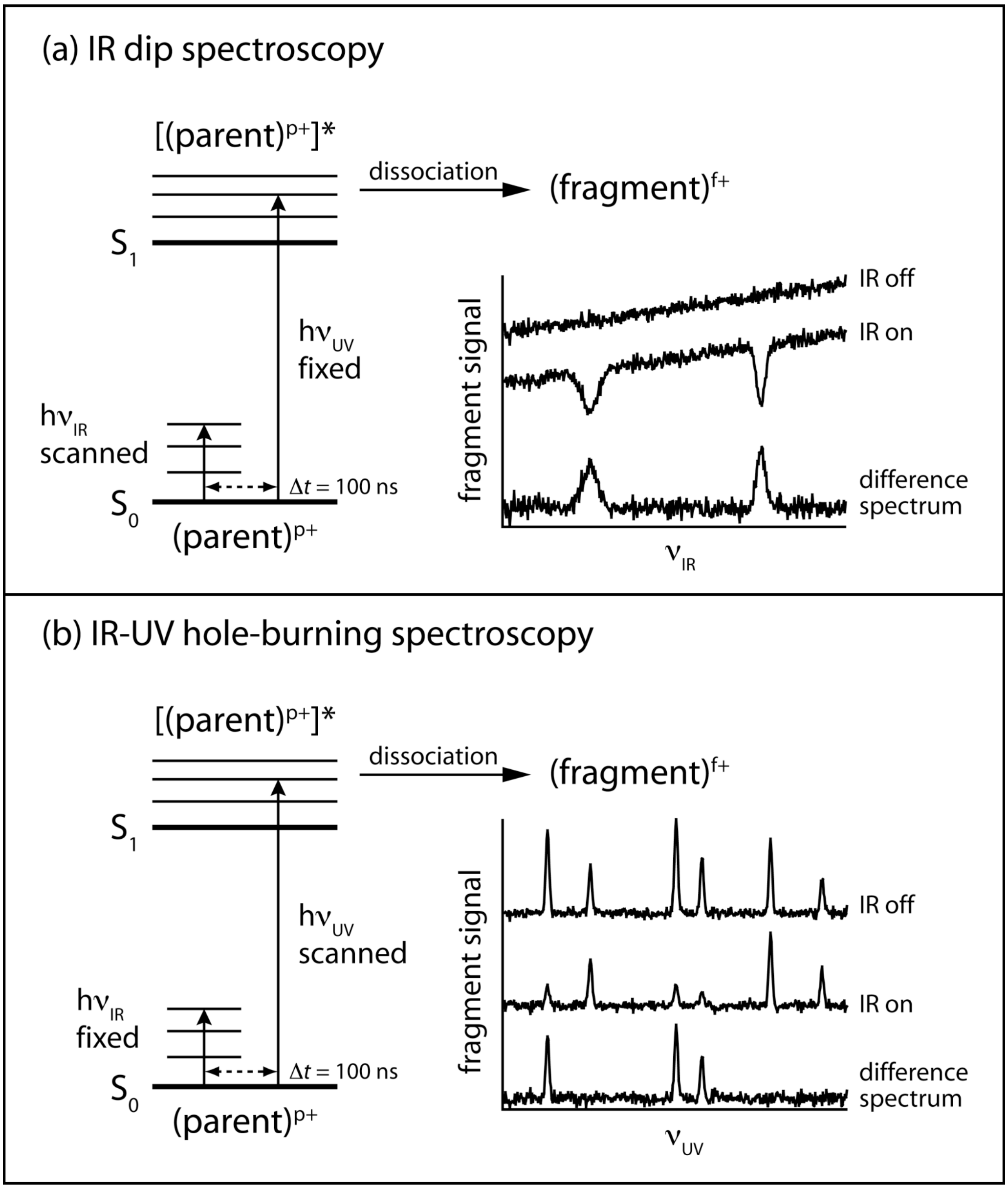
(a) IR dip spectroscopy
[(parent)p+]*
dissociation
(fragment)f+
S1
hνUV
fixed
hνIR
scanned
Δt = 100 ns
S0
(parent)p+
fragment signal
IR off
IR on
difference spectrum
νIR
(b) IR-UV hole-burning spectroscopy
[(parent)p+]*
dissociation
(fragment)f+
S1
hνUV
scanned
hνIR
fixed
Δt = 100 ns
S0
(parent)p+
fragment signal
IR off
IR on
difference spectrum
νUV

Figure 3.4: Spectroscopic schemes of IR-UV double resonance adapted to the photodissociation of cold trapped ions. (a) IR dip spectroscopy for the measurement of conformer-specific vibrational spectra. (b) IR-UV hole-burning spectroscopy for the measurement of conformer-specific electronic spectra.

Once the IR spectrum of a conformer is known, the IR wavelength ν_{IR} can be fixed on a particular transition, and an IR-UV hole-burning spectrum of this conformer is obtained by detecting the same fragment as the UV laser is scanned (see Figure 3.4(b)). Provided that this transition at ν_{IR} is unique to the conformer, all vibronic transitions stemming from the latter will be depleted by the IR laser. Again, the IR-on signal is subtracted from the IR-off signal measured simultaneously, resulting in a conformer-specific electronic spectrum.

These two spectroscopic methods have been described as *depletion* techniques, by selecting a photofragment whose intensity is greatly *reduced* at room temperature. In principle, it is also possible to monitor a fragment channel that is *enhanced* by prior IR photon absorption, thus performing *gain* experiments. While this works nicely to record IR spectra, it turns out that UV spectra measured in a *gain* mode show a very broad background signal. This is presumably due to the warming of the UV-probed ions by the IR laser, causing inhomogeneous broadening of the spectrum.

In order to obtain the final conformer-specific IR or UV spectra, corrections must be applied to the acquired signals, to compensate for variations in the parent ion intensity and laser power. This is done in an analogous manner to that described in section *3.3.2 Corrections to the measured ion signal*.

References

[1] W. D. Bowers, S. S. Delbert and R. T. McIver, *Analytical Chemistry* **1986**, *58*, 969-972.

[2] R. E. Tecklenburg, M. N. Miller and D. H. Russell, *Journal of the American Chemical Society* **1989**, *111*, 1161-1171.

[3] E. R. Williams, J. J. P. Furlong and F. W. McLafferty, *Journal of the American Society for Mass Spectrometry* **1990**, *1*, 288-294.

[4] W. Gabryelski and L. Li, *Review of Scientific Instruments* **1999**, *70*, 4192-4199.

[5] W. D. Cui, M. S. Thompson and J. P. Reilly, *Journal of the American Society for Mass Spectrometry* **2005**, *16*, 1384-1398.

[6] W. Gabryelski and L. Li, *Rapid Communications in Mass Spectrometry* **2002**, *16*, 1805-1811.

[7] A. Kamariotis, O. V. Boyarkin, S. R. Mercier, R. D. Beck, M. F. Bush, E. R. Williams and T. R. Rizzo, *Journal of the American Chemical Society* **2006**, *128*, 905-916.

[8] A. Kamariotou and T. Rizzo, *Infrared photofragment spectroscopy of charged amino acid water clusters in the gas phase*, Ph.D. Thesis, EPFL, Lausanne, 2006.

[9] M. Busman, A. L. Rockwood and R. D. Smith, *Journal of Physical Chemistry* **1992**, *96*, 2397-2400.

[10] M. Meotner, A. R. Dongre, A. Somogyi and V. H. Wysocki, *Rapid Communications in Mass Spectrometry* **1995**, *9*, 829-836.

[11] W. D. Price, P. D. Schnier, R. A. Jockusch, E. F. Strittmatter and E. R. Williams, *Journal of the American Chemical Society* **1996**, *118*, 10640-10644.

[12] W. D. Price, P. D. Schnier and E. R. Williams, *Analytical Chemistry* **1996**, *68*, 859-866.

[13] P. D. Schnier, W. D. Price, R. A. Jockusch and E. R. Williams, *Journal of the American Chemical Society* **1996**, *118*, 7178-7189.

[14] P. D. Schnier, W. D. Price, E. F. Strittmatter and E. R. Williams, *Journal of the American Society for Mass Spectrometry* **1997**, *8*, 771-780.

[15] T. R. Rizzo, Y. D. Park, L. Peteanu and D. H. Levy, *Journal of Chemical Physics* **1985**, *83*, 4819-4820.

[16] L. Li and D. M. Lubman, *Applied Spectroscopy* **1988**, *42*, 418-424.

[17] S. J. Martinez, J. C. Alfano and D. H. Levy, *Journal of Molecular Spectroscopy* **1992**, *156*, 421-430.

[18] D. F. Liu, T. Wyttenbach, P. E. Barran and M. T. Bowers, *Journal of the American Chemical Society* **2003**, *125*, 8458-8464.

[19] L. L. Griffin and D. J. McAdoo, *Journal of the American Society for Mass Spectrometry* **1993**, *4*, 11-15.

[20] C. Lifshitz, *International Journal of Mass Spectrometry and Ion Processes* **1992**, *118*, 315-337.

[21] J. Laskin and J. H. Futrell, *Mass Spectrometry Reviews* **2005**, *24*, 135-167.

[22] R. C. Dunbar, *International Journal of Mass Spectrometry and Ion Processes* **1983**, *54*, 109-118.

[23] R. C. Dunbar, *International Journal of Mass Spectrometry* **2000**, *200*, 571-589.

[24] D. P. Little, J. P. Speir, M. W. Senko, P. B. O'connor and F. W. McLafferty, *Analytical Chemistry* **1994**, *66*, 2809-2815.

[25] J. P. Speir, M. W. Senko, D. P. Little, J. A. Loo and F. W. McLafferty, *Journal of Mass Spectrometry* **1995**, *30*, 39-42.

[26] M. A. Freitas, C. L. Hendrickson and A. G. Marshall, *Journal of the American Chemical Society* **2000**, *122*, 7768-7775.

[27] R. A. Jockusch, K. Paech and E. R. Williams, *Journal of Physical Chemistry A* **2000**, *104*, 3188-3196.

[28] R. D. F. Settle and T. R. Rizzo, *Journal of Chemical Physics* **1992**, *97*, 2823-2825.

[29] O. V. Boyarkin, R. D. F. Settle and T. R. Rizzo, *Berichte der Bunsen-Gesellschaft Physical Chemistry Chemical Physics* **1995**, *99*, 504-513.

[30] O. V. Boyarkin and T. R. Rizzo, *Journal of Chemical Physics* **1995**, *103*, 1985-1988.

[31] A. L. Rockwood, M. Busman and R. D. Smith, *International Journal of Mass Spectrometry* **1991**, *111*, 103-129.

[32] A. L. Rockwood, M. Busman, H. R. Udseth and R. D. Smith, *Rapid Communications in Mass Spectrometry* **1991**, *5*, 582-585.

[33] M. E. Gimon-Kinsel, G. R. Kinsel, R. D. Edmondson and D. H. Russell, *Journal of the American Society for Mass Spectrometry* **1995**, *6*, 578-587.

[34] E. W. Schlag and R. D. Levine, *Chemical Physics Letters* **1989**, *163*, 523-530.

[35] Y. J. Hu, B. Hadas, M. Davidovitz, B. Balta and C. Lifshitz, *Journal of Physical Chemistry A* **2003**, *107*, 6507-6514.

[36] E. W. Schlag, H. L. Selzle, P. Schanen, R. Weinkauf and R. D. Levine, *Journal of Physical Chemistry A* **2006**, *110*, 8497-8500.

[37] W. D. Bowers, S. S. Delbert, R. L. Hunter and R. T. McIver, *Journal of the American Chemical Society* **1984**, *106*, 7288-7289.

[38] D. F. Hunt, J. Shabanowitz and J. R. Yates, *Journal of the Chemical Society, Chemical Communications* **1987**, 548-550.

[39] S. C. Beu, M. W. Senko, J. P. Quinn, F. M. Wampler and F. W. McLafferty, *Journal of the American Society for Mass Spectrometry* **1993**, *4*, 557-565.

[40] J. Y. Oh, J. H. Moon and M. S. Kim, *Journal of the American Society for Mass Spectrometry* **2004**, *15*, 1248-1259.

[41] J. Y. Oh, J. H. Moon and M. S. Kim, *Rapid Communications in Mass Spectrometry* **2004**, *18*, 2706-2712.

[42] M. S. Thompson, W. D. Cui and J. P. Reilly, *Angewandte Chemie, International Edition* **2004**, *43*, 4791-4794.

[43] G. Grégoire, H. Kang, C. Dedonder-Lardeux, C. Jouvet, C. Desfrançois, D. Onidas, V. Lepere and J. A. Fayeton, *Physical Chemistry Chemical Physics* **2006**, *8*, 122-128.

[44] B. Liu, P. Hvelplund, S. B. Nielsen and S. Tomita, *Physical Review A* **2006**, *74*, 052704/1-6.

[45] E. S. Worm, I. H. Andersen, J. U. Andersen, A. I. S. Holm, P. Hvelplund, U. Kadhane, S. B. Nielsen, J. C. Poully and K. Stochkel, *Physical Review A* **2007**, *75*, 042709/1-7.

[46] Y. D. Park, T. R. Rizzo, L. A. Peteanu and D. H. Levy, *Journal of Chemical Physics* **1986**, *84*, 6539-6549.

[47] T. R. Rizzo, Y. D. Park, L. A. Peteanu and D. H. Levy, *Journal of Chemical Physics* **1986**, *84*, 2534-2541.

[48] T. R. Rizzo, Y. D. Park and D. H. Levy, *Journal of Chemical Physics* **1986**, *85*, 6945-6951.

[49] C. A. Haynam, D. V. Brumbaugh and D. H. Levy, *Journal of Chemical Physics* **1983**, *79*, 1581-1591.

[50] L. A. Philips and D. H. Levy, *Journal of Chemical Physics* **1988**, *89*, 85-90.

[51] P. M. Felker, *Journal of Physical Chemistry* **1992**, *96*, 7844-7857.

[52] J. A. Dickinson, P. W. Joireman, R. W. Randall, E. G. Robertson and J. P. Simons, *Journal of Physical Chemistry A* **1997**, *101*, 513-521.

[53] D. W. Pratt, *Annual Review of Physical Chemistry* **1998**, *49*, 481-530.

[54] R. J. Lipert and S. D. Colson, *Journal of Physical Chemistry* **1989**, *93*, 3894-3896.

[55] R. H. Page, Y. R. Shen and Y. T. Lee, *Journal of Chemical Physics* **1988**, *88*, 4621-4636.

[56] R. H. Page, Y. R. Shen and Y. T. Lee, *Journal of Chemical Physics* **1988**, *88*, 5362-5376.

[57] C. Riehn, C. Lahmann, B. Wassermann and B. Brutschy, *Chemical Physics Letters* **1992**, *197*, 443-450.

[58] S. Tanabe, T. Ebata, M. Fujii and N. Mikami, *Chemical Physics Letters* **1993**, *215*, 347-352.

[59] R. N. Pribble and T. S. Zwier, *Science* **1994**, *265*, 75-79.

[60] T. Walther, H. Bitto, T. K. Minton and J. R. Huber, *Chemical Physics Letters* **1994**, *231*, 64-69.

[61] T. Ebata, N. Mizuochi, T. Watanabe and N. Mikami, *Journal of Physical Chemistry* **1996**, *100*, 546-550.

[62] A. Mitsuzuka, A. Fujii, T. Ebata and N. Mikami, *Journal of Chemical Physics* **1996**, *105*, 2618-2627.

[63] R. N. Pribble, C. Gruenloh and T. S. Zwier, *Chemical Physics Letters* **1996**, *262*, 627-632.

[64] C. Janzen, D. Spangenberg, W. Roth and K. Kleinermanns, *Journal of Chemical Physics* **1999**, *110*, 9898-9907.

[65] J. R. Carney and T. S. Zwier, *Journal of Physical Chemistry A* **2000**, *104*, 8677-8688.

[66] E. G. Robertson, M. R. Hockridge, P. D. Jelfs and J. P. Simons, *Journal of Physical Chemistry A* **2000**, *104*, 11714-11724.

[67] L. C. Snoek, E. G. Robertson, R. T. Kroemer and J. P. Simons, *Chemical Physics Letters* **2000**, *321*, 49-56.

[68] L. C. Snoek, R. T. Kroemer, M. R. Hockridge and J. P. Simons, *Physical Chemistry Chemical Physics* **2001**, *3*, 1819-1826.

[69] I. Hunig and K. Kleinermanns, *Physical Chemistry Chemical Physics* **2004**, *6*, 2650-2658.

[70] D. Reha, H. Valdes, J. Vondrasek, P. Hobza, A. Abu-Riziq, B. Crews and M. S. de Vries, *Chemistry-a European Journal* **2005**, *11*, 6803-6817.

[71] A. Abo-Riziq, B. O. Crews, M. P. Callahan, L. Grace and M. S. de Vries, *Angewandte Chemie-International Edition* **2006**, *45*, 5166-5169.

[72] T. S. Zwier, *Annual Review of Physical Chemistry* **1996**, *47*, 205-241.

[73] B. Brutschy, *Chemical Reviews* **2000**, *100*, 3891-3920.

[74] E. G. Robertson and J. P. Simons, *Physical Chemistry Chemical Physics* **2001**, *3*, 1-18.

[75] T. S. Zwier, *Journal of Physical Chemistry A* **2001**, *105*, 8827-8839.

Chapter 4 UV spectroscopy of protonated amino acids: $TrpH^+$ and $TyrH^+$

The first spectroscopic studies of gas-phase neutral tryptophan (Trp) and tyrosine (Tyr) were carried out in the mid 1980s in the environment of a molecular beam. Levy and coworkers measured the R2PI and LIF electronic spectra of jet-cooled Trp and, applying techniques of power saturation and dispersed fluorescence, they demonstrated the presence of several conformers in the expansion [1-3]. In 1988, Li and Lubman recorded the first R2PI spectrum of jet-cooled Tyr [4]. A few years later, Levy's group measured the corresponding LIF spectrum and, using the same methods as for Trp, identified ten different conformers of neutral tyrosine [5]. They concluded that some of these could likely be pairs or conformers, differing only in the orientation of the phenolic OH bond.

It is only at the beginning of the 2000s, with the advent of double resonance techniques such as hole-burning and infrared dip spectroscopies, along with the development of powerful computational quantum chemical calculations, that more thorough spectral analysis and geometrical assignments of the conformers of neutral Trp and Tyr could be achieved. Snoek et al. could thus attribute specific structures to at least five of the six Trp conformers already identified by Levy's group in the R2PI spectrum [6]. Using the same approach, they also studied the hydrated complexes of tryptophan [7, 8]. With a different strategy, Dugourd and Jarrold confirmed the structure of the most stable Trp conformer by measuring its permanent electric dipole and comparing it with the results of DFT and MP2 (second-order Møller-Plesset perturbation theory) calculations [9]. As regards tyrosine, de Vries and coworkers performed hole-burning experiments, as well as quantum chemical calculations of the conformers, and arrived at a spectral assignment that slightly differs from the one proposed by Levy [10, 11]. Indeed, this issue is still one of controversy, as Ebata and coworkers very recently published another interpretation of the electronic spectrum of Tyr, along with a complete geometrical assignment of the conformers, their study being further supported by infrared dip spectra [12].

Most of the early gas-phase studies on the protonated counterparts of these two amino acids, $TrpH^+$ and $TyrH^+$, focussed mainly on H/D exchange and CID reactions, with the goal to unravel the detailed fragmentation mechanisms of these ions [13-21]. The first investigations on their spectroscopy in the gas phase have been conducted only in the past few years. In 2004, Weinkauf's group published the first electronic spectrum of isolated $TrpH^+$ ions obtained by laser photofragmentation in a Paul trap cooled by liquid N_2 [22]. It shows that the S_0-S_1 transition is in the same energy range as for neutral Trp (~ 35 000 cm^{-1}), but the measured spectrum is much broader than for the latter, which they attribute to the congestion caused by multiple vibronic transitions and hot bands, as well as possible lifetime broadening. In the same article, they also present the results of quantum chemical calculations showing that the most stable isomer of $TrpH^+$ is protonated at the amino group. This fact had already been established by Maksić [23] and O'Hair [20]. In 2005, Talbot et al. also recorded an electronic spectrum of trapped $TrpH^+$, this time at room temperature, but on a wider spectral range [24]. Their study includes multistage mass spectrometry experiments (MS^n), from which they deduce possible structures and dissociation mechanisms for various photofragments.

Following their work on phenol and indole derivatives, Jouvet and coworkers published a series of articles about the electronic excited states of $TrpH^+$ and $TyrH^+$ studied by photodissociation, which comprises both experimental lifetime measurements using a femtosecond laser pump-probe technique and theoretical calculations of the excited states and their dynamics [25-30]. These papers will be further discussed below and in the next chapters, since they are closely related to the work set forth in this thesis.

In this chapter, the electronic spectra of protonated tryptophan and tyrosine measured by photodissociation inside our tandem mass spectrometer, both at room temperature and at a nominal temperature of 6 K, will be presented. The spectral simplification caused by the cooling of the ions will be highlighted, as well as the differences between the photophysical behaviors of TrpH^+ and TyrH^+.

4.1 Electronic spectrum of protonated tryptophan

Stereoisomerically pure tryptophan and tyrosine, L-Trp and L-Tyr, were purchased (Sigma-Aldrich Co., CH) and used without further purification. The solutions prepared to be used as samples in the nano-electrospray source generally consist of a $2\cdot10^{-4}$ M solution of the substance of interest in a 1:1 solvent mixture of ultrapure water and methanol, with 0.2% of acetic acid. The photodissociation mass spectra and electronic spectra of the species are then measured with the apparatus and laser system depicted in *Chapter 2*, according to the procedures described in *Chapter 3*. The results obtained for protonated tryptophan are presented in the current section.

4.1.1 Photofragment mass spectra at room temperature and 6 K

We sprayed the tryptophan solution, selected the mass of TrpH^+, *m/z* 205, with the first quadrupole and accumulated ion packets in the 22-pole trap containing up to ~ 10 000 ions. Photofragmentation of these parent ions was performed by pulsing UV laser light at 35 078 cm^{-1} through the trap and the products were analyzed by scanning the mass command of the second quadrupole. The resulting mass spectra, measured at room temperature and at 6 K, are shown in Figure 4.1. They correspond to the difference of ion counts between alternate irradiated and nonirradiated ion packets. Therefore, the signal at the mass of the parent ion, *m/z* 205, presents a depletion (not entirely shown) and an especially high noise level, because the parent ion signal is much more intense than that of the fragments and slightly varies from one packet to the next.

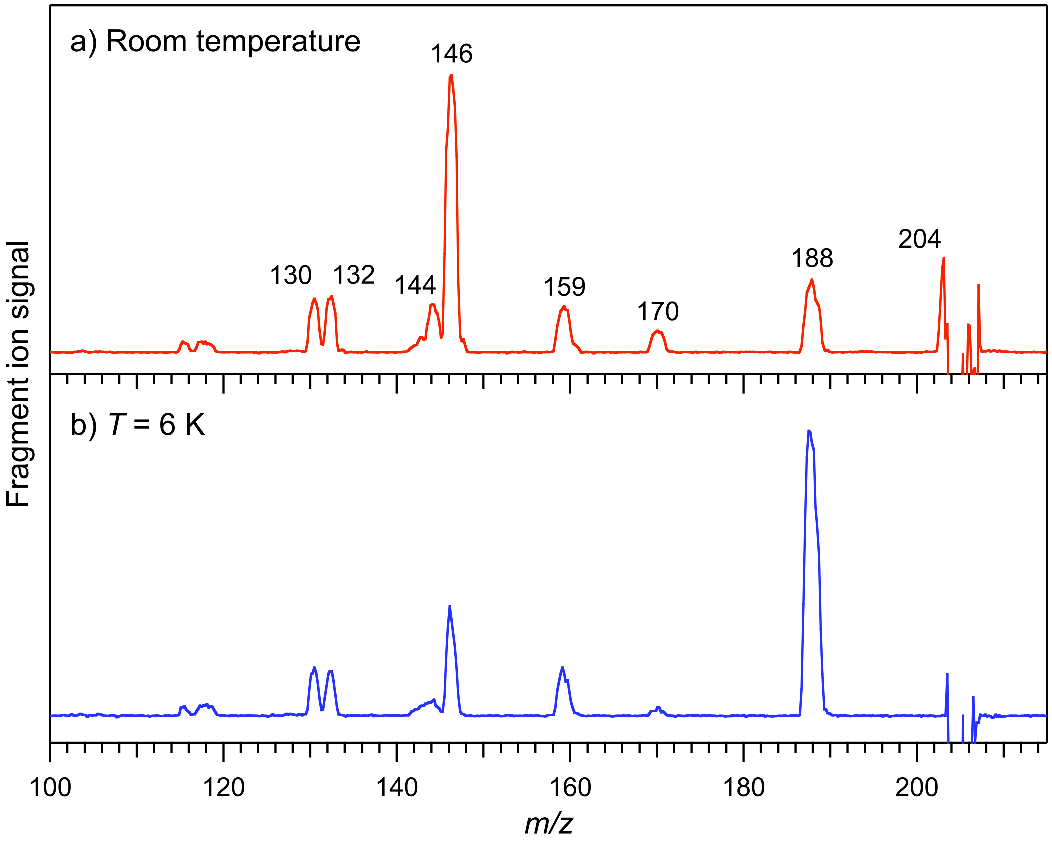

Figure 4.1: Photofragment mass spectra of protonated tryptophan (TrpH$^+$) irradiated by UV laser light at 35 078 cm^{-1}, recorded (a) at room temperature and (b) with the trap at 6 K. No fragments were observed at *m/z* values below 100.

The room-temperature spectrum is very similar to the one measured by Talbot et al. at the same UV wavelength (285 nm) [24], with *m/z* 146 being the main fragment. Their article contains possible structures for all of the observed photofragments (labeled in the above spectrum). They also present a spectrum measured with the UV at 265 nm, in which the relative intensities of the fragments are slightly different, e.g., for *m/z* 130, 132 and 188 that are comparatively higher. Kang et al. published photodissociation mass spectra of TrpH$^+$ almost identical to the latter, using a UV laser at 266 nm [25-27]. In all these papers, both groups highlight the presence of a fragment at *m/z* 204, corresponding to the loss of a hydrogen atom by the parent ion. Although the resolution of our mass spectrum is not as high as theirs, this peak clearly appears in Figure 4.1(a) as well. However, its relative intensity cannot be reliably determined, due to the close proximity of the much more intense parent ion peak.

The spectrum recorded at a trap temperature of 6 K, displayed in Figure 4.1(b), shows some significant differences with the previous one. Here, the main fragment is *m/z* 188 whose intensity dramatically increased relative to all other fragments. On the contrary, the peaks at *m/z* 144, 146 and 170 decreased in comparison with *m/z* 130, 132 and 159. Finally, there is no detectable peak of the *m/z* 204 fragment(1). Since all experimental conditions other than the temperature were practically identical for the measurements of these two spectra, the observed changes of fragmentation pattern must be the consequence of a lower internal energy of the parent ions. They can be rationalized in light of the mechanistic studies conducted by Talbot et al. with photodissociation [24] and by the group of Siu using CID [19]. There are three first-generation fragments of $TrpH^+$: *m/z* 188 (loss of NH_3), which was shown by CID to have the lowest energy threshold; *m/z* 159 (concomitant loss of H_2O and CO); and *m/z* 204 (H atom loss), which has only been observed in photodissociation experiments. The others are produced by further fragmentations of these three: *m/z* 188 fragments into *m/z* 170 ($-H_2O$), 146 ($-CH_2CO$, i.e., ketene) and 144 ($-CO_2$); *m/z* 159 fragments into *m/z* 132 (– HCN) and 130 ($-(HCN + H_2)$); and *m/z* 204 fragments exclusively into *m/z* 130 (loss of a glycine radical). Thus, in our room-temperature spectrum, most of the dissociating parent ions undergo NH_3 loss, but the majority of the resulting *m/z* 188 ions further fragment, predominantly through the *m/z* 146 channel. On the other hand, at very low temperature, the initial internal energy of the parent ions is much lower, so that after photon absorption and primary fragmentation to *m/z* 188, most of these first-generation ions no longer have enough vibrational excitation for additional dissociation. Consequently, *m/z* 188 becomes the main peak of the spectrum and all its daughter ions (*m/z* 144, 146 and 170) show a decrease in relative intensity. Surprisingly, the analogous phenomenon is not observed for *m/z* 159 and its daughter ions (*m/z* 130 and 132), whose relative intensities are similar in both spectra. Concerning the H atom loss channel (*m/z* 204), it seems that it gets totally suppressed at low temperature, although the limited resolution of our spectrum does not allow us to draw a definitive conclusion about it.

---

(1) The positive signal seen in the 6 K spectrum near *m/z* 204 consists of only a single point and appears at a higher mass than the *m/z* 204 peak of the room-temperature spectrum; hence it probably stems from the noise caused by parent signal variations.

4.1.2 Electronic spectra at room temperature and 6 K

Based on the photofragment mass spectra recorded at ambient and low temperature, we chose the fragments to be detected while scanning the frequency of the UV laser in order to measure the electronic spectrum of $TrpH^+$ parent ions. At room temperature, the most intense fragment, *m/z* 146, was selected. At 6 K, on the other hand, we measured the UV spectrum on both *m/z* 188 and *m/z* 146. These three traces, which are each the average of several scans, are presented in Figure 4.2.

The room-temperature spectrum (Figure 4.2(a)) consists of two very broad bands that are only partially resolved. The first one, which is assigned to the S_0-S_1 transition, peaks at 35 010 cm^{-1}, in the same spectral region as the band origin of neutral Trp [1]. The second one is about twice higher in signal intensity and levels off around 35 900 cm^{-1}. It is not surprising, for a molecule of this size (28 atoms), to measure a broad electronic spectrum at room temperature, because some of its low-frequency vibrational excited states are populated. The spectral congestion can thus be explained, at least to a certain extent, by thermal inhomogeneous broadening. Moreover, several different conformers of $TrpH^+$ may be present and contribute to the width of the spectrum.

The two spectra acquired at a trap temperature of 6 K (Figure 4.2(b) and (c)) are visibly narrower, but still extremely broad for molecules expected to be cooled to their ground vibrational state: the first band has, for both fragments, a full width at half maximum (FWHM) of ~ 350 cm^{-1}. The spectrum for *m/z* 146 is very similar to the one published by Weinkauf and coworkers [22], even in terms of broadness, despite the fact that their ion trap, cooled by liquid nitrogen, was at least at 77 K and possibly up to 140 K. However, there is a small shift in the position of the lowest-energy band: in their case, the maximum is at 35 150 cm^{-1} (284.5 nm), while ours peaks at 35 125 cm^{-1}. To the blue of this first band, two more intense unresolved bands can now be distinguished, with their maxima at ~ 35 900 cm^{-1} and ~ 36 500 cm^{-1}. The former being about 800 cm^{-1} above the origin, it could be due to the characteristic vibrations of the indole ring already observed in the electronic spectrum of cold neutral tryptophan [3]. The third band might be the transition to a second electronic excited state, S_2, which is predicted by Weinkauf's calculations to lie ~ 36 600 cm^{-1} above the ground state [22]. At even higher frequency (not shown), the *m/z* 146 fragment signal gets gradually more intense, with no apparent structure, at least up to 37 700 cm^{-1}. Talbot et al. observed a decrease of fragment intensity above 38 500 cm^{-1} [24], but we did not scan that far to the blue.

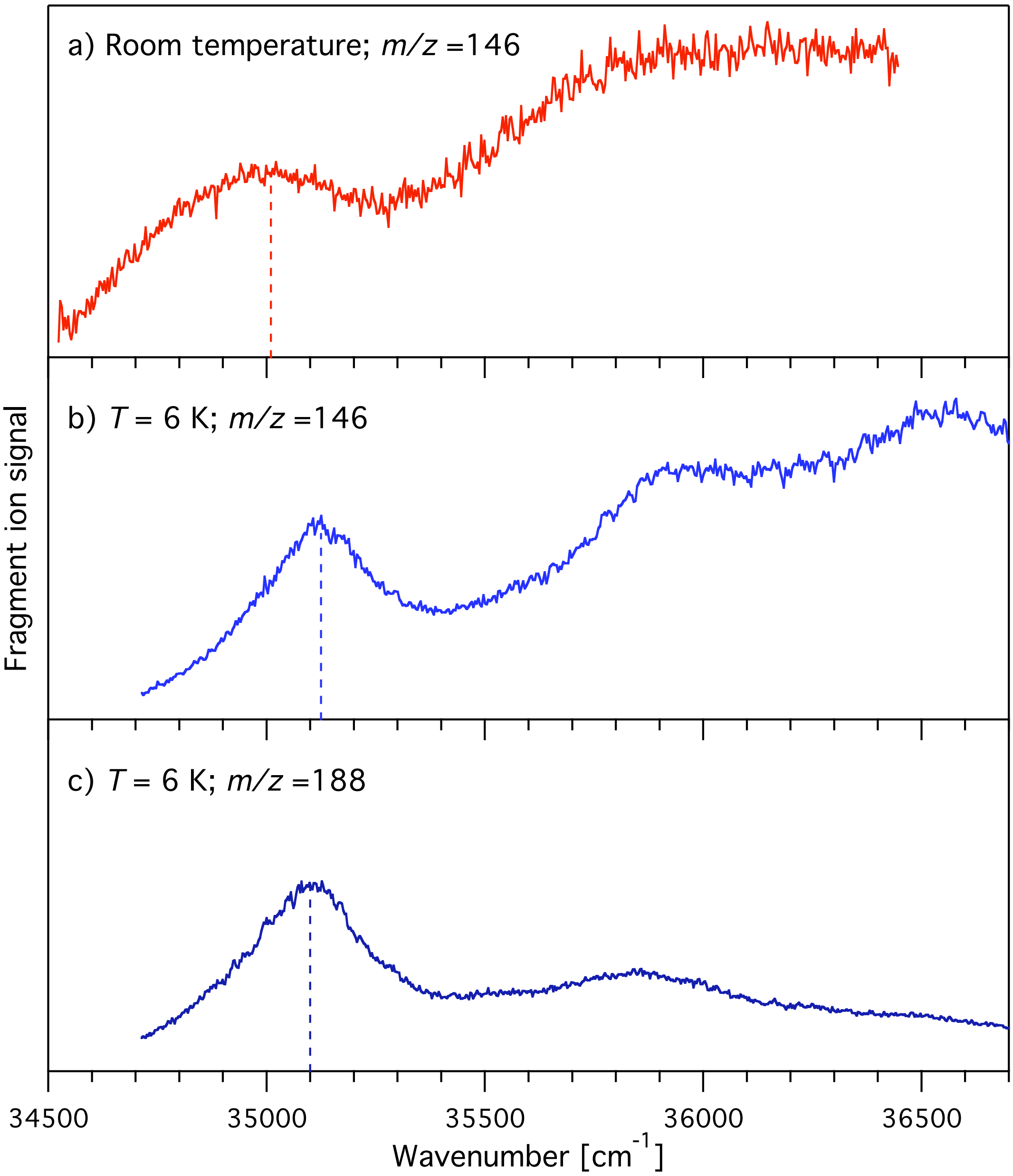

Figure 4.2: Photodissociation electronic spectrum of TrpH$^+$ obtained by monitoring fragments (a) *m/z* 146 at room temperature, (b) *m/z* 146 at 6 K and (c) *m/z* 188 at 6 K. The maximum of the S_0-S_1 transition is indicated by a dashed line in each case.

The spectrum recorded for *m/z* 188 is similar to the one for *m/z* 146 in the origin region, except for a slight red shift of the maximum, being here at 35 100 cm^{-1}. To the blue of the first band, the ion signal decreases, in contrast to what is observed for *m/z* 146, with a much less intense second band peaking at 35 850 cm^{-1}. As for the third band, it is barely discernible in this spectrum. The reason for these differences is that, as the energy of the absorbed photon increases, the *m/z* 188 ions produced by primary fragmentation of $TrpH^+$ have more residual internal energy, and thus a higher probability to undergo secondary fragmentation to yield *m/z* 146 ions. This is analog to the effect of temperature observed for the photofragment mass spectra in the preceding subsection. As a matter of fact, the vibrational energy contained in a $TrpH^+$ ion at 300 K is about 2300 cm^{-1} higher than at 10 K, so one can expect an equivalent increase of the photon energy to have a similar effect on the relative intensities of these two fragments. This progressive reduction of ion yield for *m/z* 188 as the UV wavenumber increases explains why the two first bands appear redshifted when monitoring this fragment. It is probably also for the same reason that our spectra are slightly redshifted with respect to the one of Weinkauf and coworkers, considering that they detected all fragments at the same time and therefore did not have this problem caused by secondary fragmentations.

4.2 Electronic spectrum of protonated tyrosine

The sample preparation and the acquisition of photofragment mass spectra and electronic spectra for protonated tyrosine were conducted in the same manner as for protonated tryptophan (see the previous section, *4.1 Electronic spectrum of protonated tryptophan*). These results are presented below.

4.2.1 Photofragment mass spectra at room temperature and 6 K

The photodissociation mass spectra of $TyrH^+$ (*m/z* 182), measured at room and low temperature, have already been presented in the preceding chapter to illustrate the feasibility of IR-UV double resonance spectroscopy (see *3.4.2 Adaptation to the spectroscopy of cold trapped ions*). Nevertheless, they are reproduced here in Figure 4.3 and will be analyzed in more detail. The ion packets accumulated inside the 22-pole trap could also contain up to ~ 10 000 parent ions. The UV frequency used to photodissociate them was 35 082 cm^{-1}, which corresponds to a specific transition in the electronic spectrum of cold $TyrH^+$, as will be shown in the next subsection. As mentioned before for $TrpH^+$, the noise observed in both these difference spectra at the parent ion mass, *m/z* 182, is caused by fluctuations of the nano-electrospray signal.

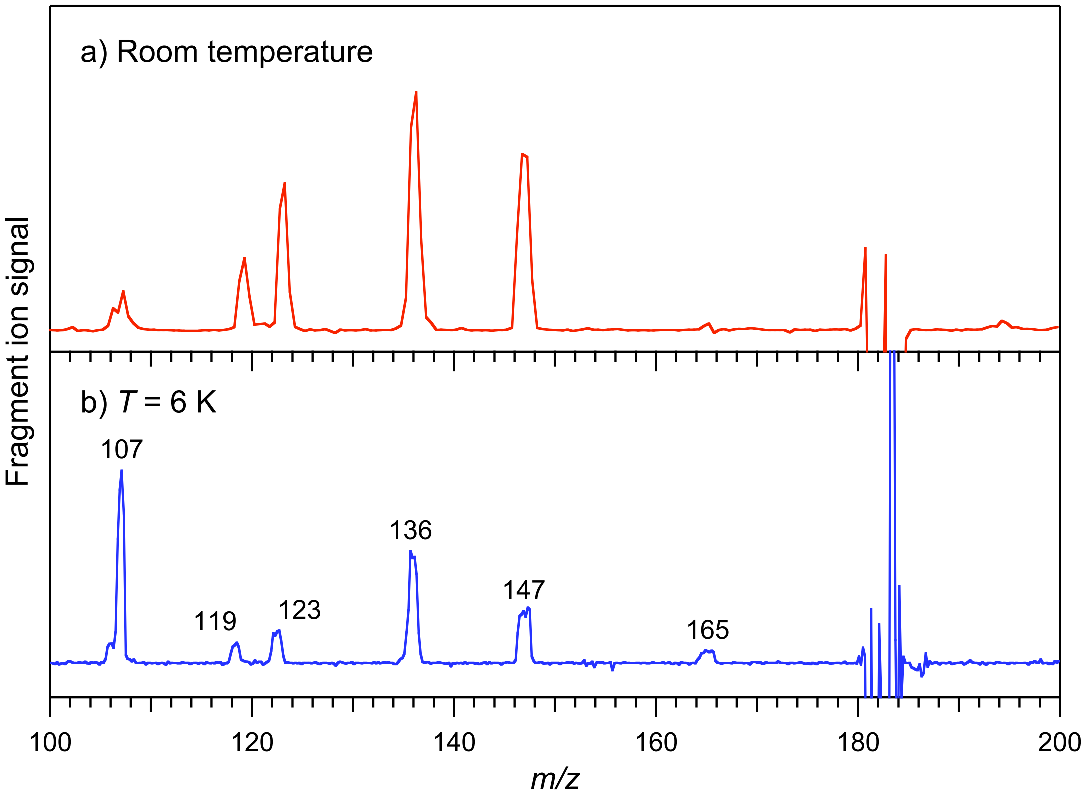

Figure 4.3: Photofragment mass spectra of protonated tyrosine ($TyrH^+$) irradiated by UV laser light at 35 082 cm^{-1}, recorded (a) at room temperature and (b) with the trap at 6 K. No fragments were observed at *m/z* values below 100.

As done before for $TrpH^+$, the interpretation of these two spectra will be based on the CID mechanistic studies of Siu and coworkers [19], and comparison will be made with the photodissociation mass spectrum of $TyrH^+$ published by Kang et al., who used a 266 nm laser (37 590 cm^{-1}) [27]. In the room-temperature spectrum (Figure 4.3(a)), the major fragment is *m/z* 136 and corresponds to the concomitant loss of H_2O and CO. The loss of NH_3, which gave the peak at *m/z* 188 in the case of $TrpH^+$, produces a fragment at *m/z* 165 for $TyrH^+$. However, this fragment is almost completely absent at room temperature. Instead, its daughter ions resulting from the subsequent loss of H_2O and CH_2CO are the two next important peaks at *m/z* 147 and 123, respectively. The *m/z* 119 fragment (loss of NH_3, H_2O

and CO) follows from secondary fragmentation of either *m/z* 165 or *m/z* 136. Finally, there is a minor fragment at *m/z* 107 that could result, according to the CID experiments of Siu, from the loss of $HCNH_2$ or HCN + H_2 by *m/z* 136, and, alternatively, from the direct loss of neutral glycine by the $TyrH^+$ parent ion. Kang et al., on the other hand, suggest from their photodissociation experiments that *m/z* 107 is the fingerprint of the H atom loss reaction after the subsequent loss of a glycine radical, analogously to what was observed for $TrpH^+$. Although, they did not detect at all the product of this H atom loss, at *m/z* 181, and neither did we. More will be said on this in the analysis of the low-temperature spectrum. Also to be noticed is the total absence of fragments below *m/z* 100, even though some can be relatively abundant in CID studies (e.g., *m/z* 91) [19].

When the trap is cooled to 6 K (Figure 4.3(b)), *m/z* 165 gains some intensity relative to its daughter ions, indicating that secondary fragmentation has been partially inhibited by the diminution in thermal internal energy of the parent ions. But the most significant difference with the room-temperature spectrum is the dramatic increase in intensity of the *m/z* 107 peak, which is now the largest. It is quite surprising that a lower mass fragment gets more abundant than all heavier fragments as the temperature is decreased, especially since absolutely no lighter ions, into which *m/z* 107 could potentially dissociate, have been observed at room temperature. A first conclusion to be drawn from this result is that the dissociation mechanism leading to *m/z* 107 is different from the one taking place in CID experiments. Indeed, in the aforementioned studies of Siu and coworkers, *m/z* 107 appears at a collisional energy threshold that is higher than for all the other fragments present in our mass spectrum. Therefore, in the case of photodissociation, it is not primarily produced by secondary fragmentation of *m/z* 136. The fact that *m/z* 107 predominates at low temperature suggests that the corresponding dissociation reaction is entropically favored over the other channels. The loss of neutral glycine, as proposed in Siu's article [19], involves the migration of a proton from the ammonium group to the α-carbon, thus it might not be particularly favorable in that regard. On the other hand, the H atom loss reaction is simply the direct cleavage of a bond between the molecular ion and a light atom, which requires no rearrangement and hence should have a high frequency factor. As pointed out by Kang et al. in their paper, the resulting Tyr radical cation (*m/z* 181) would then further dissociate and yield the detected *m/z* 107 fragment. This interpretation is in accordance with the observation by Schlag and coworkers that *m/z* 107 is the major fragment generated after multiphoton ionization (MPI) of jet-cooled neutral tyrosine [31]. The absence of signal at *m/z* 181 in the mass spectra indicates that the energy barrier for this secondary fragmentation would probably be rather low.

4.2.2 Electronic spectra at room temperature and 6 K

Similarly to what was done for $TrpH^+$, we measured the room-temperature electronic spectrum of $TyrH^+$ by monitoring the intensity of the most abundant fragment (*m/z* 136), whereas at low temperature, the spectrum was acquired for both *m/z* 107 and *m/z* 136. The results are presented in Figure 4.4.

The room-temperature spectrum of $TyrH^+$ (Figure 4.4(a)) was measured over a 3000 cm^{-1} range and shows distinctly two broad bands. The first one is attributed to the origin of the S_0-S_1 transition and peaks at 35 380 cm^{-1}, which is roughly in the same region as for neutral tyrosine [11]. The maximum of the second band is at 36 135 cm^{-1}, i.e., ~ 750 cm^{-1} to the blue of the origin. By comparison with the spectrum of neutral Tyr measured by de Vries and coworkers [11], it could correspond to the breathing mode vibration of the benzene ring, which generates a strong absorption 800 cm^{-1} above the origin in the neutral molecule. Finally, a small bump can be vaguely discerned near 36 700 cm^{-1} and could be due to the (quasi-)symmetric and antisymmetric stretching modes of the benzene ring substituents, which appear between 1200 cm^{-1} and 1300 cm^{-1} in neutral Tyr. However, this possible third band is difficult to clearly identify, due to the spectral congestion, as well as the decrease in ion signal towards the blue side of the spectrum. The latter is certainly caused, as in the case of $TrpH^+$, by enhanced secondary fragmentation at higher photon energy.

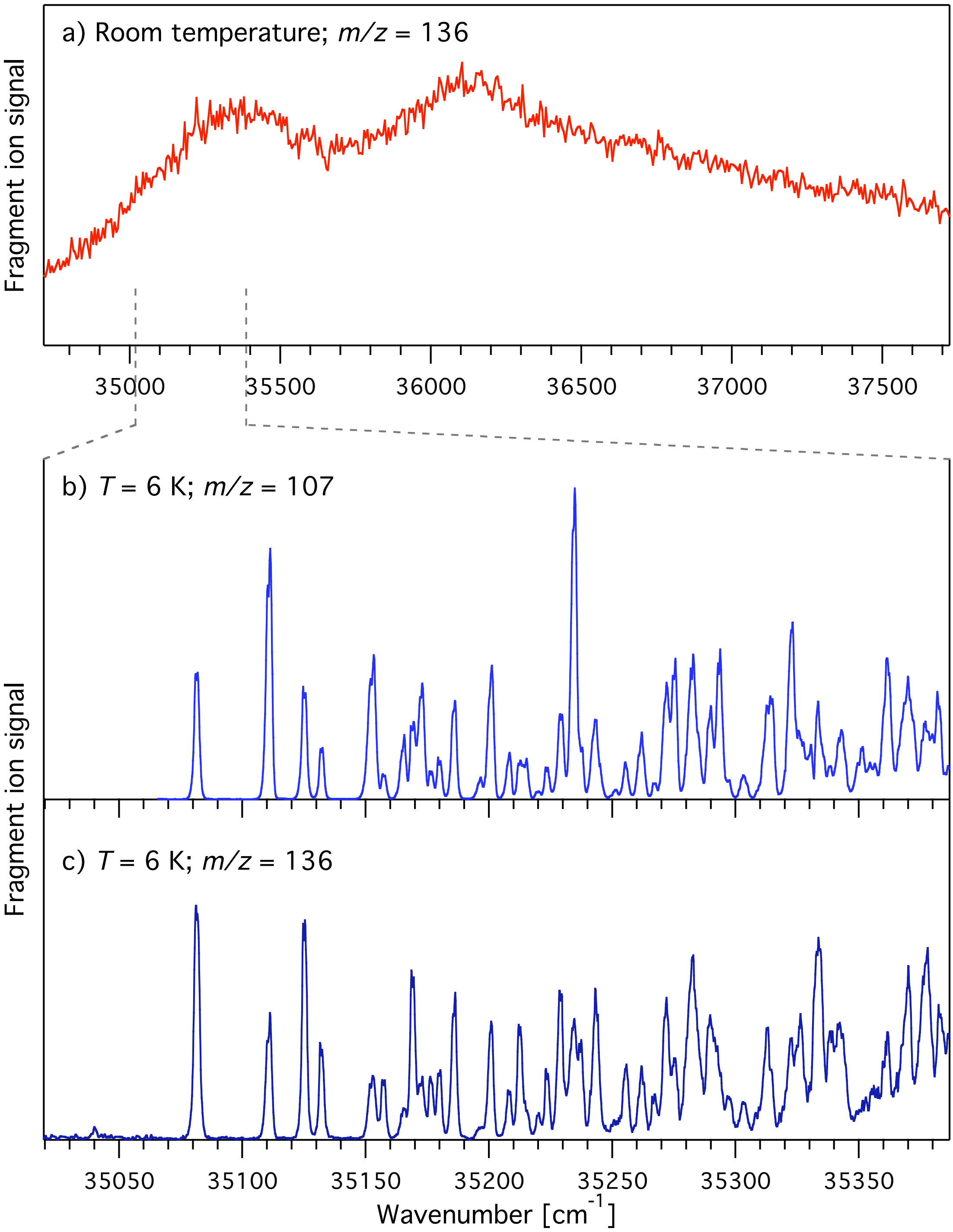

Figure 4.4: Photodissociation electronic spectrum of TyrH$^+$ obtained by monitoring fragments (a) *m/z* 136 at room temperature, (b) *m/z* 107 at 6 K and (c) *m/z* 136 at 6 K. Note that the wavenumber range of the two lower spectra is much narrower than for the upper one.

At 6 K, the spectrum was acquired separately for fragments *m/z* 107 and *m/z* 136 (Figure 4.4(b) and (c), respectively) and over a much shorter range of 350 cm^{-1}. In contrast with the low-temperature UV spectra of $TrpH^+$, these two show well-resolved transitions having a FWHM of only ~ 2.5 cm^{-1}, which is probably mainly determined by their rotational band contour. By comparing the spectra obtained for the two fragments, one notices that, even though the positions of the peaks are identical, their relative intensities differ. This is a first indication that at least two conformers of $TyrH^+$ with distinct fragmentation patterns are present in the cold ion trap. Only a brief description of this electronic spectrum is given here, while a more detailed analysis, based in part on these differences, will be done in *Chapter 6*. The lowest-energy peak at 35 082 cm^{-1}, which was chosen to produce the photodissociation mass spectra presented in the previous subsection, can be attributed to the S_0-S_1 origin transition of one conformer. Its position is ~ 400 cm^{-1} lower in energy than the lowest-energy origin measured for neutral Tyr. The small feature 42 cm^{-1} to the red of it, at 35 040 cm^{-1}, is a hot band stemming from an excited low-frequency vibrational state of S_0 for that same conformer⁽¹⁾. The corresponding 1⟵0 vibronic transition is situated at 35 125 cm^{-1}, i.e., 43 cm^{-1} above its band origin. The second lowest-energy peak, at 35 111 cm^{-1}, happens to be the origin of another conformer, as confirmed by (i) the difference in relative intensity with the first band origin between the two spectra, and (ii) the absence of a corresponding hot band to the red of the first origin. Further evidence of this assignment will be presented in *Chapter 6*. To the blue of these first few features, there are numerous sharp transitions that belong to low-frequency vibrational progressions built on these two band origins, and maybe on additional origins of different conformers.

4.3 Discussion

The goal of the present discussion is not to carry out a thorough analysis of the individual electronic spectra of $TrpH^+$ and $TyrH^+$. First, because the broadness of the $TrpH^+$ spectrum prevents us from doing so, and most of what can be said about the observed transition frequencies has been mentioned in the presentation of the results. As for the $TyrH^+$ spectrum, the detailed examination of its well-resolved vibronic transitions and the deduction

---

(1) This hot band is not visible in Figure 4.4(b), because the corresponding range has not been scanned for fragment *m/z* 107.

of information that can be extracted from them will be facilitated by the additional data from conformer-specific experiments, all of which will be presented in *Chapter 6*. Instead, we will focus here on the striking differences between the low-temperature electronic spectra measured for these two ions and try to explain them.

4.3.1 Sharpness and broadness of the spectra

First of all, we can point out that the sharpness of the $TyrH^+$ UV spectrum measured at 6 K nicely demonstrates that thermalization is efficient and eliminates most of the spectral congestion caused by thermal broadening. The faintness of the hot band at 35 040 cm^{-1} shows that the lowest-frequency vibrational mode has hardly any population in its first excited state. More quantitatively and despite the poor signal-to-noise ratio in this region, an estimate of the vibrational temperature from the intensity of this hot band yields an upper limit of 20 K. Similar calculations done on the less noisy UV spectrum of $TrpH^+{\cdot}W_2$ led up to a temperature estimate of ~ 11 K (see *2.2.3.2 Low intensities of vibrational hot bands*). The observed vibronic transitions are well-resolved, having a FWHM of ~ 2.4 cm^{-1}. Comparison of a high-resolution scan of the first band origin with numerical simulations of the rotational band contour, based on rotational constants from *ab initio* calculations and on a natural linewidth of 7.2 GHz (corresponding to a 22 ps lifetime; see below and reference [27]), indicates that the rotational temperature of the ions is ~ 15 K. All this shows that ion cooling is effective and that considerable spectral simplification can thus be achieved.

In view of this fact, one might wonder why the $TrpH^+$ UV spectrum is still so broad at a *nominal* temperature of 6 K. Since it has been measured in identical conditions to the $TyrH^+$ spectrum, it is reasonable to assume that the internal temperature of the $TrpH^+$ ions is similar and that the vast majority of them lie in their ground vibrational state. Another possible source of inhomogeneous broadening would be the presence of many different conformations in the probed ion packet. However, this is quite unlikely, because the cooling process taking place inside the trap ensures that the ions are frozen to their most stable geometries. In fact, considering the number density of the He buffer gas (~ 10^{15} cm^{-3}) and the collision cross section of $TrpH^+$ (~ 100 $Å^2$ [32]), the average time between collisions is of a few microseconds. Furthermore, based on studies of cooling rates of neutral aromatics and biomolecules in supersonic expansions [33, 34], the number of collisions needed to cool a

$\mathrm{TrpH^+}$ ion from 300 K to 15 K should be on the order of 10^3, thus setting the total thermalization time in the millisecond range. On the other hand, isomerization between the various conformers takes place on a much shorter timescale, presumably in the nanosecond to microsecond range [34]. Therefore, it is expected that thermal equilibrium between the conformers is more or less maintained all along the cooling process, insofar as the barriers to interconversion are not too high, and that the relative populations of conformers in the fully thermalized ion packet are close to a Boltzmann distribution at the temperature of the trap. Hence, only the lowest-energy conformations can contribute to the measured spectrum, and their number should be rather small according to *ab initio* calculations. This fact is exemplified by the electronic spectrum of $\mathrm{TyrH^+}$, which shows the presence of at least two conformers, but probably not many more.

4.3.2 Excited-state lifetime and what determines it

Given the above considerations, the most plausible explanation for the broadness of the low-temperature $\mathrm{TrpH^+}$ spectrum is that each vibronic transition is itself broadened by the limited lifetime of the excited state. This idea is confirmed by the experiments conducted by Jouvet and coworkers, who measured the lifetimes of electronically excited $\mathrm{TrpH^+}$ and $\mathrm{TyrH^+}$ ions at room temperature after absorption of a UV photon. Briefly, their method consists in a femtosecond pump-probe photodissociation scheme, in which a first 266 nm photon promotes the ions to an excited electronic state, while a second delayed 800 nm photon monitors the time evolution of that state by modifying the branching ratios of the subsequent dissociations [35]. Their data revealed an excited-state lifetime of 22 ps for $\mathrm{TyrH^+}$ [27], whereas the decay observed for $\mathrm{TrpH^+}$ showed two time constants of ~ 400 fs and 15 ps [26]. Although, their experimental conditions were different from ours (i.e., uncooled parent ions and higher-energy UV photons), these results are consistent, to some extent, with the electronic spectra that we obtained. The 22 ps lifetime of the $\mathrm{TyrH^+}$ excited state implies, from the energy-time uncertainty principle(1), a natural linewidth of ~ 0.25 cm^{-1}. As mentioned at the beginning of this discussion, the combination of this value with a rotational contour at 15 K yields a vibronic bandwidth of ~ 2.5 cm^{-1}, as observed in Figure 4.4(b) and (c). The much shorter lifetime measured for $\mathrm{TrpH^+}$ is in qualitative agreement with the broadness of our electronic spectrum. However, the 13 cm^{-1} linewidth corresponding to a 400 fs lifetime is clearly insufficient to account for the structureless, 350 cm^{-1} wide S_0-S_1 band that we measured. Even if a few conformers should contribute to the spectrum, we estimate that the lifetime of the $TrpH^+$ S_1 state in the conditions of our experiment is probably shorter than 100 fs. A possible reason for this discrepancy could be that the initial decay of S_1 is too fast to be probed by their femtosecond technique, whose temporal resolution is on the order of 250 fs. The 400 fs lifetime that they detected would thus correspond to a secondary decay process.

---

(1) $\Delta E \cdot \tau \geq \hbar$, where ΔE is the FWHM of the transition energy and τ is the lifetime of the excited state.

In the various articles that they published on this subject, Jouvet and coworkers proposed different possible interpretations to explain the observed excited-state lifetimes of $TrpH^+$ and $TyrH^+$. Their first explanation, supported by *ab initio* calculations, is based on the presence of a charge-transfer (CT) state of $\pi\sigma^*$ character in the vicinity of the initially excited $\pi\pi^*$ state [25, 27, 35]. This $\pi\sigma^*$ state is mainly localized on the NH_3^+ group and is dissociative along the (free) N-H coordinate. The coupling between these two states induces an electron transfer from the aromatic ring to the ammonium group, thus creating an unstable hypervalent C-NH_3 radical, which leads to the fast detachment of an H atom. As the N-H distance increases, the $\pi\sigma^*$ state crosses the ground-state potential energy surface (PES), giving rise to a competition between H atom loss and internal conversion to S_0. This is illustrated by the energy level diagram in Figure 4.5. In that context, the very different excited-state lifetimes of $TrpH^+$ and $TyrH^+$ would be related to the height of the barrier formed by the crossing of the $\pi\pi^*$ and $\pi\sigma^*$ states. Using a few assumptions, they justified that conclusion by evaluating the position of the $\pi\sigma^*$ state for both amino acids (AA): the H atom dissociation energy (D_e) is estimated using the proton affinity (PA) and ionization potential (IP) of the neutral amino acids, and the ionization potential of the hydrogen atom (IP_H), according to $D_e = PA + IP - IP_H$ [27]. The principal result of these calculations is that D_e, which correlates with the position of the $\pi\sigma^*$ state, is mainly determined by the IP of the neutral amino acid. The IP of Tyr being significantly higher than that of Trp, they obtain a D_e value that is 0.6 eV larger for $TyrH^+$, whereas its S_1 energy is almost identical.

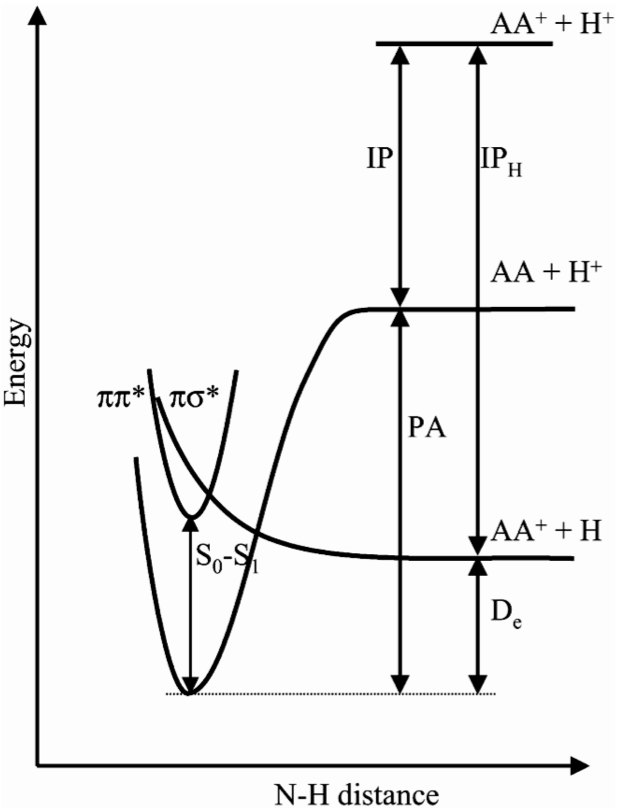

Figure 4.5: Schematic energy diagram showing the potential energy curves of the states involved in the H atom loss reaction for protonated aromatic amino acids (AAH^+). See text for details. (Taken from Kang et al. [27].)

As regards the two lifetimes measured for $TrpH^+$, additional *ab initio* calculations showed that the relative energies of the electronic excited states were strongly dependent on the conformation of the molecule, in particular the position of the NH_3^+ group with respect to the indole ring and the orientation of the carboxylic acid group around the C_α-COOH bond [28]. Their primary interpretation was thus to invoke the presence of two $TrpH^+$ conformers with different ππ*-πσ* energy gaps. However, in a recent paper [29], they present the results of new *ab initio* calculations on $TrpH^+$ and $TyrH^+$, including geometry optimizations of the excited states. For several conformers of both ions, they observe a proton transfer reaction from the NH_3^+ group to the aromatic ring, which occurs through only a small ($TyrH^+$) or no barrier ($TrpH^+$), but at the cost of significant geometrical rearrangement. On the other hand, the H atom loss reaction presents a high energetic barrier for $TyrH^+$ (~ 0.8 eV) and a smaller one for $TrpH^+$ (~ 0.2 eV). In light of this, they explain the nonobservation of

Tyr^+ photofragments by this too large barrier, and attribute the 22 ps lifetime of excited $TyrH^+$ ions to the dynamics of proton transfer to the phenol ring, which is substantially slowed by the geometrical constraints. Similarly, the 15 ps component of the $TrpH^+$ decay is assigned to the barrierless proton-transfer reaction and the 400 fs component to the entropically favored H atom loss.

Which of these scenarios, if any, can be considered compatible with our own results, keeping in mind the dissimilar experimental conditions? In the case of $TyrH^+$, as we have seen, the 22 ps lifetime is totally consistent with the measured bandwidths in our low-temperature spectrum. Nevertheless, the mechanism of proton transfer to the phenol ring, as proposed by Jouvet and coworkers, is hard to reconcile with our mass spectrometric data, as well as theirs [27]. Indeed, the proton-transfer reaction is predicted to lead to internal conversion followed by a back proton transfer to the NH_2 group, so that the subsequent fragmentations would be essentially statistical. Now, as mentioned previously, the CID experiments of Siu and coworkers showed that the *m/z* 107 fragment has a much higher energy threshold than the other fragments [19], whereas it constitutes 25% of the fragmentation yield in Jouvet's mass spectrum and is by far the most abundant signal in our 6 K mass spectrum (Figure 4.3(b)). This implies that the mechanism leading from the S_1 state of $TyrH^+$ to *m/z* 107 must be, at least in its early stages, nonstatistical. What is more, it should be entropically favored over the other dissociation channels, because *m/z* 107 predominates only at low temperature. Some possibilities have already been presented along with the mass spectra. One is the direct production of *m/z* 107 from $TyrH^+$, *via* the loss of neutral glycine (or an isomer). This pathway is inconspicuously suggested in Siu's article, but also, by analogy, in a very recent paper by Jouvet on the photodissociation pathways of $TrpH^+$ [30]. As a matter of fact, one could imagine that the proton-transfer process could preferentially trigger this specific fragmentation channel, instead of unavoidably ending up with internal conversion and a back proton transfer. Another option is simply the first mechanism proposed by Jouvet: namely, the H atom loss on a dissociative $\pi\sigma^*$ state followed by secondary fragmentation of Tyr^+ to give *m/z* 107, which is the major channel observed in MPI dissociation of neutral Tyr [31]. The intriguing point of this alternative is the absence (or nondetection) of Tyr^+ ions at *m/z* 181. This would imply that, even at low temperature, the nascent Tyr^+ radical cations still contain enough energy to undergo C_α-C_β bond cleavage with almost unit efficiency on our detection timescale. The corresponding barrier height should thus be either nonexistent or very small.

Concerning TrpH^+, we have already seen that our electronic spectrum justifies an ultrafast excited-state decay. The remaining point to be discussed is the origin of the longer lifetime component. Let's first consider the latest proposition made by Jouvet and coworkers, assigning the 15 ps lifetime to the proton-transfer dynamics and the 400 fs one to the H atom loss reaction. It seems, to our understanding, that they describe these two processes as competing deactivation pathways of the *same* initially excited $\pi\pi^*$ state. In such a case, however, the fastest one (here by a factor 40) would prevail over the slow one and the corresponding decay curve would show a single component of roughly 400 fs. The double exponential measured for TrpH^+ must imply that two *distinct* states are decaying simultaneously: (i) either in parallel, as from two separate conformers; (ii) or, possibly, in consecutive steps, e.g., a fast deactivation from $\pi\pi^*$ to an intermediate state, followed by a slower decay to the ground state [36]. The latter scheme would be consistent with the spectral broadening that we observe, since the natural linewidth is determined by the lifetime of the initially excited state. Although, the nature of this intermediate state would still have to be established. On the other hand, the hypothesis of two conformers cannot apply to our spectrum. Indeed, if two such conformers were probed in our ion packets, we would measure the superposition of a broad, low-intensity absorption from the short-lived conformer, and sharp, intense vibronic transitions from the 15 ps conformer. Nevertheless, one could suppose that this long-lived conformer is sufficiently less stable than the other that it is negligibly populated at the low temperature of our experiment.

In conclusion, our results do not support the proton-transfer mechanism recently proposed by Jouvet and coworkers. Instead, they show much better agreement with the idea that the lifetime of the excited state in TrpH^+ and TyrH^+ is essentially controlled by the coupling and the energetic gap between the $\pi\pi^*$ state and the nearby dissociative $\pi\sigma^*$ state localized on the ammonium group. The next question that we wanted to address is the following: How can the excited-state lifetime of TrpH^+ be so short in the gas phase (presumably < 100 fs), whereas it lives long enough to fluoresce in aqueous solution (~ 0.7 ns [37])? To that purpose, we measured the electronic spectra of cold TrpH^+ complexed with water molecules. These results are presented in the next chapter.

References

[1] T. R. Rizzo, Y. D. Park, L. Peteanu and D. H. Levy, *Journal of Chemical Physics* **1985**, *83*, 4819-4820.

[2] T. R. Rizzo, Y. D. Park and D. H. Levy, *Journal of Chemical Physics* **1986**, *85*, 6945-6951.

[3] T. R. Rizzo, Y. D. Park, L. A. Peteanu and D. H. Levy, *Journal of Chemical Physics* **1986**, *84*, 2534-2541.

[4] L. Li and D. M. Lubman, *Applied Spectroscopy* **1988**, *42*, 418-424.

[5] S. J. Martinez, J. C. Alfano and D. H. Levy, *Journal of Molecular Spectroscopy* **1992**, *156*, 421-430.

[6] L. C. Snoek, R. T. Kroemer, M. R. Hockridge and J. P. Simons, *Physical Chemistry Chemical Physics* **2001**, *3*, 1819-1826.

[7] L. C. Snoek, R. T. Kroemer and J. P. Simons, *Physical Chemistry Chemical Physics* **2002**, *4*, 2130-2139.

[8] P. Çarçabal, R. T. Kroemer, L. C. Snoek, J. P. Simons, J. M. Bakker, I. Compagnon, G. Meijer and G. von Helden, *Physical Chemistry Chemical Physics* **2004**, *6*, 4546-4552.

[9] I. Compagnon, F. C. Hagemeister, R. Antoine, D. Rayane, M. Broyer, P. Dugourd, R. R. Hudgins and M. F. Jarrold, *Journal of the American Chemical Society* **2001**, *123*, 8440-8441.

[10] R. Cohen, B. Brauer, E. Nir, L. Grace and M. S. de Vries, *Journal of Physical Chemistry A* **2000**, *104*, 6351-6355.

[11] L. I. Grace, R. Cohen, T. M. Dunn, D. M. Lubman and M. S. de Vries, *Journal of Molecular Spectroscopy* **2002**, *215*, 204-219.

[12] Y. Inokuchi, Y. Kobayashi, T. Ito and T. Ebata, *Journal of Physical Chemistry A* **2007**, *111*, 3209-3215.

[13] G. W. A. Milne, T. Axenrod and H. M. Fales, *Journal of the American Chemical Society* **1970**, *92*, 5170-&.

[14] C. D. Parker and D. M. Hercules, *Analytical Chemistry* **1985**, *57*, 698-704.

[15] S. Bouchonnet, J. P. Denhez, Y. Hoppilliard and C. Mauriac, *Analytical Chemistry* **1992**, *64*, 743-754.

[16] N. N. Dookeran and A. G. Harrison, *Journal of Mass Spectrometry* **1995**, *30*, 666-674.

[17] N. N. Dookeran, T. Yalcin and A. G. Harrison, *Journal of Mass Spectrometry* **1996**, *31*, 500-508.

[18] F. Rogalewicz, Y. Hoppilliard and G. Ohanessian, *International Journal of Mass Spectrometry* **2000**, *196*, 565-590.

[19] H. El Aribi, G. Orlova, A. C. Hopkinson and K. W. M. Siu, *Journal of Physical Chemistry A* **2004**, *108*, 3844-3853.

[20] H. Lioe, R. A. J. O'Hair and G. E. Reid, *Journal of the American Society for Mass Spectrometry* **2004**, *15*, 65-76.

[21] H. Lioe and R. A. J. O'Hair, *Organic & Biomolecular Chemistry* **2005**, *3*, 3618-3628.

[22] D. Nolting, C. Marian and R. Weinkauf, *Physical Chemistry Chemical Physics* **2004**, *6*, 2633-2640.

[23] Z. B. Maksić and B. Kovačević, *Chemical Physics Letters* **1999**, *307*, 497-504.

[24] F. O. Talbot, T. Tabarin, R. Antoine, M. Broyer and P. Dugourd, *Journal of Chemical Physics* **2005**, *122*, 074310/1-5.

[25] H. Kang, C. Dedonder-Lardeux, C. Jouvet, S. Martrenchard, G. Grégoire, C. Desfrançois, J. P. Schermann, M. Barat and J. A. Fayeton, *Physical Chemistry Chemical Physics* **2004**, *6*, 2628-2632.

[26] H. Kang, C. Dedonder-Lardeux, C. Jouvet, G. Grégoire, C. Desfrançois, J. P. Schermann, M. Barat and J. A. Fayeton, *Journal of Physical Chemistry A* **2005**, *109*, 2417-2420.

[27] H. Kang, C. Jouvet, C. Dedonder-Lardeux, S. Martrenchard, G. Grégoire, C. Desfrançois, J. P. Schermann, M. Barat and J. A. Fayeton, *Physical Chemistry Chemical Physics* **2005**, *7*, 394-398.

[28] G. Grégoire, C. Jouvet, C. Dedonder and A. L. Sobolewski, *Chemical Physics* **2006**, *324*, 398-404.

[29] G. Grégoire, C. Jouvet, C. Dedonder and A. L. Sobolewski, *Journal of the American Chemical Society* **2007**, *129*, 6223-6231.

[30] V. Lepère, B. Lucas, M. Barat, J. A. Fayeton, V. J. Picard, C. Jouvet, P. Çarçabal, I. Nielsen, C. Dedonder-Lardeux, G. Grégoire and A. Fujii, *Journal of Chemical Physics* **2007**, *127*, 134313/1-11.

[31] J. Grotemeyer, K. Walter, U. Boesl and E. W. Schlag, *International Journal of Mass Spectrometry and Ion Processes* **1987**, *78*, 69-83.

[32] S. J. Valentine, A. E. Counterman and D. E. Clemmer, *Journal of the American Society for Mass Spectrometry* **1999**, *10*, 1188-1211.

[33] J. R. Barker, *Journal of Physical Chemistry* **1984**, *88*, 11-18.

[34] T. S. Zwier, *Journal of Physical Chemistry A* **2006**, *110*, 4133-4150.

[35] H. Kang, C. Jouvet, C. Dedonder-Lardeux, S. Martrenchard, C. Charrière, G. Grégoire, C. Desfrançois, J. P. Schermann, M. Barat and J. A. Fayeton, *Journal of Chemical Physics* **2005**, *122*, 084307/1-7.

[36] D. Nolting, T. Schultz, I. V. Hertel and R. Weinkauf, *Physical Chemistry Chemical Physics* **2006**, *8*, 5247-5254.

[37] R. J. Robbins, G. R. Fleming, G. S. Beddard, G. W. Robinson, P. J. Thistlethwaite and G. J. Woolfe, *Journal of the American Chemical Society* **1980**, *102*, 6271-6279.

Chapter 5 UV spectroscopy of hydrated TrpH$^+$

In the preceding chapter, it has been demonstrated that the first electronically excited state S_1 of isolated protonated tryptophan, or at least of its major conformer, has an ultrashort lifetime, be it of ~ 400 fs, as measured by Jouvet and coworkers [1, 2], or of less than 100 fs, as deduced from the broadness of our electronic spectrum. This value is several orders of magnitude lower than for neutral isolated Trp, whose fluorescence lifetime has been measured by Levy and coworkers for different conformers and always ranges from 10 to 13 ns [3], in accordance with its sharp electronic spectrum [4]. Hence, protonation of the amino group in Trp opens a new, ultrafast relaxation pathway, the nature of which has just been discussed.

An analogous behavior is observed in aqueous solution, where the excited-state lifetime of Trp is seen to decrease when going from high to low pH. Many pH-dependent studies of tryptophan fluorescence lifetime have been published along the past decades [5-8], and the values slightly vary depending on the source, owing in part to different experimental conditions (e.g., temperature, excitation and emission wavelengths). Nevertheless, the same trend shows up in all cases. In basic solutions (pH ~ 11), both the amino and carboxyl groups are deprotonated (anionic form) and the mean fluorescence lifetime is of 8 to 9 ns. At pH 7, the amino group is protonated (zwitterionic form) and the mean lifetime is reduced to ~ 3 ns. In order to protonate the carboxylate and obtain the cationic form of tryptophan, corresponding to the TrpH$^+$ species that we studied in the gas phase, the solution must be made very acidic, due to its low pK_a value of 2.3 [9]. At pH 1, Robbins et al. measured a mean lifetime of about 0.7 ns [6]. Even though this last value is about ten times shorter than for the anionic form, it is still over three orders of magnitude longer than what we observed for isolated TrpH$^+$.

Clearly, the interactions between TrpH$^+$ and the water molecules must participate in the stabilization of the S_1 excited state in the bulk solution in comparison with the gas phase. With the intention of understanding, at the microscopic level, the detailed mechanism giving rise to this lifetime lengthening, we have decided to study one by one the hydrated complexes of TrpH$^+$ containing an increasing number of water molecules. Such an approach has been widely used in the research field of gas-phase biomolecules. As regards neutrals, Simons [10] and Zwier [11], among others, have examined various biologically related species in supersonic expansions and observed how their conformational preferences are influenced by microsolvation. In particular, Simons and coworkers, following the first observations carried out by Peteanu et al. [12], measured the electronic and vibrational spectra of hydrated complexes of neutral Trp and, by comparison with DFT and *ab initio* calculations, proposed possible geometries for up to the triply hydrated complex [13, 14]. In the case of ions, a profusion of such studies have been published, thanks to the ability of electrospray ionization to produce partially solvated species and to the possibility of precisely selecting the one of interest by mass spectrometry. The types of investigated molecules range from relatively small ions, such as single amino acids [15-18], to medium-sized oligopeptides [19-22], and up to entire proteins of several kilodaltons [23, 24]. In our laboratory, we have measured, by infrared photofragmentation spectroscopy, the vibrational spectra of hydrated complexes of protonated and lithiated valine and of protonated tryptophan in the hydride stretch region [25, 26]. These results revealed a common solvation mechanism, mainly driven by the charged site in each species. Moreover, they lead to a reinterpretation of conclusions from previously published BIRD experiments [15, 17] and provided spectroscopic evidence that hydration by up to four water molecules is *not* enough to stabilize the zwitterionic form of lithiated valine. Despite this last example, most of the aforementioned studies show that solvation by only a few molecules is often sufficient to induce some solution-like behavior in gas-phase molecules. Therefore, exploring the electronic spectroscopy of hydrated complexes of TrpH$^+$ is likely to help us understand the enormous difference of its excited-state lifetime between the gaseous and aqueous phases.

The rest of this chapter will begin with the presentation of the electronic spectra measured for the singly and doubly hydrated complexes of $TrpH^+$, and demonstration will thus be made that the addition of only two water molecules suffices to significantly lengthen the lifetime of the S_1 excited state. Then, in the discussion section, explanations will be put forward to rationalize these observations and supported by theoretical calculations of the excited states and simulations of their dynamics.

5.1 Electronic spectra of hydrated $TrpH^+$ complexes

For the most part, the experiments on hydrated complexes are carried out in the same manner as for the bare ions, in particular, the preparation of the sample solution is identical (see *4.1 Electronic spectrum of protonated tryptophan*). The main differences lie in the transmission of the complex ions from the atmospheric part of the nanoelectrospray source until the 22-pole ion trap. First, the source must be tuned so as to obtain an adequate degree of desolvation and maximize the signal for the desired complex size. This is done by optimizing both the spray and the voltages in the vacuum part of the source. Second, the hexapole is generally not used for pretrapping, because this induces fragmentation of the weakly bound complexes and was found to provide a lower parent ion signal in the end. Finally, the introduction of the parent ions in the 22-pole trap must be made as gentle as possible, in order to avoid their dissociation, which could potentially generate parasitic signal stemming from smaller ions in the spectra acquired for the parent ions. In the following, the photofragment mass spectra of the singly and doubly hydrated complexes of $TrpH^+$, measured at room temperature and at 6 K, will first be presented. Next, the low-temperature electronic spectra of these same species will be shown and compared, along with the one previously obtained for the bare ion.

5.1.1 Photofragment mass spectra at room temperature and 6 K

We start by pointing out that the notation of the hydrated complexes will be slightly simplified by using the letter W instead of H_2O to symbolize water molecules, so that a protonated tryptophan ion with *n* water molecules will be represented by $TrpH^+ \cdot W_n$. For both $TrpH^+ \cdot W_1$ (*m/z* 223) and $TrpH^+ \cdot W_2$ (*m/z* 241), the number of parent ions that could be accumulated in the 22-pole trap was generally between 2000 and 3000 in each packet. A small fraction of these ions fragmented collisionally inside the trap and lost a single water molecule, thus producing a peak 18 u below the parent ion mass in the laser-off mass spectra. Nevertheless, the intensity of this peak is sufficiently weak that it has a negligible influence on the distribution of photofragments measured for the parent ions.

The difference (laser-on minus laser-off) photofragment mass spectra recorded for $TrpH^+ \cdot W_1$ at room temperature and with the trap cooled to 6 K are presented in Figure 5.1. In both cases, the UV laser was fixed at a frequency of 35 176 cm^{-1}. As mentioned in the previous chapter, the difference signal at the mass of the parent ion, here *m/z* 223, appears as a depletion, but can be quite noisy due to shot-to-shot fluctuations of the very intense parent signal. This noise can also be seen, especially at low temperature, at the mass of the bare ion, *m/z* 205, which is produced exclusively by collisions with the helium atoms and not at all by the laser irradiation, so that the difference signal is practically zero(1). Interestingly, this implies that, even at low temperature, *all* the fragmenting $TrpH^+ \cdot W_1$ complexes undergo not only the loss of their water molecule, but also the cleavage of a covalent bond. An alternative explanation could be that, when water loss alone occurs, the kinetic energy of the departing $TrpH^+$ ion is such that it cannot be confined within the trap effective potential. However, this seems unlikely: considering the energy of the photon and that of the water-ion interaction, as well as their relative masses, a simple calculation yields an upper limit of only ~ 0.3 eV for the kinetic energy of the $TrpH^+$ fragment, i.e., well below the effective potential of several electronvolts. At *m/z* values below 100 (not shown), only a few peaks of very low intensity have been detected.

---

(1) In principle, the bare ion signal could also show a depletion, since $TrpH^+$ absorbs light and can thus fragment at the used UV frequency. However, the intensity of the $TrpH^+$ signal is so weak that the depletion is on the order of or smaller than the noise level.

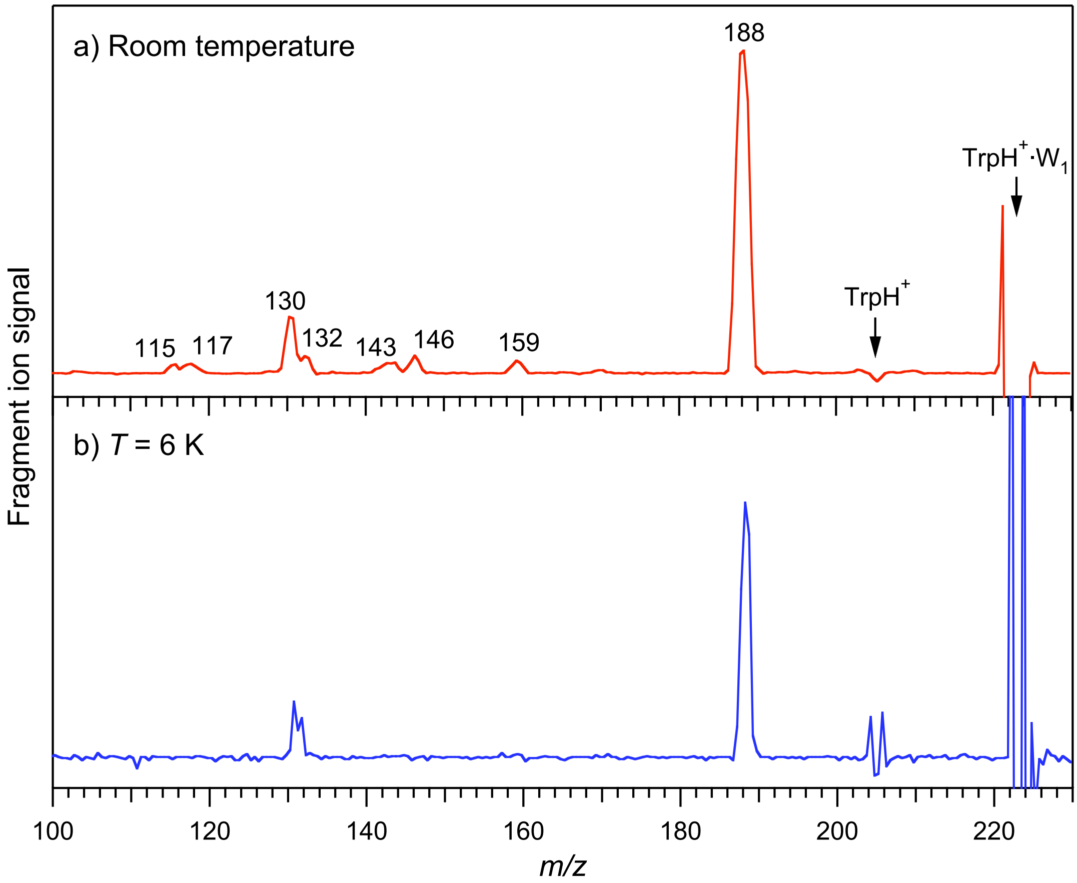

Figure 5.1: Photofragment mass spectra of singly hydrated protonated tryptophan ($TrpH^+·W_1$) irradiated by UV laser light at 35 176 cm^{-1}, recorded (a) at room temperature and (b) with the trap at 6 K. Only a few very weak fragment peaks were observed at *m/z* values below 100.

In the room-temperature mass spectrum (Figure 5.1(a)), the main fragment is *m/z* 188, corresponding to the loss of the solvent and of an NH_3 molecule. All the other fragments have also been observed in the photofragment mass spectrum of bare $TrpH^+$ (see Figure 4.1), but the relative intensities of several of them are much lower than in the latter case. This can be easily explained if one assumes that the water molecule evaporates from the $TrpH^+$ ion prior to the cleavage of covalent bonds. Part of the photon energy (~ 4.4 eV) is consumed in this first dissociation (on the order of 0.5 eV [22]), and some is probably also taken away by the water molecule as translational and internal energy. Consequently, the remaining energy in the $TrpH^+$ «fragment» is smaller than during its direct photodissociation. Therefore, the daughter ions of the *m/z* 188 fragment (*m/z* 170, 146 and 144) are barely produced by lack of sufficient internal energy. Likewise, the dissociation channel yielding *m/z* 159 (and its daughter ion *m/z* 132) was shown by CID to have a higher energy threshold [27] and hence the intensities of these peaks decrease as well. On the other hand, the relative intensities of fragments *m/z* 115, 117, 130 and 143, although rather small, are strikingly similar to those measured in the photodissociation of bare $TrpH^+$. What is more, they all appear only at very high collision energies in CID. This may suggest that, in photodissociation, they are products of primary fragmentation pathways, or at least that their formation is not subsequent to IVR or to the loss of H_2O, so that the presence of the solvent molecule has little influence on their appearance. Finally, we note that the *m/z* 204 fragment, which was observed in the room-temperature mass spectrum of $TrpH^+$ (H atom loss), has not been detected in the photodissociation of $TrpH^+{\cdot}W_1$.

At low temperature (Figure 5.1(b)), only two (maybe three) photofragments are detected. The major one is still *m/z* 188, as in the room-temperature spectrum. The second peak looks truncated and is difficult to identify without doubt, probably because of instabilities in the parent signal. It could correspond to *m/z* 130, possibly with some contribution from *m/z* 132. All other fragments labeled in Figure 5.1(a) are now absent from the spectrum, a consequence of the much lower thermal internal energy of the parent ions, similarly to what was observed for the bare protonated amino acids, although to a greater extent. Thus, the formation of three of the fragments that seemed to be independent of solvation at room temperature (*m/z* 115, 117 and 143) is nonetheless sensitive to the initial internal energy of the complex.

The photofragment mass spectra of the doubly hydrated complex, $TrpH^+{\cdot}W_2$, acquired at room and low temperature are shown in Figure 5.2(a) and (b), respectively. Here again, the UV laser was fixed at 35 176 cm^{-1} for both measurements. As was noted in the case of the monohydrated complex, the fragments corresponding to the loss of a single water molecule (i.e., $TrpH^+{\cdot}W_1$ at *m/z* 223) are only produced through collisions with the buffer gas. The resulting difference signal at this mass is then practically zero and shows even a small laser-induced depletion in the room-temperature spectrum. The mass range below *m/z* 100 is not shown here either, because no fragments at all have been detected.

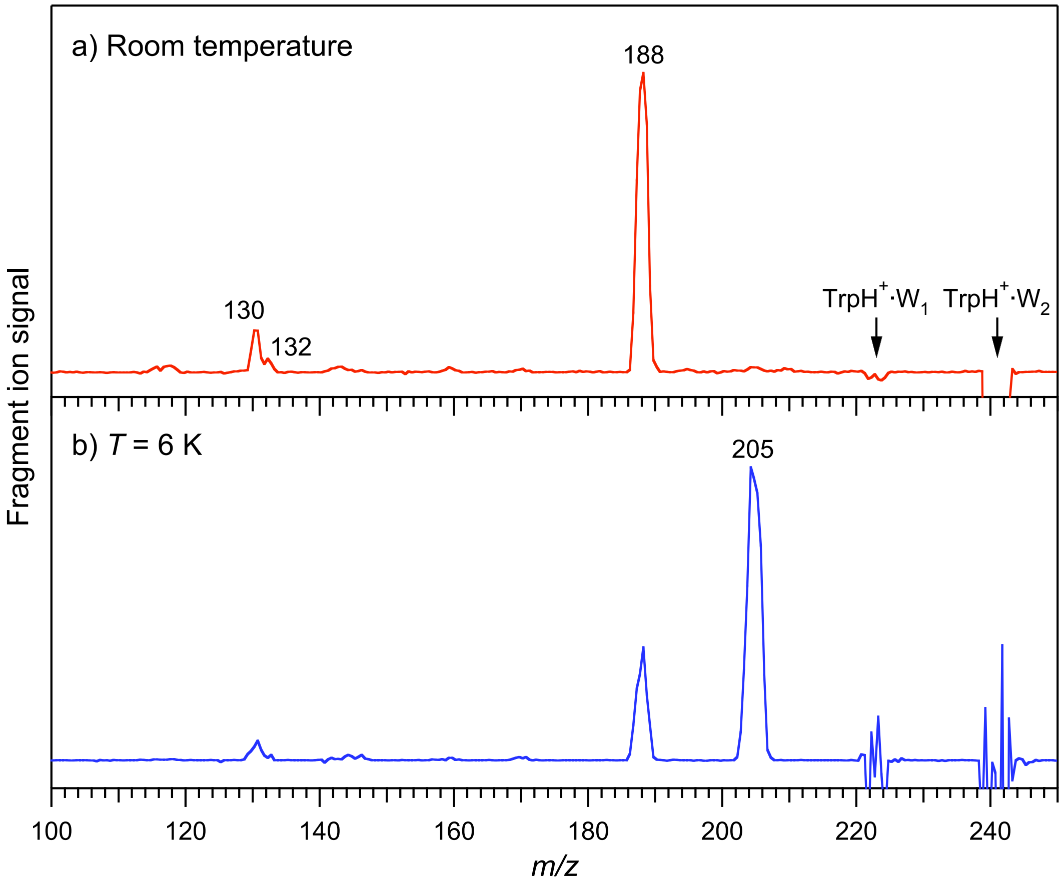

Figure 5.2: Photofragment mass spectra of doubly hydrated protonated tryptophan ($TrpH^+ \cdot W_2$) irradiated by UV laser light at 35 176 cm^{-1}, recorded (a) at room temperature and (b) with the trap at 6 K. No fragments were detected at *m/z* values below 100.

The room-temperature spectrum looks very similar to the one recorded for $TrpH^+ \cdot W_1$, with *m/z* 188 as the major fragment, except that the relative intensities of most of the minor fragments are even weaker in this case. This attests to the higher energy needed to evaporate two water molecules instead of one, which further inhibits secondary fragmentation and discriminates against more energetic dissociation channels. Besides, the detection of a very small amount (< 2% of the base peak) of laser-induced $TrpH^+$ at *m/z* 205 is now possible, facilitated by its complete absence in the laser-off spectrum.

When the trap is cooled to 6 K (Figure 5.2(b)), the intensities of the lower-mass peaks that were already small at room temperature get even weaker, as could be expected. But the most noticeable difference is that the largest fragment peak now corresponds to the bare $TrpH^+$ ion, whereas it was hardly observable at ambient temperature. It means that the removal of the thermal energy from the parent ion complexes, equivalent to only a few thousands of wavenumbers compared to the photon energy of ~ 35 000 cm^{-1}, is sufficient to suppress covalent bond dissociation in most cases.

5.1.2 Electronic spectra at low temperature

The electronic spectra of the singly and doubly hydrated complexes of protonated tryptophan in the cold 22-pole ion trap have been recorded by monitoring the intensity of their respective most intense fragments, as determined from the low-temperature mass spectra just presented, while scanning the frequency of the UV laser. For TrpH$^+\cdot$W$_1$, the probed fragment was *m/z* 188, while for TrpH$^+\cdot$W$_2$, the bare ion (*m/z* 205) was detected. The resulting spectra are shown in Figure 5.3(b) and (c), respectively. For comparison, the low-temperature electronic spectrum of the bare TrpH$^+$ ion, already presented in *Chapter 4*, is displayed again in Figure 5.3(a), though on a narrower range than previously.

We will start by the description of the TrpH$^+\cdot$W$_1$ spectrum (Figure 5.3(b)). The first band on the red side of the displayed range can be attributed to the origin region of the S$_0$-S$_1$ transition. It is still very broad, but somewhat narrower than for the bare TrpH$^+$ ion. Additionally, its maximum is slightly blueshifted with respect to the latter, being here at 35 170 cm^{-1}, while it peaked at 35 125 cm^{-1} for the TrpH$^+$ spectrum measured in the *m/z* 146 mass channel (Figure 5.3(a)). To the blue of this first band, the diffuse ion signal rises again, in about the same way as for the bare ion. However, on top of this broad absorption, a multitude of sharp vibronic transitions are now observable. Such characteristics suggest that at least two different conformers of TrpH$^+\cdot$W$_1$, or, say, two types of conformers, are present in the cold ion trap: (i) one whose excited state is extremely short-lived and is then responsible for the lifetime-broadened part of the spectrum; (ii) another one in which the interaction with the water molecule lengthens the S$_1$ lifetime and thus displays sharp, well-resolved vibronic transitions.

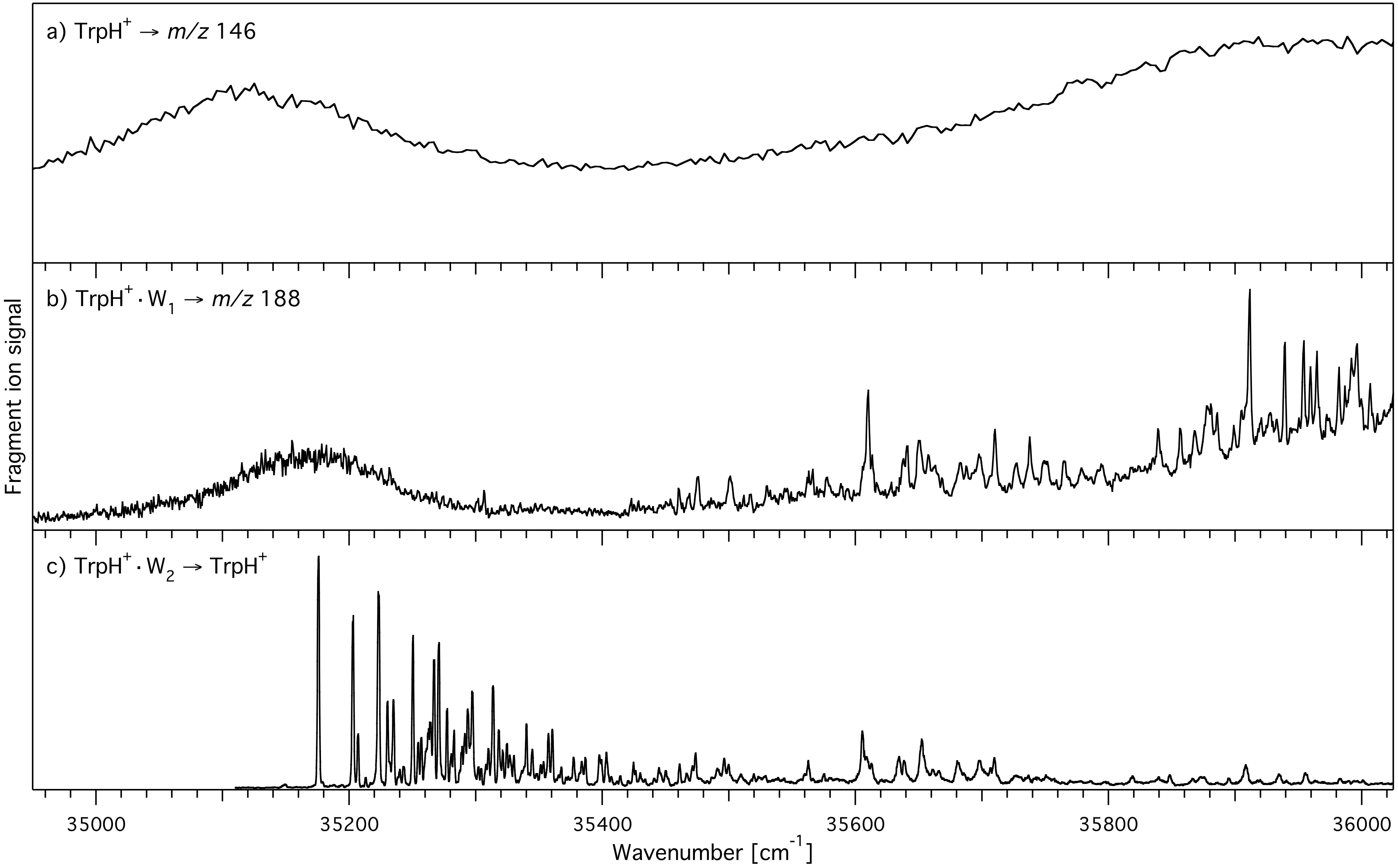

Figure 5.3: Photodissociation electronic spectra of (a) $TrpH^+$ dissociating to *m/z* 146, (b) $TrpH^+ \cdot W_1$ dissociating to *m/z* 188, and (c) $TrpH^+ \cdot W_2$ dissociating to $TrpH^+$ (*m/z* 205). The temperature of the ion trap is 6 K in each case.

Two facts can be stressed to confirm that the broad spectrum is actually stemming from the photodissociation of $\mathrm{TrpH^+{\cdot}W_1}$ complexes, and not from that of collisionally produced $\mathrm{TrpH^+}$ ions. First, there is the blue shift of the origin band mentioned above, which is even larger when compared to the spectrum of $\mathrm{TrpH^+}$ recorded in the same *m/z* 188 mass channel (maximum at 35 100 cm^{-1}; see Figure 4.2(c)). Second, the measured amount of background $\mathrm{TrpH^+}$ ions is smaller than the maximum counted signal of *m/z* 188 fragments. Even though the transition intensities do not necessarily faithfully reflect the species populations in such an action spectrum, the relative integrated intensities of the broad and sharp portions of the spectrum lead us to suppose that the short-lived conformer is predominant.

The electronic spectrum obtained for $\mathrm{TrpH^+{\cdot}W_2}$ is radically different (Figure 5.3(c)). It consists entirely of nicely resolved vibronic transitions whose narrow bandwidth is only limited by their rotational contour, at least in the origin region (FWHM of 1.5 to 2.0 cm^{-1}). The broad absorption seen in previous spectra is here totally absent. This indicates that all significantly populated conformers of $\mathrm{TrpH^+{\cdot}W_2}$ that fragment into *m/z* 205 have an excited-state lifetime that is substantially longer than that of the bare $\mathrm{TrpH^+}$ ion. It will be demonstrated in *Chapter 6* that almost all of the major features in this spectrum apparently belong to a single predominant conformer. Its S_0-S_1 origin transition occurs at 35 176 cm^{-1}, the frequency that was used to acquire all the photodissociation mass spectra presented in this chapter. 27 cm^{-1} to the red of this origin, there is a small hot band that attests to the low vibrational temperature of the probed ions. The electronic transition to the corresponding excited-state vibrational mode is situated symmetrically on the blue side of the origin, at 35 203 cm^{-1}. Similarly, most of the remaining features are due to low-frequency vibrational progressions and combination bands built on that same 0-0 transition. A close-up of the origin region will be shown in *Chapter 6* and analyzed in greater detail with the help of conformer-specific spectral data. Further to the blue, two interesting things can be noticed. First, the intensities of the peaks get progressively weaker at higher photon energy. A plausible explanation is the one given for the same trend observed in the UV spectrum of $\mathrm{TrpH^+}$ dissociating into *m/z* 188, namely, that secondary fragmentation is enhanced as the energy imparted to the parent ions increases. Secondly, it seems that the widths of the individual transitions become broader. Beside spectral congestion due to the overlap of neighboring bands, one can imagine that, as the complexes are excited to higher levels of the

S_1 state, a coupling of the latter with a nearby state increases, so that its lifetime is reduced and gives rise to a gradual broadening of the transitions.

5.2 Discussion

As already mentioned, the analysis of the sharp electronic spectrum of $TrpH^+ \cdot W_2$ will be carried out in the next chapter, aided in that by the results of IR-UV double resonance experiments. Here, the discussion will concentrate on the qualitative spectral modifications observed upon the stepwise hydration of the $TrpH^+$ ion.

5.2.1 Lifetime lengthening upon hydration

For the bare ion, the acquired spectrum is broad and rather structureless, which we attributed to broadening caused by the very short lifetime of the excited S_1 state. By adding water molecules to the ion, a sharpening of the spectrum is noted, to a moderate extent for the singly hydrated complex and quite dramatically for $TrpH^+ \cdot W_2$. This indicates that the excited-state lifetime is made considerably longer by the interactions of the water molecules with $TrpH^+$. Based on the fluorescence lifetime values of aqueous protonated tryptophan found in the literature, we expected this evolution to happen, although probably not already for such a small complex size. In the previous chapter, the behavior of $TrpH^+$ has been rationalized by a model assuming a strong coupling of the $S_1(\pi\pi^*)$ state with a nearby dissociative $\pi\sigma^*$ state. Hence, a plausible explanation for the excited-state lifetime lengthening of $TrpH^+ \cdot W_2$ would be that the presence of the water molecules shifts the relative energies of these two states, so that their interaction is significantly reduced. Similar observations have been reported for various types of (hetero)aromatic molecules. Zewail and coworkers measured an over tenfold increase in the fluorescence lifetime of jet-cooled isoquinoline when complexed with a single methanol or water molecule, additional solvent molecules inducing even longer lifetimes [28, 29]. Moreover, they noted that the effect is stronger with protic solvents than with aprotic ones such as acetone (in spite of its larger dipole moment), thus paralleling the solution behavior. These facts were explained in terms of the important coupling existing in the bare molecule between the initially excited $\pi\pi^*$ state and a closely lying $n\pi^*$ state, which gives rise to fast internal conversion (IC). Upon complexation, especially with a hydrogen-bonding molecule, this nπ* state gets destabilized and the coupling decreases, as well as the IC rate. Analogous results and interpretations have been advanced by Wallace and coworkers for 2-aminopyridine [30] and, more recently, by Mitsui et al. in their study of acridone [31], except that, in both these cases, the state coupling with the *singlet* $^1\pi\pi^*$ is a *triplet* $^3n\pi^*$ state, whose destabilization leads to a lower rate of intersystem crossing (ISC). As a final example, illustrating a third mechanism, Johnson and coworkers suggested that hydration (or dimerization) of gas-phase phenol results in the suppression of internal conversion of the excited state by the lowering of the OH group vibrational frequencies through hydrogen bonding [32]. In light of this, it seems reasonable to imagine a comparable process taking place in the hydration of $TrpH^+$. To get a confirmation of this hypothesis and a detailed understanding of how the electronic states are influenced by solvation, we have performed quantum chemical calculations to determine the most stable conformers of $TrpH^+$ and $TrpH^+{\cdot}W_2$, the energies of their electronic states and their time evolution when excited to the experimentally probed S_1 state. Only a brief description of the applied methods will be presented here, but all the computational details are given in reference [33].

5.2.2 Computation of the lowest-energy structures

The first step in the conformational search for both species consisted in molecular dynamics (MD) simulations at 300 K using the AMBER/parm96 force field [34]. They revealed that the conformational space of $TrpH^+$ can be reduced to the orientation of two dihedral angles: ϕ_1 defined by the atoms C(OOH)-C_α-C_β-C_γ, and ϕ_2 defined by the atoms C_α-C_β-C_γ-$C_{\delta 1}$ (see Figure 5.4). These angles determine the orientation of the amino acid backbone with respect to the indole ring. Based on this observation, the free energy surfaces in the (ϕ_1,ϕ_2) subspace at the temperature of the cold ion trap (~ 10 K) have been computed by metadynamics/MD simulations [35]. The result obtained for $TrpH^+$ is depicted in Figure 5.4, along with the geometrical structures of the three lowest-energy conformers: I, II and III, in ascending order of free energy. The two most stable conformers have the COOH group oriented *anti* with respect to the indole ring ($\phi_1 \cong 180°$) and differ mainly in the positioning of the amino acid backbone on either side of the indole ring ($\phi_2 \cong \pm 90°$). They are separated by a free-energy barrier of ~ 7.5 $kcal{\cdot}mol^{-1}$ and conformer II is less stable by about 0.3 $kcal{\cdot}mol^{-1}$. This may be related to a more favorable interaction between the positively charged ammonium group and the lone electron pair of the indole N atom when the former is situated on the «pyrrole side» of the ring (conformer I) rather than on the «phenyl side» (conformer II). The third conformer (~ 0.7 kcal·mol^{-1}) is separated from conformer I by a barrier of only ~ 2.4 kcal·mol^{-1} and differs from it by having both the carboxylic acid and ammonium groups pointing towards the indole ring ($\phi_1 \cong 300°$). In all three conformers, stabilization is provided through the hydrogen-bonding interactions of two of the ammonium H atoms: with the π-electron cloud of indole for one and with an oxygen atom of the carboxylic acid group for the other.

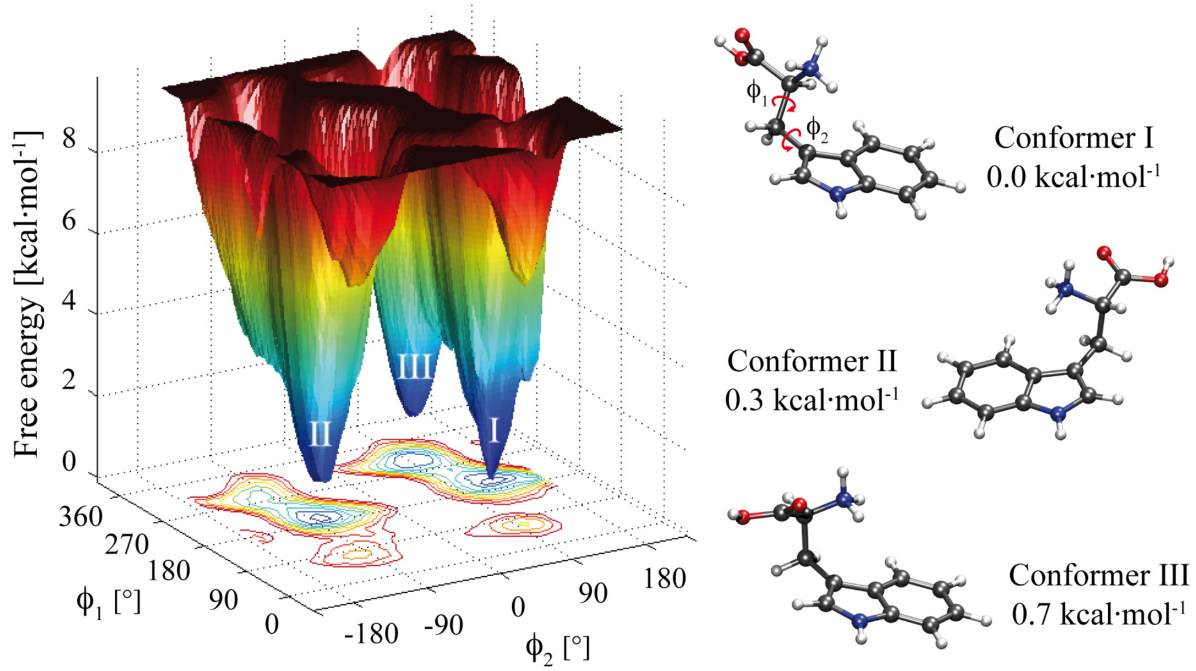

Figure 5.4: Metadynamics free energy landscape in the (ϕ_1,ϕ_2) subspace calculated for $TrpH^+$ at 10 K. The structures and relative energies of the conformers corresponding to minima I, II and III are given on the right of the figure.

The metadynamics/MD simulations performed on the doubly hydrated cluster showed that the (ϕ_1,ϕ_2) free energy landscape of $TrpH^+{\cdot}W_2$ has the same topology as for the bare ion, and that the two water molecules always remain directly attached to the charged ammonium group through hydrogen bonds. For each (ϕ_1,ϕ_2) minimum, three possible configurations are observed, with the water molecules bound to two of the three NH_3^+ hydrogen atoms. In general, the most stable has one water attached to the N-H bond pointing upwards and the other to the N-H bond lying above the indole ring, so that the water molecule itself can act as an H-bond donor to the π-electron cloud. Three examples of stable structures, reoptimized at the DFT level with the Perdew-Burke-Ernzerhof (PBE [36]) functional and the 6-311+G* basis set, are depicted in Figure 5.5 with their relative zero-point corrected energies. The global minimum corresponds to structure (a) and has a similar geometry to the lowest-energy conformer found for TrpH$^+$.⁽¹⁾

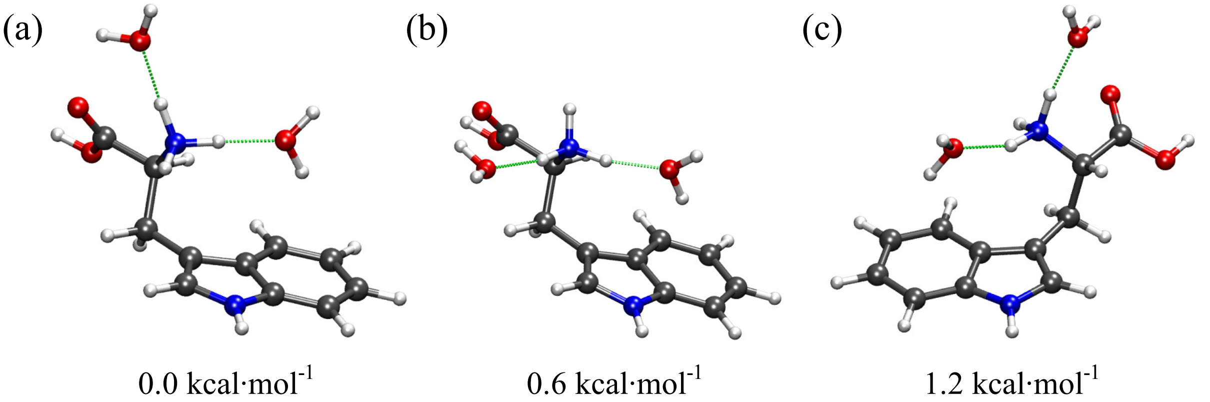

Figure 5.5: Three stable geometries of TrpH$^+$·W$_2$ obtained by metadynamics/MD simulations and reoptimized at the DFT/PBE/6-311+G* level. (a) Structure of the global minimum, which has a similar geometry to the TrpH$^+$ lowest-energy conformer (minimum I). (b) Structure analogous to (a), but with a different water configuration. (c) Structure corresponding to minimum II of the bare ion.

However, more recent geometry optimizations of TrpH$^+$·W$_2$ using other calculation methods arrived at a different conclusion than the metadynamics simulations. They consisted in a preliminary conformational search with the OPLS_2005 force field [37], followed by further optimization at the DFT level, using the Becke-3-Lee-Yang-Parr (B3LYP [38, 39]) hybrid functional and the 6-31++G** basis set⁽²⁾. According to these new results, the lowest-energy structure has only one water molecule bound to the NH_3^+ group, while the other is hydrogen-bonded to the COOH group. In contrast, the geometry corresponding to the global minimum in metadynamics/MD is predicted to be less stable by 2.2 kcal·mol^{-1} at the DFT/B3LYP level. These two structures are shown in Figure 5.6. Consequently, the actual structure of the lowest-energy conformer of TrpH$^+$·W$_2$ is still uncertain, and higher-level

---

(1) All the calculations presented thus far, as well as all the excited-state calculations described further below, were performed by Matteo Guglielmi, Dr. Michele Cascella and Dr. Ivano Tavernelli from the Laboratoire de Chimie et Biochimie Computationnelles of Prof. Ursula Röthlisberger at the EPFL.

(2) These DFT/B3LYP calculations were performed in our laboratory by Dr. Jaime A. Stearns.

calculations using coupled-cluster methods are currently under way in order to determine more accurately the relative energies of the different local minima. More will be said in *Chapter 6* about the possible geometries of the experimentally observed conformers, by comparing measured and calculated vibrational spectra.

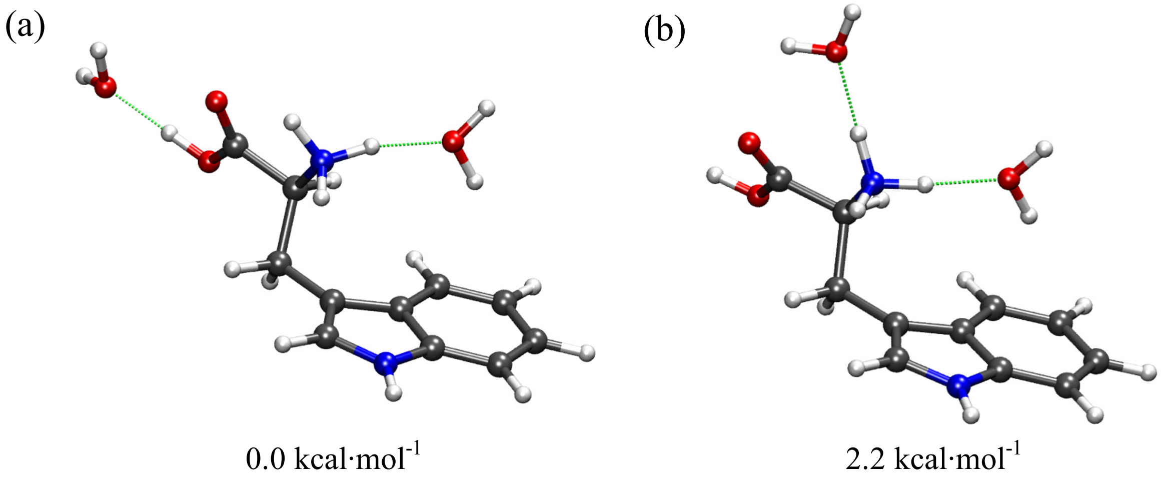

Figure 5.6: Two stable geometries of $TrpH^+ \cdot W_2$ found at the DFT/B3LYP/6-31++G** level. (a) Structure of the global minimum; note that the ammonium group is solvated by a single water molecule. (b) Stable structure whose geometry is the closest to the global minimum found by metadynamics/MD simulations.

5.2.3 Excited-state energy and dynamics calculations

Most of the excited-state calculations have been performed on the global minima of $TrpH^+$ and $TrpH^+ \cdot W_2$ found by metadynamics, i.e., on the structures depicted in Figure 5.4 (conformer I) and Figure 5.5(a), respectively. Only a few results have been obtained yet for the DFT/B3LYP global minimum of $TrpH^+ \cdot W_2$, and will be presented further below. For the metadynamics lowest-energy conformer of each species, the vertical excitation energies to the first few singlet electronic states have been calculated by two different methods: (i) time-dependent density functional theory (TDDFT), using either B3LYP or PBE; (ii) the second-order approximate coupled cluster model within the resolution-of-the-identity approximation (RI-CC2 [40, 41]). The largest basis set used for both methods was aug-cc-pVDZ on all atoms [42]. Moreover, nonadiabatic excited-state MD calculations have been carried out for $TrpH^+$ and $TrpH^+ \cdot W_2$ excited in their first photoaccessible states, in order to simulate their respective time evolution. The ground states were calculated with DFT/B3LYP, whereas for the running excited states, TDDFT was used with PBE. A consequence of this use of different functionals is a lowering of all calculated excited-state energies by a constant shift of about 0.6 to 0.7 eV. However, the results of these TDDFT/PBE dynamics simulations have been validated both qualitatively (by the characters of the excited-state orbitals) and quantitatively (up to this constant shift) by a few single-point calculations at the RI-CC2 level along the trajectory obtained for TrpH$^+$.

The vertical excitation energies computed for the most stable conformer of TrpH$^+$ obtained from metadynamics at its equilibrium geometry are reported in Table 5.1 and the results of MD simulations for TrpH$^+$ and TrpH$^+ \cdot$W$_2$ are shown in Figure 5.7. For bare TrpH$^+$, RI-CC2 and TDDFT give comparable excited-state energies, except for two dark states labeled $\pi\pi^*_{CO}$, which are CT states involving the excitation of a π-electron of the indole ring to a π^* orbital mainly localized on the carboxyl group and whose energies are markedly underestimated by TDDFT (< 4 eV, whereas RI-CC2 yields energies > 5 eV). This effect is due to the failure of local exchange-correlation functionals to correctly describe long-range CT states in TDDFT and has already been pointed out in the literature [43, 44]. The first optically accessible state is predicted by RI-CC2 with the larger basis set to have a vertical excitation energy of 4.46 eV. This is almost the same as that computed by Weinkauf and coworkers, although with another method and on a different conformer [45], and can be compared with the experimental value of 4.35 eV for the maximum of the broad 0-0 transition. At the TDDFT level, this state corresponds to the excitation of a π-electron of the indole ring to an orbital consisting of a mixture of $\sigma^*_{N\text{-}H}$ (57%), $\sigma^*_{C\alpha\text{-}N}$ (6%), indole π^* (19%) and carboxyl π^*_{CO} (8%) orbitals. Similar percentages are found with the highest-level RI-CC2 calculation: $\sigma^*_{N\text{-}H} + \sigma^*_{C\alpha\text{-}N}$ (67%), indole π^* (10%) and π^*_{CO} (6%). Jouvet and coworkers recently published RI-CC2 calculations that also revealed, for different conformers of TrpH$^+$, significant σ^* contributions to the excited-state orbital [46]. This characteristic is clearly illustrated in the leftmost orbital representation of Figure 5.7(a).

Table 5.1: Vertical excitation energies (in eV) to the first singlet electronic states of $TrpH^+$ with different methods. The smaller basis set is aug-cc-pVDZ on O and N atoms, and cc-pVDZ on H and C atoms. The larger basis set is aug-cc-pVDZ on all atoms. The character of the excited states refers to their largest orbital component.

Excited-state character	RI-CC2 smaller basis set	RI-CC2 larger basis set	TDDFT/B3LYP larger basis set
$\pi\sigma^*$	4.64	4.46	4.28
$\pi\pi^*$	4.92	4.80	4.71
$\pi\pi^*$	5.18	5.01	4.73
$\pi\pi^*_{CO}$	> 5.0	> 5.0	3.43
$\pi\pi^*_{CO}$	> 5.0	> 5.0	3.89

The first 45 fs of the MD simulation obtained for $TrpH^+$ excited in this $S_1(\pi\sigma^*)$ state are represented in Figure 5.7(a-c), showing the evolution of the ground-state and running excited state energies, the length of the N-H and C_α-N bonds, and a few snapshots of the excited-state orbital. At the beginning of the trajectory, the excited state has a predominant $\sigma^*_{N\text{-}H}$ character, indicating the transfer of an electron from the indole ring to the ammonium group and the consequent localization of the positive charge on the former. A fast relaxation of this state takes place over the first 10 fs period, during which the $\sigma^*_{N\text{-}H}$ and π^* contributions decrease, while the $\sigma^*_{C_\alpha\text{-}N}$ antibonding character increases. As a result, the initial stretching of one N-H bond is followed by the elongation of the C_α-N bond, which eventually leads to the detachment of a neutral NH_3 molecule. This fragmentation corresponds to the main channel that we observed in the low-temperature photodissociation mass spectrum of $TrpH^+$ (*m/z* 188; see Figure 4.1(b)). The black and magenta circles in Figure 5.7(b) show the results of the aforementioned single-point RI-CC2 calculations of the ground and excited states and are in good agreement with the TDDFT curves, which corroborates the validity of the latter. The varying contributions to the excited-state molecular orbital computed during the TDDFT simulation are also confirmed at the RI-CC2 level (not shown here; see reference [33] and its Supporting Information).

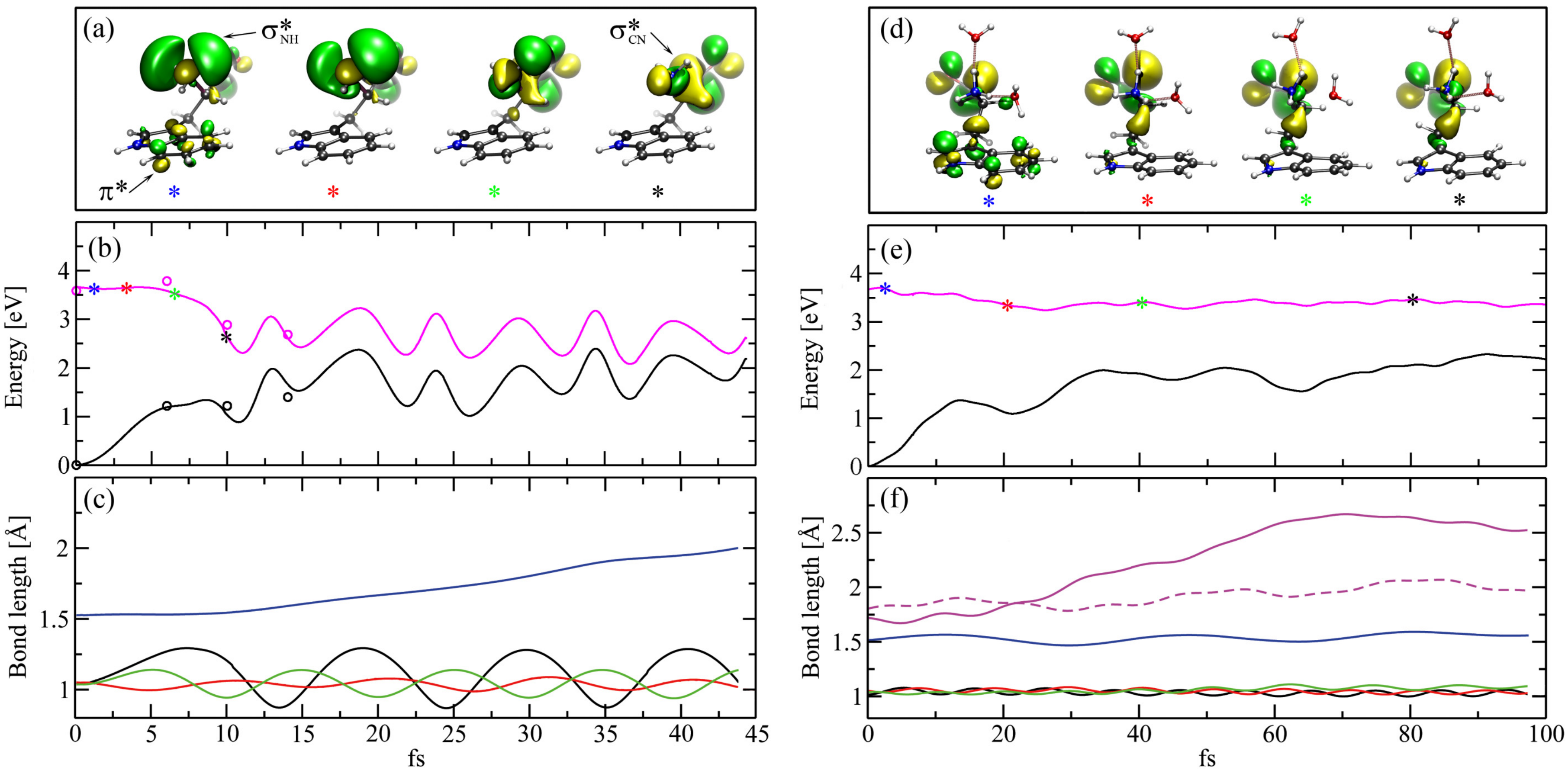

Figure 5.7: Time evolution of TrpH$^+$ (a-c) and TrpH$^+$·W$_2$ (d-f) excited to their respective first photoaccessible electronic states. (a,d) Dominant Kohn-Sham orbital contributions to the excited state during TDDFT dynamics at different times indicated by the colored asterisks. (b,e) Energies of the ground state (black line) and running diabatic excited state (magenta line) along the TDDFT dynamics run. (c,f) N-H (black, red and green lines) and C$_\alpha$-N (blue line) bond lengths, and H$_2$NH···OH$_2$ distances (magenta lines). In panel (b), black and magenta circles correspond to RI-CC2 energies computed at the corresponding geometries (to facilitate comparison, the RI-CC2 excited-state energies are shifted down by a constant amount to best match the TDDFT curve; see text).

The results of excited-state calculations for the most stable conformer of $\mathrm{TrpH^+ \cdot W_2}$ obtained from metadynamics show that the two water molecules significantly alter the electronic structure of the lowest excited singlet states. The first optically accessible state S_1 is now mainly of $\pi\pi^*$ character (> 98%) and the relative energies of the $\sigma^*_{\mathrm{N\text{-}H}}$ orbitals are shifted up by ~ 1.3 eV. This destabilization can be explained by the strong CT and repulsive electrostatic interactions between the vacant orbitals of the ammonium group and the lone electron pairs of the two water oxygen atoms [47]. The MD simulation calculated for $\mathrm{TrpH^+ \cdot W_2}$ excited in the $S_1(\pi\pi^*)$ state is depicted in Figure 5.7(d-f) over a 100 fs range. In this case, there is hardly any change of the electronic structure, in contrast with the fast relaxation (~ 10 fs) observed for the bare ion. Such a behavior is consistent with the long excited-state lifetime evidenced by our sharp electronic spectrum. Moreover, the curves in Figure 5.7(f) show that the release of electronic energy induces the dissociation of water, rather than the cleavage of a covalent bond, which again agrees with the most abundant fragmentation channel detected experimentally (see Figure 5.2(b)).

As for the $\mathrm{TrpH^+ \cdot W_2}$ lowest-energy structure predicted by the DFT/B3LYP geometry optimization (Figure 5.6(a)), no TDDFT excited-state dynamics have been computed to this day. Nonetheless, RI-CC2 calculations of vertical excitation have been performed and yielded results that are qualitatively similar to those obtained for the other conformer. The first two excited states are almost entirely of $\pi\pi^*$ character and have similar energies. The third one gets its largest contribution from a $\sigma^*_{\mathrm{N\text{-}H}}$ orbital, but it lies > 0.4 eV above S_1. Therefore, even in this structure where only one of the two water molecules is directly attached to the ammonium group, the σ^* orbitals are sufficiently destabilized that the $\pi\pi^*$ and $\pi\sigma^*$ states are essentially decoupled. One can thus reasonably expect, in light of the arguments presented above, that the S_1 state of this conformer would also exhibit a much longer lifetime than the unsolvated $\mathrm{TrpH^+}$ ion.

5.2.4 Generality of the observed phenomenon

In order to test whether the lifetime-shortening effect displayed by bare $\mathrm{TrpH^+}$ is specific to this particular ion (or to peptides having a protonated N-terminal Trp), we have also measured the low-temperature electronic spectra of $\mathrm{GlyTrpH^+}$ and $\mathrm{GlyGlyTrpH^+}$, in which the Trp residue lies at the C-terminus and is thus separated from the protonated amino group by additional bonds. Both species exhibit very broad spectra, similar to that of TrpH$^+$, indicative of an ultrashort excited-state lifetime. In addition, TDDFT calculations of electronic excited states have been carried out for the lowest found conformer of GlyTrpH$^+$, whose protonated N-terminus lies even closer to the indole ring than in TrpH$^+$ (see Figure 5.8(a)). They reveal that the first optically accessible state also possesses a strong πσ* character centered on the ammonium group, as demonstrated by the orbital representation in Figure 5.8(b). Finally, to further assess the importance of bond connectivity and determine whether the interaction occurs through bonds or through space, we have performed analogous calculations on a model 3-methylindole-methylammonium complex fixed in the geometry of the most stable GlyTrpH$^+$ structure, so that there is no covalent interconnection between the electron donor and the electron acceptor (Figure 5.9(a)). Again, the first optically accessible state corresponds to the promotion of a π-electron of the indole ring to a $\sigma^*_{\text{N-H}}$ orbital localized on the charged ammonium (Figure 5.9(b) and (c), respectively). What is more, in both these calculations, the energies and oscillator strengths of the transitions are similar to those obtained for the πσ* state of bare TrpH$^+$.

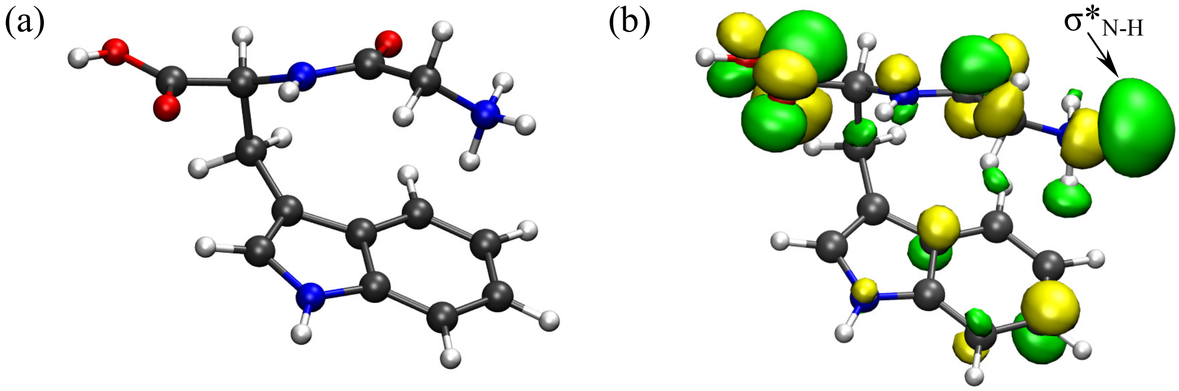

Figure 5.8: GlyTrpH$^+$. (a) Calculated lowest-energy conformer showing the proximity of the ammonium group to the indole ring. (b) Dominant Kohn-Sham orbital contributions to the electronic excited state.

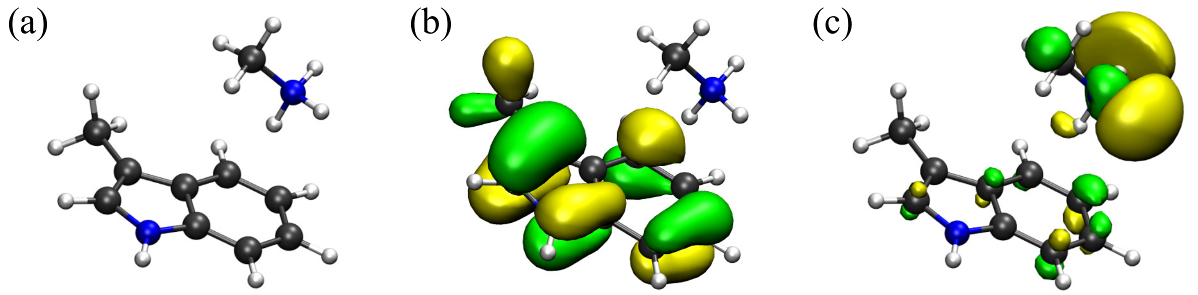

Figure 5.9: 3-Methylindole-methylammonium complex. (a) Model of the complex fixed in the geometry of the GlyTrpH$^+$ structure of Figure 5.8. (b) Ground electronic state orbital. (c) Excited electronic state orbital.

The experimental and theoretical results presented in this chapter demonstrate the extreme importance of local environment on the electronic excited-state behavior of the amino acid tryptophan and hence on its fluorescence properties, which are extensively used in biochemistry and biophysics. First, we have shown that the presence of a protonated amino group, and presumably of any potential electron acceptor, in the vicinity of the indole ring creates low-lying charge-transfer states that can mix with the $\pi\pi^*$ state of the chromophore and thus modulate its lifetime. Besides, the findings on GlyTrpH$^+$, GlyGlyTrpH$^+$ and the model 3-methylindole-methylammonium complex have established that this influence is not a through-bond but a through-space effect, so that the electron acceptor could in fact be very distant from the Trp residue in terms of bond connectivity. Secondly, we have determined that solvation of the TrpH$^+$ ammonium group by only two water molecules is sufficient to shift up the energy of its σ^* orbitals and decouple the $\pi\sigma^*$ and $\pi\pi^*$ states. One could imagine that the same role could also be played by other types of hydrogen-bond acceptors within a protein.

As an example of how our results can give insights into the interpretation of tryptophan fluorescence in proteins, we can cite two recent studies of human serum albumin (HSA), a 585-amino acid protein containing a single Trp residue at position 214, situated at the bottom of a 12 Å deep crevice of the molecule. Siemiarczuk et al. determined the fluorescence lifetime of Trp214 in wild-type HSA and several of its mutants in which a single amino acid is substituted [48]. In particular, they noted significant lifetime increases when replacing Arg218 with methionine, histidine or alanine. This arginine residue is located on the same side of an α-helix as Trp214, only one turn away, so that its charged guanidinium group lies very close to the indole chromophore (~ 4 Å). Our findings suggest that this charged group possesses low-energy σ* orbitals that couple with the first π* orbital of Trp and can thus induce an electron transfer that quenches the fluorescence in wild-type HSA. The second study, by Zewail and coworkers, probed the solvation dynamics and local rigidity of HSA by femtosecond-resolved fluorescence measurements of that same Trp214 residue for various structures of the protein at different pH values [49]. As illustrated by our results on $TrpH^+\cdot W_2$, the presence of water molecules in the vicinity of the chromophore, depending on their location, could significantly reduce the influence of the surrounding quenchers, especially Arg218.

References

[1] H. Kang, C. Jouvet, C. Dedonder-Lardeux, S. Martrenchard, G. Grégoire, C. Desfrançois, J. P. Schermann, M. Barat and J. A. Fayeton, *Physical Chemistry Chemical Physics* **2005**, *7*, 394-398.

[2] H. Kang, C. Dedonder-Lardeux, C. Jouvet, G. Grégoire, C. Desfrançois, J. P. Schermann, M. Barat and J. A. Fayeton, *Journal of Physical Chemistry A* **2005**, *109*, 2417-2420.

[3] L. A. Philips, S. P. Webb, S. J. Martinez, G. R. Fleming and D. H. Levy, *Journal of the American Chemical Society* **1988**, *110*, 1352-1355.

[4] T. R. Rizzo, Y. D. Park, L. A. Peteanu and D. H. Levy, *Journal of Chemical Physics* **1986**, *84*, 2534-2541.

[5] W. B. de Lauder and P. Wahl, *Biochemistry* **1970**, *9*, 2750-2754.

[6] R. J. Robbins, G. R. Fleming, G. S. Beddard, G. W. Robinson, P. J. Thistlethwaite and G. J. Woolfe, *Journal of the American Chemical Society* **1980**, *102*, 6271-6279.

[7] A. G. Szabo and D. M. Rayner, *Journal of the American Chemical Society* **1980**, *102*, 554-563.

[8] C. A. Marquezin, L. Y. Hirata, L. Juliano and A. S. Ito, *Biopolymers* **2003**, *71*, 569-576.

[9] K. Včeláková, I. Zusková, E. Kenndler and B. Gaš, *Electrophoresis* **2004**, *25*, 309-317.

[10] E. G. Robertson and J. P. Simons, *Physical Chemistry Chemical Physics* **2001**, *3*, 1-18.

[11] T. S. Zwier, *Journal of Physical Chemistry A* **2001**, *105*, 8827-8839.

[12] L. A. Peteanu and D. H. Levy, *Journal of Physical Chemistry* **1988**, *92*, 6554-6561.

[13] L. C. Snoek, R. T. Kroemer and J. P. Simons, *Physical Chemistry Chemical Physics* **2002**, *4*, 2130-2139.

[14] P. Çarçabal, R. T. Kroemer, L. C. Snoek, J. P. Simons, J. M. Bakker, I. Compagnon, G. Meijer and G. von Helden, *Physical Chemistry Chemical Physics* **2004**, *6*, 4546-4552.

[15] R. A. Jockusch, A. S. Lemoff and E. R. Williams, *Journal of Physical Chemistry A* **2001**, *105*, 10929-10942.

[16] S. J. Xu, M. Nilles and K. H. Bowen, *Journal of Chemical Physics* **2003**, *119*, 10696-10701.

[17] A. S. Lemoff and E. R. Williams, *Journal of the American Society for Mass Spectrometry* **2004**, *15*, 1014-1024.

[18] S. Nonose, S. Iwaoka, K. Mori, Y. Shibata and K. Fuke, *European Physical Journal D* **2005**, *34*, 315-319.

[19] S. E. Rodriguez-Cruz, J. S. Klassen and E. R. Williams, *Journal of the American Society for Mass Spectrometry* **1997**, *8*, 565-568.

[20] S. E. Rodriguez-Cruz, J. S. Klassen and E. R. Williams, *Journal of the American Society for Mass Spectrometry* **1999**, *10*, 958-968.

[21] M. Kohtani and M. F. Jarrold, *Journal of the American Chemical Society* **2002**, *124*, 11148-11158.

[22] D. F. Liu, T. Wyttenbach, P. E. Barran and M. T. Bowers, *Journal of the American Chemical Society* **2003**, *125*, 8458-8464.

[23] M. F. Jarrold, *Accounts of Chemical Research* **1999**, *32*, 360-367.

[24] J. Woenckhaus, *International Journal of Mass Spectrometry* **2002**, *213*, 9-24.

[25] A. Kamariotis, O. V. Boyarkin, S. R. Mercier, R. D. Beck, M. F. Bush, E. R. Williams and T. R. Rizzo, *Journal of the American Chemical Society* **2006**, *128*, 905-916.

[26] A. Kamariotou, *Infrared photofragment spectroscopy of charged amino acid water clusters in the gas phase*, Ph.D. Thesis, EPFL, Lausanne, 2006.

[27] H. El Aribi, G. Orlova, A. C. Hopkinson and K. W. M. Siu, *Journal of Physical Chemistry A* **2004**, *108*, 3844-3853.

[28] P. M. Felker and A. H. Zewail, *Chemical Physics Letters* **1983**, *94*, 448-453.

[29] P. M. Felker and A. H. Zewail, *Chemical Physics Letters* **1983**, *94*, 454-460.

[30] J. Hager and S. C. Wallace, *Journal of Physical Chemistry* **1985**, *89*, 3833-3841.

[31] M. Mitsui, Y. Ohshima and O. Kajimoto, *Journal of Physical Chemistry A* **2000**, *104*, 8660-8670.

[32] A. Sur and P. M. Johnson, *Journal of Chemical Physics* **1986**, *84*, 1206-1209.

[33] S. R. Mercier, O. V. Boyarkin, A. Kamariotis, M. Guglielmi, I. Tavernelli, M. Cascella, U. Rothlisberger and T. R. Rizzo, *Journal of the American Chemical Society* **2006**, *128*, 16938-16943.

[34] W. D. Cornell, P. Cieplak, C. I. Bayly, I. R. Gould, K. M. Merz, D. M. Ferguson, D. C. Spellmeyer, T. Fox, J. W. Caldwell and P. A. Kollman, *Journal of the American Chemical Society* **1995**, *117*, 5179-5197.

[35] A. Laio and M. Parrinello, *Proceedings of the National Academy of Sciences of the United States of America* **2002**, *99*, 12562-12566.

[36] J. P. Perdew, K. Burke and M. Ernzerhof, *Physical Review Letters* **1996**, *77*, 3865-3868.

[37] G. A. Kaminski, R. A. Friesner, J. Tirado-Rives and W. L. Jorgensen, *Journal of Physical Chemistry B* **2001**, *105*, 6474-6487.

[38] A. D. Becke, *Journal of Chemical Physics* **1993**, *98*, 5648-5652.

[39] C. Lee, W. Yang and R. G. Parr, *Physical Review B* **1988**, *37*, 785-789.

[40] O. Christiansen, H. Koch and P. Jørgensen, *Chemical Physics Letters* **1995**, *243*, 409-418.

[41] F. Weigend, M. Häser, H. Patzelt and R. Ahlrichs, *Chemical Physics Letters* **1998**, *294*, 143-152.

[42] D. E. Woon and T. H. Dunning Jr., *Journal of Chemical Physics* **1993**, *98*, 1358-1371.

[43] A. Dreuw, J. L. Weisman and M. Head-Gordon, *Journal of Chemical Physics* **2003**, *119*, 2943-2946.

[44] A. Dreuw and M. Head-Gordon, *Journal of the American Chemical Society* **2004**, *126*, 4007-4016.

[45] D. Nolting, C. Marian and R. Weinkauf, *Physical Chemistry Chemical Physics* **2004**, *6*, 2633-2640.

[46] G. Grégoire, C. Jouvet, C. Dedonder and A. L. Sobolewski, *Journal of the American Chemical Society* **2007**, *129*, 6223-6231.

[47] H. Umeyama and K. Morokuma, *Journal of the American Chemical Society* **1977**, *99*, 1316-1332.

[48] A. Siemiarczuk, C. E. Petersen, C. E. Ha, J. S. Yang and N. V. Bhagavan, *Cell Biochemistry and Biophysics* **2004**, *40*, 115-122.

[49] W. H. Qiu, L. Y. Zhang, O. Okobiah, Y. Yang, L. J. Wang, D. P. Zhong and A. H. Zewail, *Journal of Physical Chemistry B* **2006**, *110*, 10540-10549.

Chapter 6 Identification of conformers by IR-UV double resonance spectroscopy

In this chapter, we will carry out the detailed analysis of the well-resolved electronic spectra of cold protonated tyrosine and doubly hydrated tryptophan, which have been presented in the two preceding chapters. The objective is to identify the number of different conformers contributing to each spectrum, thus reflecting their distribution inside the 22-pole ion trap, and possibly to relate each of them to a particular geometry. The tools at our disposal to reach that goal are both experimental and theoretical. The measurement of conformer-specific vibrational spectra in the hydride stretch region and IR-UV hole-burning electronic spectra, whose techniques have been presented previously (see *3.4 Conformer-specific spectra by IR-UV double resonance spectroscopy*), will be used to determine how many conformers are responsible for all the observed vibronic transitions. Moreover, as already suggested in *Chapter 4*, the variations in fragmentation patterns of mass spectra recorded for different vibronic transitions of $\mathrm{TyrH^+}$ can also assist in the conformer assignment of peaks. Finally, the results of quantum chemical calculations on these two species will help us interpret both their vibrational and electronic spectra, as well as propose possible structures for the conformers.

Briefly, the methodology can be described as follows. Vibrational IR dip spectra and electronic IR-UV hole-burning spectra are measured alternately and several times. For the former, one tries to set the UV wavelength on vibronic transitions that potentially belong to different conformers, so as to obtain distinct vibrational spectra. Similarly, for the latter, one must select infrared transitions that are unique to a given conformer, so that only this one will appear depleted in the hole-burning spectrum. This procedure is applied repeatedly, until all vibronic transitions in the composite electronic spectrum can be attributed to one of the identified conformers. The precise assignment of these peaks can then be carried out by measuring their spacings and relative intensities, and trying to recognize vibrational progressions and combination bands. In that process, the harmonic frequencies predicted by calculations are a useful guide to identify low-frequency vibrational modes. Finally, comparison between the calculated high-frequency modes and the experimental IR spectra is used to determine the geometries of the observed conformers.

The following sections of this chapter will present the results of such measurements and analyses conducted on the electronic spectra of $\mathrm{TyrH^+}$ and $\mathrm{TrpH^+{\cdot}W_2}$. Next, the discussion will focus on the geometrical assignments of the experimentally identified conformers and on the nature of the interactions that dictate the structural preferences of the studied ions.

6.1 Detailed analysis of the $\mathrm{TyrH^+}$ electronic spectrum

6.1.1 Conformer-specific vibrational spectra of $\mathrm{TyrH^+}$

The IR dip spectra recorded on the 3250-3700 $\mathrm{cm^{-1}}$ range with the UV laser fixed on the two redmost vibronic transitions of $\mathrm{TyrH^+}$ (35 082 $\mathrm{cm^{-1}}$ and 35 111 $\mathrm{cm^{-1}}$) and by detecting fragment *m/z* 107 are shown in Figures 6.1 and 6.2, respectively. As will be detailed below, they exhibit some measurable differences and can thus be associated with two distinct conformers, which will be labeled A for the first one and B for the second. Underneath each of them are represented the best-matching calculated spectra, among the most stable structures found computationally, as well as illustrations of the corresponding geometries and their relative energies. All calculations of $\mathrm{TyrH^+}$ conformers have been performed by Dr. Jaime A. Stearns and consisted in a preliminary conformational search using the AMBER force field [1] within the MacroModel program [2], followed by further geometry optimizations of the lowest-energy structures and harmonic frequency calculations at the DFT/B3LYP/6-31++G** level [3, 4] in the Gaussian03 program [5]. The frequency scale of the displayed calculated spectra was multiplied by a constant factor of 0.956 to account for the anharmonicity of the vibrations and other computational approximations, and obtain a better match with the experimental spectra. The indicated relative energies of the structures are corrected for the zero-point energy, using the unscaled harmonic frequencies. The other geometries found computationally having much higher relative energies (~ 4 kcal·mol^{-1} and above) and showing poorer agreement with the experimental spectra, they have been discarded.

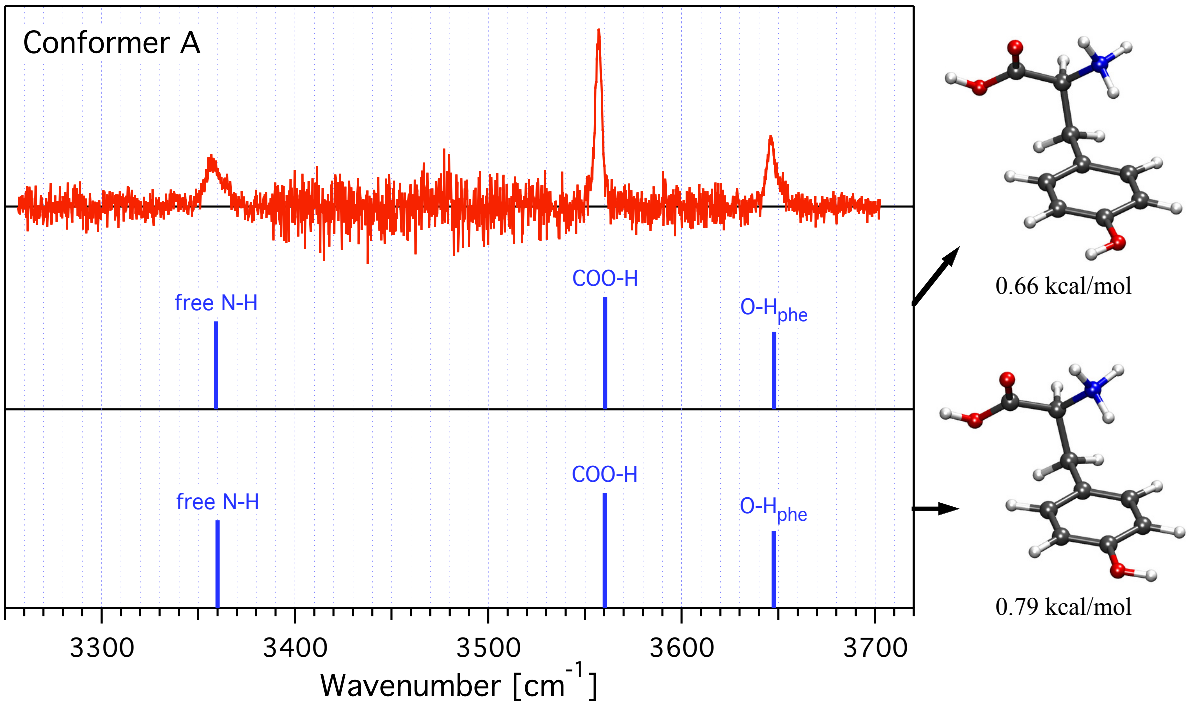

Figure 6.1: Infrared dip spectrum recorded for TyrH$^+$ by setting the UV laser on the vibronic transition at 35 082 cm^{-1} (conformer A) and detecting fragment *m/z* 107. Underneath are displayed the best-matching calculated spectra corresponding to the structures shown on the right. The theoretical harmonic frequencies are scaled by a factor of 0.956.

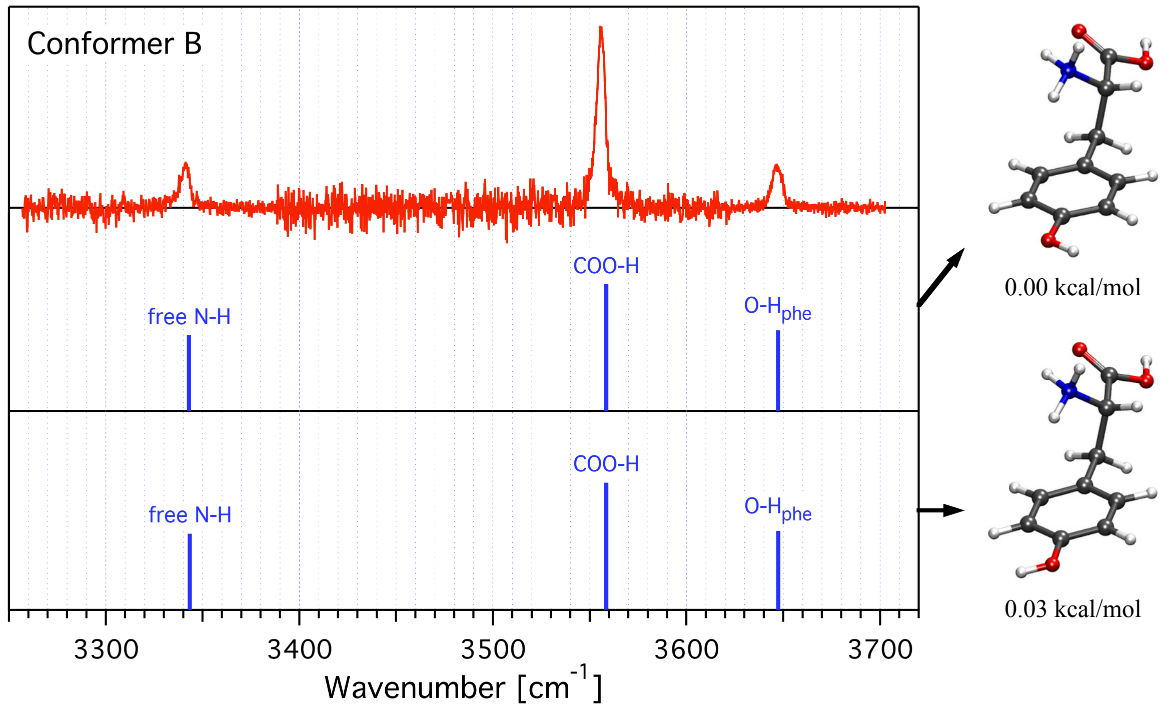

Figure 6.2: Infrared dip spectrum recorded for TyrH$^+$ by setting the UV laser on the vibronic transition at 35 111 cm^{-1} (conformer B) and detecting fragment *m/z* 107. Underneath are displayed the best-matching calculated spectra corresponding to the structures shown on the right. The theoretical harmonic frequencies are scaled by a factor of 0.956.

Both experimental spectra distinctly show the presence of three vibrational transitions over the scanned range. The noise level across the spectra varies significantly, which can be explained by two reasons. First, the whole IR range was subdivided in several regions, for which different amount of data have been acquired. Secondly, the laser power across the range showed important fluctuations depending on the efficiency of the frequency-conversion crystals and on atmospheric water absorption, which induces a variable noise level through power-normalization of the spectra. The agreement between the predicted spectra of the four lowest-energy conformers and the experimental ones is excellent (< 4 cm^{-1} differences for all peaks). This permits the assignment of the observed transitions as follows. The highest-frequency mode corresponds to the stretching of the phenolic O-H bond (O-H$_{phe}$) and occurs at 3646.6 cm^{-1} for conformer A and 3647.0 cm^{-1} for conformer B. The second highest, appearing at 3557.0 cm^{-1} for A and 3555.8 cm^{-1} for B, is ascribed to the O-H bond stretch of the carboxylic acid group (COO-H). Finally, the third peak is due to a free N-H stretch mode and is situated at 3358.1 cm^{-1} for conformer A and at 3341.0 cm^{-1} for B.

The only notable differences between the two recorded spectra are the small but reproducible ~ 1 cm^{-1} shift of the intense COO-H transition and the larger 17 cm^{-1} gap between the free N-H modes. For comparison with the calculated spectra, only the second one can be reliably taken into account. The accurate match between the experimental and predicted spectra leads to the conclusion that the structures of conformers A and B differ mainly in the orientation of the amino acid backbone with respect to the aromatic ring. The former has both the carboxylic acid and ammonium groups pointing towards the phenol ring (Figure 6.1), while in the latter, the COOH is oriented *anti* relative to the ring (Figure 6.2). However, the calculations do not allow to make a distinction between conformers differing only in the orientation of the phenolic O-H bond, as demonstrated by the strong similarity of the predicted spectra. Besides, the quasi-correspondence of the O-$\mathrm{H}_{\mathrm{phe}}$ and COO-H peak positions for A and B implies that, depite their lower intensities, only the free N-H transitions can be used to measure IR-UV hole-burning spectra and distinguish between the vibronic peaks of both conformers. The results of these measurements and the subsequent analysis of the TyrH^+ electronic spectrum are presented in the following subsection.

6.1.2 IR-UV hole-burning and vibronic assignment of TyrH^+

IR-UV hole-burning electronic spectra have been acquired for both the A and B conformers by setting the IR laser on their respective free N-H transitions at 3358 cm^{-1} and 3341 cm^{-1}, respectively, and recording the intensity of the *m/z* 107 fragment. Portions of the obtained traces near the electronic origins are shown in Figure 6.3, displayed as a superposition of the «IR laser off» and «IR laser on» signals. In spite of the relatively low intensities of these IR absorptions (~ 15% ion signal depletion in both cases), the differences between Figure 6.3(a) and (b) are sufficiently clear-cut to unambiguously attribute each vibronic peak to either conformer A or conformer B, as illustrated in the figure. Further to the blue of the origins, increasingly more peaks present partial or complete overlap, making the conformational assignment quite difficult and uncertain in some cases. Nonetheless, all the vibronic transitions observed over the scanned UV range (35 050 - 35 400 cm^{-1}) get depleted by setting the IR laser to one and/or the other of these two IR frequencies.

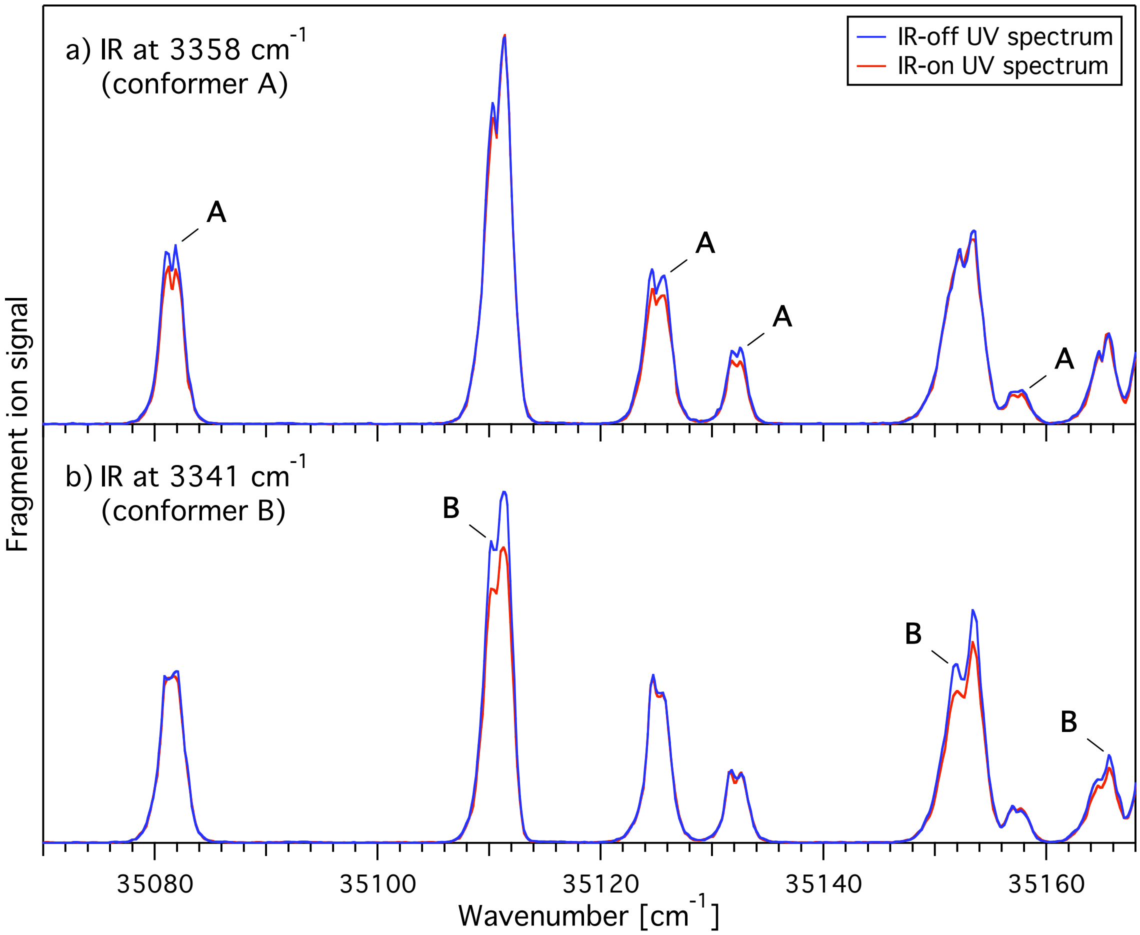

Figure 6.3: Results of IR-UV hole-burning measurements in the origin region of TyrH^{+}, recorded by setting the IR laser on the free N-H transitions of (a) conformer A at 3358 cm^{-1} and (b) conformer B at 3341 cm^{-1}. In both cases, the *m/z* 107 ion signals detected with and without the IR laser are displayed.

The low-frequency vibrations predicted by the harmonic frequency calculations, which all correspond to various torsional modes of the molecule, are helpful to get an estimate of the frequency spacings to be expected when searching for vibrational progressions and combination bands. Although the calculations are performed for the electronic ground state S_0, while the vibronic peaks relate to the S_1 vibrations, the fact that the observed hot bands and their corresponding 1←0 transitions are positioned almost symmetrically with respect to their common origin (a point highlighted in previous chapters for TyrH^{+} and TrpH$^{+}\cdot W_2$) indicates that the vibrational frequencies of the excited electronic state should not be very different from their ground-state counterparts. Many vibronic peaks of the TyrH$^+$ UV spectrum can thus be associated with a particular vibrationally excited state in the electronic S_1 state of either the A or the B conformer. However, some other significant transitions do not match any combination or progression of vibrational modes, which strongly suggests the presence of additional conformers beside A and B. As a matter of fact, this is not surprising and was prefigured by the geometry calculations showing pairs of conformers that have opposite orientation of the phenolic O-H bond but almost the same relative energy. Therefore, each of the hole-burning spectra presented in Figure 6.3 actually corresponds to the depletion of two such conformers having similar vibrational spectra over the measured IR range. More recent experiments have been carried out in our laboratory, using a new infrared laser system, and have confirmed this idea by revealing small but perceptible differences below 3200 cm^{-1} in the IR dip spectra measured for vibronic peaks that apparently belonged to the same conformer in the hole-burning spectra presented here. These new data have been published in reference [6] and permit the identification of two other conformers, C and D, which have backbone/ring orientations analogous to A and B, respectively.

The assignments of vibronic peaks, some of which should be considered as tentative, are given in Table 6.1. The first two columns list the positions and relative intensities of all peaks in the TyrH$^+$ electronic spectrum, up to 35 300 cm^{-1}. In the next columns, three pieces of information are shown for each conformer associated with a particular peak: (i) the spacing between the peak and the conformer origin; (ii) the relative intensity of the peak due to that conformer; (iii) one or several plausible assignments. Because of peak overlapping, the intensities indicated for the conformers are often different from the ones listed in the second column. In such cases, they are roughly estimated from the depletion levels observed in the hole-burning spectra. The assignments are given in terms of numbered vibrational modes (e.g., v_2), whenever these can be ascribed without doubt, and otherwise by using the relative position of other peaks (e.g., v_1+89.9). Of course, the assignments get more uncertain, and sometimes impossible, at larger distances from the origin region, since both the spectral congestion and the number of possible combinations rapidly increase. The most unclear assignments are indicated in parentheses.

Table 6.1: Peak assignments for the electronic spectrum of $TyrH^+$ in the origin region. $\tilde{\nu}$ and I are the positions and relative intensities of the peaks in the composite spectrum. $\Delta\tilde{\nu}(X)$ and I(X) are, for conformer X, the peak distances from the origin of X and the estimated relative intensity due to X. The most tentative assignments are indicated in parentheses.

$\tilde{\nu}$ [cm^{-1}]	I [%]	$\Delta\tilde{\nu}$(A) I(A)	Assignment	$\Delta\tilde{\nu}$(B) I(B)	Assignment	$\Delta\tilde{\nu}$(C) I(C)	Assignment	$\Delta\tilde{\nu}$(D) I(D)	Assignment
35081.6	44	0.0 (44)	Origin						
35110.9	82			0.0 (82)	Origin				
35125.2	38	43.7 (38)	ν_1						
35132.2	18	50.6 (18)	ν_2						
35152.7	45			41.8 (45)	ν_1				
35157.3	8	75.7 (8)	ν_3						
35165.1	19			54.3 (19)	ν_2				
35169.3	25	87.7 (25)	$2\nu_1$						
35172.6	37			61.8 (37)	ν_3				
35176.3	9	94.8 (9)	$\nu_1+\nu_2$						
35180.0	13	98.4 (13)	ν_4						
35185.9	33			75.0 (9)	(?)	0.0 (24)	Origin		
35196.1	7			85.3 (7)	($2\nu_1$)				
35200.8	43	119.2 (10)	$\nu_1+\nu_3$	89.9 (30)	(ν_4)				
35207.9	15	126.4 (5)	$\nu_2+\nu_3$	97.0 (10)	$\nu_1+\nu_2$				
35212.6	13	131.1 (10)	$3\nu_1$						
35214.7	13			103.9 (13)	$\nu_1+\nu_3$				
35220.2	3	138.6 (3)	$2\nu_1+\nu_2$						
35223.6	11	142.0 (11)	$\nu_1+\nu_4$						
35229.1	29			118.2 (8)	(?)	43.2 (21)	ν_1		
35234.6	100	153.0 (33)	(ν_5) and/or C	123.7 (67)	($2\nu_3$) or only D	48.7 (33)	(ν_2) and/or A	0.0 (67)	Origin (and also B?)
35237.3	17	155.8 (10)	(ν_5) or only C			51.4 (10)	(ν_2) or only A		
35242.7	24			131.8 (18)	ν_1+89.9				
35244.6	14	163.0 (11)	$2\nu_1+\nu_3$						
35251.1	3			140.2 (3)	ν_2+85.3				
35255.6	12	174.4 (6)	$\nu_3+\nu_4$; $4\nu_1$	144.3 (6)	ν_2+89.9				
35262.0	20			151.1 (15)	ν_3+89.9	76.1 (5)	ν_3		
35267.2	5	185.6 (5)	$2\nu_1+\nu_4$						
35272.0	37			161.1 (21)	(ν_5) and/or D	86.1 (16)	$2\nu_1$	37.4 (21)	(ν_1) and/or B
35275.3	45	193.8 (13)	($\nu_1+\nu_2+\nu_4$; ν_6) and/or C	164.5 (32)	(ν_5) and/or D	89.4 (13)	(ν_4) and/or A	40.8 (32)	(ν_1) and/or B
35282.6	45	199.4 (10)	(ν_1+155.8) and/or C			95.1 (10)	(ν_1+51.4) and/or A	48.0 (40)	(ν_2)
35284.9	22	203.3 (12)	(ν_2+153.0) and/or C			99.0 (12)	(ν_4) and/or A		
35289.7	29	208.2 (10)	(ν_7) and/or C	178.9 (20)	(ν_2+123.7 ; ν_6 ; 2·89.9) and/or D	103.8 (10)	2·51.4 and/or A	55.2 (20)	(ν_2) and/or B
35293.3	47	211.7 (12)	(ν_7) and/or C			107.4 (12)	(?) and/or A	58.7 (35)	(ν_3)

6.1.3 Alternative method for conformer assignment of peaks

It has been shown in *Chapter 4* that the low-temperature electronic spectra of protonated tyrosine recorded in mass channels *m/z* 107 and *m/z* 136 present significant differences in the peaks relative intensities, which can most likely be related to different fragmentation patterns of conformers (see Figure 4.4). This fact is more clearly exemplified by the photofragment mass spectra of TyrH$^+$ acquired with the UV laser set on the S_0-S_1 origins of conformers A and B. These are depicted below in Figure 6.4.

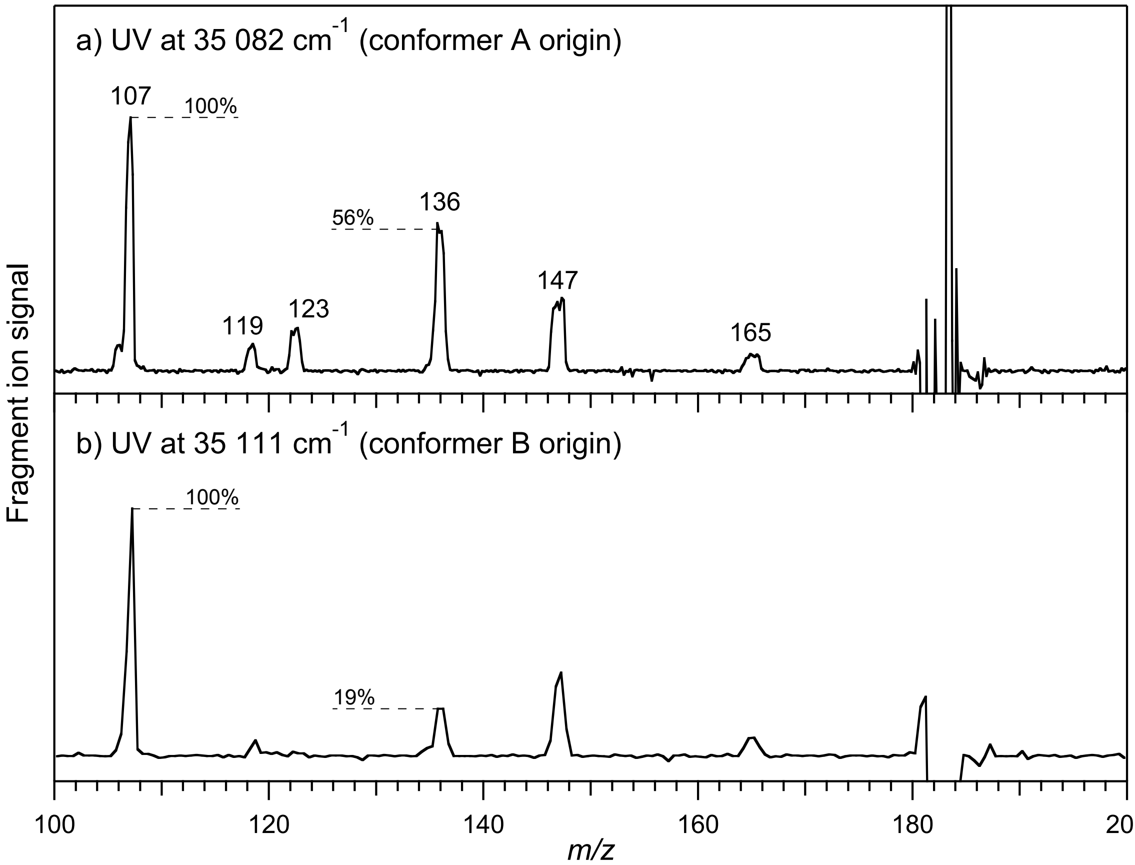

Figure 6.4: Photofragment mass spectra of TyrH$^+$ irradiated by UV laser light at (a) 35 082 cm^{-1} (origin of conformer A) and (b) 35 111 cm^{-1} (origin of conformer B). The temperature of the ion trap was 6 K in both cases.

As noted previously for other difference mass spectra, the large noise at the parent ion mass (*m/z* 182), especially in Figure 6.4(a), results from shot-to-shot fluctuations of the parent signal. These spectra demonstrate that the branching ratios between different fragmentation channels are not the same for conformers A and B. In particular, fragments *m/z* 119 and *m/z* 123 are barely observed in the photodissociation of conformer B and the relative intensity of *m/z* 136 is about 3 times lower than for conformer A. This implies that dissociation occurs on a faster timescale than the interconversion of conformers on the excited-state potential energy surface. In addition, it provides an alternative method for discriminating between different conformers. Indeed, comparison of the vibronic peak intensities in the two TyrH^+ electronic spectra of Figure 4.4(b) and (c) has proven useful in making or confirming some of the assignments presented above. Furthermore, this approach may become essential in cases where the various conformers cannot be differentiated on the basis of their available IR spectra.

6.2 Detailed analysis of the $\mathrm{TrpH}^+\cdot\mathrm{W}_2$ electronic spectrum

6.2.1 Conformer-specific vibrational spectra of $\mathrm{TrpH}^+\cdot\mathrm{W}_2$

Applying the same methods as for TyrH^+, three different IR dip spectra have been acquired for doubly hydrated protonated tryptophan on the 3250-3750 cm^{-1} range and are displayed in Figure 6.5. The vibronic transitions that have been monitored, in the *m/z* 205 mass channel, to obtain these vibrational spectra are at 35 176 cm^{-1}, 35 243 cm^{-1} and 35 281 cm^{-1}, respectively, and the corresponding conformers are labeled A, B and C, in that order. It will be shown further below that conformer A is by far the most abundant, the vibronic peaks of B and C being about 10 times less intense.

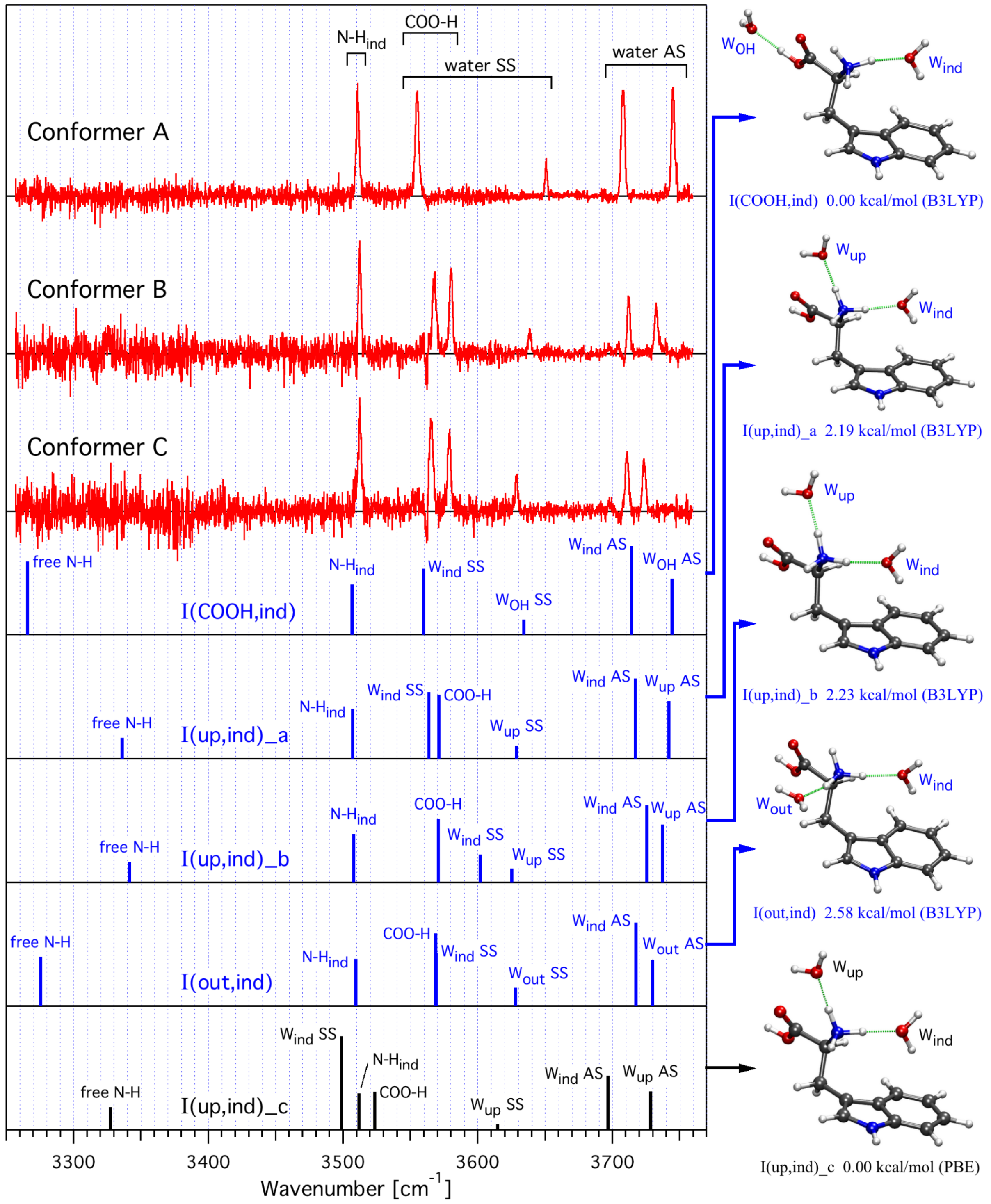

Figure 6.5: Infrared dip spectra recorded for $TrpH^{+}{\cdot}W_2$ by setting the UV laser on the vibronic transition at 35 176 cm^{-1} (conformer A), 35 243 cm^{-1} (conformer B) and 35 281 cm^{-1} (conformer C), and detecting fragment *m/z* 205 (i.e., TrpH^{+}). Underneath are displayed the calculated spectra corresponding to the structures shown on the right. The theoretical harmonic frequencies are scaled by a factor of 0.956 for the B3LYP structures (in blue) and of 0.983 for the PBE structure (in black). See text for details and legend.

As already explained in *Chapter 5*, two separate series of calculations have been performed to determine the lowest-energy structures of $TrpH^+ \cdot W_2$. The first one consisted in optimizations up to the DFT/PBE level and predicted a global minimum structure where both water molecules are hydrogen-bonded to the ammonium group (Figure 5.5(a)). The second one, at the DFT/B3LYP level, yielded several geometries that have a lower relative energy, the most stable of them having one water attached to the carboxylic O-H bond (Figure 5.6(a)). For both series of calculations, harmonic vibrational frequencies have been computed, using the corresponding functionals, in order to compare them with the experimental IR spectra. As it turned out, the DFT/PBE frequency predictions do not match the experimental transitions nearly as well as the DFT/B3LYP results. Therefore, only one PBE spectrum is depicted in Figure 6.5 (in black) to illustrate this fact, while the other displayed spectra are the best-matching ones obtained from B3LYP (in blue). The frequency scaling factor used for the PBE spectrum was 0.983, using the indole N-H vibration (N-H_{ind}) as a reference. For the DFT spectra, the same 0.956 factor as for $TyrH^+$ was applied. To facilitate the discussion, the calculated structures, shown on the right of the figure, are given a descriptive name: a Roman numeral specifies the geometry of the $TrpH^+$ ion as defined in *Chapter 5* (here, all are of type I); next to it are given, in parentheses, the positions of the two water molecules; finally, in case of closely similar structures, an additional letter differentiates between them. The relative zero-point corrected energies of the structures are given below each of them(1). All the calculated frequencies presented here correspond to local vibrational modes and are labeled accordingly (SS and AS stand for the water symmetric and antisymmetric stretches, respectively).

In all three experimental spectra, the lowest-frequency transition appears consistently between 3511 cm^{-1} and 3513 cm^{-1} and corresponds to the stretch vibration of the indole N-H bond, as demonstrated by the calculated spectra. The two highest-frequency vibrations, also present in the three spectra but at various positions, are due to the antisymmetric stretch modes of the two water molecules. According to the computed spectra, the most redshifted of the two is always associated with the water lying above the indole ring, which is certainly caused by a hydrogen-bonding interaction to the π-electron cloud. A lower-intensity transition, situated between 3625 cm^{-1} and 3650 cm^{-1} in the IR dip spectra, is attributable to a water symmetric stretch mode. Here again, all the theoretical spectra coincide in ascribing it to the water molecule that is *not* H-bonded to the indole π-cloud. Between these transitions and the N-H$_{ind}$ peaks, roughly on the 3550-3580 cm^{-1} range, two absorptions appear in the IR spectra of conformers B and C, whereas only one is present for conformer A. The vibrations predicted in this region by the B3LYP calculations are the redshifted symmetric stretch of the «indole» water (W$_{ind}$ SS) and the carboxylic O-H stretch mode (COO-H), but only when this bond is unsolvated (i.e., for the I(up,ind) and I(out,ind) structures). The PBE spectrum depicted for I(up,ind)_c, despite the close resemblance of the latter to the B3LYP I(up,ind) geometries, shows that the frequencies of these two modes are highly underestimated, at least relative to the N-H$_{ind}$ stretch frequency. This is also the case for other computed PBE spectra (not shown here), which illustrates the poor reliability of this method for such predictions. For that reason, the comparison between theory and experiment will be based solely on the B3LYP calculations. For conformers B and C, these two peaks, separated respectively by 12 cm^{-1} and 13 cm^{-1}, can be confidently assigned to those W$_{ind}$ SS and COO-H modes, although one cannot ascertain which is which. Indeed, the frequencies calculated for the water stretch modes, and particularly W$_{ind}$, happen to be extremely sensitive to the precise positions of the water molecules. This fact is exemplified by the marked differences beween the spectra of I(up,ind)_a and I(up,ind)_b, whose geometries are very similar and would presumably correspond to a single conformer experimentally. The case of conformer A is quite intriguing. At first sight, it seems to correlate really well with structure I(COOH,ind), inasmuch as the calculated spectrum shows a rather good correspondence with the experimental one. In addition, this geometry is predicted to be the most stable, which agrees with the fact that A is the major conformer present in the ion trap. Hence the single absorption at 3555 cm^{-1} would be attributed to the W$_{ind}$ symmetric stretch mode, while the COO-H stretch would be shifted to much lower frequencies, beyond the measured range, due to its hydrogen-bonding interaction with the second water (the theoretical frequency is 2926 cm^{-1}). However, another interpretation is possible, where the geometry associated with conformer A would have both water molecules solvating the charged NH$_3$ group. First, one must keep in mind that the predicted stability of the computed structures is not an entirely reliable criterion, since, as already mentioned in *Chapter 5*, different methods yielded contradictory results for relative energies. In light of this, one cannot exclude that the peak at 3555 cm^{-1} may coincidentally correspond to the overlapped W$_{ind}$ and COO-H transitions. As a matter of fact, the spectrum calculated for structure I(out,ind) illustrates such an occurrence. On the other hand, a weakness of this second interpretation is that it would not explain the shift of the COO-H band in conformer A, compared to B and C (i.e., the peaks at ~ 3567 cm^{-1} or ~ 3580 cm^{-1}). A final point to address is the apparent absence in the experimental spectra of free N-H transitions, which are theoretically expected between 3250 cm^{-1} and 3350 cm^{-1}. Two explanations can be advanced to justify this. (i) For the same reasons given in the case of $TyrH^+$, the noise level is higher in this region of the spectrum. Moreover, free N-H transitions can be less intense and possibly broader than other bands, so that they would remain undetected in these spectra. (ii) Alternatively, it could be that the predicted frequencies are overestimated and that the actual N-H transitions are outside the range that we measured.

---

(1) Note that the energy of the PBE structure can obviously not be compared with the B3LYP energies.

To summarize, the six distinct peaks observed in the IR spectra of conformers B and C denote structures where both water molecules are bound to the ammonium group and the COO-H bond is virtually unperturbed. The spectrum of conformer A, with one less peak, is more ambiguous, but strongly suggests a different type of geometry, where one of the water molecules solvates the carboxylic acid group. The theoretical data currently available do not allow to make more specific structural assignments, for which higher-level calculations and more accurate numerical results will be necessary. Nevertheless, the IR-UV hole-burning experiments conducted on $TrpH^+{\cdot}W_2$, and presented in the next subsection, will give some more insights into these questions.

6.2.2 IR-UV hole-burning and vibronic assignment of $TrpH^+{\cdot}W_2$

For each identified conformer, the hole-burning electronic spectrum was obtained by fixing the infrared laser on its highest-frequency antisymmetric stretch peak, because these transitions are both sufficiently intense and specific to their respective conformers. The corresponding frequencies are 3745.0 cm^{-1}, 3732.7 cm^{-1} and 3723.6 cm^{-1} for conformers A, B and C, respectively. The recorded signals were the «IR-on» and «IR-off» intensities of the *m/z* 205 fragment and are displayed in Figure 6.6 for a 100 cm^{-1} range spanning the origin region. The situation here is different from that of $TyrH^+$, for which the two (types of) conformers had comparable relative contributions to the electronic spectrum. The spectrum shown in Figure 6.6(a) indicates that most of the vibronic transitions belong to conformer A, making it the major species present in the trapped ion cloud. Only a few small peaks, labeled «not A», are not depleted by the IR laser at 3745 cm^{-1} and hence suggest the existence of other minor conformers. The one at 35 243 cm^{-1} and another at 35 281 cm^{-1} (not shown here) are the transitions that were monitored to acquire the IR dip spectra which revealed the presence of conformers B and C. Figure 6.6(b) and (c) confirm that the vibronic peaks of B and C are responsible for only a small fraction of the overall composite spectrum.

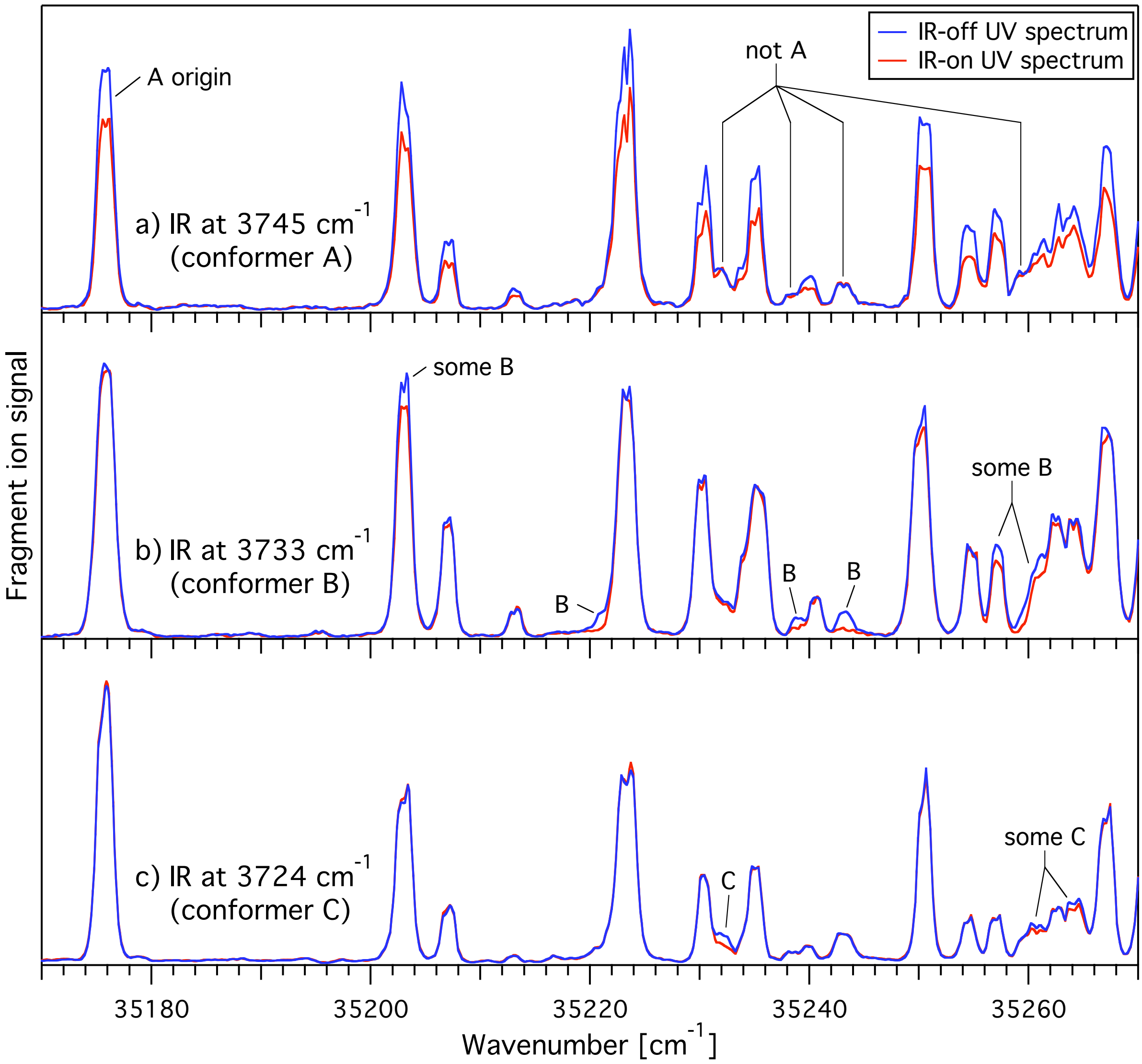

Figure 6.6: Results of IR-UV hole-burning measurements in the origin region of TrpH$^+$·W$_2$, recorded by setting the IR laser on the water antisymmetric stretch transitions of (a) conformer A at 3745.0 cm^{-1}, (b) conformer B at 3732.7 cm^{-1} and (c) conformer C at 3723.6 cm^{-1}. The intensity of the *m/z* 205 fragment, detected with and without the IR laser, is displayed in each case.

In some regards, the search for vibrational progressions and combination bands in the electronic spectrum of $TrpH^{+}{\cdot}W_2$ is made easier than for protonated tyrosine, by the fact that each IR-UV hole-burning spectrum corresponds to a single conformer, and not to a pair of conformers, as was the case for $TyrH^{+}$. On the other hand, the bigger size of $TrpH^{+}{\cdot}W_2$ implies a larger quantity of low-frequency vibrational modes, so that the number of possible combinations, and hence the spectral congestion, increase faster as one moves away from the origin. Moreover, the lower proportions of conformers B and C make it difficult to identify all their vibronic transitions and several of them probably remained undetected. Nevertheless, the assignments of these vibronic peaks have been determined as thoroughly as possible, using the same approach as for $TyrH^{+}$, and are presented in Table 6.2 for the first 150 cm^{-1} to the blue of the origin of conformer A. Here also, the ones given in parentheses should be considered as only tentative. Further to the blue, almost all considered assignments are very uncertain and are not reported in this work. However, the hole-burning spectra measured for conformer A (up to 36 000 cm^{-1}), B or C (both up to 35 450 cm^{-1}) show depletion for all the observed vibronic transitions, thus demonstrating that no other conformer is significantly populated at the temperature of the ion trap.

Table 6.2: Peak assignments for the electronic spectrum of TrpH$^+$·W$_2$ in the origin region. $\tilde{\nu}$ and I are the positions and relative intensities of the peaks in the composite spectrum. $\Delta\tilde{\nu}$(X) and I(X) are, for conformer X, the peak distances from the origin of X and the estimated relative intensity due to X. The most tentative assignments are indicated in parentheses.

$\tilde{\nu}$ [cm^{-1}]	I [%]	$\Delta\tilde{\nu}$ (A)	I(A)	Assignment	$\Delta\tilde{\nu}$ (B)	I(B)	Assignment	$\Delta\tilde{\nu}$ (C)	I(C)	Assignment
35175.8	100	0.0	(100)	Origin						
35203.0	73	27.2	(60)	v_1	0.0	(13)	Origin			
35207.0	24	31.2	(24)	v_2						
35213.1	5	37.3	(5)	(v_3)						
35221.0	7				18.0	(6)	v_1			
35223.3	85	47.5	(85)	(v_4)						
35230.3	38	54.5	(38)	2v_1						
35232.1	11							0.0	(11)	Origin
35234.0	12	58.2	(8)	v_1+v_2	30.9	(2)	(v_2)			
35235.2	38	59.4	(38)	(v_5)						
35238.6	5				35.5	(4)	2v_1			
35240.0	8	64.2	(8)	v_1+37.3						
35243.2	10				40.2	(10)	(v_2 ; v_3)			
35250.4	64	74.6	(64)	v_1+47.5						
35254.7	20	78.9	(20)	v_2+47.5						
35257.2	22	81.4	(14)	3v_1	54.1	(8)	3v_1 (and v_4)			
35259.4	9				56.3	(8)	(v_5)			
35260.7	15	84.9	(6)	(37.3+47.5)	58.1	(4)	v_1+40.2	28.6	(6)	v_1
35262.5	24	86.7	(22)	v_1+59.4						
35264.2	28	88.4	(21)	(v_7)				32.1	(7)	v_2
35267.1	55	91.3	(55)	(v_8)	63.4	(6)	(v_6)			
35270.9	63	95.1	(63)	2·47.5						
35272.6	10	96.8	(5)	37.3+59.4						
35274.3	5				71.3	(5)	(v_1+54.1 ; 30.9+40.2)			
35277.4	34	101.5	(30)	2v_1+47.5	74.3	(4)	v_1+56.3			
35280.7	14	105.4	(4)	v_1+v_2+47.5				48.6	(10)	v_3
35282.9	24	107.1	(18)	47.5+59.4	80.2	(6)	2·40.2			
35285.6	3	109.8	(3)	(?)						
35287.3	7	111.5	(4)	v_1+37.3+47.5				55.2	(3)	(v_4)
35289.1	16	113.3	(8)	2v_1+59.4				57.0	(8)	2v_1
35291.5	22	115.7	(16)	v_1+88.4				59.4	(6)	(v_5)
35293.8	33	118.0	(33)	v_1+91.3						
35295.8	18				92.7	(7)	(2v_1+56.3 ; v_7)			
35297.3	41	121.5	(41)	v_1+2·47.5 (and v_9)						
35299.7	6				96.7	(4)	40.2+56.3			
35302.2	9	126.4	(7)	v_2+2·47.5	99.3	(3)	2v_1+63.4			
35304.3	9	128.5	(9)	(3v_1+47.5 ; 37.3+91.3)						
35307.8	9							75.7	(6)	(v_6)
35308.6	9	132.8	(4)	(2v_1+v_2+47.5 ; 37.3+2·47.5)						
35309.5	13				106.5	(4)	(2v_1+71.3 ; v_8)			
35310.2	17	134.4	(14)	v_1+47.5+59.4						
35312.6	16							80.5	(7)	v_2+v_3
35313.7	45	137.9	(40)	47.5+91.3	110.6	(5)	(v_1+92.7 ; 54.1+56.3)			
35318.3	25	142.5	(22)	3·47.5	115.3	(3)	(v_1+96.7 ; 2v_1+2·40.2)			
35319.5	11	143.7	(8)	(2v_1+88.4 ; v_{10})						
35320.8	11				117.8	(3)	54.1+63.4			
35321.4	16	145.6	(13)	2v_1+91.3				89.2	(4)	(2v_1+v_2)
35323.5	8				120.5	(3)	3·40.2	91.8	(3)	v_2+59.4
35324.6	19	148.8	(18)	2v_1+2·47.5						

6.3 Discussion

6.3.1 Geometrical assignment of $TyrH^+$ conformers

The agreement between the experimental and theoretical vibrational spectra of protonated tyrosine allows one to confidently assign the geometries of the four observed conformers, apart from the orientation of the phenolic O-H bond: conformers A and C have both the COOH and NH_3^+ groups *syn* with respect to the aromatic ring, while in conformers B and D, the COOH group is in the *anti* position. Our DFT/B3LYP calculations predict that the *anti* structures are ~ 0.7 kcal·mol^{-1} lower in energy than the *syn* ones. Recent MP2 calculations performed by Grégoire et al. yielded an opposite ordering, with the *syn* geometry being ~ 0.7 kcal·mol^{-1} more stable than the *anti* [7]. Our experimental results suggest that the truth should lie somewhere in between. Indeed, a 0.7 kcal·mol^{-1} energy difference implies that the most stable conformer would be about 3 times more abundant than the other at room temperature, a ratio that would undoubtedly increase upon cooling. However, a rough estimation based on the respective vibronic intensities and on the fragmentation patterns of conformers A and B show that their relative populations in the trapped ion cloud are approximately equivalent. Therefore, the *anti* and *syn* conformations seem to be almost isoenergetic, which would then be the case of all four conformers (A, B, C and D), since the orientation of the phenolic O-H bond should have a negligible influence on their relative energies, as confirmed by the calculations. According to these, the conformational preferences are mainly determined by two stabilizing interactions. The first one takes place between the charged ammonium group and the π-electron cloud of the phenol ring, so that structures where these two moieties are oriented *anti* to each other are less stable by 5 to 6 kcal·mol^{-1}. The second interaction is the hydrogen bond from the NH_3^+ group to the carbonyl oxygen (N-H···O=C), which is significantly stronger than that to the hydroxyl oxygen (N-H···OH): a rotation of ~ 180° around the C_α-COOH bond destabilizes the lowest-energy conformers by about 4 kcal·mol^{-1}.

The relatively low number of conformers that we observe for $TyrH^+$ is in contrast to the results of several spectroscopic studies of jet-cooled neutral tyrosine, for which eight to ten separate conformers have been identified, depending on the authors [8-11]. This observation is reinforced by the computational data reported by Inokuchi et al., who calculated twelve structures of Tyr within 2 kcal·mol^{-1} of the global minimum at the DFT/B3LYP/6-31+G* level of theory [11], whereas our fifth most stable conformation of TyrH^{+} has a relative energy of ~ 4 kcal·mol^{-1}. Despite the distinct cooling mechanisms of molecules involved in these experiments and ours$^{(1)}$, these differing numbers of conformers can be easily explained by the protonation state of tyrosine. Indeed, the NH_2 group of neutral Tyr can potentially adopt three different orientations and, in some structures, acts as an H-bond acceptor with the carboxylic O-H bond. This possibility is obviously missing in the protonated species, since the NH_3^+ group has a threefold symmetry axis along the C_α-N bond and can only act as an H-bond donor.

Another distinction with neutral tyrosine [10, 11] is that TyrH^{+} apparently exhibits a much more important vibronic activity, showing progressions, however short, in many low-frequency vibrational modes (see Table 6.1). A possible interpretation of this fact is the following. As mentioned above, the charge on the ammonium group plays a major role in the stabilization of the conformers through its interaction with the π-electron cloud of the phenol ring. When the ion is excited to the S_1 electronic state, some electron density is displaced from the ring to the NH_3^+ group, owing to a partial πσ* character of that state. As a consequence, the charge on the ammonium, and hence its interaction with the π-cloud, is somewhat reduced, so that the equilibrium geometry of the excited state is sensibly different from that of S_0. In particular, the dihedral angles of the C_α-C_β and C_β-C_γ bonds, which are involved in most of the low-frequency torsional modes, may change significantly and thus induce vibronic activity in these modes. This explanation is consistent with the fact that protonated phenylalanine, which supposedly has a lower πσ* excited-state character than TyrH^{+} [12], shows much less vibronic activity in its electronic spectrum [6].

6.3.2 Geometrical assignment of TrpH^{+}·W_2 conformers

All experimental conformers of TrpH^{+}·W_2 possess one redshifted intense W SS band, indicative of hydrogen bonding of a water molecule to the indole π-cloud. The DFT/B3LYP structures that present this characteristic are not necessarily predicted among the most stable, and other geometries have a lower calculated relative energy. This suggests that the applied theoretical model underestimates the stabilizing power of the water-indole hydrogen bond, which may play a key role in determining which conformers have the lowest energy. This deficiency has already been pointed out in studies comparing the results of DFT and MP2 calculations on systems where water binds to an aromatic ring [13, 14]. If one takes a $TrpH^+$ conformer of type I, i.e., having the COOH group *anti* to the indole ring and the NH_3^+ group on the «pyrrole side» of it, and attaches one water molecule to the ammonium and above the π-cloud, there are three plausible locations for the second water: to either of the two remaining NH_3^+ hydrogen atoms (structures I(up,ind) and I(out,ind)) or to the carboxylic O-H bond (structure I(COOH,ind)). These three structures are the ones represented in Figure 6.5 and could presumably correspond to the three conformers observed experimentally. If that is the case, I(COOH,ind) would clearly be the geometry of conformer A, with an intense redshifted W_{ind} SS transition and a COO-H stretch frequency shifted outside the range of the experimental spectrum. Conformers B and C would then be associated with structures I(up,ind) and I(out,ind). The lower intensity and smaller shift of W_{ind} SS in the calculated spectrum of I(up,ind)_b suggest that I(up,ind)_a should be a better candidate geometry. We can thus tentatively assign I(up,ind)_a to conformer B and I(out,ind) to conformer C by considering the respective splits of the W AS and W SS frequencies in the experimental and theoretical spectra: the two W AS transitions of conformer B are separated by 20 cm^{-1} and those of conformer C by 13 cm^{-1}, while the calculated splits are 25 cm^{-1} for I(up,ind)_a and 12 cm^{-1} for I(out,ind). Likewise, the W SS splitting is ~ 8 cm^{-1} larger for B than for C(1), and the predicted values are 65 cm^{-1} for I(up,ind)_a and 59 cm^{-1} for I(out,ind). This assignment is further supported by comparing the calculated ground-state low-frequency vibrations with the spacings of vibronic transitions in the conformer-specific electronic spectra (see Table 6.2). Indeed, the vibronic peak attributed to ν_1 appears 18 cm^{-1} to the blue of the origin in the spectrum of conformer B and at 29 cm^{-1} for C, whereas the predicted (unscaled) frequencies of this mode are 16 cm^{-1} for I(up,ind)_a and 23 cm^{-1} for I(out,ind). Such considerations also tend to confirm the assignment of the lowest-energy structure I(COOH,ind) to the major conformer A, because its calculated ν_1 frequency of 29 cm^{-1} is in reasonable agreement with the 27 cm^{-1} measured experimentally.

---

(1) Supersonic expansion cooling can trap higher-energy conformers in their local minima, while our technique presumably allows interconversion and selects the most stable ones.

---

(1) Even though one cannot distinguish between the W_{ind} SS and COO-H transitions of both B and C, their frequencies are almost the same in the two spectra, so that this difference of ~ 8 cm^{-1} between B and C applies regardless of which peak is considered as W_{ind} SS.

Assuming that the above geometrical assignments are correct, it may seem surprising that the most stable conformer of $TrpH^+{\cdot}W_2$ has only one water attached to the ammonium group, while one might intuitively expect the charge to get entirely solvated before any other site starts to be so. However, a careful examination of I(COOH,ind) helps rationalize this eventuality. The lack of a second water-NH_3^+ hydrogen bond is of course partially compensated by the one formed with the carboxylic O-H bond. Moreover, this structure happens to have the shortest distance, among all calculated geometries, between one of the free ammonium H atoms and the carbonyl oxygen (< 2 Å), which likely contributes to its stabilization. Finally, the orientation of the NH_3^+ group suggests that the second free N-H bond might have some favorable interaction with the aromatic ring. These ideas are corroborated by the calculated stretching frequencies of these two «free» N-H bonds, which show considerable red shifts in comparison with other structures.

From a combined experimental and computational study of hydrated complexes of neutral jet-cooled Trp, Simons and coworkers deduced that the binding of water molecules is primarily driven by the solvation of the COOH group [14]. On the other hand, room-temperature spectroscopic experiments conducted in our laboratory led to the conclusion that the stepwise hydration of protonated valine and tryptophan begins with the filling of a complete solvation shell around the charged site [15, 16]. Thus, the current findings seem to contradict this proposed mechanism, at least in the particular case of $TrpH^+{\cdot}W_2$. Two important advantages of the results presented here over these earlier studies are the increased spectral resolution provided by the low temperature of the ions and the conformer-specificity achieved through the use of double resonance spectroscopic schemes. Nevertheless, as pointed out previously, it cannot be completely excluded that the single peak observed at 3555 cm^{-1} in the IR spectrum of conformer A may stem from an accidental overlap of the COO-H and W_{ind} SS transitions, in which case the associated structure would not be I(COOH,ind). Multiple approaches could be implemented to help clarify this question. From a computational point of view, higher-level calculations would be necessary to obtain more reliable relative energies of the predicted structures, as well as more accurate theoretical frequencies of the water stretch modes. Anharmonic frequency calculations would also permit more faithful comparisons with the recorded spectra. Experimentally, the extension of IR dip spectra measurements to lower frequencies, particularly in the bound N-H stretch region where the various theoretical spectra show strong dissimilarities, would facilitate the geometrical assignments of conformers. Additionally, the acquisition of higher-resolution electronic spectra, in combination with simulated rotational band contours, could also assist in this task. This strategy has been applied by several groups to determine the structures of many flexible molecules and their hydrated complexes [17-25]. A possible alternative would be to measure the IR spectra of $TrpH^{+}\cdot W_2$ isotopically substituted with ^{18}O, so that the COO-H stretch and W_{ind} SS frequencies would potentially show different shifts, which would reveal if the 3555 cm^{-1} transition of conformer A is a single or a double peak.

References

[1] W. D. Cornell, P. Cieplak, C. I. Bayly, I. R. Gould, K. M. Merz, D. M. Ferguson, D. C. Spellmeyer, T. Fox, J. W. Caldwell and P. A. Kollman, *Journal of the American Chemical Society* **1995**, *117*, 5179-5197.

[2] *MacroModel*, version 9.1; Schrödinger, LLC, New York NY, 2005.

[3] A. D. Becke, *Journal of Chemical Physics* **1993**, *98*, 5648-5652.

[4] C. Lee, W. Yang and R. G. Parr, *Physical Review B* **1988**, *37*, 785-789.

[5] *Gaussian 03*, Revision C.02; M. J. Frisch, et al.; Gaussian, Inc., Wallingford CT, 2004.

[6] J. A. Stearns, S. Mercier, C. Seaiby, M. Guidi, O. V. Boyarkin and T. R. Rizzo, *Journal of the American Chemical Society* **2007**, *129*, 11814-11820.

[7] G. Grégoire, C. Jouvet, C. Dedonder and A. L. Sobolewski, *Journal of the American Chemical Society* **2007**, *129*, 6223-6231.

[8] S. J. Martinez, J. C. Alfano and D. H. Levy, *Journal of Molecular Spectroscopy* **1992**, *156*, 421-430.

[9] R. Cohen, B. Brauer, E. Nir, L. Grace and M. S. de Vries, *Journal of Physical Chemistry A* **2000**, *104*, 6351-6355.

[10] L. I. Grace, R. Cohen, T. M. Dunn, D. M. Lubman and M. S. de Vries, *Journal of Molecular Spectroscopy* **2002**, *215*, 204-219.

[11] Y. Inokuchi, Y. Kobayashi, T. Ito and T. Ebata, *Journal of Physical Chemistry A* **2007**, *111*, 3209-3215.

[12] H. Kang, C. Jouvet, C. Dedonder-Lardeux, S. Martrenchard, G. Grégoire, C. Desfrançois, J. P. Schermann, M. Barat and J. A. Fayeton, *Physical Chemistry Chemical Physics* **2005**, *7*, 394-398.

[13] U. Zimmerli, M. Parrinello and P. Koumoutsakos, *Journal of Chemical Physics* **2004**, *120*, 2693-2699.

[14] P. Çarçabal, R. T. Kroemer, L. C. Snoek, J. P. Simons, J. M. Bakker, I. Compagnon, G. Meijer and G. von Helden, *Physical Chemistry Chemical Physics* **2004**, *6*, 4546-4552.

[15] A. Kamariotis, O. V. Boyarkin, S. R. Mercier, R. D. Beck, M. F. Bush, E. R. Williams and T. R. Rizzo, *Journal of the American Chemical Society* **2006**, *128*, 905-916.

[16] A. Kamariotou, *Infrared photofragment spectroscopy of charged amino acid water clusters in the gas phase*, Ph.D. Thesis, EPFL, Lausanne, 2006.

[17] L. A. Philips and D. H. Levy, *Journal of Chemical Physics* **1988**, *89*, 85-90.

[18] J. A. Dickinson, P. W. Joireman, R. W. Randall, E. G. Robertson and J. P. Simons, *Journal of Physical Chemistry A* **1997**, *101*, 513-521.

[19] R. T. Kroemer, K. R. Liedl, J. A. Dickinson, E. G. Robertson, J. P. Simons, D. R. Borst and D. W. Pratt, *Journal of the American Chemical Society* **1998**, *120*, 12573-12582.

[20] D. W. Pratt, *Annual Review of Physical Chemistry* **1998**, *49*, 481-530.

[21] M. R. Hockridge, S. M. Knight, E. G. Robertson, J. P. Simons, J. McCombie and M. Walker, *Physical Chemistry Chemical Physics* **1999**, *1*, 407-413.

[22] M. Mons, E. G. Robertson, L. C. Snoek and J. P. Simons, *Chemical Physics Letters* **1999**, *310*, 423-432.

[23] J. R. Carney and T. S. Zwier, *Journal of Physical Chemistry A* **2000**, *104*, 8677-8688.

[24] L. C. Snoek, E. G. Robertson, R. T. Kroemer and J. P. Simons, *Chemical Physics Letters* **2000**, *321*, 49-56.

[25] E. G. Robertson and J. P. Simons, *Physical Chemistry Chemical Physics* **2001**, *3*, 1-18.

Chapter 7 Conclusions

7.1 Summary

This thesis has described the construction of a novel apparatus which combines the multiple advantages of ESI tandem mass spectrometry with the very efficient ion cooling provided by collisional thermalization in a cryocooled 22-pole ion trap. A nanospray source potentially allows the production of arbitrarily large biomolecular ions and a first quadrupole mass filter selects the species of interest according to its mass and number of charges. These ions are then accumulated and thermalized in the ion trap *via* collisions with a pulsed helium buffer gas. Photodissociation spectroscopy is carried out on the ions by irradiating them with infrared and/or ultraviolet laser light, and the resulting charged fragments are subsequently released and mass analyzed by a second quadrupole mass filter. A few experiments have shown that trapping times of several seconds can readily be achieved and that the vibrational temperature of trapped ions is on the order of 10 K.

To demonstrate the potential applications of this instrument, we started by studying the spectroscopy of two protonated aromatic amino acids. Photodissociation electronic spectra are reported for cold protonated tyrosine ($TyrH^+$) and tryptophan ($TrpH^+$), and for two hydrated complexes of the latter ($TrpH^+{\cdot}W_1$ and $TrpH^+{\cdot}W_2$). The first striking feature that we observed is the difference between the spectrum of $TyrH^+$, showing well-resolved vibronic transitions (FWHM of ~ 2.4 cm^{-1}), and that of $TrpH^+$, which presents a broad S_0-S_1 transition ~ 350 cm^{-1} wide. This dissimilarity has been attributed to a large difference between the excited-state lifetimes of the two species, in (partial) agreement with the femtosecond pump-probe experiments of Jouvet and coworkers [1]. Although the 22 ps lifetime that they measured for $TyrH^+$ is consistent with the vibronic bandwidth of our peaks, the value of 400 fs reported for $TrpH^+$ seems overestimated, considering the broadness of our spectrum. This discrepancy could be caused by distinct experimental conditions or explained by the fact that they probed a different (possibly secondary) deactivation process. Nevertheless, the contrast of excited-state dynamics for $TyrH^+$ and $TrpH^+$ is now clearly established, and has been explained by the coupling between the initially excited $\pi\pi^*$ state and a nearby dissociative $\pi\sigma^*$ state, which would be much stronger for $TrpH^+$ and thus trigger an ultrafast decay of S_1. On the other hand, there is no consensus yet on the detailed deactivation mechanisms that take place in these two molecules. In fact, some of our experimental results are not compatible with the latest interpretations reported by Jouvet and coworkers, based on quantum chemical calculations. In particular, they ascribed the 22 ps lifetime of $TyrH^+$ to a proton-transfer process followed by internal conversion and dissociation in the electronic ground state [2], which implies a *statistical* fragmentation of the ion. However, the major fragment in its cold photodissociation mass spectrum is *m/z* 107, which results from a *nonstatistical* dissociation. The case of $TrpH^+$ is not entirely clear either, because a second 15 ps decay component is observed in the time-resolved experiments, whereas no long-lived conformer (i.e., having sharp transitions) is detected in our spectrum. Again, the differing experimental conditions of the two approaches complicates the interpretation of these results, but our current data are overall more consistent with a fast deactivation of the mixed $\pi\pi^*/\pi\sigma^*$ state (possibly followed by H atom loss) than with the proton-transfer mechanism.

The electronic spectra acquired for the hydrated complexes revealed, quite surprisingly, that solvation of $TrpH^+$ by a small number of water molecules dramatically increases the lifetime of its excited state. In particular, the spectrum of $TrpH^+\cdot W_2$ is fully vibrationally resolved and shows no contribution from a short-lived conformer. Based on the model assumed for the bare ion, we interpreted this observation as resulting from a decoupling of the $\pi\pi^*$ and $\pi\sigma^*$ states, owing to a destabilization of the latter by its interaction with the oxygen electrons of the water molecules. This hypothesis has been supported by TDDFT calculations of the excited-state energies of $TrpH^+$ and $TrpH^+\cdot W_2$, which predict a strong $\pi\sigma^*$ character for the S_1 state of the bare ion and a 1.3 eV destabilization of the σ^* orbitals in the complex. Additionally, computations of the excited-state time evolution have shown an ultrafast relaxation (~ 10 fs) of the $TrpH^+$ S_1 orbitals followed by the rapid cleavage of a covalent bond, whereas the electronic structure of $TrpH^+\cdot W_2$ remains practically unchanged over at least 100 fs. Some sharp spectral features in the spectrum of $TrpH^+{\cdot}W_1$ indicate that this effect probably also occurs in a minor conformer of the monohydrated complex. Finally, similar calculations and spectroscopic measurements on $GlyTrpH^+$ and $GlyGlyTrpH^+$ confirmed that the coupling of the $\pi\pi^*$ and $\pi\sigma^*$ states results from a *through-space* interaction between the indole ring and the charged ammonium group, which underlines the universal importance of such phenomena in tryptophan-containing peptides and proteins.

In the last part of this dissertation, we have demonstrated the successful implementation of IR-UV double resonance techniques by measuring conformer-specific vibrational and electronic spectra of $TyrH^+$ and $TrpH^+{\cdot}W_2$. These results have shown that, in the conditions of our experiments, four conformers of protonated tyrosine are present, with relatively similar populations. In contrast, the spectra of $TrpH^+{\cdot}W_2$ reveal the presence of only three different conformers, two of which exist in minor quantities. By comparison with DFT calculated structures and infrared spectra, we have attempted to ascribe specific geometries to each of the experimentally observed conformers. The excellent agreement between the predicted and measured vibrational spectra of $TyrH^+$ allowed us to give reliable structural assignments of its conformers, except for the orientation of the phenolic O-H bond that has very little influence on the vibrational frequencies. All of them exhibit a backbone/ring orientation where the ammonium group is *syn* relative to the aromatic ring, which suggests that the interaction between the charge and the π-electron cloud is strongly stabilizing. For $TrpH^+{\cdot}W_2$, tentative assignments have been proposed, but would require further study to get confirmed. Notably, the geometry of the main conformer is made uncertain by the «absence» of a transition in its infrared spectrum when compared with the two others. Two possible interpretations could explain this observation. One is the coincidental overlap of the COO-H stretch and one of the water symmetric stretches. In this case, the corresponding structure would have the two water molecules hydrogen-bonded to the charged ammonium group. On the other hand, it may be more likely that the COO-H stretch transition is redshifted outside the range of our spectrum, which would mean that one of the water molecules is attached to the the carboxylic O-H bond. This alternative, if confirmed, would have important implications for our understanding of the solvation mechanism of gas-phase ions. Indeed, earlier studies conducted in our own laboratory seemed to indicate that solvation was primarily taking place at the charged site [3, 4]. Nonetheless, despite the uncertainty of our assignments, two features are common to all lowest-energy structures and must hence play a decisive role in their stabilization. One is the geometry of the tryptophan molecule, which is similar to the global minimum calculated for the bare ion, probably due to a favorable interaction between the ammonium group and the aromatic ring, as is the case for $TyrH^+$. The second is the presence of a water molecule that simultaneously solvates the charge and acts as proton donor to the indole ring. This characteristic emphasizes the importance of hydrogen bonding to π-systems in determining the conformational preferences of biomolecules.

7.2 Future perspectives

The electronic and vibrational spectra that we measured for relatively small protonated species have established the feasibility of conformer-specific spectroscopy on cold gas-phase biomolecular ions, which shows very promising prospects for future research on a variety of possible systems. Following the experiments presented herein, our group has already pursued analogous investigations on different molecules, starting with the third aromatic amino acid, phenylalanine, whose ultraviolet and infrared spectra have been recorded [5]. These results revealed the presence of only two stable conformers of $PheH^+$ having similar structures to $TyrH^+$. Then, two tyrosine-containing dipeptides were examined, alanyltyrosine and tyrosylalanine, and their conformer assignments further highlighted the stabilizing strength of the interaction between the charged N-terminus and the aromatic ring [6]. The most recent research aims at probing the spectroscopic signatures of short helical polypeptides, based on the work of Jarrold and coworkers, who showed that adding a lysine residue to the C-terminus of protonated polyalanines favors the formation of helices in the gas phase [7, 8]. The UV and IR spectra measured for such molecules having an N-terminal Phe residue are amazingly simple and well-resolved [9], and a combination of DFT calculations and ^{15}N isotopic substitution has confirmed their helical structure.

These latest results are quite encouraging and suggest that even larger biomolecules would yield reasonably structured and hence informative spectra, so that entire proteins or other naturally occurring molecules could eventually be studied by such techniques. However, as already discussed in *Chapter 3* (see *3.3.3 Molecular size and lifetime* *considerations*), a primary limitation to the photodissociation of very large systems is the dilution of the photon energy by IVR, which could preclude their fragmentation. Among the possible strategies that we proposed to circumvent this restriction, one has very recently been put into practice with surprising success. Using CO_2 laser pulses in an IRLAPS-like spectroscopic scheme [10, 11], protonated polypeptides containing 17 residues have been fragmented upon absorption of a UV photon followed by IRMPD. This method resulted in a increase of signal by two orders of magnitude compared to the UV-only excitation. A similar procedure could potentially be implemented by replacing the infrared by UV laser light, whose photons are considerably more energetic (~ 35 000 cm^{-1} versus ~ 1000 cm^{-1}), thus creating a so-called UVLAPS technique. Clearly, many different spectroscopic tools, already existing or to be invented, remain to be designed and/or tested on our instrument. One of them could be the *triple* resonance IR-IR-UV hole-burning that Zwier and coworkers reported a few months ago [12]. The ability of this method to obtain conformer-specific IR spectra from a congested electronic spectrum may well become of use for investigating larger molecules, or even in the case of lifetime-broadened spectra such as that of $TrpH^+$.

Finally, we can suggest some modifications of the apparatus that will improve its performances. First, the second quadrupole mass filter used for fragment ion analysis should be replaced (or completed) by a device that allows the acquisition of a complete mass spectrum for each ion packet. Indeed, on the current instrument, optical spectra obtained by detecting different fragments must be recorded one at a time, making it a very time-consuming task. As a consequence, photofragment electronic spectra are rarely measured in more than one or two fragment mass channels. However, knowing the particular fragmentation pattern of a molecule at each point of its electronic spectrum can be extremely informative, as exemplified by the different photofragment mass spectra that we measured for $TyrH^+$ (see Figure 6.4), or by the study of Talbot et al. on the photodissociation pathways of protonated tryptophan [13]. More importantly, the electronic spectrum recorded only in a single mass channel can be misleading, since the quantum yield of dissociation for a given fragment can be wavelength-dependent, e.g., owing to enhanced secondary fragmentation at high photon energy. We have observed such an occurrence in the electronic spectra of $TrpH^+$ (see Figure 4.2). Implementing a time-of-flight mass spectrometer, for instance, would make such two-dimensional measurements possible. On the other hand, combining TOF fragment detection with the linear 22-pole ion trap would certainly raise some technical problems that will have to be dealt with [14]. In particular, the ion packet exiting the trap after photodissociation can be quite elongated, so that only a fraction of it would be in the acceleration region of the TOF at the moment of the extraction pulse. Different possibilities exist to minimize the loss of signal caused by this. For instance, the extraction plates can be pulsed at short intervals, in order to analyze several «samples» from a single ion packet [15-17]. Another alternative would be to install, around the 22-pole ion trap, a series of ring electrodes that can be applied individual voltages, so as to create a potential well in the axial direction, which would spatially compress the ion packet and thus the detection efficiency [18-20].

Another possible modification is the coupling of the ESI source with an ion mobility stage in order to combine both mass and conformational selectivities. A FAIMS source, whose principles of operation have been very briefly presented in the *Introduction*, would typically be the design of choice, since it provides a continuous flow of conformationally selected ions [21]. However, the question must be adressed whether the selected ions will retain their conformation until laser probing or if interconversion would occur beforehand. Such considerations are currently being discussed in our group in the process of designing a new-generation instrument.

References

[1] H. Kang, C. Jouvet, C. Dedonder-Lardeux, S. Martrenchard, G. Grégoire, C. Desfrançois, J. P. Schermann, M. Barat and J. A. Fayeton, *Physical Chemistry Chemical Physics* **2005**, *7*, 394-398.

[2] G. Grégoire, C. Jouvet, C. Dedonder and A. L. Sobolewski, *Journal of the American Chemical Society* **2007**, *129*, 6223-6231.

[3] A. Kamariotis, O. V. Boyarkin, S. R. Mercier, R. D. Beck, M. F. Bush, E. R. Williams and T. R. Rizzo, *Journal of the American Chemical Society* **2006**, *128*, 905-916.

[4] A. Kamariotou, *Infrared photofragment spectroscopy of charged amino acid water clusters in the gas phase*, Ph.D. Thesis, EPFL, Lausanne, 2006.

[5] J. A. Stearns, S. Mercier, C. Seaiby, M. Guidi, O. V. Boyarkin and T. R. Rizzo, *Journal of the American Chemical Society* **2007**, *129*, 11814-11820.

[6] J. A. Stearns, M. Guidi, O. V. Boyarkin and T. R. Rizzo, *Journal of Chemical Physics* **2007**, *127*, 154322/1-7.

[7] R. R. Hudgins and M. F. Jarrold, *Journal of the American Chemical Society* **1999**, *121*, 3494-3501.

[8] M. F. Jarrold, *Physical Chemistry Chemical Physics* **2007**, *9*, 1659-1671.

[9] J. A. Stearns, O. V. Boyarkin and T. R. Rizzo, *Journal of the American Chemical Society* **2007**, *129*, 13820-13821.

[10] R. D. F. Settle and T. R. Rizzo, *Journal of Chemical Physics* **1992**, *97*, 2823-2825.

[11] O. V. Boyarkin and T. R. Rizzo, *Journal of Chemical Physics* **1995**, *103*, 1985-1988.

[12] V. A. Shubert and T. S. Zwier, *Journal of Physical Chemistry A* **2007**, *111*, 13283-13286.

[13] F. O. Talbot, T. Tabarin, R. Antoine, M. Broyer and P. Dugourd, *Journal of Chemical Physics* **2005**, *122*, 074310/1-5.

[14] D. J. Douglas, A. J. Frank and D. M. Mao, *Mass Spectrometry Reviews* **2005**, *24*, 1-29.

[15] J. M. Campbell, B. A. Collings and D. J. Douglas, *Rapid Communications in Mass Spectrometry* **1998**, *12*, 1463-1474.

[16] C. S. Hoaglund, S. J. Valentine, C. R. Sporleder, J. P. Reilly and D. E. Clemmer, *Analytical Chemistry* **1998**, *70*, 2236-2242.

[17] E. R. Badman, C. S. Hoaglund-Hyzer and D. E. Clemmer, *Analytical Chemistry* **2001**, *73*, 6000-6007.

[18] D. Gerlich and S. Horning, *Chemical Reviews* **1992**, *92*, 1509-1539.

[19] D. Gerlich, *Journal of the Chemical Society, Faraday Transactions* **1993**, *89*, 2199-2208.

[20] A. Luca, S. Schlemmer, I. Cermak and D. Gerlich, *Review of Scientific Instruments* **2001**, *72*, 2900-2908.

[21] R. Guevremont, *Journal of Chromatography A* **2004**, *1058*, 3-19.

List of figures

Figure 1.1: Growth of activity in the field of biomolecular structure determination 2
Figure 2.1: Section view of the tandem mass spectrometer 24
Figure 2.2: Sequence of events during a typical photodissociation experiment 25
Figure 2.3: Spray formation and droplet fission in an ESI source 30
Figure 2.4: The nano-electrospray source used in this work 32
Figure 2.5: The static quadrupole potential 34
Figure 2.6: Stability diagram showing the lower stability region in the (a,q) plane 35
Figure 2.7: Relative effective potentials for a quadrupole, an octupole and a 22-pole 37
Figure 2.8: Calculated ion trajectories in an octupole and a 32-pole rf trap 38
Figure 2.9: Energy distribution of C^+ ions in a ring-electrode trap with H_2 at 80 K 39
Figure 2.10: Schematic section view and picture of the 22-pole ion trap 40
Figure 2.11: Timing diagram used to probe the helium pumping time 43
Figure 2.12: Variation of the trapping efficiency of the 22-pole as helium is evacuated ... 44
Figure 2.13: Trapping efficiency of the 22-pole as a function of the trapping time 46
Figure 2.14: Mass spectrum of $TyrH^+$ at low temperature showing some $TyrH^+{\cdot}He$ 47
Figure 2.15: Origin region of the electronic spectrum of $TrpH^+{\cdot}W_2$ at low temperature ... 50
Figure 2.16: Schematic diagram of the UV generation setup 51
Figure 2.17: Schematic diagram of the IR generation setup 53
Figure 3.1: Typical timing diagram for a photodissociation experiment 58
Figure 3.2: Spectroscopic schemes of electronic and vibrational photodissociation 61
Figure 3.3: Photofragment mass spectra of $TyrH^+$ at room temperature and at 6 K 71
Figure 3.4: Spectroscopic schemes of IR-UV double resonance 73
Figure 4.1: Photofragment mass spectra of $TrpH^+$ at room temperature and at 6 K 82
Figure 4.2: Electronic spectrum of $TrpH^+$ at room temperature and at 6 K 85
Figure 4.3: Photofragment mass spectra of $TyrH^+$ at room temperature and at 6 K 87

Figure 4.4: Electronic spectrum of $TyrH^+$ at room temperature and at 6 K 90
Figure 4.5: Energy diagram of the states involved in the H atom loss reaction 95
Figure 5.1: Photofragment mass spectra of $TrpH^+{\cdot}W_1$ at room temperature and at 6 K 105
Figure 5.2: Photofragment mass spectra of $TrpH^+{\cdot}W_2$ at room temperature and at 6 K 107
Figure 5.3: Electronic spectra of $TrpH^+$, $TrpH^+{\cdot}W_1$ and $TrpH^+{\cdot}W_2$ at 6 K 109
Figure 5.4: Metadynamics free energy landscape in the (ϕ_1,ϕ_2) subspace for $TrpH^+$ 113
Figure 5.5: Three stable geometries of $TrpH^+{\cdot}W_2$ obtained by metadynamics/MD 114
Figure 5.6: Two stable geometries of $TrpH^+{\cdot}W_2$ found at the DFT level 115
Figure 5.7: Time evolution of photoexcited $TrpH^+$ and $TrpH^+{\cdot}W_2$ 118
Figure 5.8: Lowest-energy conformer and excited-state orbital of $GlyTrpH^+$ 120
Figure 5.9: Geometry and orbitals of the 3-methylindole-methylammonium complex . 121
Figure 6.1: Infrared dip spectrum of $TyrH^+$ recorded with the UV at 35 082 cm^{-1} 127
Figure 6.2: Infrared dip spectrum of $TyrH^+$ recorded with the UV at 35 111 cm^{-1} 128
Figure 6.3: IR-UV hole-burning measurements in the origin region of $TyrH^+$ 130
Figure 6.4: Photofragment mass spectra of $TyrH^+$ at 35 082 cm^{-1} and 35 111 cm^{-1} 133
Figure 6.5: Infrared dip spectra of $TrpH^+{\cdot}W_2$ 135
Figure 6.6: IR-UV hole-burning measurements in the origin region of $TrpH^+{\cdot}W_2$ 139

List of tables

Table 2.1: Estimates of the vibrational temperature of $TrpH^+ \cdot W_2$ in the cold trap 50

Table 5.1: Vertical excitation energies of $TrpH^+$ by RI-CC2 and TDDFT/B3LYP 117

Table 6.1: Peak assignments for the electronic spectrum of $TyrH^+$ 132

Table 6.2: Peak assignments for the electronic spectrum of $TrpH^+ \cdot W_2$ 141

List of abbreviations and acronyms

B3LYP: Becke-3-Lee-Yang-Parr hybrid functional
BIRD: blackbody infrared radiative dissociation
CID: collision-induced dissociation
CT: charge transfer
DFM: difference frequency mixing
DFT: density functional theory
ESI: electrospray ionization
FAIMS: high-field asymmetric waveform ion mobility spectrometry
FD: field desorption
FT-ICR: Fourier transform ion cyclotron resonance
FWHM: full width at half maximum
i.d.: inner diameter
IC: internal conversion
IR: infrared
IRLAPS: infrared laser-assisted photofragment spectroscopy
IRMPD: infrared multiphoton dissociation
IVR: intramolecular vibrational energy redistribution
LD: laser desorption
LIF: laser-induced fluorescence
m/z: mass-to-charge ratio
MALDI: matrix-assisted laser desorption/ionization
MD: molecular dynamics
MPI: multiphoton ionization
MPn: n^{th}-order Møller-Plesset perturbation theory
MS^n: multistage mass spectrometry
NMR: nuclear magnetic resonance
OPO: optical parametric oscillator
PA: proton affinity
PES: potential energy surface
R2PI: resonantly enhanced two-photon ionization
rf: radio frequency
SID: surface-induced dissociation
TDDFT: time-dependent density functional theory
TOF: time-of-flight
UV: ultraviolet
YAG: yttrium aluminum garnet

Acknowledgements

There are quite a few people who made it possible for me to achieve this thesis (maybe in part because of its exceptional duration!), and I would like to express my profound gratitude to all of them. Hopefully, the following list will do justice to the most part:

To begin with, Prof. Tom Rizzo: firstly, for giving me the opportunity to work in his group and particularly on this nascent «bioproject», which, despite its rather slow burgeoning, has eventually become extremely fruitful; and secondly, for his constant support and patience in the course of this difficult writing.

Prof. Christophe Jouvet, Prof. John Maier, Prof. Yury Tsybin and Prof. Hubert Girault for kindly accepting to evaluate this work and be part of the examination committee.

Dr. Oleg Boyarkin, for the wonderful ion trap that he designed and built, his knowledge of lasers of which I could grasp but a little slice, and his invaluable assistance and advice in the lab. This work would not have been possible without him (or it would have been much worse).

Dr. Anthi Kamariotis, for her solidarity during the sometimes tough times spent together in the lab, the amount of «petits yaourts RÀB» that we shared, and her continuous support and encouragement, even after she left our group.

All other members of the LCPM group, past and present, that I had the chance to meet, and in particular those with whom I closely collaborated: Amanz Ruf, Dr. Rainer Beck, Antoine Milon, Rachele Chianese, Monia Guidi, Dr. Jaime Stearns (thanks for the calculations!), Caroline Seaiby, Dr. Annette Svendsen and Ulrich Lorenz.

Marianne Dang, our secretary, for her crucial help in many critical moments and for her incredible kindness.

The group of Prof. Ursula Röthlisberger and in particular Matteo Guglielmi, Dr. Michele Cascella and Dr. Ivano Tavernelli, who have performed very neat calculations to help us interpret our results.

André, Gérard and Jean-Luc from the mechanical workshop, Gaby and Nono from the electrical workshop, without whom none of our instruments would be functioning.

Finally, of course, my family and friends, many of whom I have met here at the EPFL, for their support and patience all along these years, and for keeping telling me, against all likelihood, that I could do it. Thank you guys!

Curriculum vitae

Sébastien R. Mercier
Born on 31 March 1978 in Lausanne, Switzerland
Swiss nationality

Education

2001-2008: Ph.D. thesis in Physical Chemistry at the École Polytechnique Fédérale de Lausanne (EPFL), Switzerland, in the group of Prof. Thomas Rizzo
Electronic and vibrational spectroscopy of cold protonated amino acids in the gas phase

1996-2001: Undergraduate studies in Chemical Engineering at EPFL
Diploma work at Purdue University, IN, USA
Laser-based spectroscopic studies of flexible biomolecules

Non-academic experience

Sept. 2006 - Apr. 2007: Civilian service at the Berne Declaration, a Swiss nongovernmental organization based in Lausanne.

Languages

French (mother tongue), English (fluent), German (basics)

Publications

- **Electronic spectroscopy of cold, protonated tryptophan and tyrosine**, O. V. Boyarkin, S. R. Mercier, A. Kamariotis and T. R. Rizzo, *Journal of the American Chemical Society* **2006**, *128*, 2816-2817.
- **Microsolvation effects on the excited-state dynamics of protonated tryptophan**, S. R. Mercier, O. V. Boyarkin, A. Kamariotis, M. Guglielmi, I. Tavernelli, M. Cascella, U. Röthlisberger and T. R. Rizzo, *Journal of the American Chemical Society* **2006**, *128*, 16938-16943.
- **Conformation-specific spectroscopy and photodissociation of cold, protonated tyrosine and phenylalanine**, J. A. Stearns, S. Mercier, C. Seaiby, M. Guidi, O. V. Boyarkin and T. R. Rizzo, *Journal of the American Chemical Society* **2007**, *129*, 11814-11820.